CARDIAC NON-LINEAR DYNAMICS AND CHAOS CONTROL IN THE CARDIAC ELECTRICAL ACTIVITY WITH PRACTICAL APPLICATIONS

By

ILIJA UZELAC

Dissertation

Submitted to the Faculty of the

Graduate School of Vanderbilt University

in partial fulfillment of the requirements

for the degree of

DOCTOR OF PHILOSOPHY

in

Physics

December, 2012

Nashville, Tennessee

Approved:

Professor John P. Wikswo

Professor Shane M. Hutson

Professor Franz J. Baudenbacher

Professor Veniamin Sidorov

Dr. Richard A. Gray

Professor Kalman Varga

ACKNOWLEDGMENTS

I would like to express my deepest gratitude to my advisor, Dr. John Wikswo, for giving me a wonderful opportunity to work in his group and his extreme patience, caring and guidance. As a great advisor for my professional and private life during my graduate studies, he helped me to build myself both professionally and as a person, overcoming many hurdles and challenges. Moreover, I'm the most thankful to John for showing me a "direction" where to go and how to master skills and gain the ability to find my own research directions.

I am thankful to Dr. Veniamin Sidorov and Dr. Richard Gray from whom I have learnt many valuable skills and broadened my knowledge in other areas not directly related to physics that gave me ability to perform research that was beneficial for my PhD studies. With the assistance of Dr. Veniamin Sidorov almost all experiments are performed, and through our collaborative work I have learnt many experimental skills techniques without which this dissertation wouldn't be possible. Through collaboration with Dr. Gray I had a wonderful experience of working in Food and Drug Administration labs (FDA) and I'm thankful to him as he introduced me into a field of non-linear dynamics and ideas of a feedback control.

During my studies I had countless talks with VIIBRE engineers Ron Reisser and Phil Samson and I'm grateful for their altruistic help during my designing the high current voltage-to-current converter. The code for the voltage-to-current converter and the feedback controller was written by Mark Holcomb and I'm thankful for his work. I'm thankful to Allison Price, for proofreading of the whole Dissertation, her comments and suggestions.

I'm thankful to my wife Danijela for all the love and support to finish the studies.

The work presented in Chapter II was supported by the American Heart Association [0635037N]; and by the National Institutes of Health [R01 HL58241-11] through the American Recovery and Reinvestment Act of 2009.

The work presented in Chapter IV work is supported in part by FDA contract, NIH Grant R01 HL58241-11 through the American Recovery and Reinvestment Act of 2009, and the Vanderbilt Institute for Integrative Biosystems Research and Education (VIIBRE).

TABLE OF CONTENTS

Page

LIST OF FIGURES

Figure Page

CHAPTER I

CHAPTER II

CHAPTER III

CHAPTER IV

CHAPTER V

CHAPTER VI

CHAPTER VII

APPENDIX B

LIST OF TABLES

TABLE Page

CHAPTER I

DEFINITION, MEANING AND DETECTION OF PHASE SINGULARITIES IN CARDIAC ELECTRICAL ACTIVITY WITH PRACTICAL APPLICATIONS

Summary

Phase space analysis applied to raw fluorescent images obtained from cardiac transmembrane electrical activity has offered a unique perspective into cardiac fibrillatory behavior for a decade. There are many different methods and procedures for phase map generation, detection of phase singularities (wave breaks and origin of rotors), and phase singularity (PS) tracking. These methods and procedures do not provide a unique set of steps that lead to PS detection. The underlying mathematical and physical background from which they emerge is well developed, but connections are not systematically studied – mathematicians often don't know the practical extent of their "tools," while physiologists and biologists don't know about the existence of these tools that may address some of their problems.

One aim of this paper is to present the underlying mathematical and physical background in which cardiac electrical activity is treated as one of many possible representations. In this light, many different studies related to cardiac electrical activity can be applied more generally than is currently is done.

A second aim is to devise a unique automated procedure, accommodated to the physiological characteristics of the rabbit heart, to detect phase singularities efficiently. This involves detailed exploration of current methods and their limitations as well as propositions for further research.

These are not, however, the only goals; another of the aims is to present the power of the general ideas arising from the theory of topological spaces, that go beyond phase singularity

detection, that is, to present the theory of phase singularities as a tool for various studies involving electrophysiological heterogeneities.

Keywords: *topological space, ring, mapping, hourglass, clock, phase singularities, coordinate singularities, state space, variables, observables, organizing center, winding number, topological charge, phase space, manifold, embedded dimension, cathodal make/break, anodal make/break.*

Introduction

Heart rhythm disorders can develop life-threatening ventricular fibrillation. Ventricular fibrillation (VF) is an irregular disturbance of the heart rhythm that quickly renders the heart incapable of sustaining life, and it kills thousands of people each week[2]. There can be many underlying substrates for an induction of a VF, such as rate[3,4,5], ischemia/infarction[6], dilatation/stretch[7], fiber orientation[8], wall thickness[9], Purkinje fibers[10], trabeculae[11], valves[12] and heart geometry[13]. These substrates can create heterogeneities in the electrophysiological properties of myocardium and interaction between any of the listed substrate, and a transient trigger[14] can create spiral waves or rotors[15,16], and develop VF. Fibrillation can result from a rapidly firing ectopic focus[17], a single reentrant circuit[18,19], or multiple meandering wavelets[20].

In the early phase of VF, high spatial and temporal resolution mapping of optical transmembrane potential can easily detect transient erupting rotors as one of the dominant features of VF[21]. Rotors may remain stationary, drift or give a rise to multiple reentrant pathways[22,23]. Therefore, it is of great importance to detect and trace spiral waves and rotors that rotate around organizing centers, which are thought to be non-excited but excitable elements[24]. The organizing center is commonly referred to as a *phase singularity* in chaos theory.

The surface of the heart can be represented as a set of excitable elements (hourglasses) where each hourglass has its own independent phase space that has a ring-like topological structure. Excitation consists of inverting an hourglass after all the sand has flowed into the lower

chamber (rest state). In this visualization an hourglass that has been flipped can invert adjacent hourglasses that are in the rest state. Ideally, each cardiomyocyte should be observed as a single hourglass. In methods relying on CCD cameras that record fluorescence signals emerging from transmembrane voltage sensitive dyes, each pixel in the sensor of the CCD camera represents an average transmembrane potential of many individual cardiomyocytes in the corresponding physical location in cardiac tissue. Sets of these cardiomyocytes still can be treated as a single excitable element or hourglass under certain conditions that preserve coherent cardiomyocyte activity within each set. The time course of each hourglass can be represented in phase space as a trajectory that represents the unique time course[25,26]. The hourglass under normal conditions remains at one stable location until an above-threshold stimulus perturbs the system and forces the excitable element into a closed-loop trajectory around an attractor. It will be proven that an hourglass is a phase singularity, if and only if, the sum of phase differences between adjacent hourglasses on a closed loop that surrounds it is $|2n_t\pi|$ where n_t is an integer. This is the necessary and sufficient condition for forming the organizing center that may form a reentrant excitatory wave, a phenomenon which occurs in cardiac fibrillation.

An integer number n_t is called the winding number in topology and the topological quantum number or topological charge[27,28] in physics. It is defined as

$$n_t(\vec{r},t) = \frac{1}{2\pi}\oint_c \nabla\theta(\vec{r},t)\cdot\overrightarrow{dl} \qquad (1)$$

where $\theta(\vec{r},t)$ is the angle or local phase in the phase space of an excitable element at position $\vec{r}$. Integration goes over other excitable elements on a closed path ***c,*** surrounding the excitable element for which we are calculating the topological charge.

To construct a ring-like topological structure for each hourglass, many different methods can be used. A common one, the time-embedded method, uses transmembrane potential *V(t)* as one observable for each hourglass and *V(t-τ)* as the second observable. In this way it can reconstruct the attractor from these two dimensions[29,30].

The overarching objective of the present proposal is to develop a methodology, encompassing a single automated algorithm, for efficient detection of phase singularities in topological spaces and establishing a connection with the real system, that is, cardiac electrical activity. The subsequent paragraphs introduce the terminology, definitions and examples corresponding to the relevant concepts behind this proposal: singularity; states, variables, and observables; hourglasses and clocks; winding number; and phase mapping.

The Term "Singularity"

The aim of this chapter is to give an overall sense of phase singularity terminology through a simple example in which phase singularities emerge.

In a descriptive definition, a singularity is a point, an argument of a function at which its value is ambiguous.

A simple example can be illustrated by imagining a globe, divided into time zones (Figure 1.1). One can imagine that in each time zone there is a watch that moves toward the north. In this way, each watch stays in its local zone and need not be reset as it moves. Eventually, all watches will end up at the North Pole, aligned on a circle whose radius tends to be zero. Now, what time is it: all times, no time? If clocks don't agree, we can look at the Sun (if it is summer), but we notice that the Sun is circling around us at a fixed altitude on the horizon as we stand fixed. Therefore, every direction is south. This can be confusing and with good reason, since this location is a so-called *phase singularity.* But why are we using the word "phase" and what does "singularity" mean? Is singularity a property of a system, or is it a "mind trap" in our observation?

A point from a ring-like topological space, such as $\boldsymbol{S}^1$ (one-dimensional ring), $\boldsymbol{S}^2$ (two-dimensional ring), etc., is usually called a phase, to emphasize its belonging to a ring-like topological space. As such, a phase is nothing else than a position on a ring just as a coordinate is a position on an interval. At every instant, local time is a function of position on the globe that maps it to the circle (ring); mapping from $\boldsymbol{S}^2 \rightarrow \boldsymbol{S}^1$, Figure 1.2. Imagine any circle inside the disk encircling its center. If we move along that circle one full cycle, the phase on the corresponding

S^1 ring should progress one full cycle as well (so-called winding number is equal to one), but this can't be done continuously. Nevertheless, this way of mapping makes a point at the center of the disk distinct from other points. This point can be mapped to any point on a circle, but it also can be left out of mapping, depending on how we want to overcome this problem. For this point we can say that it is an ambiguous point for a mapping function. In other words, this point forms a discontinuity in mapping and such discontinuity has as its name *phase singularity*: a point that pulls the map apart to all phases, and a point where all phases converge.

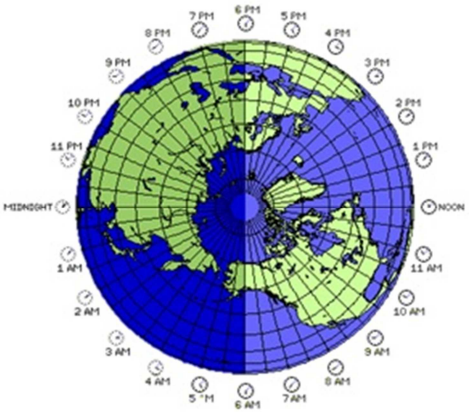

Figure 1.2.Time zones.
http://www.quadibloc.com/science/images/zone.gif[1]

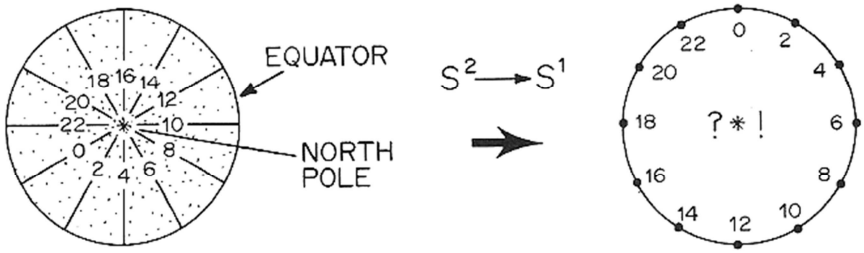

Figure 1.1. Mapping a disk onto a ring[1].

So far we can conclude that singularity is a kind of discontinuity, but the question that is raised now is whether singularities exist in the real world or are they only metaphysical entities? To answer this question, let's examine the following. Let us invent a new temperature scale called PS, on which the temperature PS is defined as reciprocal of Celsius temperature[1]. PS

temperature has a singularity at the freezing point of water (0ºC). This singularity has no physical significance, so let's call it a *coordinate singularity*, a mathematical artifact of choosing a peculiar coordinate system. However, there may be other kinds of singularities that cannot be removed by any reasonable change of coordinates. Examples are the space-time singularities associated with black holes. Let's call these singularities *real singularities.*

The phase singularity in the example with time zones is a coordinate singularity in essence, but it is common to use the word "phase" to emphasize that it emerges from ring-like topological space.

In some points of view, singularities only happen in models, while in real life, the singularity is always evaded. So models and experiments that seem to imply singularity mean that something is left out in our thinking that makes a real system evade the demand to achieve the impossible.

The initial question, do singularities exist in the real world, can be rephrased now since we know that coordinate singularities are not real. The question should be: How do we model the system so that we are sure that if singularities emerge from the model, they are real singularities? Of course, real singularities still may not exist in the real world, but the point is that we don't have at the present time a better theory to describe physical phenomena, so let's call singularities emerging from such models "real singularities," unless it is proven otherwise.

This leads to the next chapter which aims to answer what are the proper quantities in terms of which the world functions rationally and continuously.

How to Describe a System? States, Variables, Observables

The *state* of a system consists of everything we need to know about it right now in order to know what it will do next in response to a select stimulus. What represents that state, and how? State is determined by a collection of *variables of state.* Each individual variable takes its values within some topological space. In the example of Earth time zones, that topological space is a sphere or $\boldsymbol{S}^2$. Systems can have a lot of variables, but some variables are more important

than others. The subsequent question is: How do we define which variables are more important than others? This leads us to the definition of observables.

An *observable* is something that we can measure or interact with. Like state variables, different kinds of observables can be defined on different topological spaces. In the example of Earth time zones, an observable is a local time and its topological space is a S^1 ring. The value of each observable or measurement is determined by the present state of a system, so it tells us something about the system. It may not depend on some state variables, but it still can be called an observable. Therefore, an observable can be imagined as a projection from the system's state space onto some (usually) lower dimensional space.

Now the question, "What are the proper quantities in terms of which the world functions rationally and continuously?" can be answered. Those are the state variables. If singularities emerge from the model, then we are still "observing" and we didn't "break" into the nature of the system. Then, through observations we can learn more about the system, make new observables, and test them again. But sometimes we want to create a model so that singularities emerge from it. Those singularities are not real, but they have a property that carries extra information that tells us something distinct and unique about the observed system. As will be presented, in mapping cardiac electrical activity, singularities are created in a specific mapping process. Their detection reveals distinct phenomena of cardiac electrical activity: rotors and spiral waves.

In light of this, singularities in cardiac electrical activity can be viewed rather as organizing centers than (intuitively) as centers of chaos or a catastrophic event. Of course, singularities in cardiac electrical activity create chaos, but locally there are organizing centers for spiral waves and rotors.

We can invent any number of observables, but if a system has N state variables, then the first N independent observables are sufficient to determine the state of a system. The system's behavior may depend on external (environmental) conditions: temperature, external stimulus, etc. These environmental conditions are variables as well, but they don't change spontaneously

like the other variables, so they are called *parameters,* while other variables are called state variables.

To describe the system mathematically, we can go back to the definition of a state and write the following set of differential equations that completely describe the system:

$$\frac{dX_i}{dt} = F(\vec{X}, \vec{P}), \quad i = 1..N \tag{2}$$

X_i is the i-th state variable and $\vec{P}$ is a set of parameters. Observables depend on parameters and state variables:

$$\frac{dY_i}{dt} = G_i(\vec{X}, \vec{P}), \quad i = 1..M \tag{3}$$

Y_i is the i-th observable, M≤N. For example, the color of a certain octopus species is an observable that depends on its emotional state (state variable), but it is dependent on ambient light (a parameter) as well.

Circular Logic: Spaces, Rings and Mappings

So far, the relevant terminology has been defined and explained using a more philosophical than mathematical approach. From here on, the material will be articulated with more mathematical rigor.

The topological spaces that are of interest to us will be rings, or in other words, the domain and range of periodic functions. Such a one-dimensional topological space will not be a familiar $\Re^1$ space. As already introduced, it will be a S^1 topological space or simply a ring. Examples are angles, compass direction, time of day, etc. An example of two-dimensional S^2 is a torus. I will use the sole term "ring" to refer in general to any n-dimensional ring until otherwise noted. Emphasis will be on S^1 rings. In the examples with the octopus and the time zones, we can say that the ring is naturally embedded in the corresponding topological spaces. In

some other examples with higher dimensional state space, the ring won't be a S^1 ring, but some abstract multidimensional ring.

When we think of a ring, we tend to associate numbers with it, as $[0,2\pi]$ interval or an integer interval of [0,24] hours. This gives us the impression that something spectacular has to happen as we pass discontinuity at the end of an interval and "jump" back to the beginning. But nothing happens when we cross the International Date Line[1], so there is no discontinuity in this "jump."

An interval in a $\Re^1$ space doesn't have a property of continuity as a ring does. A ring is a more general topological structure, and numbers are just one way of representing it. A line of degrees $[0,2\pi]$ is commonly chosen as a representation of a S^1 ring with a silent note that 2π and 0 are equal, but the information that they represent physically equal points on the corresponding abstract ring is usually overlooked.

This generality is present as well in the example of the octopus. In that example, observables are not numbers, and since they operate on ring-like topological spaces, it follows as well that there are more abstract topological spaces than the commonly used finite intervals.

Let's examine another example. A single cardiomyocyte can be described with a set of system states: *"rest," "excited," "refractory," "relatively refractory."* These four states or points in topological space should be seen as if they are making a ring so that rest and the relative refractory states are connected to each other. When we do a measurement on this system, we can determine in which state the cardiomyocyte is, but even if the measurement process is a function of these states, results are expressed as numbers rather than words. This means that in the process of a measurement, we are associating the familiar topological space while, on the other side, nature doesn't care about our representation and has its own natural topological space in which the system functions properly.

The process of a measurement therefore can be seen as mapping between two topological spaces. The mapping of interest for us always will be mapping between rings, but not

necessarily continuous. There will be isolated points of a special interest where the argument of a mapping function represents a singularity point.

The measurement of a state of a cardiomyocyte can be done using electrodes or potentiometric optical dyes, and each way defines its own topological space. For electrodes, that will be an interval of voltages, and for potentiometric optical dyes, that will be an interval of fluorescence intensity. Since these topological spaces are obtained as a map from the same nature-chosen topological space, to which they are equivalent, it follows that they are mutually equivalent as well. Moreover, topologically they are rings since "nature chose" the topological space of an hourglass to be a ring.

With this we have proved the theorem of circular logic: Any periodic function, which is the measurement, representing biological rhythmic patterns in space and/or time must have as its domain a ring. Moreover, the co-domain of this function is a ring as well, and they are topologically equivalent.

For example, if we measure the transmembrane voltage potential of a single cardiomyocyte, and stimulate the cardiomyocyte periodically, the results will be that membrane potential, measured either with electrodes or with potentiometric fluorescence dyes, is bounded between some numbers. These numbers define the interval in $\Re^1$ noted as I^1, and by the theorem of circular logic I^1 and S^1 are topologically equivalent. More generally we can say that all closed one-dimensional manifolds are topologically equivalent to the S^1 ring. In that way, any periodic function as it progresses in time should be visualized as moving along the ring.

The measurement of a transmembrane voltage potential is a mapping from $S^1 \to I^1$ and we don't know a priori in which state the cardiomyocyte resides. In other words, the results of a measurement construct I^1 topological space, and then we have to determine the opposite mapping, $I^1 \to S^1$. Note that this S^1 is not the "nature-chosen ring" above, but it is topologically equivalent to it. This mapping everyone applies since it is the process of an interpretation of data. I must note here that this mapping is not necessarily between one-

dimensional spaces, as in the example of cardiomyocyte states. It can be $I^2 \to S^1$ or $I^2 \to S^2$ or anything else that is specific to a system of consideration.

In phase mapping of cardiac electrical activity a common way of mapping is actually $I^1 \to I^2 \to S^1$. Through the measurement process, I^1 space first is obtained, and by the time-embedded method I^1 is mapped to I^2. After that, I^2 is mapped to S^1, usually with a four-quadrant *arctan* function[26] that will be introduced in the subsequent sections.

Hourglasses and Clocks

Cardiomyocytes can be thought of as "resting" until "excited" beyond some "threshold" so that the cardiomyocyte goes "refractory." Afterward, a standard sequence of changes ensues in which the cardiomyocyte will go through a phase of "relative refractoriness" and relax back to "rest." Idealization of such a process can be made as an analog to an hourglass, so the cardiomyocyte can be called an "hourglass device." Many other systems have first and last states that are not a resting state, so that cycle after cycle goes without interruption, without a need of external stimulus to initiate each new cycle. Examples are the astrophysical cycles that give us the seasons and day repeats. These systems are called "clocks," or oscillatory systems.

A similar analogy can be made in electronics, where we have monostable (hourglass) and multistable (clock) vibrators. In this analogy, a clock can be connected with an hourglass in the following way: Multistable vibrators are initially in resting state and external triggers set them away from the resting state so that they turn themselves over and over, while hourglasses need to be turned over and over externally. Mathematically speaking, we can think about hourglass devices as having a stable equilibrium state, while systems with an unstable equilibrium point should be thought as a clock.

Next, we will examine how the spatial distribution of hourglasses and the finite speed of wavefront propagation give them one unique property. A single hourglass sees a wavefront as a stimulus, while an observer from the outside sees it as a wavefront, so both terminologies will be

used equivalently in this paragraph. A single hourglass inside the set can be turned only by a stimulus from some neighboring hourglass. That neighboring hourglass was turned at some instant before, by one of its neighboring hourglasses. We can think of this as a chain reaction that extends through the set. The origin of the first stimulus can be outside of the set so that propagation extends from one boundary of the set to the other boundary. Obviously, one boundary creates and another boundary destroys wavefront propagation viewed from inside the set so that there is only one time propagation. Since hourglasses not adjacent to the boundaries of the system are not excited by external stimulus, can it happen that there is a continuous rhythmic excitation, without external stimulus? This is possible if we imagine that two boundaries can be connected, making a ring, and that the hourglasses at one boundary are in a resting state while hourglasses on another boundary are in an excited state. Generalization follows from the fact that each hourglass doesn't have a property to distinguish whether a stimulus came from a boundary or from a neighboring hourglass. Therefore, the spatial distribution of a cardiomyocyte and the finite time needed to complete one cycle for each hourglass make it possible to have ring-like stimulus propagation in a set of hourglasses. In other words, high spatial fluctuations among the states (phases) of hourglasses can be enough to cause each hourglass in the set to be turned over and over by stimulus from neighboring hourglasses without need for a stimulus outside of a set.

In conclusion, it follows that a set of cardiomyocytes is not just a big hourglass, but it has a property that is not a sole property of any cardiomyocyte alone. This property includes reentrant patterns such as spiral waves, where there is no need for external stimulus to turn the hourglasses over and over.

Both hourglasses and clocks have in common that they are restricted to a one-dimensional ring. They can be seen as embedded structures in the corresponding systems that isolate their features.

Winding Number

From now on we are interested only in observables which have a ring as their topological space and we will use the simple term "observables" to mean this restriction.

Since observables are defined as mapping from the state space, it is natural to ask, are all states actually mapped? Each point in the state space should have some phase value. If there is a state that has no phase then it must correspond to some kind of irregularity in the map: maybe a singularity? In subsequent paragraphs, these questions will be addressed.

$S^1 \to S^1$ mapping is of particular interest for us. The periodicity inherent in a domain ring results in the kind of quantization that classifies continuous $S^1 \to S^1$ maps into distinctly different types. Each type is associated with an integer value called a winding number. In mathematics, the winding number is the net number of times the co-domain variable runs through a full cycle around its ring (co-domain) as the domain variable is run through a ful cycle around its ring (domain). The winding number can be positive and negative. Counterclockwise motion counts as positive, while clockwise motion counts as negative. This idea about winding number can be easily illustrated in the x-y plane representation as given in Figure 1.3.

We can observe a closed curve in a plane around a given point. The path of each curve has a S^1 ring as a domain, and let the co-domain be a 2π circle. We can imagine an observer that sits inside each curve and observes a virtual point that moves along the curve for one full

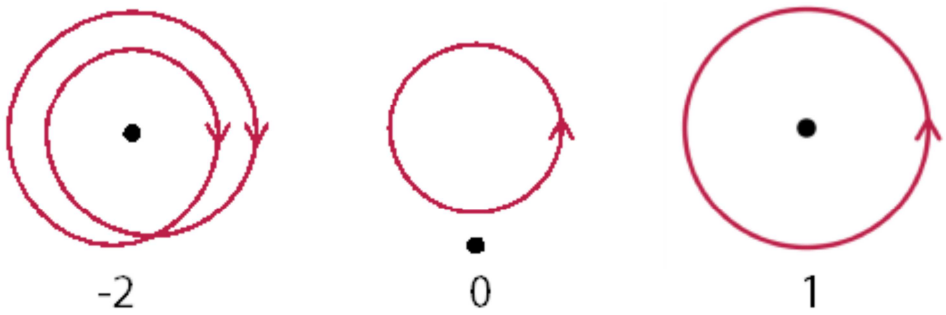

Figure 1.3. Idea of a winding number. Curves, with associated winding numbers, represent the idea of a winding number.

cycle. As it does that, the observer will rotate him/herself for a certain number of $2\pi\cdot$cycles, and that number is called a winding number.

This intuitive description can be mathematically shaped. To each point on a curve we can assign an angle between the line that connects the observer with a point on a curve and some reference line.

Winding number is then defined as

$$W = \frac{1}{2\pi}\oint_l d\theta(l) = \frac{1}{2\pi}\oint_l grad_l\theta(l)d\vec{l}\,. \qquad (4)$$

Integration is performed along a path (curve as in Figure 1.3) with an angle gradient θ. In physics, the winding number is often referred to as *topological quantum number* or *topological charge.*

Now, let's see how topological charge or winding number can be used to identify phase singularities as the origin of rotors/spiral waves in cardiac electrical activity. Consider a wave circulating around a ring of cardiac tissue. Small enough pieces of a ring of tissue can be treated as a single hourglass. Each hourglass is described by its phase and the physical distance around the ring of tissue makes a spatial distribution of phases. Since we have a case of a wave circulating along this ring of tissue, it follows that spatial phase distribution must be such that it makes topologically a S^1 ring. Phase on this ring represents spatial location and time is a parameter.

Each hourglass as a segment of a ring of tissue also has a ring as its topological space, which we may call a S'^1 ring. Phase on this ring is dominantly time–dependent, while spatial position is a parameter.

Let's see how the S'^1 ring is embedded in the S^1 ring. As an example let's take the double circulating wavefronts along the S^1 ring and divide it into N hourglasses-S'^1 rings. To each S'^1 ring we can define a set of states. Let that be an interval [0,1]. Now let's freeze a circulating wavefront in time and imagine an observer that walks along the S^1 ring and

measures the spatial phases on it. This spatial phase is equal to the actual temporal phase of each S'^1 that the observer steps on in each time step. In other words, the observer is mapping $S^1 \rightarrow S'^1$, as shown in Figure 1.4. This can be seen as N hourglasses travel along the S^1 ring. As they travel they take all local S^1 phases distinguished by a spatial phase on a S'^1 ring. With this analogy, N-dimensional problems can be treated as a set of N one-dimensional problems that are interdependent in terms of variables but interdependent in terms of parameters.

It follows that to each physical phase a temporal phase can be assigned so that at any instant, each point on the physical S^1 ring is somewhere in the imaginary S'^1. This represents $S^1 \rightarrow S'^1$ mapping, and therefore we can associate a winding number to it. In Figure 1.4, the winding number of this mapping will be 2 since as we walk once along the S^1 ring, phase in the S'^1 will complete two cycles. If the S^1 ring beats homogeneously, then the winding number is 0.

Analogy with cardiac tissue can be made in the following way: Circulating rings in cardiac tissue are defined by the arms of a spiral wave that extends from the center of a ring (that is PS), so that each piece of the arm draws a circular trajectory as the spiral wave rotates. An analogy can be made by attaching a pencil(s) to a wiper(s) that rotates, so that the pencil(s) will draw a circle on a sheet below (Figure 1.5).

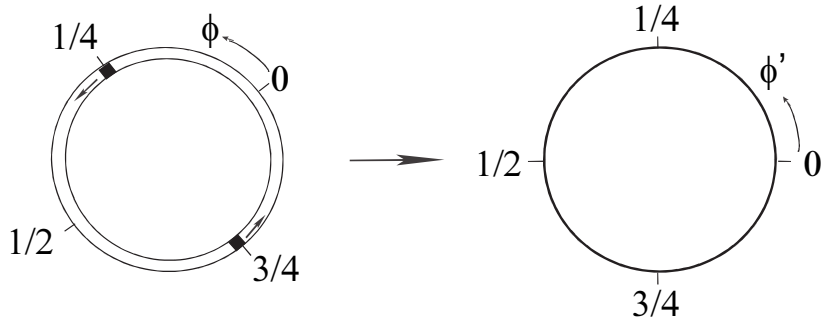

Ring of tissue S^1 (ϕ is physical distance) S'^1 ring (ϕ' phase represents

Figure 1.4. Phase mapping. Phases are described with an interval [0,1] and phase represents physical distance. Right: phases are described with an interval [0,1], but phase here represents time.

With this analogy arises the power of a calculation of a winding number as a powerful tool for the detection of rotors in the cardiac electrical activity and their classification based on their multiplicity (single, double spiral, etc.) and helicity (moving orientation).

Phase Singularity as a Mapping Discontinuity

The goal of this chapter is to mathematically describe and to develop a method for detection of rotors and spiral waves in cardiac tissue. In the example related to Figures 1.4 and 1.5, a ring of tissue is taken as an imaginary trajectory of a segment(s) of an arm(s) of a rotor, but there was no mention of the radius of a ring. Obviously any segment from an arm of a spiral wave will make a ring as well as its trajectory, but with a different radius.

Now let's state the following theorem: *In a mapping of* $S^2 \rightarrow S'^1$ *, for almost all phases from* S^1*, a small change in phase from* S^1 *results in a small change in phases from* S'^1*.*

This theorem will be proved by contradiction. Let ϕ represent phase in S^1 and ϕ' phase in S'^1. When ϕ is increased through a full cycle, then ϕ' must change in such way that it returns to its first value. This periodic dependence between ϕ and ϕ' has an integer winding number W (in Figure 1.4, W=2). Until this point there wasn't any limit on the radius of a physical ring of tissue. Allowing that the physical ring may shrink down to a point, through this process of shrinking we always get a physical ring that is equivalent with the initial ring, so that the winding number stays the same. The process of shrinking defines the disk as an infinite set of smaller and smaller

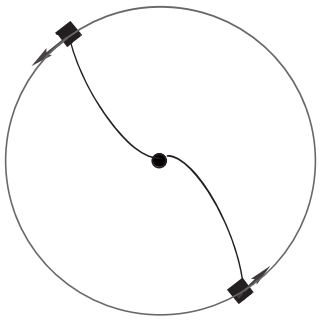

Figure 1.5. Mapping of a double armed spiral. Double arm spiral drawing a circle as the one in Figure 1.4. The circle can be of a different radius limited by the length of the arms.

rings and subsequently the whole mapping can be seen as $S^2 \rightarrow S^1$.

What happens when the radius of a ring becomes so small that it collapses to a point? Since winding number cannot change, at the limit when the ring shrinks to a point, virtual zero changes of phase ϕ will cause that phase ϕ' to cycle W times. This proves the theorem, since there can be small changes in ϕ that result in not small changes in ϕ'. This implies that there are some special points, so that the theorem is valid for almost all phases from S^2, but not for all.

What will it be if the winding number is 0? Then by the same analogy, taking a smaller and smaller physical ring, the winding number has to stay the same. When the physical ring shrinks to a point, that point can be mapped to a single point on a circle, which implies that the winding number is still zero. Therefore if the winding number is 0, that means there are no PS inside the ring of integration.

One implication of the stated theorem is the following theorem: *The only continuous map from the certain area of a disk to the circle is when the winding number is 0, and that is when that area doesn't comprise the center of a disk. If the winding number is not zero, then the map of a disk to a circle cannot be continuous.*

The first consequence of this theorem is that if the winding number is not zero, then a circle that is being mapped from a disk containing a point that cannot be mapped to any phase on the corresponding ring. Actually, this point can be mapped to any point on a S^1 ring, and that point is already named: it is a *phase (coordinate) singularity*.

The second consequence of this theorem is that if the winding number is 0 around the circumference of a disk, then all points inside a disk can be mapped to a circle of states. This means that inside the disk there is no phase singularity point; therefore there are no spiral waves that would extend from the phase singularity point otherwise.

This in summary explains equation 4 and provides one useful aspect of a winding number.

Methods

System for Optical Mapping

New Zealand White rabbits weighing 3 to 5 kg were used in these studies. After general anesthesia, the rabbit hearts were rapidly excised through midline sternotomy and immersed in cold Tyrode's solution. The ascending aorta was immediately cannulated and perfused with warm oxygenated Tyrode's solution. The excitation-contraction decoupler 2,3-butanedione monoxime was used to suppress motion artifacts caused by cardiac contraction.

Voltage-sensitive fluorescent dyes bound to cell membranes allow recording of the transmembrane potential without insertion of microelectrodes or the use of extracellular electrodes. Optical mapping with voltage-sensitive dyes is used to record action potentials from cardiac and neuronal tissues.

A typical optical mapping system consists of three major components: 1) the preparation, which is stained with a voltage-sensitive dye; 2) a system of optics that filters the fluoresced light emanating from the preparation and focuses it onto a photodetector; 3) a photodetector (CCD camera) that measures the fluoresced light. These key components are shown schematically in Figure 1.6.

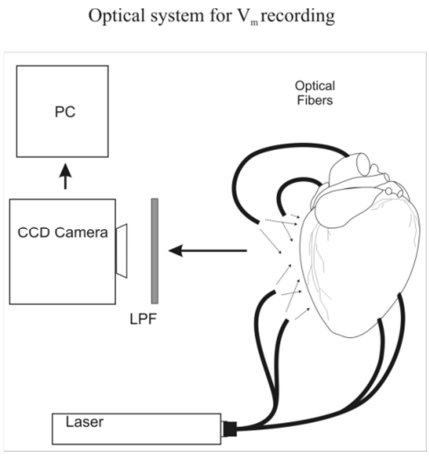

Figure 1.6. Experimental setup. A diagram of our experimental setup configured for recording of a transmembrane potential V_m. Laser light (532 nm) is delivered to the heart with optical fibers. Longpass (LPF) Omega Optical filters are used to image V_m fluorescence, with a DALSA DS-12-16K5H CCD camera (128x128 pixels, 490 frames/sec).

A chromophore is the part of a dye with fluorescent properties and is responsible for the color of the dye. Certain chromophores such as Naphthylstyryl respond directly to the local electric field generated by the voltage gradient across the cardiac cell membrane. The fluorescence recorded from these dyes is linearly related to the true transmembrane potential.[31]

When a photon is absorbed through a process of fluorescence, the chromophore emits a photon of a longer (most probable, as two-photon absorption is several orders of magnitude weaker than single photon absorption) wavelength than the initially absorbed one. The shift in wavelength between the excitation photon and the emitted photon is known as a Stoke's shift, and is on the order of 100 nm. With the use of optical filters, the emission light can be separated from the excitation light and measured with a photodetector.

Electrochromic dyes have a response time on the nanosecond time scale, and are well suited for mapping the action potential. When placed in the bilayer membrane of the cardiomyocyte at the outer side of a membrane, their fluorescent properties will be highly dependent on the local electrical field. As a result of coupling with the local electric field, the energy needed to absorb a photon will be minimized when the membrane is polarized. As transmembrane potential changes from negative to positive potentials, the energy gap between HOMO and LUMO orbitals in the chromophore molecule increases and is manifested as a blue shift in both excitation and emission spectra.

A voltage-dependent emission fluorescence spectrum is shown in Figure 1.7. The spectral shift alters the magnitude of the fluorescent light that is passed by a longpass filter (Figure 1.7, shaded region). As a result, the magnitude of the fluorescent light that is passed by the longpass filter decreases as the transmembrane potential increases.

One of the most sensitive and widely used electrochromic dyes is di-4-ANEPPS, a styryl dye that exhibits a fluorescence intensity change of 8–10% per 100 mV change in transmembrane potential. Because the peaks of the excitation and emission spectra are separated by over 100 nm, it is straightforward to separate the excitation and emission spectra using simple optical filters.

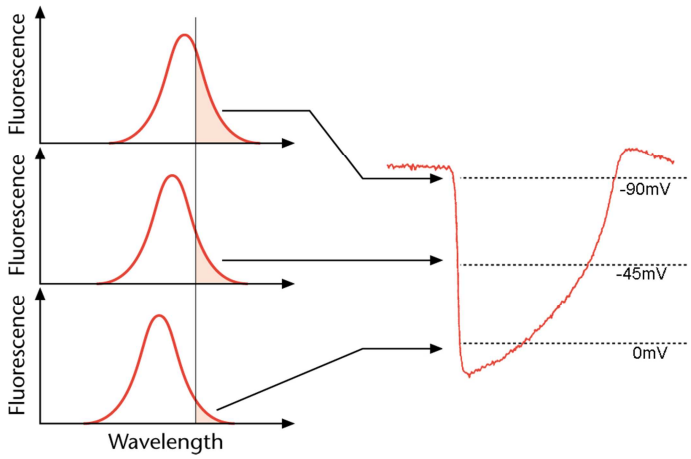

Figure 1.7. Shift of the emission spectrum. An increase of transmembrane potential causes the blue shift of fluorescence emission spectrum. The spectral shift alters the magnitude of fluorescent light that is passed by a longpass filter (shaded region).

As light penetrates into cardiac tissue two processes are dominant: absorption and scattering. In absorption the photon is lost unless it is absorbed by voltage-sensitive dye, while in scattering the photon is not lost, but changes its direction. For wavelengths of interest, above 600nm to near infrared, scattering is predominant, and for biological tissues it is highly forwardly directed. This is favorable since it makes the excitation beam penetrate deeper into cardiac tissue. However, the effective penetration depth, i.e., 1/e attenuations, is small, about 1/3 mm[32].

When the fluorescence photon is emitted by a chromophore, on its way to the surface of cardiac tissue it may undergo absorption or scattering. However, longer wavelengths in biological tissues have a higher transmittance[33]. Therefore it is highly probable that the fluorescence photon will escape to the surface of the heart.

CCD camera resolution and magnification define the size of the smallest physical area mapped by each pixel, and typically can contain 1 to 10^4 cardiomyocytes.[34] The fluorescence recorded by a single pixel originating from that area represents an average fluorescence over all cardiomyocytes it maps. If the activity of these cardiomyocytes is coherent in the time interval defined by the sampling interval of the CCD camera, then each pixel can be treated as one big hourglass. Of course this assumption is not 100% true, and the higher the spatial resolution, the more correct it becomes. This is also dependent on sampling rate.

Transmembrane potential as a function of time has the smallest amplitude at the rotor that is the organizing center for spiral wave patterns on the surface of the heart.

A signal recorded at each pixel is linearly related to the change in the transmembrane potential $\cdot V$, as given by:

$$F(x,y,t) = F_0(x,y) + C_0(x,y) \int_{t}^{t+\Delta t} \int_{x}^{x+\Delta x} \int_{y}^{y+\Delta y} \delta V(x',y',t')dx'\,dy'\,dt' \ , \qquad (5)$$

where x and y represent location on the heart, t is the sampling start moment, and F_0 and C_0 are parameters that are related to the excitation and emission properties at a location (x,y) and Δx and Δy are the spatial dimensions of the area mapped by each pixel. Temporal integration is done by the iris of the camera being open during the sampling interval, and it is responsible for blurring of the propagating waves. The spatial extent of this smearing is equal to the conduction speed times the sampling interval Δt. F_0 represents background fluorescence originating from the dyes that do not depend on the change of membrane potential at that location. These dyes can be bound to the blood vessels, connective tissue, etc.

The first step in digital processing is to subtract the background fluorescence F_0 from each frame. Since C_0 represents spatial non-uniformities in fluorescence intensity in the area $\cdot x \cdot y$ due to the heterogeneities in dye concentration, the second step is to normalize signals from each site to C_0. As a final step, spatial and temporal filters are applied if it is necessary and if the information that we are looking for won't be altered.

For the purpose of our studies, data are digitally processed in a slightly different way before analysis.

Fluorescent signals originating from the side edges of the heart have significantly lower amplitudes than other signals, which make them hard to process due to typical noise. To overcome this problem the following step is done as the first step in digital processing. Pixel traces with the maximal signal intensity of 30% in comparison to the maximal observed intensity in the trace are marked and excluded from further processing.

In the next step, background fluorescence is subtracted in an automatic way. For each pixel, the background level of the trace is independently found and subtracted.

As the next step, data are filtered spatially and temporally. For spatial filtering we used an adaptive Wiener filter with various kernel sizes depending on noise levels. Wiener adaptive filters were chosen because they preserve better edges than Gaussian, median or average spatial filters and are adaptive to the local estimated noise.

In the next step data are filtered temporally. For temporal filtering we used a 4th order low-pass Butterworth filter with a cut-off frequency ranging from 10 to 40 Hz, depending on the noise levels. As the last step in digital pre-processing, the amplitude of the trace of each pixel is normalized to 1.

Phase Mapping

Each pixel that can be treated as a big hourglass has a ring-like topological space I^1 that doesn't correspond exactly to the natural topological ring associated with an hourglass because of the following: the transmembrane signal is equal to a certain value (e.g., 10mV) twice, once during depolarization and once during repolarization. We know that the topological space of an hourglass must be a ring with uniqueness in the phases. Therefore non-uniqueness in transmembrane potential within one cycle means that we are observing a projection from a higher dimensional space in which trajectories during one cycle don’t overlap. Although trajectories in higher dimensional space don’t overlap, this is not necessarily true for a projection onto a lower dimensional space (Figure 1.8).

How can the true state space be reconstructed from the lower dimensional projection? For this to be true, information about higher dimensional space must be embedded in the projection onto lower dimensional state space.

In topology, a manifold is the topological space that on a small enough scale resembles the Euclidean space of a certain dimension, called the dimension of the manifold. In light of this, a ring is a one-dimensional manifold. The Whitney Embedding Theorem holds that a mapping

from an n-dimensional manifold to 2n+1 dimensional Euclidean space is an embedding. In other words, all information that describes an n-dimensional manifold are embedded in the 2n+1 dimensional Euclidean space. 2n+1 independent signals measured from the n-dimensional manifold are enough to describe it.

Takens[30] proved in 1981 that the same goal could be reached with a single measured quantity. Takens proved that instead of 2n+1 generic signals, the time-delayed versions $\vec{x}(t) = [x(t), x(t-\tau),..., x(t-2n\tau))]$ of only one generic signal suffice to embed the n-dimensional manifold. Therefore, since a ring is a one-dimensional manifold, a one-dimensional signal as its projection and a time-delayed version of a projected signal are enough to "unwrap" the ring.

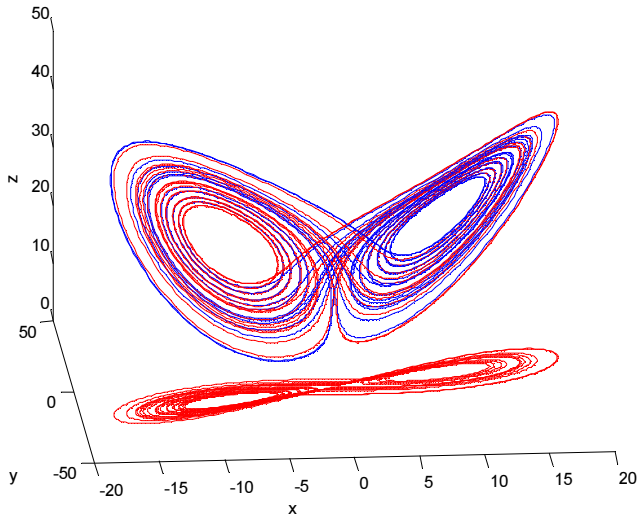

Figure 1.8. Lorentz attractor and its 2D projection. Trajectories extend into three dimensions and don't overlap. However, projected trajectories in the X-Y plane overlap.

The embedding theorem guarantees that the full knowledge of the system behavior is contained in a time series of a given measurement in a lower dimensional state space. The purpose of time delay embedding is to unfold the projection to the higher true dimensional state space. In practice, the natural questions regarding the choice of a time delay τ and embedded dimension *d* have a variety of answers.

There are several methods for estimating the time delay, and they are classified as follows:

- Autocorrelation and power spectrum functions;

- Average Mutual Information (AMI) function;

- Degree of separation function;

- Lyapunov exponents

These methods can give a different time-embedded delay, and the choice should be based on the nature of the data. The choice of time delay can be crucial. In previous work[24,26], delay was first suggested to be the first zero of an autocorrelation function. Delay obtained in such a manner is longer than the duration of the action potential (AP) upstroke, and falls into the plateau region of an AP. Since the transmembrane potential is equal to a certain value twice, a delay that is longer than the duration of an AP upstroke will lead into non-unique representation in phase space. Consequently phase trajectories tend to be concentrated on the diagonal in the reconstructed phase space (Figure 1.9b). Later studies indicated[35] that for the cardiac AP, a delay that is on the order of the action-potential upstroke duration has reduced the amount of trajectory folding that leads to a non-unique calculation of the phase. However, this argument is empirical and, moreover, there is no unique algorithm that automatically calculates AP upstroke duration. Here, we propose an automatic method for the time delay calculation based on the AMI function. AMI is derived from notions of entropy in communications systems[36]. It determines how much information measurements $x(t)$, $t=[0,t_f]$ contain relative to the measurements delayed in time $x(t+\tau)$, $t=[0,t_f]$. The time delay τ must be large enough that independent information about the system is in each set of measurements. However, τ must not be so large that sets of measurements are fully independent of each other. Conversely, if the time delay is too short, the set of measurements will not be independent enough and will not contain any new information. A good rule for estimating the time delay τ is to use the first minimum of the average mutual information[37]. Here we show that the time delays obtained empirically and by the AMI function are the same, therefore proving the empirical argument for time delay (Figure 1.9c and 1.9d).

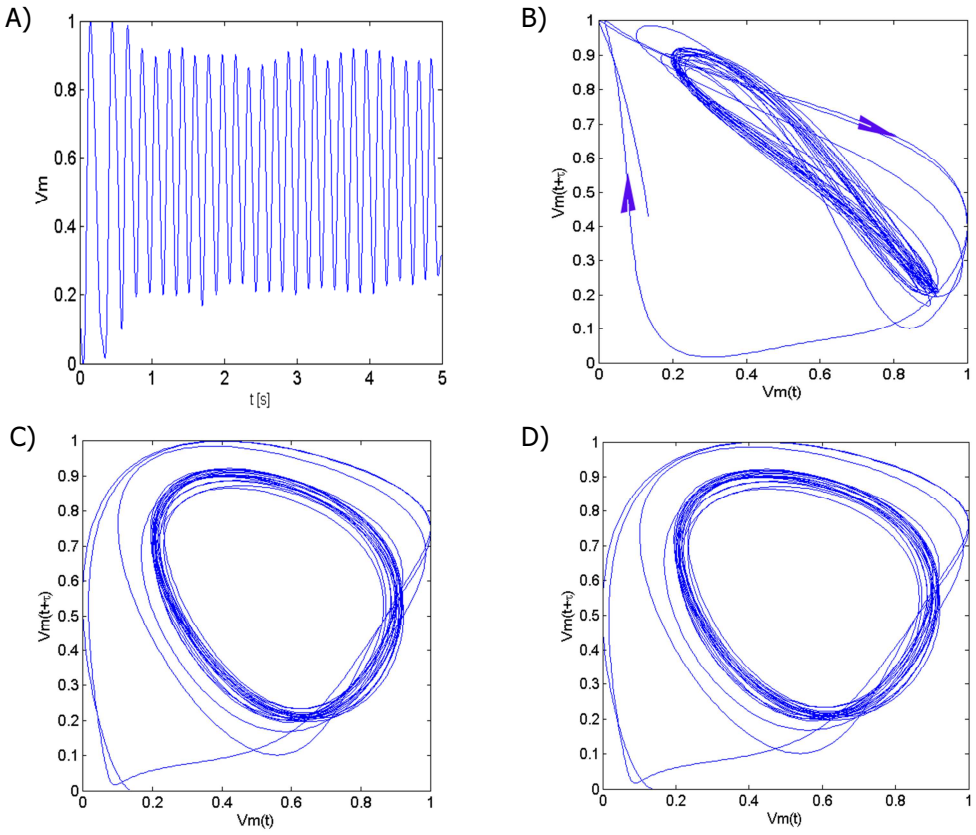

Figure 1.9. Trace of a transmembrane potential and phase space mapping. A) An example of a normalized transmembrane action potential V_m. B) 2D phase space portrait obtained using auto correlation function for an embedded delay τ=95 a.u. C) 2D phase space portrait obtained with an AP upstroke duration of τ=54 a.u. taken as embedded delay. Upstroke duration is measured as duration of an AP upstroke rise from 10% to 90%. D) 2D phase space portrait obtained using AMI function.

Reasoning that confirms that the attractor present in optical imagining of cardiac electrical activity is two-dimensional follows from topology. The topological space of an hourglass is a ring. This is an abstract topological space, and any attempt with an interval-representation in 1D may necessarily lead to non-uniqueness in phases during one cycle and necessarily leads to discontinuity at the ends of an interval. As Takens states, 2D Euclidian space is necessary, where the mentioned discontinuity and non-uniqueness are solved.

Since the topological space of an hourglass is a ring and the phase is a coordinate, it is convenient to describe this phase with a $[-\pi,\pi]$ interval rather than with the 2D Cartesian system. To do this we must find a function that maps 2D Cartesian coordinates to a $[-\pi,\pi]$ interval. Figure

1.10 shows how this mapping can be done. For one cycle of $V_m(t)$ and $V_m(t+\tau)$ the trajectory in I^2 space makes one full loop. Mapping to a $[-\pi,\pi]$ interval can be done as an angle between the two lines. The first line connects the origin and trajectory point references to the second line from which the angle is measured.

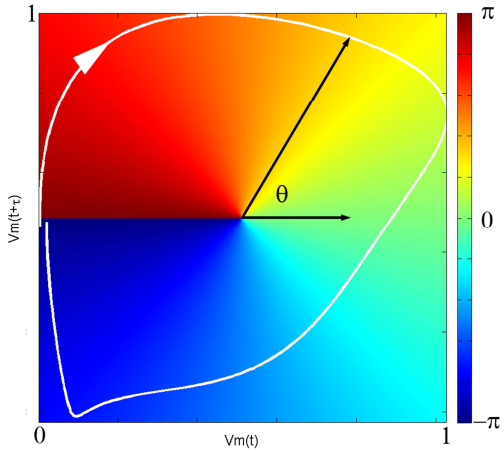

Figure 1.10. Phase angle for a single period of $V_m(t)$. Phase angle at the beginning of an AP upstroke is ideally equal to $-\pi$ and during the rise of an AP it jumps ideally to π. As the membrane is repolarizing the phase angle is gradually returning to its initial value.

For each hourglass we can define the phase angle as:

$$\theta(x,y,t)=\begin{Bmatrix} \arctan\left(\frac{V_m(t+\tau)-V_m^*}{V_m(t)-V_m^*}\right) & V_m(t)-V_m^* \geq 0 \\ \arctan\left(\frac{V_m(t+\tau)-V_m^*}{V_m(t)-V_m^*}\right)+\pi & V_m(t)-V_m^* < 0 \end{Bmatrix}, \qquad (6)$$

x and y are spatial positions (pixel coordinates); $V_m(t+\tau)$ is the transmembrane potential shifted with the delay τ; V_m^* is the origin. In this way, any periodic signal can be mapped in the phase space as a set of loops, where one loop corresponds to one period of a signal.

An origin is necessary, and its necessity lies in the nature of the *arctan* function. Full mapping onto the $[-\pi,\pi]$ interval is obtained when the argument of an *arctan* covers the full $\Re^1$ space $(-\infty,+\infty)$. When $V_m(t)$ is close to the origin, then the argument of *arctan* goes to $\pm\infty$, depending on an approach from the left or right side of the origin. In this way, one cycle of any

temporal signal is non-linearly stretched to cover the $\Re^1$ space, and then mapped onto the $[-\pi,\pi]$ interval, Figure 1.11.

In phase mapping to the $[-\pi,\pi]$ interval with data obtained experimentally there are some obstacles. Pixel traces can be noisy and spatio-temporal resolution limited so that the phase of a certain pixel trace on the rise of an AP doesn't necessarily "jump" from $-\pi$ to π. This can be seen in Figure 1.12, where the trace in the phase space doesn't reach actual $\pm\pi$ values.

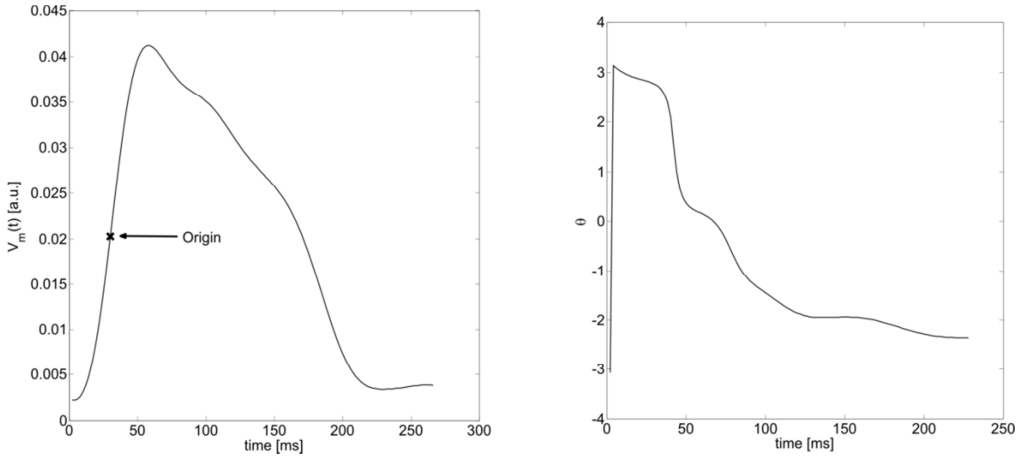

Figure 1.11. Mapping of one cycle of an AP. Left: One cycle of an AP after digital processing from pixel trace that corresponds to a recording with spatial resolution of 128x128pixels at 487fps. Images are filtered first spatially with Wiener 5x5 filter and temporally with 20Hz 4th order Butterworth filter. Right: Phase-space representation of the AP on the left.

A problem arises in calculation of a topological charge, when integration goes over the wavefront (Figure 1.12). Ideally the angle should change by 2π, while the actual angle is changed by $\Delta\theta=2\pi+(2\pi-\theta)=(2\pi-\theta)$. Since "jump" in phase angle only occurs when integration goes over the wavefront, a good rule is to treat any jump higher than π as actually a "jump" over 2π. In that case actual change should be taken, as seen before, as its 2π complement.

This can be proved as well from the perspective of topological spaces. An interval $[-\pi, \pi]$ is a representation of a ring and $-\pi$ and π represent the same phase on a ring. Any change in phase of $\pm2\pi$ along the integration line should be treated as a zero. In experimental data it is

hard to see $\pm 2\pi$ differences, so a good rule is to treat any difference higher than $\pm\pi$ as actually its 2π complement difference.

The choice of the origin is important for phase angle calculation and cannot be selected randomly. Ideally, the phase at a given spatial position should progress through the whole interval of $[-\pi,\pi]$ during one complete cycle. The ideal state-space origin is the one that is

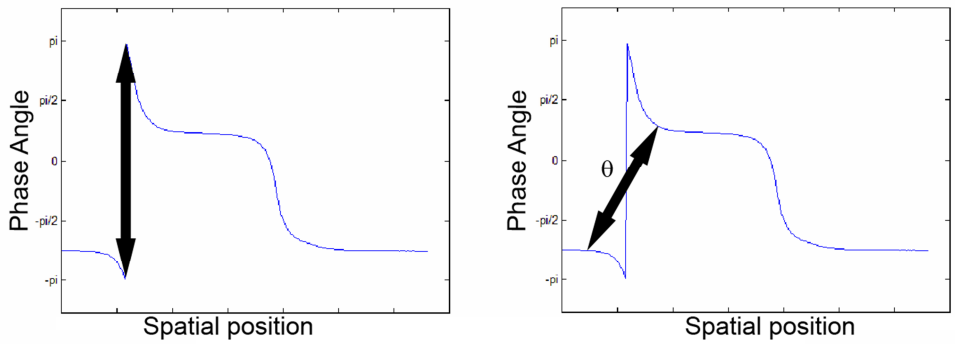

Figure 1.12. Phase angle at the wavefront. Left: Ideal case for integration over the wavefront. Right: Real situation with experimental data.

encircled by all "real" trajectories regardless of their originating spatial location. In the previous published work by Gray *et al.* [26], the origin was taken as the mean value of V_m. While this approach generally gives sufficiently satisfactory results, it may fail in the case of unstable drifting reentrant patterns such as those occurring in fibrillation. Since the amplitude of the action potential tends to decrease with increasing proximity to the filament, the trajectories from points close to the filament circumscribe smaller orbits. This may present a problem since small amplitudes are hard to interpret, and since they may also occur when the vortex meanders near a particular location[38,39]. These amplitudes are not real, but they may cross the mean value, and in the phase space this will be represented as a fake circle, as in Figure 1.13. If small amplitudes are real they will correspond to rotations with a small circumferential length in the phase space. If they are near a drifting organizing center, then there is no guarantee that they will encircle the origin in the phase when origin is defined as V_{mean}.

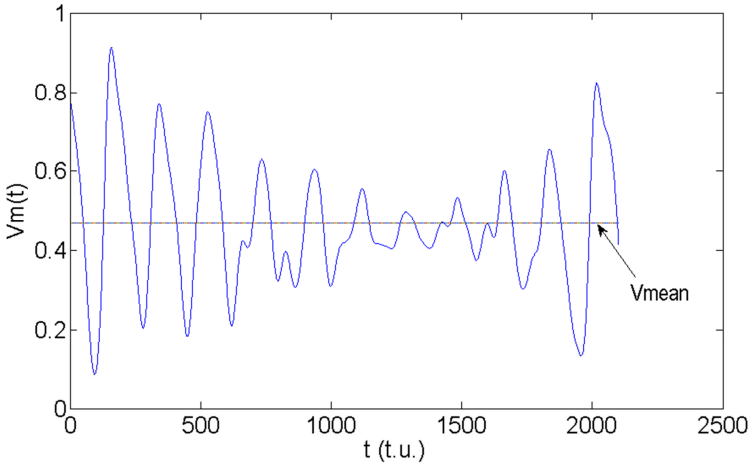

Figure 1.13. Transmembrane potential and its mean value. If an origin is defined as a mean value, a small hump crosses an origin. In the phase space this will be represented as a circular trajectory with small radius.

A solution to this is to modify the state variables (e.g., $V_m(t)$, $V(t+\tau)$) in order to ensure a fixed center of rotation. With the experimental data, the situation is more difficult due to noise, and it is not easy to determine which oscillations should be accounted for as proper rotations in the corresponding phase space and which should be rejected as noise. One approach to ensure a fixed center of rotation was presented by Bray *et al.*[20] with a pseudo-EMD method, where data are basically detrended by applying pseudo-EMD with the sliding minimum and maximum filter. The length of these filters was based on the dominant frequency component in the data. While this approach guarantees that humps separated by the width of the sliding window won't be taken into consideration, it doesn't guarantee that noise humps or fake oscillations at distances greater than the width of the sliding filter will not be encountered.

Direct Phase Mapping

We suggest an alternative approach that promises to work better with experimental data than commonly applied methods, and that is especially advantageous for use in instances when data are corrupted with noise. This method is called *direct phase mapping* from a time domain to

a phase domain $I^1 \rightarrow I^1$. A time-embedding method is not required, and consequently the necessity of an origin is eliminated.

The idea behind a direct mapping is to assign a π value to every value in each pixel trace that corresponds to the peak wavefront and $-\pi$ to every point that is a local minimum in each trace. The wavefront is defined as the instance when the derivative of an AP upstroke has a maximum. In order to accomplish this, the first step is to determine the AP wavefront.

Amplitudes in each trace are found and then a criterion of 30% is applied that discards all amplitudes that are smaller than 0.1 (each trace is normalized to 1). Amplitudes are found by a so-called time-dilatation filter that finds in every pixel trace all local maximums and minimums separated by a certain window size. By experimenting with various window sizes, 50 ms was found to be optimal.

The next step is to map all time points between the assigned π, $-\pi$ points and the $[\pi,-\pi]$ interval. To better preserve the dynamic of the signal inherent in the time domain, the mapping is done as an integral over the absolute value of the derivative of the transmembrane potential signal between two successive maxima and minima of an AP. This can be described as:

$$\theta(x,y,t) = \pi - 2\pi \frac{\int_{t(n)}^{t} \left| \frac{\partial V_m(x,y,\tau)}{\partial \tau} \right| d\tau}{\int_{t(n)}^{t(n+1)} \left| \frac{\partial V_m(x,y,\tau)}{\partial \tau} \right| d\tau}, \qquad t(n) < t < t(n+1) \qquad (7)$$

where *n* represents cycle number and *t(n)* represents AP wavefront instance. Values between each wavefront instance and the maximum of an AP are mapped to π phase value, while to values between each min of an AP and wavefront instance are assigned a $-\pi$ value. An illustration of this method is shown in Figure 1.14.

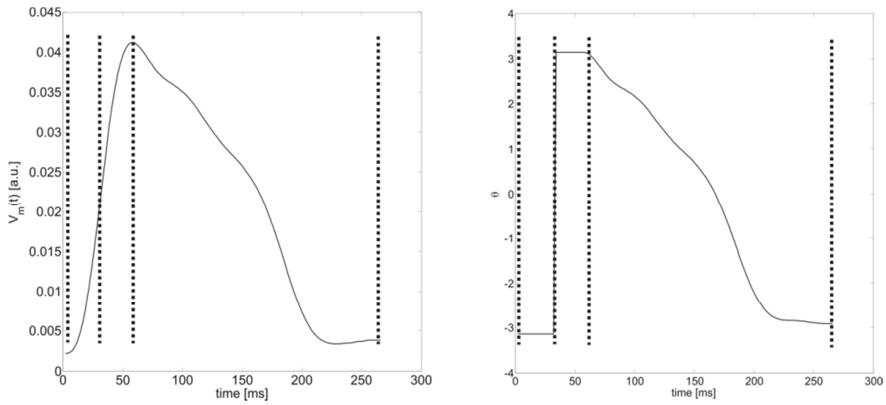

Figure 1.14. Direct mapping of an AP. Left: Action potential from Figure 1.13. Right: Illustration of a direct mapping method that preserves the dynamics inherent in the time domain. Comparison of these two methods is discussed in the text.

Topological Charge Calculation

Once the angles in the phase space are calculated for the trace of each pixel, the next step is to find the topological charge at that pixel by applying equations 1 and 4. From equation 4 it follows that the new vector space can be constructed as:

$$\vec{k}(\vec{r},t) = \nabla\theta(\vec{r},t) \tag{8}$$

In a discrete representation, the nabla operator can be represented as a forward difference:

$$\begin{aligned} k_x(n,m) &= \frac{\partial\theta}{\partial x} = \theta(n+1,m,t) - \theta(n,m,t) \\ k_y(n,m) &= \frac{\partial\theta}{\partial y} = \theta(n,m+1,t) - \theta(n,m,t) \end{aligned} \tag{9}$$

In this way, the line of integration goes over surrounding pixels in a 2x2 box defining a radius of integration as one pixel.

The line integral in Eq. 1 by the Stokes theorem can be transformed to a surface integral. Since θ is in the x-y plane, only the z component of the curl counts

$$n_t = \frac{1}{2\pi}\oint_c \nabla\theta\cdot\vec{dl} = \frac{1}{2\pi}\oint_c \vec{k}\cdot\vec{dl} = \frac{1}{2\pi}\int_S \nabla\times\vec{k}\cdot d\vec{S} \tag{10}$$

$$d\vec{S} = dydz\vec{e}_x + dxdz\vec{e}_y + dxdy\vec{e}_z = dxdy\vec{e}_z \tag{11}$$

In the discrete case, *dx=1,* dy*=1* so that Eq. 10 simplifies to

$$n = \frac{1}{2\pi}(\nabla \times \vec{k}) \cdot \overrightarrow{e_z} = \frac{1}{2\pi}\left(\frac{\partial}{\partial x}k_y - \frac{\partial}{\partial y}k_x\right) = \frac{1}{2\pi}\left\{\left[k_y(n+1,m,t) - k_y(n,m,t)\right] + \left[k_x(n,m,t) - k_x(n,m+1,t)\right]\right\} \quad (12)$$

Computational routines can be speeded up by expressing Eq. 12 by tensor product with the use of convolution nabla matrices[25]

$$n = \frac{1}{2\pi}\left(\nabla_x \otimes k_y + \nabla_y \otimes k_x\right)$$
$$\nabla_x = \begin{pmatrix} -1 & 1 \end{pmatrix} \quad (13)$$
$$\nabla_y = \begin{pmatrix} 1 \\ -1 \end{pmatrix}.$$

Practical use of topological charge calculation applied to analysis of cardiac electrical activity is illustrated on simplified scenarios in Figures 1.15 and 1.16. In these simplifications, the phase will only change when the line of integration crosses the wavefront, otherwise changes are zero.

In Figure 1.15, the idea behind the topological charge is that the topological charge is always zero when a trajectory loop does not encompass the origin of a rotor. In the left figure, the total phase change is zero since the wavefront is outside of the integration loop. In the right figure, the phase will change by $+2\pi$ when the integration loop crosses a wavefront from one side and by -2π when it crosses from the other side. This makes the total phase change zero.

From this example it can be concluded that the total phase change will be different from zero only if the integration path crosses the wavefront an odd number of times. That is only possible if the origin of a wavefront is inside the integration loop, i.e., a phase singularity. In Figure 1.16 two examples are shown when the total phase change is non-zero.

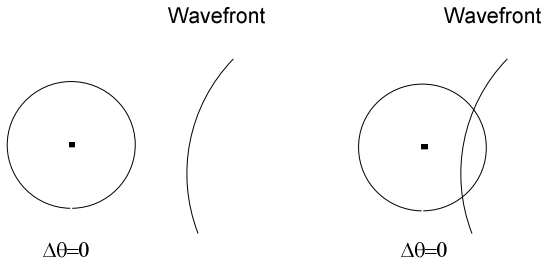

Figure 1.15. Topological charge calculation in the vicinity of a wavefront. Circles represent path of integration and curves represent position of a wavefront.

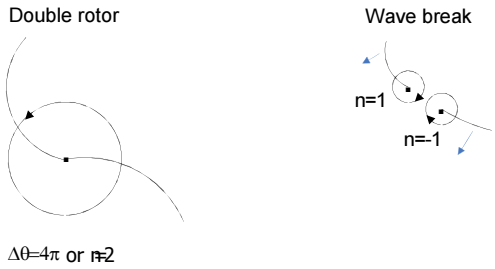

Figure 1.16. Topological charge calculation in the case of a rotor and a wavebreak. Simplification of the two possible situations when the origin of a rotor is inside the integration loop. On the left figure, the wavefront represents a double rotor and the integration loop crosses the wavefront two times from the same side, resulting in a non-zero total phase change. The figure on the right represents a situation of a wavefront break where two PSs are formed.

As the final example that illustrates topological charge calculation, the left panel in Figure 1.17 shows electrical activity of a rabbit heart in the angular phase space representation. Arrows indicate the rotational distribution of phases driven by the phase singularity point at which all phases converge. The figure on the right represents topological charge calculation applied to the figure on the left that indicated position and chirality of phase singularities.

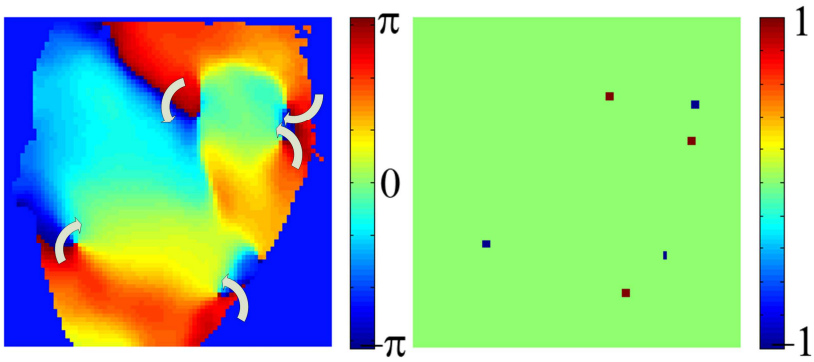

Figure 1.17. Example of a phase space mapping of the electrical activity on the surface of the heart. Left: Phase angle map with indicated four rotors rotating around corresponding phase singularity point. Right: topological charge of the figure on the left.

Practical Applications-Phase Singularities in Pinwheel Experiment

Summary

This section answers the question regarding how a phase singularity is created, through the classical pinwheel experiment, where multiple phase singularities may occur in the form of figure-of-eight or quatrefoil reentry. Two rotors are present in the figure-of-eight and four rotors in quatrefoil reentry. The proceeding paragraphs describe figure-of-eight reentry analyzed in experimental data obtained with the optical mapping method. The pinwheel experiment is conducted via the so-called S1L-S2C[40] protocol. S1 stimulus is applied longitudinally to the fiber orientation using a planar electrode, followed by a unipolar S2 cathodal point stimulus. Figure-of-eight reentry is observed and phase analysis is applied. Two phase singularities are observed and tracked in time. Observations were consistent with the theoretical prediction that these two rotors form figure-of-eight reentry.

The most fundamental experiment for arrhythmia induction is a pinwheel experiment: a planar S1 wavefront interacting with a unipolar S2 point stimulus.

From a historical perspective, Winfree *et al.*[1,41,42] proposed a mechanism for the induction of cardiac arrhythmias by electrical stimulation, given by the critical point hypothesis. The pinwheel experiment shown in Figure 1.18 (taken from Roth *et al.*[43]) illustrates this hypothesis. A planar AP wavefront S1 propagates to the left through a two-dimensional sheet of a cardiac tissue. The shaded region represents a plateau and a repolarization tail. The tissue is refractory within this region and no action potential can be elicited. Winfree defined the critical phase *T**, as the time during the cardiac repolarization when a stimulus of appropriate strength results in an arrhythmia[1,42]. The dot in the center represents the electrode of an S2 stimulus.

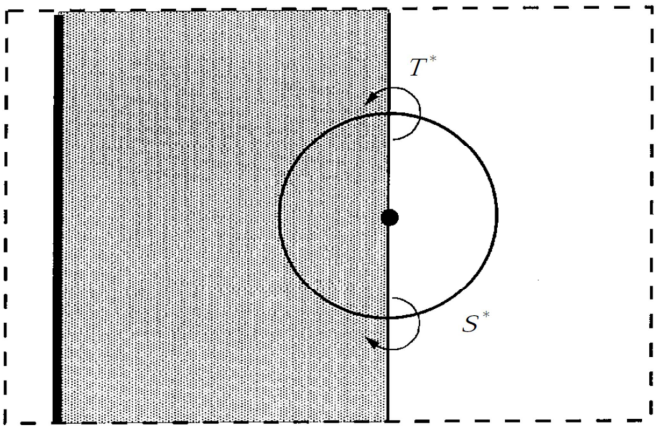

Figure 1.18. (Courtesy of Brad Roth). The pinwheel experiment. An S1 wavefront propagates to the left: Dashed line= edge of tissue; thick line=depolarization front; shaded region=refractory tissue; T* = critical phase; dot= stimulus electrode; S*=critical depolarization induced by the S2 stimulus; vertical thin line separates refractory tissue in the left and excitable tissue on the right. The S2 stimulus initiates two rotors, located where S* and T* intersect. One rotor rotates counterclockwise about the upper intersection and the other rotates clockwise about the lower intersection.

As *T** passes the electrode, a stimulus S2 is applied. Winfree postulated that there exists some critical stimulus strength *S** that corresponds to the threshold for the cardiac tissue at state *T**. The intersection of *S** and *T** is the critical point around which a rotor is formed. Two critical points are generated, each becoming the core of a rotating wave. The upper rotor rotates counterclockwise and the lower rotor rotates clockwise.

By treating the cardiac tissue as a bidomain model, Sepulveda *et al.*[44] found that under a unipolar cathode stimulus, the contours of transmembrane potential resemble a "dog bone" of depolarization shown in Figure 1.19 (taken from Roth *et al.*[43]). The area of depolarization extends upward rather than to the side as a result of anisotropy. In addition, areas of hyperpolarization form on either side of the dog bone. These areas are called virtual electrodes (virtual anodes). If stimulus is anodal, a dog bone of hyperpolarization will be formed with two virtual electrodes of depolarization (virtual cathodes).

In the case with the cathodal stimulus, if a unipolar stimulus of sufficient strength is applied to the refractory tissue, the induced hyperpolarization in virtual anodes deexcites the tissue, rendering it to be excitable[45,46]. This mechanism can be seen as S2 stimulus on both sides of a dog bone opening an excitable pathway in regions of previously unexcitable tissue. Reentry is generated by break excitation of this tissue and subsequent propagation through polarized and

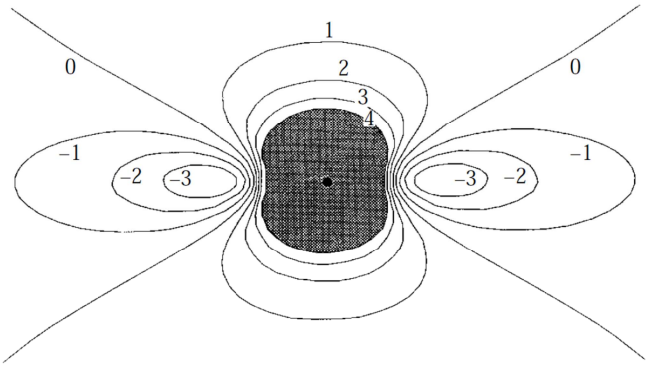

Figure 1.19. (Courtesy of Brad Roth). The steady-state transmembrane potential induced by an extracellular unipolar electrode in a two-dimensional passive bidomain with unequal anisotropy ratios. The dot indicates the position of the electrode. Fibers are oriented horizontally. The units of transmembrane potential are arbitrary. Tissue having a depolarization greater than four is shaded.

repolarized areas of myocardium.

Efimov *et al.*[47] have shown that producing a strong virtual electrode pattern resulted in post-shock reentrant arrhythmias via a mechanism of phase singularities. Phase singularities were created by the shock at the intersections of depolarized, deexcited and zero polarized areas. Tissue was excited by break excitation, and rotors formed around the virtual electrode. Under certain conditions that involve shorter coupling S1-S2 intervals and stronger stimulus, Roth[48] and Lin *et al.*[49] have observed a quatrefoil reentry.

Schematic diagrams of all four possible protocols[40] for reentry initiation are shown in Figure 1.20. The S1 planar electrode can be placed either on the right or on the bottom side, resulting in a longitudinal or transversal planar AP wavefront propagation with respect to the fiber orientation. Afterwards, an S2 monophasic shock is applied at a given S1-S2 coupling interval by a point electrode located within an extracellular region and can be either anodal or cathodal. Depending on stimulus strength and a coupling interval S1-S2, the S2 stimulus can be anodal make or break, or cathodal make or break, or a combination of the two. In the S1L-S2C protocol, the cathodal stimulus is mostly cathodal break.

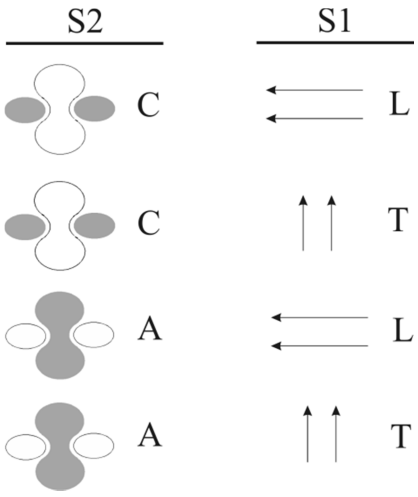

Figure 1.20. Four possible protocols for reentry initiation: For S1 planar wavefront, arrows indicate direction of propagation, longitudinal (L) or transverse (T). S2 stimulus is either cathodal (C) or anodal (A). Shock induced tissue response is shown, where gray = hyper polarization and white = depolarization.

Methods

An optical mapping system was used as described in the Methods section on page 19. The time-embedded delay was 20 ms. An S1 stimulus was applied to initiate planar AP wavefront propagation. At the coupling interval of 160 ms, an S2 stimulus of strength -20mA and width 14 ms was applied via cathode and initiated the cathodal break excitation at the end of a stimulus.

Raw data that represent fluorescent images of cardiac electrical activity were first digitally processed as described in the Methods section on page 19. Due to high noise levels, a Wiener filter was applied twice for spatial filtering, with kernel sizes 13x13 and 5x5, respectively. For temporal filtering a 4^{th} order low-pass Butterworth filter with 10 Hz cut-off frequency was applied afterwards.

Due to excessive spatial and temporal filtering, "dog bone" and virtual electrode patterns that occur in the pinwheel experiment were blurred within the surrounding pixels in the image sequences. However, excessive filtering was necessary since the algorithm for phase singularities detection is significantly dependent on the noise levels. Therefore, only for the demonstration to show the "dog bone" pattern and virtual electrodes, data were filtered differently as it will be indicated.

Results and Discussion

An S1 planar wavefront is initiated via planar electrode, and planar wavefront propagation is observed along the fiber direction (Figure 1.21). The purpose of the planar wavefront was to create a spatial distribution of refractoriness longitudinally (along the fiber orientation).

After the S1-S2 coupling interval of 160 ms, an S2 cathodal stimulus is applied via a point electrode located at the center. An electric field around the cathode creates a current flow towards the cathode. Due to the bidomain model (theory), currents are greater along the fiber

direction, and areas extending along the fiber direction from a cathode that were originally refractory will become polarized (virtual anodes). On the other side, a shape of a dog bone will be formed around the cathode, indicating a depolarized region (Figure 1.22).

Four phase singularities are created by the shock at the intersection of areas of depolarization, deexcitation and zero polarization. However, not all of them will "survive" to create rotors that drive a reentry.

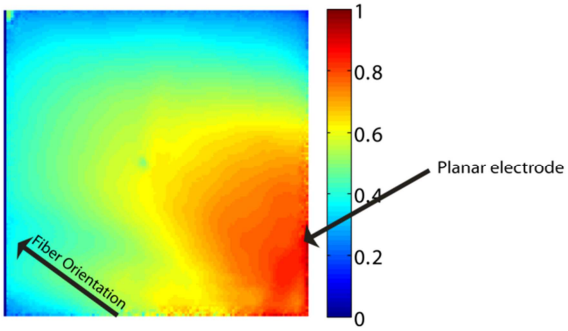

Figure 1.21. Propagation of a planar wave longitudinally, i.e., along the fiber orientation. The transmembrane potential is color coded, normalized on the interval [0,1].

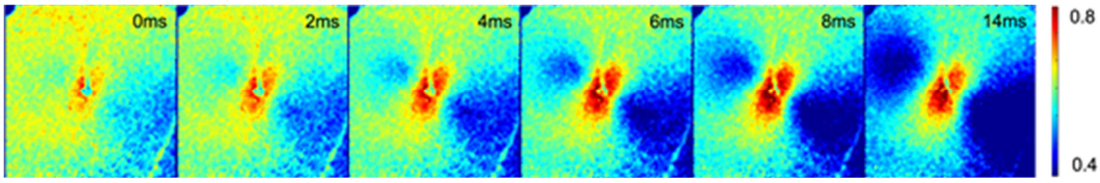

Figure 1. 22. Figures of a transmembrane potential with less filtered data; 3x3 Wiener spatial filter and a 4th order Butterworth 40 Hz low-pass temporal filter. A "dog bone" is formed in the direction transverse to the fiber direction. Virtual electrodes are formed on the sides along the fiber orientation. Virtual electrodes represent opening of an excitable pathway in the region that was previously refractory at 0 ms.

The presence of depolarized membranes in the immediate vicinity of the deexcited regions of virtual electrodes will give rise to local wavefronts at the termination of S2 stimulus, i.e., anodal break. The left side wavefront survives and develops into a figure-of-eight reentry driven by the two rotors (Figure 1.23), while the wavefront on the right is terminated due to overcritical wavefront curvature[50] that is more critical. Figures 1.24 and 1.25 represent the phase space of Figures 1.22 and 1.23, respectively.

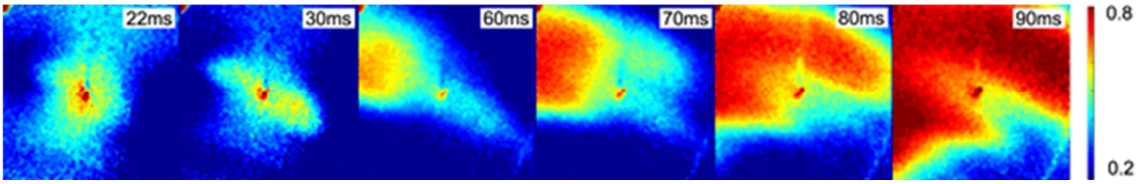

Figure 1.23. Figures of a transmembrane potential with less filtered data using a 3x3 Wiener spatial filter and a 4th order Butterworth 40 Hz low-pass temporal filter. At the end of the S2 stimulus, excitation in the regions of virtual electrodes occurs by the anodal break mechanism.

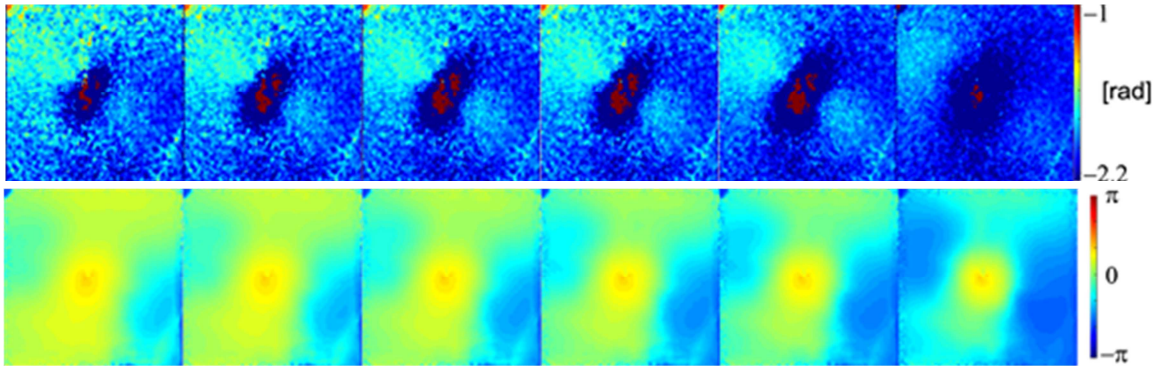

Figure 1.24. Phase space representation of Figure 1.22. π phase corresponds to fully depolarized regions while - π value corresponds to the fully polarized regions. Upper: Phase space with less filtered data; (3x3 Wiener spatial filter and 4th order Butterworth 40 Hz low-pass temporal filter). Bottom: Phase space with data filtered as described in the Methods section.

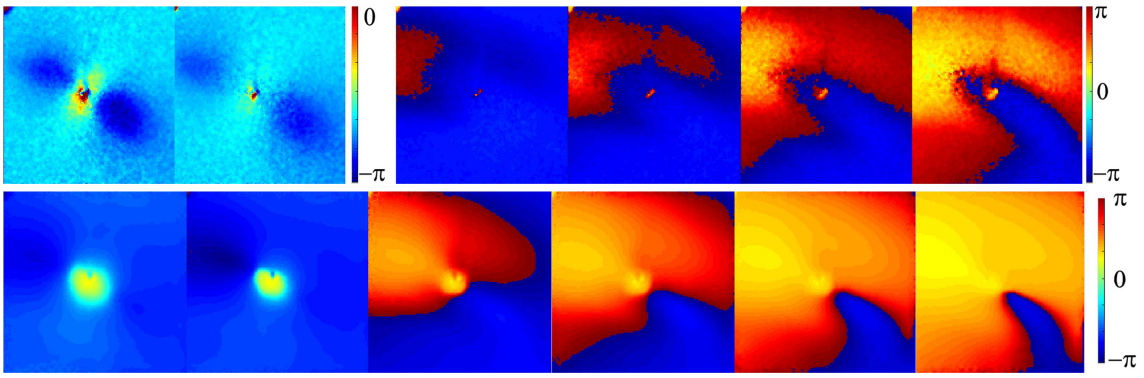

Figure 1.25. Phase space representation of Figure 1.23. π phase corresponds to fully depolarized regions while - π value corresponds to the fully polarized regions. Upper: Phase space with less filtered data (3x3 Wiener spatial filter and 4th order Butterworth 40 Hz low-pass temporal filter). Bottom: Phase space with filters as described in the

For comparison purposes, mapping into phase space is also done with a direct mapping method. Direct phase space representations of Figures 1.23 and 1.24 are shown in Figures 1.26 and 1.27, respectively.

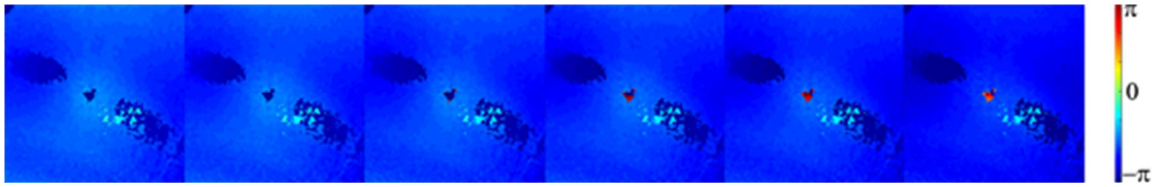

Figure 1.26. Direct mapping. Phase space representation of Figure 1.22.

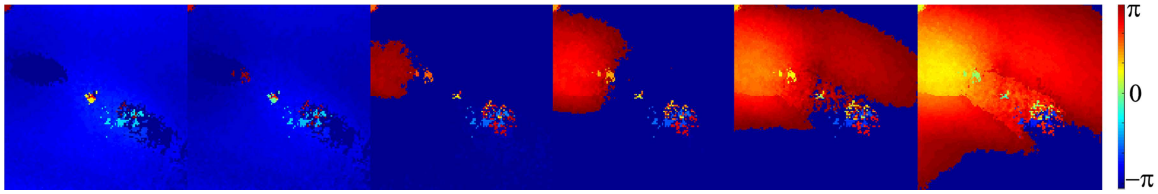

Figure 1.27. Direct mapping. Phase space representation of Figure 1.23.

Two rotors originating on the left side of a dog bone forms reentry with drifting phase singularities at the tip of the rotors. The upper rotor rotates clockwise, while the bottom rotor rotates counterclockwise. The trajectory of a drifting phase singularity should form a figure-of-eight that can be observed and proved by PS tracking methods. For each image represented in phase space, the topological charge is calculated, resulting in an image that shows at which pixel a PS has occurred at least once after S2 stimulus is applied (Figure 1.28). Due to high noise, levels of topological charge are calculated along the diameter of 3 pixels rather than 1, as described in the Methods section on page 19. Additionally, pixels are color coded to represent chirality of a PS. In this way is obtained a 2D PS trajectory map. The upper rotor that rotates clockwise has chirality +1, while the bottom rotor that rotates counterclockwise has chirality -1. Figure 1.29 plots the locus of points in 2D that contained a phase singularity to observe the effect of noise. For this purpose data are only filtered temporally with a Butterworth 4th order low pass filter at 40 Hz.

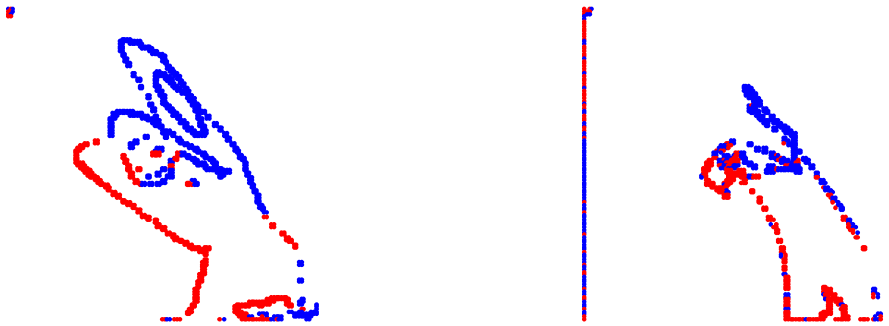

Figure 1.28. Trajectories of two phase singularities represented with the topological charge after an S2 stimulus is applied tracked for ~950ms. +1 charge (red) represents a PS that rotates counterclockwise. -1 charge (blue) represents a PS that rotates clockwise. Left: PS trajectory map obtained with time-embedded method. Right: PS trajectory map obtained with direct-mapping method.

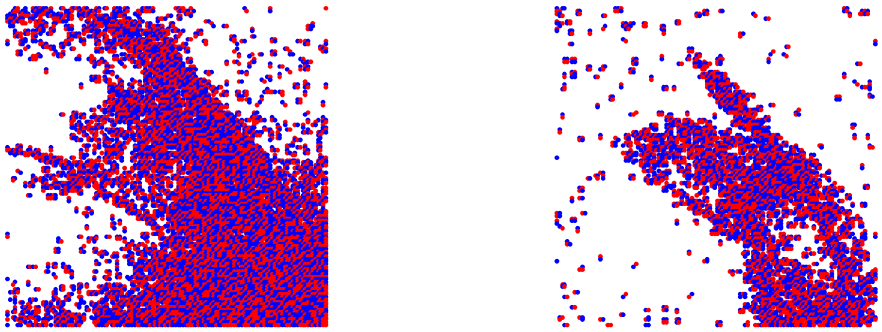

Figure 1.29. Two-dimensional map with minimal filtering to observe effects of noise. Left: PS map obtained with time-embedded method. Right: PS map obtained with direct mapping method.

In Figure 1.30, PS trajectories are represented in a three-dimensional space representation where the z component represents time relative to the initiation of an S2 stimulus. Two PSs that represent positive chirality are assigned future time progression, while for PSs that represent negative chirality, time runs in the past.

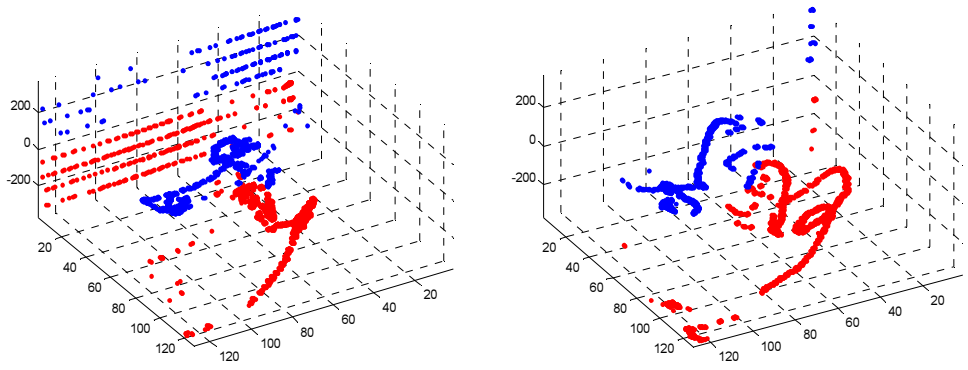

Figure 1.30. 3D representation of trajectories from Figure 1.28; z axis represents time. For PSs with a negative chirality time is negative (progression in the past), while for PSs with a positive chirality time is positive (progression in the future).

Conclusion

From comparing direct mapping and time-embedded mapping, it can be seen that direct mapping has more potential in terms of spatial resolution (Figure 1.27). In the direct-mapping method information about time is preserved. Each phase map image corresponds to the time domain image with the same time index, while in the embedded method the phase space image indices are shifted in time by the time-embedded delay that was used.

The direct-mapping method is capable of resolving the small signal differences that occur at the time of dog bone and virtual electrode formation, while the time-embedded method doesn't resolve these small signal differences when viewed from the full dynamic range. That is why the upper sequence of images in Figures 1.22 and 1.23 is shown at the smaller dynamic range extended to full color scale to emphasize these small differences.

From Figure 1.29 it can be concluded that the direct-mapping method is much less affected by noise than the time-embedded method.

However, for the topological charge calculation, PS detection and PS tracking by the direct-phase method is very limited. Despite these limitations the direct-mapping method clearly shows its potential, and further studies are needed that may lead to improvements in direct mapping from the time domain to the phase space domain.

Novel Method for PS Detection

Summary

This section compares briefly the direct phase mapping method with the commonly used time-embedded method. For comparison purposes data are analyzed from previous examples with regional $[K^+]_o$ perfusion. Figures are taken from poster presentations and reflect current progress at that time.

Introduction

Detection of PSs requires the transition from time-domain signals of cardiac activation to the phase space domain. Each excitable element in the time domain has a periodic trace while in the phase space domain; this trace becomes a series of concentric loops where each loop corresponds to one cycle in the time domain. To map a 1D time trace to 2D phase space, one must define an origin and extend the 1D time signal to a pseudo 2D time domain. Moreover, the origin for each excitable element has to be the same. Many problems arise in the process of origin definition and the creation of the 2D time domain.

Here, we present a novel method that does not require origin definition and extension of the 1D time domain to a 2D time domain. There still must be a consensus about certain aspects, but there are fewer restrictions and problematic situations.

Purpose

- Phase singularity detection is not fully documented.
- Singularity theory is well established for homogenous substrates but not for inhomogeneous.

- Singularity tracking and statistics are unclear.
- PS behavior at a boundary between two regions has not been studied.

The aim of this study is to create a fully functional automatic procedure for PS detection, and to overcome common obstacles in processing raw data in the process of mapping into phase space.

Methods

Our PS algorithm was tested on the experimental data obtained from regionally perfused isolated rabbit hearts. Raw data were digitally preprocessed as described in the Methods section on the page 19.

The direct phase mapping method is applied in the following way (Figure 1.35): In each trace, local maxima and minima that are separated for more than 50 ms are marked. In this way action potential (AP) upstrokes are identified using a 30% criterion to count each AP upstroke. AP upstrokes with amplitudes lower than 30% in comparison to the maximal amplitude in each trace are not taken into account.

Mapping into phase space is done by assigning to each maximum a $+\pi$ phase and to each minimum a $-\pi$ phase. Time points between each maximum and each minimum are linearly interpolated to correspond to the phase values in the $[-\pi,\pi]$ interval. With this method each cycle in the time domain is mapped onto a 2π circle in the phase space. With linear mapping, the dynamics of the signal in the time domain between each local maximum and local minimum are mostly lost. However, the time domain is mapped into a full 2π circle, as we associated maximum and minimum in the time domain to the $+\pi$ phase and the $-\pi$ phase.

After direct phase mapping, a standard analysis that is based on the definition of topological charge is afterwards applied.

Panel A of Figure 1.35 shows in a series of steps the main idea behind direct mapping between the time domain and the phase space domain. Detection of local maxima and minima is done by consensus that each subsequent pair of maximums and minimums must be separated for more than 50 ms. Next, a 30% criterion is applied. Amplitudes smaller than 30%, in comparison to the maximal amplitude in each trace, are excluded. Direct phase space mapping is done by assigning $+\pi$ value to each maximum and $-\pi$ value to each minimum, and linear interpolation is done for time points between to be mapped onto a $[-\pi,\pi]$ interval. The upper image of panel B represents a phase space image as an example of the novel mapping method.

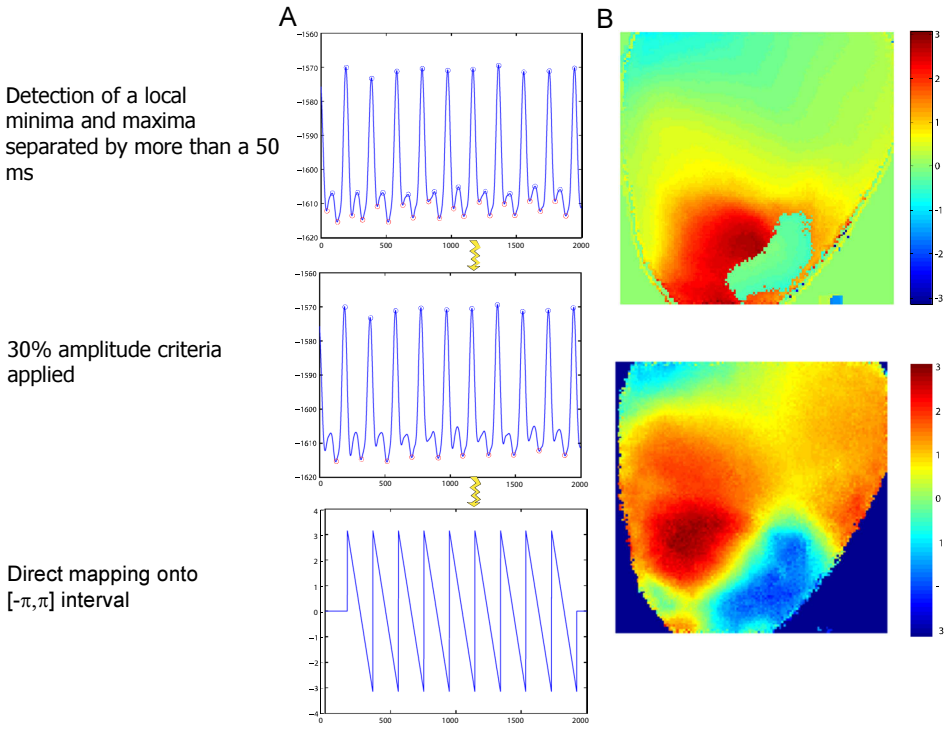

Figure 1.31. Novel method for PS detection. A) Series of steps that describe direct phase space mapping. B) Phase maps: Upper figure: Phase map obtained with direct phase space mapping. Bottom figure: Phase map obtained with time-embedded method.

For comparison purposes, the bottom figure of panel B represents the ordinary time-embedded method that corresponds to the same time domain image. After phase space mapping, for both

methods phase singularity maps are constructed (Figure 1.36). For comparison purposes, the wave block map is predicted and constructed as well.

Figure 1.32. Comparison of methods for phase singularity detection in the phase space mapping of the electrical activity on the surface of the heart. A) PS density map constructed with the time-embedded method. B) PS density map constructed with direct phase space mapping. C) Actual map of a wave block that is used as reference for actual location of PSs and for comparison purposes.

Conclusion

The presented method based on direct phase space mapping overcomes the main obstacles, such as origin and definition and proper lag time for the time-embedded method. Problematic situations of whether some small AP amplitudes will or will not be encircled are eliminated. The necessity for choosing the origin is also eliminated.

There is still a need for a consensus about which local extremes and corresponding AP amplitudes should be taken into account. However, these are less restrictive criteria than those used in the time-embedded method.

In the process of direct phase space mapping, the dynamics of a signal are partially lost, but for the purpose PS detection, the results from Figure 1.36 imply that this loss is not relevant.

By comparing phase singularity distribution maps and wave block maps (Figures 1.35 and 1.36), we see that direct mapping has an advantage over the time-embedded method in preserving time-space correlation. The time-embedded method doesn't preserve correlation

between time-space, and as a consequence PSs are shifted in space at the positions where the wavefront was in the past and shifted in time by the time-embedded constant as well.

Further studies that involve different situations are needed to present a unique argument about AP amplitude criteria and to test this method in different experimental and theoretical situations.

Final Words

In this section phase singularities are studied using the general ideas inherited from topological spaces. Ideas about ring-like topological spaces, winding number and hourglasses have their direct implementation in studies of the electrical activity of cardiac tissue. It is shown that phenomena of rotors and spiral waves appearing in cardiac electrical activity have deep roots in the mathematical theory about topological spaces. The connection between ideas from topological spaces and cardiac electrical activity tissue is made through various examples and analogies. The Methods section describes a procedure for actual phase mapping of fluorescent images that represents cardiac electrical activity. Obstacles and problematic situations are emphasized and presented. At the end, practical application of phase mapping is demonstrated with a few examples.

The power of phase space analysis is not limited to use as a tool for PS detection. Studies can be extended to analyze the effects of various factors that cause heterogeneities in the electrophysiological properties of cardiac tissue. Connections between topological spaces and certain cardiac electrical phenomena have yet to be studied adequately. Studies related to these connections may lead to novel perspectives about phenomena in cardiac electrical activity.

References

1. Winfree, A. T. *When time breaks down: the three-dimensional dynamics of electrochemical waves and cardiac arrhythmias*. Princeton University Press, Princeton, N.J. (1987).
2. Myerburg RJ, Kessler KM, Interian A & et al. *From Cell to Bedside*. Zipes DP & Jalife J (eds.) (Saunders Co., Philadelphia,1990).
3. Wijffels, M. C., Kirchhof, C. J., Dorland, R. & Allessie, M. A. Atrial fibrillation begets atrial fibrillation. A study in awake chronically instrumented goats. *Circulation* **92**, 1954-1968 (1995).
4. Elvan, A., Wylie, K. & Zipes, D. P. Pacing-induced chronic atrial fibrillation impairs sinus node function in dogs. Electrophysiological remodeling. *Circulation* **94**, 2953-2960 (1996).
5. Zipes, D. P. Electrophysiological remodeling of the heart owing to rate. *Circulation* **95**, 1745-1748 (1997).
6. Janse, M. J. Vulnerability to ventricular fibrillation. *Chaos* **8**, 149-156 (1998).
7. Satoh, T. & Zipes, D. P. Unequal atrial stretch in dogs increases dispersion of refractoriness conducive to developing atrial fibrillation. *Journal of Cardiovascular Electrophysiology* **7**, 833-842 (1996).
8. Fenton, F. & Karma, A. Vortex dynamics in three-dimensional continuous myocardium with fiber rotation: Filament instability and fibrillation. *Chaos* **8**, 20-47 (1998).
9. Winfree, A. T. Electrical Turbulence in Three-Dimensional Heart Muscle. *Science* **266**, 1003-1006 (1994).
10. Janse, M. J., Kleber, A. G., Capucci, A., Coronel, R. & Wilmsschopman, F. Electrophysiological Basis for Arrhythmias Caused by Acute-Ischemia - Role of the Subendocardium. *Journal of Molecular and Cellular Cardiology* **18**, 339-355 (1986).
11. Gray, R. A., Pertsov, A. M. & Jalife, J. Incomplete Reentry and Epicardial breakthrough patterns during Atrial Fibrillation in the Sheep Heart. *Circ. Res.* **94**, 2649-2661 (1996).

12. Mines GR On circulating excitation on heart muscles and their possible relation to tachycardia and fibrillation. *Trans R Soc Can* **4**, 43-53 (1914).
13. Gray, R. A. & Jalife, J. Ventricular fibrillation and atrial fibrillation are two different beasts. *Chaos* **8**, 65-78 (1998).
14. Zipes, D. P. & Wellens, H. J. J. Sudden cardiac death. *Circulation* **98**, 2334-2351 (1998).
15. Allessie, M. A., Bonke, F. I. M. & Schopman, F. J. G. Circus Movement in Rabbit Atrial Muscle as a Mechanism of Tachycardia. *Circ. Res.* **23**, 54-62 (1973).
16. Hoffman, B. F. & Rosen, M. R. Cellular Mechanisms for Cardiac Arrhythmias. *Circ. Res.* **49**, 1-15 (1981).
17. Scherf, D. The atrial arrhythmias. *N. Engl. J. Med.* **252**, 928-933 (1955).
18. Schuessler, R. B., Grayson, T. M., Bromberg, B. I., Cox, J. L. & Boineau, J. P. Cholinergically Mediated Tachyarrhythmias Induced by A Single Extrastimulus in the Isolated Canine Right Atrium. *Circulation Research* **71**, 1254-1267 (1992).
19. Gray, R. A. *et al.* Mechanisms of cardiac fibrillation. *Science* **270**, 1222-1225 (1995).
20. Moe, G. K. & ABILDSKOV, J. A. Atrial fibrillation as a self-sustaining arrhythmia independent of focal discharge. *Am. Heart J.* **58**, 59-70 (1959).
21. Witkowski, F. X. *et al.* Spatiotemporal evolution of ventricular fibrillation. *Nature* **392**, 78-82 (1998).
22. Gray, R. A. *et al.* Nonstationary vortexlike reentrant activity as a mechanism of polymorphic ventricular tachycardia in the isolated rabbit heart. *Circulation* **91**, 2454-2469 (1995).
23. Davidenko, J. M., Pertsov, A. M., Salomonsz, R., Baxter, W. P. & Jalife, J. Spatiotemporal irregularities of spiral wave activity in isolated ventricular muscle. *J. Electrocardiol.* **24** Suppl, 113-122 (1992).
24. Ikeda, T. *et al.* Mechanism of spontaneous termination of functional reentry in isolated canine right atrium. Evidence for the presence of an excitable but nonexcited core. *Circulation* **94**, 1962-1973 (1996).

25. Bray, M.-A., Lin, S.-F., Aliev, R. R., Roth, B. J. & Wikswo, J. P., Jr. Experimental and theoretical analysis of phase singularity dynamics in cardiac tissue. *J. Cardiovasc. Electrophysiol.* **12**, 716-722 (2001).

26. Gray, R. A., Pertsov, A. M. & Jalife, J. Spatial and Temporal Organization during Cardiac Fibrillation. *Nature* **392**, 75-78 (1998).

27. Mermin, N. D. The Topological Theory of Defects in Ordered Media. *Rev. Mod. Phys.* **51**, 591-648 (1979).

28. Goryachev, A. & Kapral, R. Spiral Waves in Chaotic Systems. *Phys. Rev. Lett.* **76**, 1619-1622 (1996).

29. Packard, N. H., Crutchfield, J. P., Farmer, J. D. & Shaw, R. S. Geometry from a Time-Series. *Phys. Rev. Lett.* **45**, 712-716 (1980).

30. Takens, F. *Dynamical Systems and Turbulence, Warwick 1980: Proceedings of a Symposium Held at the University of Warwick 1979-80*. Dold, A. & Eckmann, B. (eds.), pp. 366-381 (Springer-Verlag, Berlin / Heidelberg / New York,1981).

31. Salama, G. & Morad, M. MEROCYANINE 540 AS AN OPTICAL PROBE OF TRANSMEMBRANE ELECTRICAL-ACTIVITY IN HEART. *Science* **191**, 485-487 (1976).

32. Baxter, W. T., Mironov, S. F., Zaitsev, A. V., Jalife, J. & Pertsov, A. M. Visualizing Excitation Waves inside Cardiac Muscle Using Transillumination. *Biophys. J.* **80**, 516-530 (2001).

33. Preuss, L. E., Bolin, F. P. & Cain, B. W. A comment on spectral transmittance in mammalian skeletal muscle. *Photochem. Photobiol.* **37**, 113-116 (1983).

34. Rosenbaum, D. S. & Jalife, J. *Optical mapping of cardiac excitation and arrhythmias*. Futura, Armonk, NY (2001).

35. Gray, R. A. & Jalife, J. *Cardiac Electrophysiology: From cell to bedside*. Zipes, D. P. & Jalife, J. (eds.), pp. 432-439 (W.B. Saunders Company, Philadelphia,2000).

36. Shannon, C. & Weaver, W. *The Mathematical Theory of Communication*. *Univ of Illinois Press*, (1949).

37. Fraser, A. M. & Swinney, H. L. Independent coordinates for strange attractors from mutual information. *Phys. Rev. A* **33**, 1134-1140 (1986).

38. Bray, M.-A. & Wikswo, J. P., Jr. Considerations in phase plane analysis for non-stationary reentrant cardiac behavior. *Phys. Rev. E* **65**, Art. No.-051902 (2002).

39. Huang, N. E. *et al.* The empirical mode decomposition and the Hilbert spectrum for nonlinear and non-stationary time series analysis. *Proceedings of the Royal Society of London Series A-Mathematical Physical and Engineering Sciences* **454**, 903-995 (1998).

40. Lindblom, A. E., Roth, B. J. & Trayanova, N. A. Role of virtual electrodes in arrhythmogenesis: Pinwheel experiment revisited. *J. Cardiovasc. Electrophysiol.* **11**, 274-285 (2000).

41. Winfree, A. T. Sudden Cardiac Death - A Problem in Topology. *Scientific American* **248**, 144-& (1983).

42. Winfree, A. T. Electrical Instability in Cardiac Muscle: Phase Singularities and Rotors. *J. Theor. Biol.* **138**, 353-405 (1989).

43. Roth, B. J. The pinwheel experiment revisited. *J. Theor. Biol.* **190**, 389-393 (1998).

44. Sepulveda, N. G., Roth, B. J. & Wikswo, J. P., Jr. Current injection into a two-dimensional anisotropic bidomain. *Biophys. J.* **55**, 987-999 (1989).

45. Wikswo, J. P., Jr., Lin, S.-F. & Abbas, R. A. Virtual electrodes in cardiac tissue: a common mechanism for anodal and cathodal stimulation. *Biophys. J.* **69**, 2195-2210 (1995).

46. Efimov, I. R. *et al.* Transmembrane voltage changes produced by real and virtual electrodes during monophasic defibrillation shock delivered by an implantable electrode. *J. Cardiovasc. Electrophysiol.* **8**, 1031-1045 (1997).

47. Efimov, I. R., Cheng, Y., Van Wagoner, D. R., Mazgalev, T. N. & Tchou, P. J. Virtual electrode - induced phase singularity: A basic mechanism of defibrillation failure. *Circ. Res.* **82**, 918-925 (1998).

48. Roth, B. J. Nonsustained reentry following successive stimulation of cardiac tissue through a unipolar electrode. *J. Cardiovasc. Electrophysiol.* **8**, 768-778 (1997).

49. Lin, S.-F., Roth, B. J. & Wikswo, J. P., Jr. Quatrefoil reentry in myocardium: An optical imaging study of the induction mechanism. *J. Cardiovasc. Electrophysiol.* **10**, 574-586 (1999).

50. Fast, V. G. & Kleber, A. G. Role of wavefront curvature in propagation of cardiac impulse. *Cardiovascular Research* **33**, 258-271 (1997).

CHAPTER II

REGIONAL INCREASE OF EXTRACELLULAR POTASSIUM LEADS TO ELECTRICAL INSTABILITY AND REENTRY OCCURRENCE THROUGH THE SPATIAL HETEROGENEITY OF APD RESTITUTION*

Veniamin Y. Sidorov, Ph.D.,[1,3] Ilija Uzelac, M.S.,[2] John P. Wikswo, Ph.D.[1-4]

[1]Department of Biomedical Engineering, [2]Department of Physics and Astronomy, [3]Vanderbilt Institute for Integrative Biosystems Research and Education, [4]Department of Molecular Physiology and Biophysics, Vanderbilt University, Nashville, Tennessee

Abstract

The heterogeneities of electrophysiological properties of cardiac tissue are the main factors that control both arrhythmia induction and maintenance. Though the local increase of extracellular potassium ($[K^+]_o$) due to coronary occlusion is a well-established metabolic response to acute ischemia, the role of local $[K^+]_o$ heterogeneity in phase 1a arrhythmias has yet to be determined. In this work we created local $[K^+]_o$ heterogeneity and investigated its role in fast pacing response and arrhythmia induction. The left marginal vein of a Langendorff-perfused rabbit heart was cannulated and perfused separately with solutions containing 4, 6, 8, 10, and 12 mM of K^+. The fluorescence dye was utilized to map the voltage distribution. We tested stimulation rates starting from 400 ms down to 120 ms with steps of 5-50 ms. We found that local $[K^+]_o$ heterogeneity causes action potential (AP) alternans, 2:1 conduction block, and wave breaks. The effect of $[K^+]_o$ heterogeneity on electrical stability and vulnerability to arrhythmia induction was largest during regional perfusion with 10 mM of K^+. We detected three concurrent dynamics: normally propagating activation when excitation waves spread over tissue perfused with normal K^+, alternating 2:2 rhythm near the border of $[K^+]_o$ heterogeneity, and 2:1

* This is a peer reviewed manuscript published in *Am J Physiol Heart Circ Physiol* 301: H209–H220, 2011. doi:10.1152/ajpheart.01141.2010

aperiodicity when propagation was within the high $[K^+]_o$ area. $[K^+]_o$ elevation changed the action potential duration (APD) restitution and shifted the restitution curve towards longer diastolic intervals and shorter APD. We conclude that spatial heterogeneity of the APD restitution, created with regional elevation of $[K^+]_o$, can lead to AP instability, 2:1 block, and reentry induction.
Keywords: extracellular potassium, restitution heterogeneity, regional perfusion, optical mapping

Introduction

The stationary and dynamic heterogeneities of electrophysiological properties of cardiac tissue play a key role in the induction and maintenance of cardiac arrhythmias (1, 10, 16, 59) . Cardiac tissue heterogeneities increase drastically when acute regional ischemia occurs. The early stage of acute ischemia is characterized by abrupt metabolic and electrophysiological changes in the affected area (11). Among them the more prominent are increased extracellular potassium ($[K^+]_o$) (25, 26), decreased creatine phosphate (43, 63), elevated intracellular inorganic phosphate (63), acidosis (27, 46), catecholamine release (39), and partial depolarization of transmembrane potential (V_m) (28, 36).

Since an early change in V_m closely relates to $[K^+]_o$ accumulation (34, 60), the K^+ imbalance is considered to be the major factor affecting excitability and responsible for slow impulse propagation and induction of reentry (51). The elevation of $[K^+]_o$ displays a triphasic time course and can be affected by an acceleration of pacing rate (35, 58). The first phase starts immediately after occlusion, lasts 5 - 10 min, and ends when $[K^+]_o$ rises up to 14 mM (12, 25). The second phase represents a plateau and continues 5 - 20 min (25, 57). The third phase is characterized by secondary slower increase of $[K^+]_o$ (57). The regional ischemia causes a very inhomogeneous $[K^+]_o$ distribution, with the highest level of $[K^+]_o$ at the center of the ischemic area and a sharply decreased level at the border zone (17, 30). This heterogeneity, developing

during the first phase of $[K^+]_o$ accumulation, can be a source of wave fragmentation and underlie 1a arrhythmias.

Although numerous studies have been devoted to investigation of both metabolic and electrophysiological events accompanying the early stage of ischemia, there is a lack of systematic examination of the particular role of K^+ heterogeneity in arrhythmogenesis during suddenly increased heart rate, due to the rapidity of electrophysiological changes after coronary artery occlusion and the complexity of the regional changes in metabolic substrate during ischemia. We address these limitations with a study that has the goals of a) creating well-defined K^+ heterogeneities by means of regional perfusion with solution containing different concentrations of K^+, and b) investigating the role of K^+ heterogeneities in the response of cardiac tissue to rapid pacing and arrhythmia induction.

Methods

Experimental Preparation

All experiments conformed to the *Guide for the Care and Use of Laboratory Animals* published by the U.S. National Institutes of Health and were approved in advance by the Vanderbilt Institutional Animal Care and Use Committee. New Zealand white rabbits (N = 17) of either sex weighing 2.7 to 3.1 kg were used in the experiments. The detailed description of the heart preparation has been published previously (52-54). The animals were preanesthetized with ketamine (50 mg/kg), heparinized (1,000 units), and anesthetized with sodium pentobarbital (60 mg/kg). After a midsternal incision, the heart was quickly removed from the chest and mounted on a Langendorff apparatus for retrograde perfusion with oxygenated Tyrode's solution of the following composition (mM): 133 NaCl, 4 KCl, 2 $CaCl_2$, 1 $MgCl_2$, 1.5 NaH_2PO_4, 20 $NaHCO_3$, and 10 D-glucose, buffered with 95% O_2 and 5% CO_2 (pH = 7.35 at 37°C). The excitation-contraction uncoupler 2,3-butanedione monoxime (BDM [Fluka, St. Louis, MO]) was added to the perfusate

(15 mM) to eliminate contractile optical artifacts. Coronary perfusion pressure was adjusted to 50 mmHg and flow rate was 44 – 49 ml/min.

After an equilibration time of 20 min the heart was stained with 200 μM of di-4-ANEPPS (AnaSpec, San Jose, CA) stock solution (0.5 mg/mL DMSO) gradually administered via an injection port above the aortic cannula. To create a local gradient of $[K^+]_o$, the left marginal vein was cannulated with a custom-made polyethylene catheter and perfused separately with Tyrode's solution containing K^+ concentrations of 4, 6, 8, 10 and 12 mM. The concentration of Na^+ was decreased proportionally to maintain constant osmolarity. The hearts were exposed to air during the experiments. The experimental setup was located in a light-tight Faraday shield and the temperature inside was kept at 37 ± 0.5°C by a precision heater controller (Air-Therm, World Precision Instruments, Sarasota, FL). At the end of the experiment an additional amount of di-4-ANEPPS was infused via the polyethylene catheter to visualize the area of regional perfusion.

Imaging System and Data Acquisition

The fluorescence was excited by a diode-pumped, solid-state laser (Verdi, Coherent, Santa Clara, CA) at a wavelength of 532 nm. The illumination was delivered to the heart with bundles of optical fibers (Schott North America, Inc.). The emitted light was passed through a cutoff filter (607 nm, Tiffen) and imaged with a DALSA CCD camera (DS-12-16K5H, 128 x 128 pixels, 490 fps, Dalsa, Inc., Waterloo, ON, Canada). The digitized pixel intensity was transferred to a Bitflow R3 frame grabber board (Bitflow, Boston, MA) installed in a Dell 650 Pentium IV/3 GHz Precision Workstation. Custom-developed C-based software controlled data acquisition, camera synchronization, external stimulation, and laser illumination. The magnification was adjusted to focus on a square area of 18 – 28 mm.

Stimulation Protocols

The stimulation protocols included base line stimulation at a cycle length of 300 ms, a dynamic pacing protocol when the pacing interval (PI) was gradually reduced to 120 ms with

steps of 5 – 50 ms, and a burst pacing protocol. The stimulating current was delivered via a bipolar glass-coated platinum electrode (0.25 mm wire diameter; 1 mm electrode separation) located on the anterior surface at the right ventricle near the septum. The stimulus was 4 ms in duration with strength adjusted to between three and four times the diastolic threshold of excitation.

After cannulation of the left marginal vein, the local area of the left ventricle was perfused separately by constant flow at a flow rate of 10 – 12 mL/min with regular solution for 30 min. During this period the heart was stimulated at the basic cycle length. Thereafter, if no ischemic changes in shape of the optical action potential (AP) were detected, the dynamic pacing protocol was implemented. After each increase in stimulation rate, the heart was continuously paced for 2 min before data acquisition. Once the fast pacing protocol was completed, the stimulation was switched back to the basic PI of 300 ms, and the supply system for the regional perfusion (RP) was exchanged for one with a solution with 6 mM of K^+. After 15 min of perfusion at the normal rate, the fast pacing protocol was executed again. This algorithm of stimulation was repeated for each subsequent elevation of $[K^+]_o$.

The burst pacing protocol was implemented in RP experiments (N = 6) to assess vulnerability to arrhythmia induction at different concentrations of regional $[K^+]_o$. In this protocol the basic pacing was interrupted with a pulse train consisting of 10 successive stimuli, each of which was ten times threshold in amplitude and 10 ms in duration. The PI was progressively shortened in 5 - 20 ms steps starting from 200 ms down to the effective refractory period.
To estimate the effect of $[K^+]_o$ on APD and conduction velocity (CV) restitution, $[K^+]_o$ was increased globally. In those experiments (N = 4) the stimulation current was delivered by means of a 10 mm long linear wire electrode. The electrode was placed gently against the epicardium on the upper-left corner of the image area close to septum and oriented perpendicularly to the fibers to allow steadily propagation along the fiber direction. The hearts were paced at a basic cycle length of 400 ms. Similarly to the RP experiments, dynamic pacing protocol was applied to test each level of $[K^+]_o$.

Data Processing and Statistical Analysis

The fluorescence data were filtered by an 8 × 8 Gaussian spatial filter and five-point mean temporal filter. To create a phase plot the filtered data were normalized pixel-by-pixel according to fluorescence change during normal pacing rate. To detect the time of activation and repolarization, the data were additionally preprocessed by applying a 5 × 5 Gaussian filter and five-point mean temporal filter. For phase singularity analysis, data were filtered using the fourth-order low pass Bessel filter.

The activation time (AT) was computed as the time elapsed between the end of the stimulus and the time at which optical AP reached an activation level equal to 50% of AP amplitude. The repolarization time (RT) was measured at 70% repolarization. The diastolic interval (DI) was computed as the time interval between RT_n and AT_{n+1}, and APD was computed as a difference between AT_n and RT_n.

To assess statistically the alternans of AP amplitude, AT, and APD, the relative standard deviations (RSD = std/mean*100) of AP amplitude, AT, and APD were computed for every location and then mapped. In order to construct the dominant frequency (DF) map, a fast Fourier transform was utilized for each pixel and the maxima of power the spectra were considered as the DF for that pixel.

To create the restitution curve, APD was measured within two different spots (each of 5 × 5 pixels) and then averaged to obtain mean values for odd and even waves. In total, 50 traces were analyzed to attain the APD for each pacing rate. An exponential curve was fit to a restitution relationship by means of the equation (OriginLab):

$$y = a - b * e^{-x/t},$$

where units of *t*, *a*, and *b* are milliseconds. The slopes of the restitution curves were obtained by computing the derivative of these curves. To create CV restitution curve, the CV was measured along the fiber direction transverse to propagating planar wave and then averaged to attain mean CV for odd and even waves.

To estimate arrhythmia susceptibility, each pulse train was applied six times and episodes of arrhythmias and extrasystoles were counted. Then the probability of arrhythmia induction was calculated. We discriminated extrasystolic from arrhythmic activities based on their duration. If extra beats stopped within one second after termination of the last pacing pulse, those were considered as extrasystoles. Usually, the number of extrasystoles did not exceed four beats.

Data are presented as mean ± standard deviation. Statistical analysis was accomplished using the unpaired t-test. Differences were considered significant if $P < 0.05$.

Phase Singularity Detection

To find the phase singularities the V_m traces were translated into phase space, where amplitude cycles in the time domain correspond to the loops in phase domain, rotating around a single origin (7, 8). To identify the origin, the median line connecting the middle points of amplitude was determined by data detrending. During this procedure all local minima and maxima of signal amplitude are detected and middle points are connected with interpolation using linear piecewise polynomials. After median line subtraction and data normalization, the phase plot was generated for each pixel using time-lag embedding (32). Each period was depicted as a 2π circle, resulting in a series of closed loops. The phase angle, $\theta(t)$, was calculated using

$$\theta(t) = \arctan\ ((V_m(t+\tau) - V_m^*)/(V_m(t) - V_m^*)),$$

where $V_m(t + \tau)$ is the transmembrane potential shifted with the time-lag τ, V_m^* is the origin, and *arctan* is a four-quadrant inverse tangent such that $\theta(t)$ is in the range $[-\pi,\pi]$. Given $\theta(t)$, the spatial phase maps can be created and phase singularities (PSs) can be identified. The PS is the spatial point where all phase values converge (62) and may be localized by means of topological charge calculation (9, 24), defined as (23, 44),

$$n_t = 1/2\pi \oint_c \nabla\theta \cdot \dot{dl},$$

where the line integral is taken over a closed curve c surrounding the singularity and n_t is an integer value whose sign depends on the chirality of phase surrounding the singularity. If the line of integration does not enclose the phase singularity, the result is 0; if it does enclose the phase singularity, the result of integration is an integer number, different from zero.

Results

AP Amplitude Alternans and Conduction Block at the Boundary of $[K^+]_o$ Heterogeneity

Figure 2.1 demonstrates the analysis of tissue response to fast pacing (PI = 145 ms) when the heterogeneity was created by means of RP with Tyrode's solution containing 10 mM of K^+. The heart image with superimposed isochrones is illustrated in Figure 2.1A. Panel B presents phase plots and corresponding optical traces extracted from the five pixels marked by black squares in panel A and positioned on the line segment intersecting the boundary of the heterogeneity. The alternans, which occurs as a beat-to-beat change in AP amplitude, starts to develop near the $[K^+]_o$ heterogeneity. In phase plots these irregularities appear as smaller inner loops that shrink as the observation point approaches the RP area and finally vanish, indicating transition to a new rhythm. The transition from normal to 2:1 rhythm is also evident in the time-space plot constructed along the line segment linking pixels 1 and 5 (Figure 2.1C). Panel D includes AP maxima and minima of all pixels of the line segment and illustrates the alternans dynamics as a function of distance.

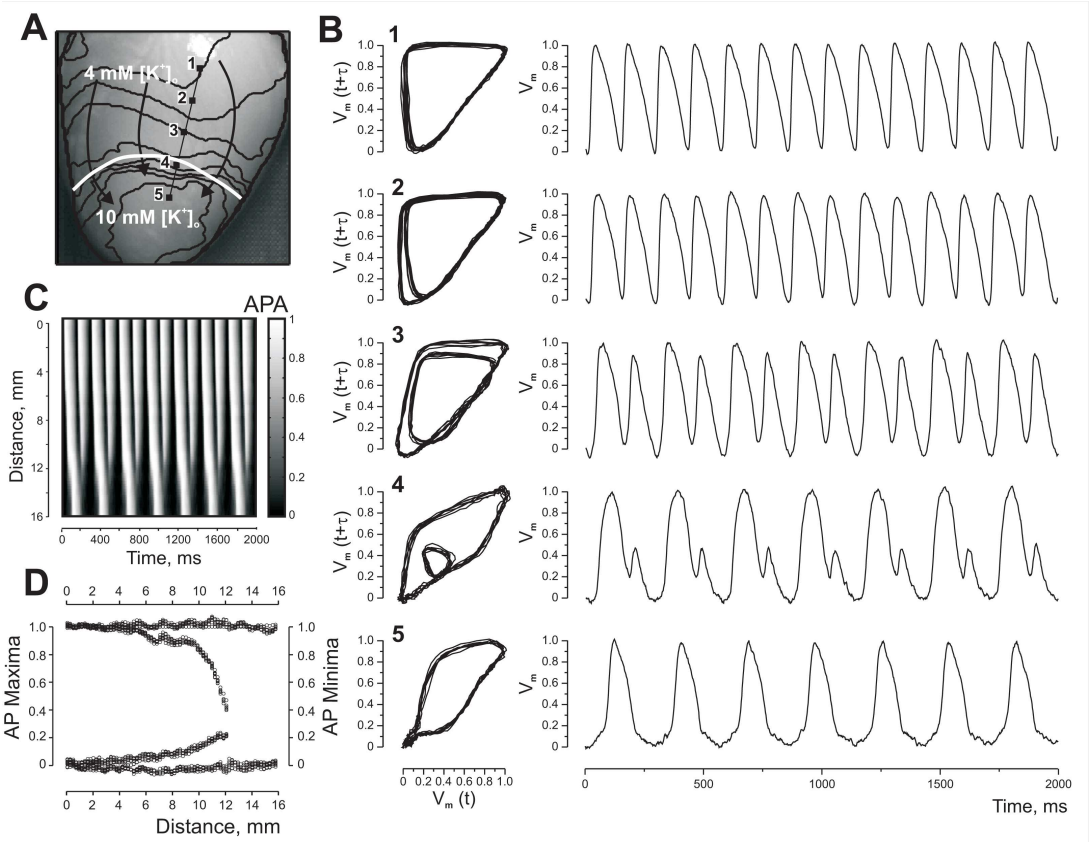

Figure 2.1. Alternans of AP amplitude and 2:1 conduction block induced by fast pacing at the border of a K^+ heterogeneity. The heterogeneity was created by regional perfusion (RP) with 10 mM of K^+. A: Image of the heart with superimposed isochrones (black lines). The white curve outlines the upper boundary of the RP zone. Black arrows indicate the direction of wave front propagation. The stimulation electrode is located above the top of the image, at the right ventricle near the septum. The stimulation interval is 145 ms. B: Phase-space trajectories and corresponding optical traces for the pixel locations marked with black squares in panel A. The phase encoding time lag is 16 ms. C: Time-space plot along the straight black line linking pixels 1 and 5 in panel A, showing clearly the period doubling within the RP zone. Pixel 1 is at 0 mm. D: AP maxima and minima changes as a function of distance between pixels 1 and 5 in panel A.

To assess the spatial distribution of the alternans, the RSD of the AP amplitude was calculated for each time trace and presented as a RSD map in Figure 2.2A. The darker areas in the RSD map correspond to the larger alternans, which precede the conduction block. Figure 2.2B shows the profile of the RSD map extracted from the line segment between pixels 1 and 5 in 2A. The RSD profile slowly rises up, indicating an increase of AP amplitude variability, and then sharply falls down when crossing the line of block. The DF map in Figure 2.2C and 2.2D illustrates two times decrease in frequency within RP area (3.5 Hz) as compared with tissue

perfused with normal $[K^+]_o$ (7 Hz).

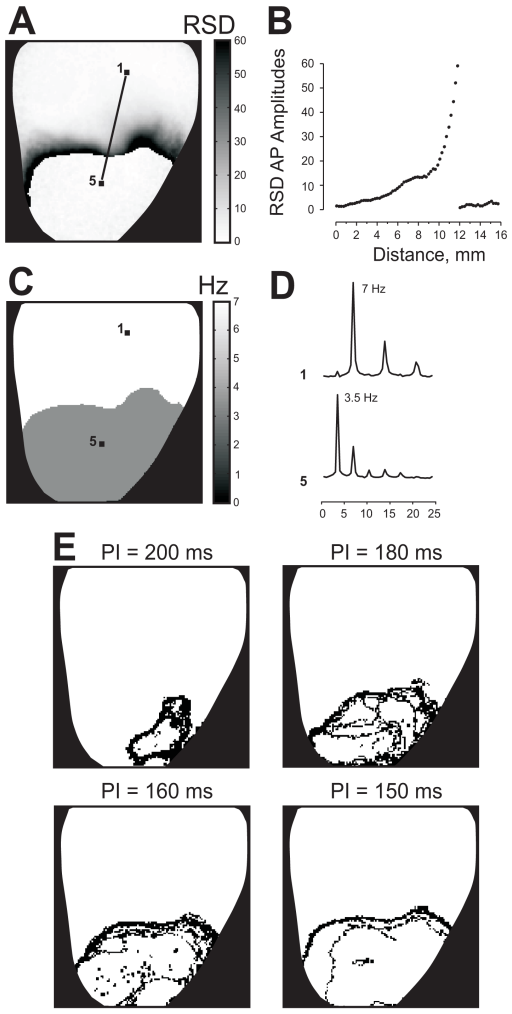

Figure 2.2. AP dynamics resulting from RP with 10 mM $[K^+]_o$ and fast pacing. A: The map of the spatial distribution of the relative standard deviations of the AP amplitude (RSD). B: The profile of the RSD map along the line linking pixels 1 and 5 in panel A. C: The spatial distribution of dominant frequency. D: The power spectra of two individual signals at the labeled pixels. E: The phase singularity maps created for pacing intervals of 200, 180, 160, and 150 ms.

The effect of K^+ heterogeneity on the tissue response dynamics is very prominent in the PS maps presented in Figure 2.2E. The PSs start to precipitate in the RP area when PI is decreased from 300 ms to 200 ms. The distribution of PSs signifies the area of unstable electrical activity, which expands with increasing pacing rate. The similar dynamics of AP alternans and PSs were observed in five experiments. In two experiments we did not observe 2:1 aperiodicity

during RP with 10 mM of K^+ at as short a PI as 140 ms, though alternans was very prominent and the unstable area also enlarged with acceleration of pacing rate.

Effect of $[K^+]_o$ Heterogeneity on Distribution of Activation Times

Figure 2.3 shows mean AT maps in conjunction with histograms created from data obtained during RP with different levels of $[K^+]_o$ at the basic pacing rate (PI = 300 ms). The activation is most homogeneous when the heart was regionally perfused with a solution containing a normal level of K^+ (4 mM). The elevation of the regional $[K^+]_o$ up to 10 mM progressively slows down conduction and causes ample AT delay in the apical part of the heart.

The delay is most prominent transverse to the fiber direction close to the boundary of the RP area. However, no AP alternans was observed at the basic stimulation rate. The related histogram of AT mean values becomes broader and then splits, revealing a bimodal distribution for RP with 10 mM of K^+. The two separate peaks with local maxima at 44 and 98 ms correspond to activation of normal tissue and tissue perfused with high K^+. Further elevation of K^+ in perfusate to 12 mM led to complete depression of excitability of the RP area in 5 of the 7 analyzed experiments. In two experiments the RP tissue became unexcitable when the local $[K^+]_o$ was elevated to 14 mM.

The change in the AT histogram as a result of acceleration of the pacing rate is illustrated in Figure 2.4. The shortening PI from 300 ms to 250 ms increases the delay between two maxima from 54 ms to 65 ms. When PI is decreased to 200 ms, the first hump starts to divide into two peaks, wherein the second peak reflects increasing delay of activation of the transitional zone between tissue with normal and high elevated $[K^+]_o$. At the same pacing rate, the right hump, which signifies the activation of the high $[K^+]_o$ area, becomes broader and lessens in amplitude with the maximum shifted to 130 ms from 98 ms at PI of 300 ms.

The AT histogram reveals very slow and heterogeneous propagation when PI is 180 ms. The shortening of the PI to 150 ms leads to a different behavior of the AT distribution of normal as compared to high $[K^+]^o$ regions. In particular, as compared with PI of 160 ms the first and

second humps at PI of 150 ms slightly moved towards longer time interval, whereas the activation of the RP area (third hump) becomes markedly more homogeneous, with a peak at 120 ms. Such unexpected "improving" of activation of high $[K^+]_o$ area occurs due to the transition to steady 2:1 rhythm with PI shortening to 150 ms.

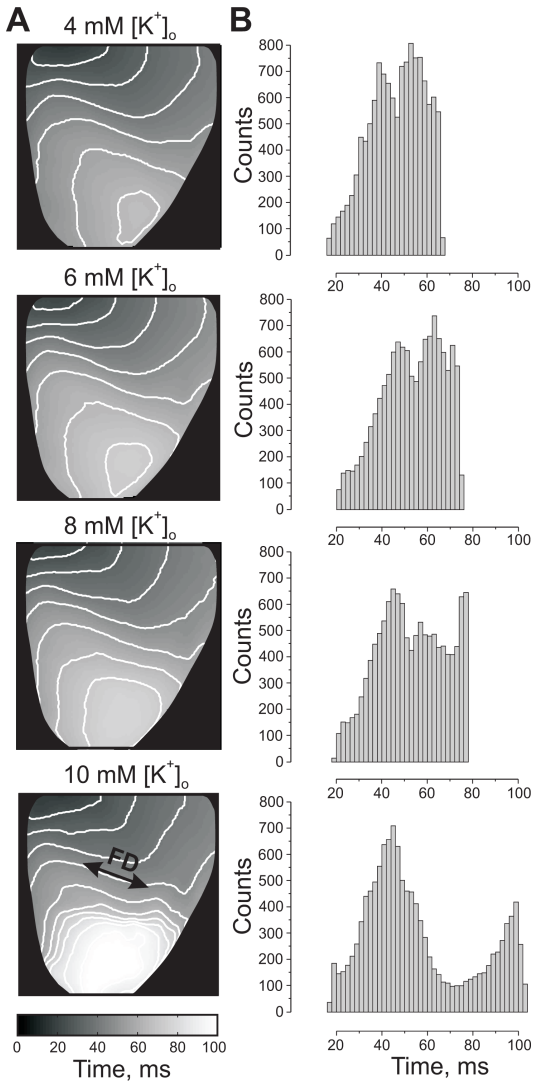

Figure 2.3. Effect of $[K^+]_o$ heterogeneity on the activation time distribution. A: The spatial distribution of mean activation time (MAT) as a function of regional $[K^+]_o$ elevation. B: The corresponding MAT histograms.

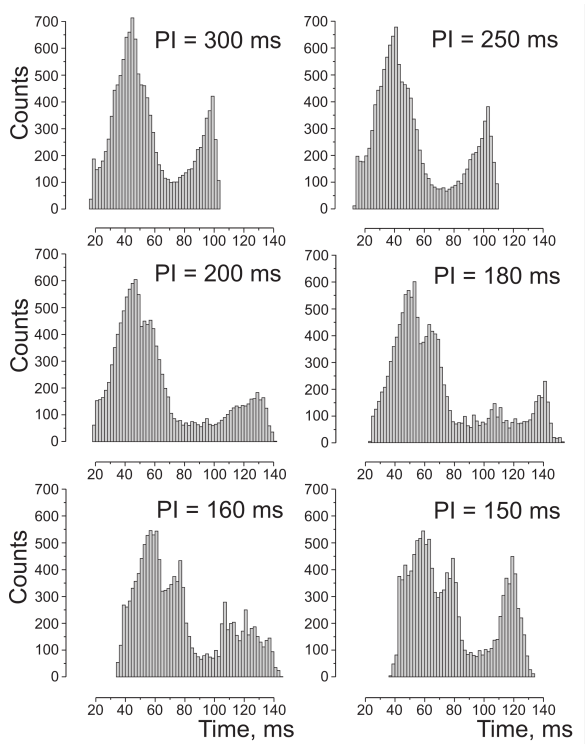

Figure 2.4. Effect of $[K^+]_o$ heterogeneity and stimulation rate on the histogram of MAT. The regional $[K^+]_o$ is 10 mM.

Effect of Elevated $[K^+]_o$ on Restitution Properties

To elucidate the mechanism of induction of AP alternans by high $[K^+]_o$, we examined AT along with APD variations at short PI when alternans was most prominent. Figure 2.5 presents a comparative data analysis of RP experiments when the apical part of the heart was perfused separately with Tyrode's solution containing different levels of K^+. The stimulation protocol was the same as in above described experiments. In this case decreasing of PI to 140 ms produced substantial AP alternans but did not exhibit 2:1 conduction block at RP with 10 mM of K^+. The high K^+ induced considerable shortening of APD is evident in the lower part of the preparation at basic pacing rate (Figure 2.5A). The vigorous AP alternans develop during fast pacing when excitation propagates from the normal to the high $[K^+]_o$ area. It is clearly seen in the time-space plot (Figure 2.5B) constructed along the dashed line transverse to the wave front in Figure 2.5A.

To assess the propagation alternans, which could potentially cause the local electrical instability at the high $[K^+]_o$ region, we examined activation times along with APDs in a Poincaré

plot, which is the generally accepted way to investigate the cardiac cycle beat-to-beat variability (31, 42). Figures 2.5C and 2.5D illustrate the Poincaré plot generated by plotting activation time of wave n (AT_n) versus activation time of the wave n+1 (AT_{n+1}) for 4 mM and 10 mM of regional $[K^+]_o$ during fast pacing (PI = 140 ms). The time traces for analysis were from the black rectangle in Figure 2.5A, which includes both normal and high $[K^+]_o$ areas. Visual inspection of the shape of the Poincaré plot reveals a very uniform and narrow distribution across the line of identity (y = x) for RP with 4 mM of K^+ (Figure 2.5C) and for the most part of the distribution for RP with 10 mM of K^+ (Figure 2.5D). The AT distribution becomes slightly broader at the end for ATs more than 32 ms. Such broadening implies some increase in beat-to-beat variability of conduction when the wave propagates over a high $[K^+]_o$ region. A Poincaré plot built as APD_n versus APD_{n+1} demonstrates a drastic disparity in AP dynamics for 10 mM of regional $[K^+]_o$ (Figure 2.5F) in comparison with 4 mM of local $[K^+]_o$ (Figure 2.5E).

When RP is performed with 4 mM of K^+, APD distribution is very clustered in the upper-right corner. The symmetry with respect to the identity line indicates some APD alternans. A Poincaré plot created for 10 mM of regional $[K^+]_o$ also has a clustered region in the upper-right corner, which relates to the area with normal $[K^+]_o$. However, it splits into two symmetrical branches, implying progressive increase of APD alternans in the high $[K^+]_o$ zone.

To test the hypothesis that spatial heterogeneity of APD restitution due to high regional $[K^+]_o$ can result in AP instability and reentry induction, we conducted additional experiments to investigate the effect of elevated $[K^+]_o$ on APD restitution characteristics. In those experiments (N = 4) $[K^+]_o$ was increased globally and a dynamic pacing protocol was applied to reconstruct the restitution relationship for different levels of $[K^+]_o$. Figure 2.6 illustrates the APD restitution relationships resulting from perfusion with Tyrode's solution containing 4, 6, 8, and 10 mM of K^+.The elevation of $[K^+]_o$ up to 10 mM shortened APD at fast pacing rate from 84.3 ± 6.1 ms (PI = 125 ms) to 69.6 ± 8.7 ms (PI = 185 ms) and at slow stimulation from 175.4 ± 2.4 ms (PI = 400 ms) to 141.4 ± 10.8 ms (PI = 400 ms). However, DI increased during fast pacing from 39.9 ± 5.2 (PI =

125 ms) to 112.9 ± 7.4 ms (PI = 185). At the same PI of 185 ms the DI for 10 mM of $[K^+]_o$ was significantly longer ($P < 0.01$) than for 4 mM of $[K^+]_o$.

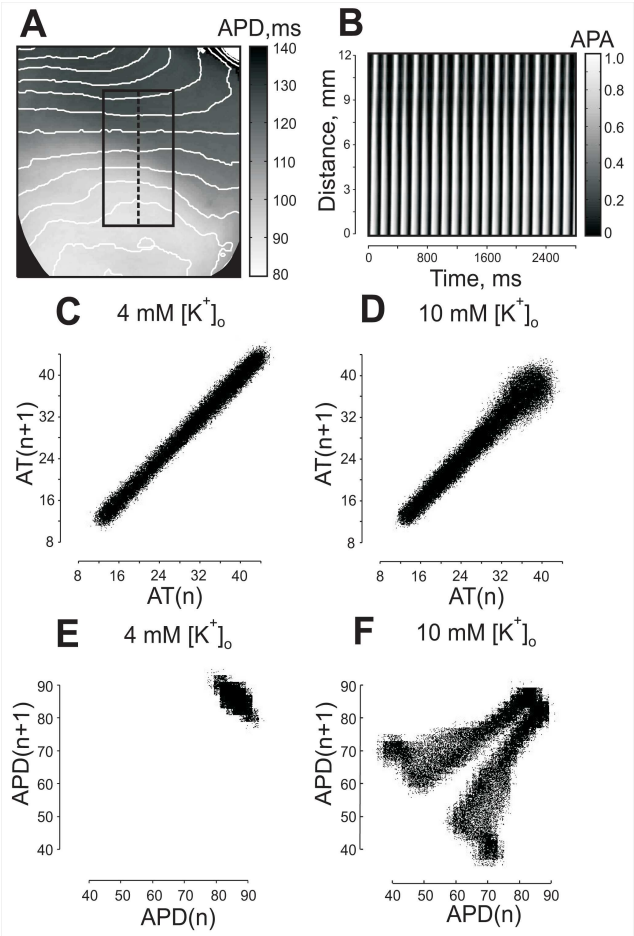

Figure 2.5. Dynamics of AT and APD revealed in Poincaré plots during RP with 4 and 10mM of $[K^+]_o$. A: High local $[K^+]_o$ induced heterogeneity of APD distribution with superimposed isochrones. PI is 300 ms. The black rectangle outlines the area for Poincaré analysis. B: Time space plot along dashed line in panel A. PI is 140 ms. C: AT Poincare plot during RP with 4 mM of K+. D: AT Poincaré plot during RP with 10 mM of K^+. E: APD Poincaré plot for 4mM of regional $[K^+]_o$. F: APD Poincaré plot for 10 mM of local $[K^+]_o$.

Figure 2.7 demonstrates the slopes of restitution curve fits shown in Figure 2.6B. It is clearly seen that elevation of $[K^+]_o$ flattens the restitution relationship, but the region of steep slope (>1) persists for all levels of $[K^+]_o$ at short DI. The slope is > 1 for DI < 100 ms for 10 mM of K^+ and DI < 76 ms for 8 mM of K^+. The derivative of the restitution curves for 4 mM and 6

mM of K^+ have a point of intersection at slope = 1, such that for both curves the slope > 1 is for DI < 62 ms.

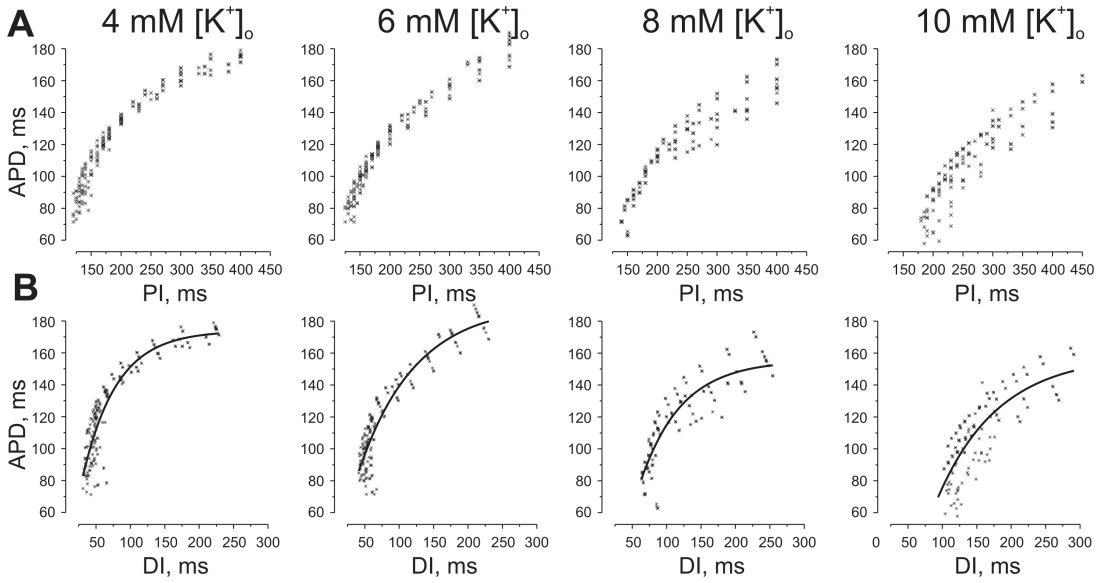

Figure 2.6. Effect of whole-heart $[K^+]_o$ elevation on APD restitution. A: Relationship between APD and PI, and B between APD and DI as a function of different levels of $[K^+]_o$.

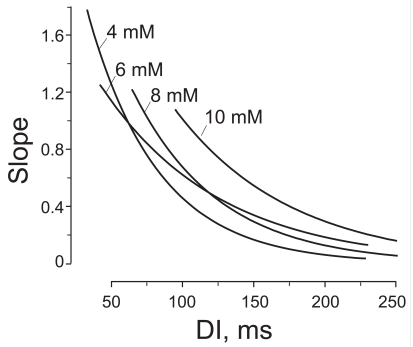

Figure 2.7. Effect of whole-heart $[K^+]_o$ elevation on slope of APD restitution curve. The slopes of the APD restitution curves were computed as derivatives of the restitution relationship fits shown in Figure 2.6.

As expected the increase of $[K^+]_o$ affected refractory period. The $[K^+]_o$ elevation from 4 to 6 mM slightly extended refractoriness from 125 ± 5.8 ms to 126.3 ± 4.8 ms respectively. Further increase of $[K^+]_o$ to 8 mM lengthened refractory period to 143 ± 7.5 ms. The perfusion

with solution containing 10 mM of $[K^+]_o$ significantly prolonged refractoriness to 185 ± 10 ms as compared with 4, 6, and 8 mM of $[K^+]_o$ (N = 4, P < 0.05).

The effect of $[K^+]_o$ elevation on the CV restitution is illustrated in Figure 2.8. Perfusion with solution containing 10 mM of KCl decreased CV at slow stimulations (PI = 300 ÷ 350 ms) from 57.2 ± 5 cm/s (N = 14) to 19.6 ± 1.7 cm/s (N = 20) and at fastest pacing rates from 40.8 ± 4.9 cm/s (PI = 120 ÷ 135 ms, N = 8) to 13.7 ± 0.7 cm/s (PI = 190 ÷ 210 ms, N = 8). The maximum slope of CV restitution curve reduced from 0.354 cm/s2 to 0.086 cm/s. The increase of $[K^+]_o$ significantly lessened the maximum CV alternans from 4.6 ± 1.7 cm/s (N = 4) to 0.3 ± 0.3 cm/s (N = 4) (Figure 2.8C).

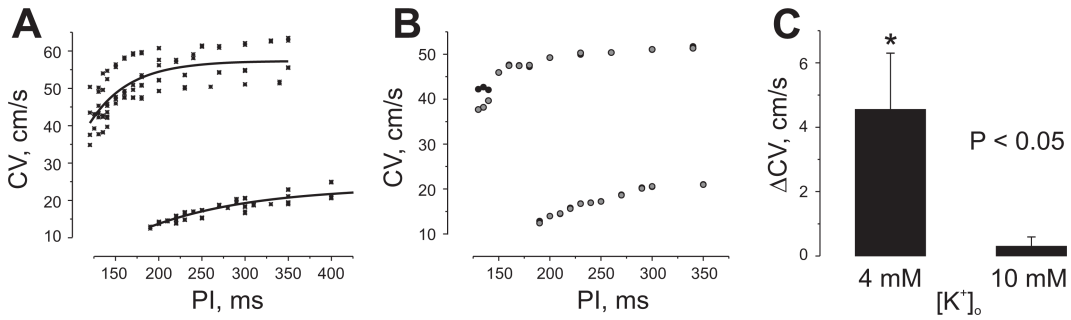

Figure 2.8. Effect of whole-heart $[K^+]_o$ elevation on CV restitution. CV was measured along the fiber direction. A: Relationship between CV and PI as a function of 4 mM and 10 mM of $[K^+]_o$ (N = 4). B: CV restitution exhibits CV alternans at 4 mM of $[K^+]_o$ but not at 10 mM. C: Maximum alternans detected at 4 mM and at 10 mM of $[K^+]_o$

Effect of $[K^+]_o$ Heterogeneity on Arrhythmia Induction and Susceptibility

Figure 2.9 shows the role of K^+ heterogeneity in arrhythmia induction by burst pacing (PI = 140 ms). The K^+ heterogeneity was created by RP with solution containing 10 mM of K^+. In this case the reentrant arrhythmia was initiated after application of four S2 pulses. The excitation wave propagates through the upper basal part of the heart but it is blocked in downward direction at the upper border of the high K^+ region, travels around RP area along the boundary and finally reenters into the high K^+ region from the apical side (Figure 2.9A). The AP alternans during burst pacing can be clearly observed in optical traces presented in Figure 2.9B. The upper and lower traces were extracted from two pixels located at tissue perfused with normal level of

K^+ and at site close to boundary (white line in Figure 2.9A) respectively. The Vm maps in Figure 2.9C demonstrate one complete cycle of reentry during course of the arrhythmia.

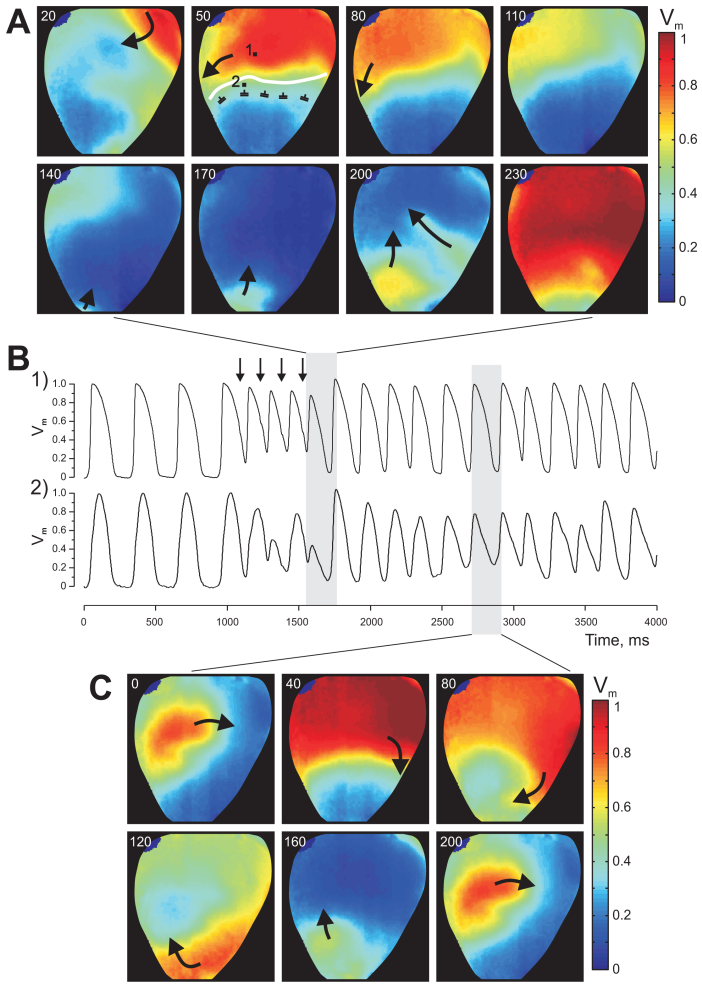

Figure 2.9. Example of reentry initiation with burst pacing (PI = 140 ms). The heart was regionally perfused with solution containing 10 mM of K^+. A: Vm maps of the first reentry cycle. The numbers at upper left in each image represent the elapsed time (ms) since last S2 termination. White curve line delineates the boundary between normal and high K^+ areas. B: Vm traces corresponding two pixel locations marked with black squares in panel A. Black vertical arrows point time of S2 application. C: Vm maps of one cycle reentry rotation during sustained arrhythmia.

To quantify the relationship between K^+ heterogeneity and vulnerability to ventricular arrhythmias, we conducted six separate experiments wherein a burst of ten successive stimuli at shorter pacing intervals was tested. Figure 2.10 demonstrates how the rate of arrhythmia

induction depends upon local $[K^+]_o$ and PI during burst pacing. The elevation of the local $[K^+]_o$ from 4 mM up to 6 mM extends the vulnerable interval from 10 ms to 20 ms.

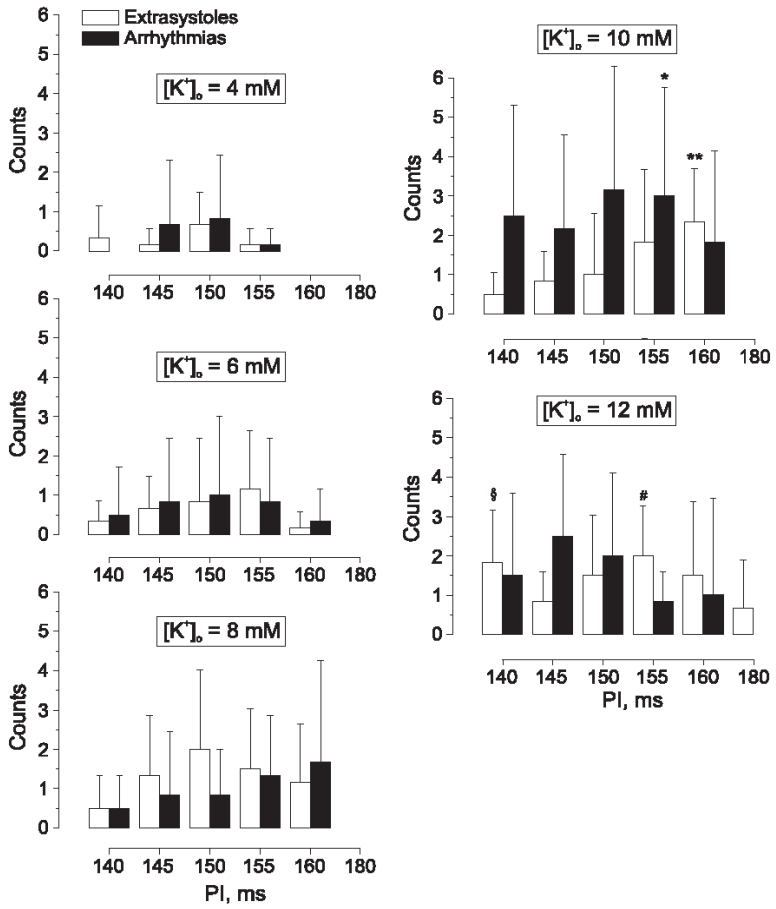

Figure 2.10. Effect of $[K^+]_o$ heterogeneity on arrhythmia susceptibility as measured by the occurrence of either extrasystoles or arrhythmias at different values of the pacing interval (PI). The $[K^+]_o$ heterogeneities were created by RP with Tyrode's solution containing 4, 6, 8, 10, and 12 mM of K^+. The data were acquired in six separate experiments. *$P < 0.05$ compared with arrhythmias induced at 4 mM of $[K^+]_o$, PI = 155 ms; **$P < 0.01$ compared with extrasystoles induced at 6 mM of $[K^+]_o$, PI = 160 ms; $^{§}P < 0.05$ compared with extrasystoles induced at 6 mM of $[K^+]_o$, PI = 140 ms; $^{\#}P < 0.01$ compared with extrasystoles induced at 4 mM of $[K^+]_o$, PI = 155 ms.

Subsequent augmentation of the regional $[K^+]_o$ up to 8 mM substantially increases the probability of extrasystole occurrence in the interval of stimulation periods between 140 ms and 160 ms and also accelerates the arrhythmia incidence. The RP with 10 mM of K^+ is associated with the highest rate of arrhythmia induction with a maximum at PI of 150 ms. The following

elevation of the local $[K^+]_o$ to 12 mM decreases the probability of arrhythmia induction for all except 145-ms stimulation intervals. However, the rate of extrasystole incidence increases for 140, 150, 180-ms stimulation intervals and decreases for PIs of 145, 155, and 160 ms.

Discussion

AP alternans in amplitude and duration are frequently observed at the onset of ischemia (21, 45) and during rapid pacing (15, 48). It was demonstrated that elevation of $[K^+]_o$ can also cause AP alternans (19, 38). In isolated preparations of canine endocardial muscle, the fast pacing, along with a global increase in $[K^+]_o$ from 8 to 12 mM, enhanced the magnitude of APD alternans (38). The combination of $[K^+]_o$ 12 mM and 120-ms pacing interval led to 2:1 conduction block (38). In a theoretical study Arce and Lopez (2) observed AP alternans in a modified Luo-Rudy (LRd) ionic model (41) of one-dimensional normal myocardium strand with an embedded area of elevated $[K^+]_o$. In their work alternans was detected in a narrow range of elevated $[K^+]_o$ around 13.19 mM under a fixed pacing cycle length of 400 ms. As $[K^+]_o$ was increased, a transition from 1:1 rhythm to 2:2 alternating rhythm and then from 2:2 rhythm to 2:1 block was observed. Despite an evident relationship between increased $[K^+]_o$ and occurrence of alternans on the one hand and between macroscopic local $[K^+]_o$ heterogeneity, which takes place during the first minutes after coronary occlusion, and phase 1a arrhythmias on the other hand, studies linking these important issues are lacking.

In this work we investigated experimentally the effect of an artificially created stable local K^+ heterogeneity on the propagation pattern and demonstrated three dynamics: regular 1:1 sequence, alternating 2:2 rhythm, and 2:1 aperiodicity during fast pacing. These dynamics existed concurrently and were associated with tissue as affected by different levels of $[K^+]_o$ that ranged between 4 and 10 mM. The size of the area of alternating AP was not stable; it depended on the PI and expanded with acceleration of pacing rate. The local AP alternans appeared when PI decreased to 200-180 ms. When the PI was shortened to 150-140 ms, the area of unstable

2:2 rhythm relocated from the central zone to the border of K^+ heterogeneity, whereas the central RP area exhibited 2:1 rhythm. The activation of this locally perfused area became more homogeneous due to the longer diastolic interval resulting from 2:1 rhythm.

Two basic mechanisms of alternans have been considered. The first one is related to the dynamics of V_m and is attributed to the restitution properties of tissue. The second mechanism is linked to Ca^{2+} cycling instability (20, 49). Because V_m and intracellular Ca^{2+} ($[Ca^{2+}]_i$) are bidirectionally coupled, usually these two mechanisms coexist. Since the elevation of $[K^+]_o$ causes APD shortening and depression of excitability, and creates post-repolarization refractoriness, the traditional view is that it changes the character of interaction of the front and tail of subsequent waves during fast pacing and thereby creates CV alternans, which in turn lead to APD alternans and conduction block. In our work we tested the alternative hypothesis that local elevation of $[K^+]_o$ creates the spatial heterogeneity of the APD restitution and thereby forms a substrate for AP alternans and reentry induction. We found that successive elevation of $[K^+]_o$ i) flattens APD restitution, ii) shifts the restitution relationship towards shorter APD and a longer DI, and iii) preserves the steep slope of the restitution curve. The maximum slope of the APD restitution curve decreased from 1.8 for 4 mM to 1.1 for 10 mM of $[K^+]_o$, which signifies a shortening of the region of PIs where alternans could appear. The displacement of the restitution relationship to longer DI is evidence of post-repolarization refractoriness. In theory, the sustained APD alternans can occur in tissue if an APD restitution relationship has a maximum slope >1 (18, 47). Due to post-repolarization refractoriness and maintenance of steep slope of restitution curve in the high K^+ perfused tissue, this region cannot accommodate the fast pacing. When stimulation rate progressively increases, it starts to generate alternans and then develops 2:1 aperiodicity, while the most of tissue is still able to support normal 1:1 rhythm.

The elevation of the $[K^+]_o$ also affected the CV restitution relationship. It slowed down propagation and flattened restitution curve and thereby precluded occurrence of CV alternans (Figure 2.8). Note that CV alternans at 4 mM of $[K^+]_o$ started to develop at PI ≤ 140 ms, whereas AP alternans at high K^+ region appeared when PI was decreased to 200 – 180 ms, and 2:1

aperiodicity was detected at PI ≤ 150 ms. This excludes the contribution of alternating conduction originated at tissue perfused with normal K^+ in formation of AP alternans observed in high K^+ area. Does the propagation instability at high K^+ area cause AP alternans? Based on our analysis of CV restitution relationship and lack of CV alternans at 10 mM of $[K^+]_o$, we conclude that spatial heterogeneity of APD restitution is mainly responsible for occurrence of AP alternans, conduction block and reentry.

Our restitution results are consistent with the data of Koller et al.,(38) where the authors observed analogous behavior of the APD restitution relationship, though in an preparation of isolated sections of canine myocardium. In particular, the increase in $[K^+]_o$ from 2.7 to 10 mM decreased the slope of APD restitution ratio at long, but not short DI, and decreased the range of DI where the slope was >1. Our findings are also comparable to results of the theoretical study of Bernus et al., (5) where the authors used the LRd model to simulate the three main components of ischemia at cellular level: hyperkalemia, acidosis, and anoxia. When pacing rate was increased they observed a 2:1 conduction block on the periphery of the border zone and complete conduction block at the edge of the ischemic area. They found that hyperkalemia alone (14.5 mM of K^+) is sufficient to induce such complex dynamics and that voltage-dependent gating of Ca^{2+} current is an ionic mechanism for alternating conduction block. We observed similar AP dynamics at close $[K^+]_o$ level. As already mentioned, due to tight V_m – $[Ca^{2+}]_i$ bidirectional coupling, $[Ca^{2+}]_i$ dynamics can play a substantial role in causing AP alternans and block in conditions of elevated $[K^+]_o$. Studies with concurrent V_m and $[Ca^{2+}]_i$ registrations would be very valuable in addressing this issue.

Several factors determine the reentry inducibility in the regionally perfused rabbit heart preparation. The most important are the stimulation rate, the dimensions of the RP area, the location of stimulation, and the extent of excitability depression due to different levels of $[K^+]_o$. In our data, arrhythmia susceptibility predictably increased with rising $[K^+]_o$ from 4 to 10 mM. However, further $[K^+]_o$ elevation to 12 mM decreased arrhythmogenicity at most of the stimulation cycle lengths. During RP with 10 mM of K^+, the activation of the RP area occurred

with a significant delay (Figure 2.4), which increases with PI shortening and thereby promotes occurrence of the wave breaks at the border zone and facilitates reentry induction. Increasing $[K^+]_o$ to 12 mM elevates the resting membrane potential to about - 65 mV (50, 51). At such a level of transmembrane potential the sodium inactivation gates are closing (4) and tissue becomes unexcitable (55). As a result, the contribution of $[K^+]_o$ heterogeneity to wave fragmentation is reduced and this region plays a role mainly as an obstacle to anchor the reentry.

It was postulated that "injury" currents flowing through the ischemic border are related to occurrence of ectopic beats and initiation of reentry (29, 36). In our work we did not detect a focal ectopic activity at the border zone. One possible reason is that the maximum level of local $[K^+]_o$ was still low to create sufficient gradient in resting Vm and meet sink-source requirements for excitation. The inability to form sharp transition from high to low $[K^+]_o$ could be another cause preventing reexcitation. On the other hand high cell-to-cell coupling also contributes in precluding of abrupt gradient in resting Vm.

In conclusion, the stable K^+ concentrations that we used to create a myocardial heterogeneity correspond to the levels of $[K^+]_o$ detected during the first 10 min after coronary occlusion (58, 61). This early period of acute ischemia is characterized by a maximum rate of incidence of ventricular arrhythmias (13, 33), and the phenomenon described in this work can be one of the scenarios for reentry induction in phase 1a arrhythmias. The power of our preparation and analysis lies with our ability to control the severity of the regional heterogeneity and quantify the resulting changes in AP dynamics, conduction, and increases in arrhythmogenicity, which play important roles in the electrophysiological disturbances associated with acute myocardial ischemia.

Limitations

To abolish the motion artifact from recorded data, the optical mapping techniques require the use of excitation-contraction uncouplers. In the current study we utilized BDM, which is known to change several membrane conductances (6, 56) and thereby causes some

electrophysiological effects (14, 37, 40), including flattening the APD restitution curve (3). To examine the potential effect of BDM on the dynamics of cardiac response we conducted two additional experiments using a new excitation-contraction uncoupling agent, Blebbistatin, which is considered to have no effects on the action potential morphology in rabbit cardiac tissue (22). Similarly to our experiments using BDM we observed three concurrent dynamics: normal, 2:2, and 2:1 rhythm when $[K^+]_o$ was regionally elevated and PI was shortened to 140 ms. Hence we concluded that the effects we observed were not dependent upon the use of BDM.

Acknowledgment

The authors would like to thank Bradley J. Roth for his comments and suggestions and Allison Price for her assistance with the preparation of this manuscript.

Grants

This work was supported by the American Heart Association [0635037N]; and by the National Institutes of Health [R01 HL58241-11] through the American Recovery and Reinvestment Act of 2009.

References

1. Antzelevitch C, Shimizu W, Yan GX, Sicouri S, Weissenburger J, Nesterenko VV, Burashnikov A, Di Diego J, Saffitz J and Thomas GP. The M cell: Its contribution to the ECG and to normal and abnormal electrical function of the heart. *J Cardiovasc Electrophysiol* 10: 1124-1152, 1999.
2. Arce H, Lopez A and Guevara MR. Triggered alternans in an ionic model of ischemic cardiac ventricular muscle. *Chaos* 12: 807-818, 2002.
3. Banville I and Gray RA. Effect of action potential duration and conduction velocity restitution and their spatial dispersion on alternans and the stability of arrhythmias. *J Cardiovasc Electrophysiol* 13: 1141-1149, 2002.
4. Beeler GW and Reuter H. Reconstruction of the action potential of ventricular myocardial fibres. *J Physiol* 268: 177-210, 1977.
5. Bernus O, Zemlin CW, Zaritsky RM, Mironov SF and Pertsov AM. Alternating conduction in the ischaemic border zone as precursor of reentrant arrhythmias: a simulation study. *Europace* 7 Suppl 2: 93-104, 2005.
6. Biermann M, Rubart M, Moreno A, Wu J, Josiah-Durant A and Zipes DP. Differential effects of cytochalasin D and 2,3 butanedione monoxime on isometric twitch force and transmembrane action potential in isolated ventricular muscle: implications for optical measurements of cardiac repolarization. *J Cardiovasc Electrophysiol* 9: 1348-1357, 1998.
7. Bray MA, Lin SF, Aliev RR, Roth BJ and Wikswo JP, Jr. Experimental and theoretical analysis of phase singularity dynamics in cardiac tissue. *J Cardiovasc Electrophysiol* 12: 716-722, 2001.
8. Bray MA, Lin SF and Wikswo J. Three-dimensional visualization of phase singularities on the isolated rabbit heart. *J Cardiovasc Electrophysiol* 13: 1311, 2002.

9. Bray MA and Wikswo JP. Use of topological charge to determine filament location and dynamics in a numerical model of scroll wave activity. *IEEE Trans Biomed Eng* 49: 1086-1093, 2002.
10. Cao JM, Qu ZL, Kim YH, Wu TJ, Garfinkel A, Weiss JN, Karagueuzian HS and Chen PS. Spatiotemporal heterogeneity in the induction of ventricular fibrillation by rapid pacing importance of cardiac restitution properties. *Circ Res* 84: 1318-1331, 1999.
11. Carmeliet E. Cardiac ionic currents and acute ischemia: From channels to arrhythmias. *Physiol Rev* 79: 917-1017, 1999.
12. Cascio WE, Yan GX and Kleber AG. Early changes in extracellular potassium in ischemic rabbit myocardium. The role of extracellular carbon dioxide accumulation and diffusion. *Circ Res* 70: 409-422, 1992.
13. Cascio WE, Yang H, Muller-Borer BJ and Johnson TA. Ischemia-induced arrhythmia: the role of connexins, gap junctions, and attendant changes in impulse propagation. *J Electrocardiol* 38: 55-59, 2005.
14. Cheng Y, Li L, Nikolski V, Wallick DW and Efimov IR. Shock-induced arrhythmogenesis is enhanced by 2,3-butanedione monoxime compared with cytochalasin D. *Am J Physiol Heart Circ Physiol* 286: H310-H318, 2004.
15. Chialvo DR, Gilmour RF, Jr. and Jalife J. Low dimensional chaos in cardiac tissue. *Nature* 343: 653-657, 1990.
16. Choi BR, Liu T and Salama G. The distribution of refractory periods influences the dynamics of ventricular fibrillation. *Circ Res* 88: e49-e58, 2001.
17. Coronel R, Fiolet JW, Wilms-Schopman FJ, Schaapherder AF, Johnson TA, Gettes LS and Janse MJ. Distribution of extracellular potassium and its relation to electrophysiologic changes during acute myocardial ischemia in the isolated perfused porcine heart. *Circulation* 77: 1125-1138, 1988.
18. Courtemanche M. Complex spiral wave dynamics in a spatially distributed ionic model of cardiac electrical activity. *Chaos* 6: 579-600, 1996.

19. Cranefield PF, Klein HO and Hoffman BF. Conduction of the cardiac impulse. 1. Delay, block, and one-way block in depressed Purkinje fibers. *Circ Res* 28: 199-219, 1971.
20. Diaz ME, O'Neill SC and Eisner DA. Sarcoplasmic reticulum calcium content fluctuation is the key to cardiac alternans. *Circ Res* 94: 650-656, 2004.
21. Dilly SG and Lab MJ. Electrophysiological alternans and restitution during acute regional ischaemia in myocardium of anaesthetized pig. *J Physiol* 402: 315-333, 1988.
22. Fedorov VV, Lozinsky IT, Sosunov EA, Anyukhovsky EP, Rosen MR, Balke CW and Efimov IR. Application of blebbistatin as an excitation-contraction uncoupler for electrophysiologic study of rat and rabbit hearts. *Heart Rhythm* 4: 619-626, 2007.
23. Goryachev A and Kapral R. Spiral waves in chaotic systems. *Phys Rev Lett* 76: 1619-1622, 1996.
24. Gray RA, Pertsov AM and Jalife J. Spatial and temporal organization during cardiac fibrillation. *Nature* 392: 75-78, 1998.
25. Hill JL and Gettes LS. Effect of acute coronary artery occlusion on local myocardial extracellular K^+ activity in swine. *Circulation* 61: 768-778, 1980.
26. Hirche H, Franz C, Bos L, Bissig R, Lang R and Schramm M. Myocardial extracellular K^+ and H+ increase and noradrenaline release as possible cause of early arrhythmias following acute coronary artery occlusion in pigs. *J Mol Cell Cardiol* 12: 579-593, 1980.
27. Jacobus WE, Pores IH, Lucas SK, Weisfeldt ML and Flaherty JT. Intracellular acidosis and contractility in the normal and ischemic heart as examined by 31P NMR. *J Mol Cell Cardiol* 14 Suppl 3: 13-20, 1982.
28. Janse MJ and Kleber AG. Electrophysiological changes and ventricular arrhythmias in the early phase of regional myocardial ischemia. *Circ Res* 49: 1069-1081, 1981.
29. Janse MJ, van Capelle FJ, Morsink H, Kleber AG, Wilms-Schopman F, Cardinal R, d'Alnoncourt CN and Durrer D. Flow of "injury" current and patterns of excitation during early ventricular arrhythmias in acute regional myocardial ischemia in isolated porcine

and canine hearts. Evidence for two different arrhythmogenic mechanisms. *Circ Res* 47: 151-165, 1980.

30. Johnson TA, Engle CL, Boyd LM, Koch GG, Gwinn M and Gettes LS. Magnitude and time course of extracellular potassium inhomogeneities during acute ischemia in pigs. Effect of verapamil. *Circulation* 83: 622-634, 1991.
31. Kamen PW, Krum H and Tonkin AM. Poincare plot of heart rate variability allows quantitative display of parasympathetic nervous activity in humans. *Clin Sci (Lond)* 91: 201-208, 1996.
32. Kaplan D and Glass L. Time-series analysis. In: Understanding nonlinear dynamics, New York: Springer-Verlag, 1995, p. 308-314.
33. Kaplinsky E, Ogawa S, Balke CW and Dreifus LS. Two periods of early ventricular arrhythmia in the canine acute myocardial infarction model. *Circulation* 60: 397-403, 1979.
34. Kleber AG. Resting membrane potential, extracellular potassium activity, and intracellular sodium activity during acute global ischemia in isolated perfused guinea pig hearts. *Circ Res* 52: 442-450, 1983.
35. Kleber AG. Extracellular potassium accumulation in acute myocardial ischemia. *J Mol Cell Cardiol* 16: 389-394, 1984.
36. Kleber AG, Janse MJ, van Capelle FJ and Durrer D. Mechanism and time course of S-T and T-Q segment changes during acute regional myocardial ischemia in the pig heart determined by extracellular and intracellular recordings. *Circ Res* 42: 603-613, 1978.
37. Knisley SB and Hill BC. Effects of bipolar point and line stimulation in anisotropic rabbit epicardium: assessment of the critical radius of curvature for longitudinal block. *IEEE Trans Biomed Eng* 42: 957-966, 1995.
38. Koller ML, Riccio ML and Gilmour RF, Jr. Effects of $[K^+]_o$ on electrical restitution and activation dynamics during ventricular fibrillation. *Am J Physiol* 279: H2665-H2672, 2000.

39. Lameris TW, de Zeeuw S, Alberts G, Boomsma F, Duncker DJ, Verdouw PD, in't Veld AJM and van den Meiracker AH. Time course and mechanism of myocardial catecholamine release during transient ischemia in vivo. *Circulation* 101: 2645-2650, 2000.

40. Liu Y, Cabo C, Salomonsz R, Delmar M, Davidenko J and Jalife J. Effects of diacetyl monoxime on the electrical properties of sheep and guinea pig ventricular muscle. *Cardiovasc Res* 27: 1991-1997, 1993.

41. Luo CH and Rudy Y. A model of the ventricular cardiac action potential. Depolarization, repolarization, and their interaction. *Circ Res* 68: 1501-1526, 1991.

42. Makikallio TH, Seppanen T, Airaksinen KE, Koistinen J, Tulppo MP, Peng CK, Goldberger AL and Huikuri HV. Dynamic analysis of heart rate may predict subsequent ventricular tachycardia after myocardial infarction. *Am J Cardiol* 80: 779-783, 1997.

43. Marban E, Kitakaze M, Koretsune Y, Yue DT, Chacko VP and Pike MM. Quantification of [Ca2+]i in perfused hearts. Critical evaluation of the 5F-BAPTA and nuclear magnetic resonance method as applied to the study of ischemia and reperfusion. *Circ Res* 66: 1255-1267, 1990.

44. Mermin ND. Topological theory of defects in ordered media. *Rev Mod Phys* 51: 591-648, 1979.

45. Mohabir R, Franz MR and Clusin WT. In vivo electrophysiological detection of myocardial ischemia through monophasic action potential recording. *Prog Cardiovasc Dis* 34: 15-28, 1991.

46. Mohabir R, Lee HC, Kurz RW and Clusin WT. Effects of ischemia and hypercarbic acidosis on myocyte calcium transients, contraction, and pHi in perfused rabbit hearts. *Circ Res* 69: 1525-1537, 1991.

47. Nolasco JB and Dahlen RW. A graphic method for the study of alternation in cardiac action potentials. *J Appl Physiol* 25: 191-196, 1968.

48. Pastore JM, Girouard SD, Laurita KR, Akar FG and Rosenbaum DS. Mechanism linking T-wave alternans to the genesis of cardiac fibrillation. *Circulation* 99: 1385-1394, 1999.

49. Pruvot EJ, Katra RP, Rosenbaum DS and Laurita KR. Role of calcium cycling versus restitution in the mechanism of repolarization alternans. *Circ Res* 94: 1083-1090, 2004.

50. Roth BJ and Patel SG. Effects of elevated extracellular potassium ion concentration on anodal excitation of cardiac tissue. *J Cardiovasc Electrophysiol* 14: 1351-1355, 2003.

51. Shaw RM and Rudy Y. Electrophysiologic effects of acute myocardial ischemia - A mechanistic investigation of action potential conduction and conduction failure. *Circ Res* 80: 124-138, 1997.

52. Sidorov VY, Holcomb MR, Woods MC, Gray RA and Wikswo JP. Effects of unipolar stimulation on voltage and calcium distributions in the isolated rabbit heart. *Basic Res Cardiol* 103: 537-551, 2008.

53. Sidorov VY, Woods MC and Baudenbacher F. Cathodal stimulation in the recovery phase of a propagating planar wave in the rabbit heart reveals four stimulation mechanisms. *J Physiol* 583: 237-250, 2007.

54. Sidorov VY, Woods MC, Baudenbacher P and Baudenbacher F. Examination of stimulation mechanism and strength-interval curve in cardiac tissue. *Am J Physiol* 289: H2602-H2615, 2005.

55. Sidorov VY, Woods MC and Wikswo JP. Effects of elevated extracellular potassium on the stimulation mechanism of diastolic cardiac tissue. *Biophys J* 84: 3470-3479, 2003.

56. Watanabe Y, Iwamoto T, Matsuoka I, Ohkubo S, Ono T, Watano T, Shigekawa M and Kimura J. Inhibitory effect of 2,3-butanedione monoxime (BDM) on Na(+)/Ca(2+) exchange current in guinea-pig cardiac ventricular myocytes. *Br J Pharmacol* 132: 1317-1325, 2001.

57. Weiss J and Shine KI. Extracellular K^+ accumulation during myocardial ischemia in isolated rabbit heart. *Am J Physiol* 242: H619-H628, 1982.

58. Weiss J and Shine KI. $[K^+]_o$ accumulation and electrophysiological alterations during early myocardial ischemia. *Am J Physiol* 243: H318-H327, 1982.

59. Wiegerinck RF, van Veen TAB, Befterman CN, Schumacher CA, Noorman M, de Bakker JMT and Coronel R. Transmural dispersion of refractoriness and conduction velocity is associated with heterogeneously reduced connexin43 in a rabbit model of heart failure. *Heart Rhythm* 5: 1178-1185, 2008.

60. Wilde AA and Aksnes G. Myocardial potassium loss and cell depolarisation in ischaemia and hypoxia. *Cardiovasc Res* 29: 1-15, 1995.

61. Wilde AA, Escande D, Schumacher CA, Thuringer D, Mestre M, Fiolet JW and Janse MJ. Potassium accumulation in the globally ischemic mammalian heart. A role for the ATP-sensitive potassium channel. *Circ Res* 67: 835-843, 1990.

62. Winfree AT. *When time breaks down*. Princeton: Prinston University Press, 1987.

63. Wu F, Zhang EY, Zhang JY, Bache RJ and Beard DA. Phosphate metabolite concentrations and ATP hydrolysis potential in normal and ischaemic hearts. *J Physiol* 586: 4193-4208, 2008.

CHAPTER III

CHAOS CONTROL IN EXCITABLE MEDIA

Summary

Current commercial single shock defibrillators use a single, fixed waveform to shock the heart, and defibrillation is terminated upon empirical observation that the heart has "exited" ventricular fibrillation (VF) and returned to the sinus rhythm. There is a lack of systematic and unifying study that connects detection of phase singularities and subsequently the associated VF with the optimal shape, amplitude, timing and duration of a defibrillation shock. Also, the mechanisms by which a defibrillation shock terminates VF are currently not well understood.

The goals of my research are first to devise a method for the early detection of VF and second to create an optimized defibrillation waveform shock that avoids the need of a large, whole-heart defibrillation shock. The ultimate goal is to prove that methods based on small perturbations will require much lower energies than are currently utilized in single shock defibrillators or even Low-Energy Anti-fibrillation Pacing (LEAP) defibrillators[1]. Biological systems such as the heart have an embedded control system that provides life support and must resist a wide variety of perturbations during its lifetime. However, this system is not designed to operate properly during VF since it is unlikely that VF will ever occur in a healthy heart, and as we know, cardiac control fails under these circumstances.

This chapter explores the role of phase singularities during VF, gives a general overview of VF from the perspective of non-linear dynamics and explains why the cardiac control system fails during VF. In order to devise control methods that will be applied externally to the cardiac tissue, concepts of control are summarized from the perspective of engineering and parallels are drawn between biological systems and manmade control systems. From these parallels, control

systems based on the feedback are chosen as the most efficient and effective control methods. Two feedback methods that are applied as an external continuous feedback control of cardiac dynamics are analyzed: delayed feedback control (DFC) and proportional-integral-derivative (PID) phase space control.

An overview of the key characteristics of chaotic systems and the concepts behind chaos control will elucidate the mechanisms of these two control methods. All chaos control methods are based on the idea of making small, time-dependent perturbations and are distinguished by being based on feedback control or not. Feedback control algorithms can be further divided into continuous and non-continuous feedback algorithms. Continuous feedback control methods are of special interest in cardiac control, but to date there have been a very limited number of related publications. It is important to note that DFC and PID control methods are based on continuous feedback control by self-controlling feedback that vanishes when stabilization is achieved. At the end of the chapter is a summary of various cardiac control methods separated into three categories: global control, multisite local control, and local control. Most of these methods are not based on feedback control. Therefore, our approach with continuous feedback control is a novel method of local control of spatiotemporal chaos.

Introduction

The theory of non-linear dynamics uses a special space called phase space where each point represents a possible state of a system. Phase space, which is almost always multidimensional, is more easily understood by making an analogy with the geometrical space we live in. Of particular interest are dynamical systems that have periodic behavior in time, thus making closed orbits in their phase space, much as planets circle around the sun. These orbits are not always stable, particularly when there are multiple, interacting planets. Just as there are black holes in the universe, there may be such states that if some object passes close enough, it can exhibit a new trajectory or even a new, highly stable orbit. The same effects occur in cardiac

arrhythmias. In non-linear dynamics, the analogy to black holes is a mathematical entity called an attractor or a phase singularity. The presence of phase singularities is often an undesirable situation in cardiac dynamics, as will be explained.

The heart beats periodically, thus in phase space every state of the heart can be represented as a set of overlapping closed orbits, but this is a macroscopic property that is a statistical quantity derived from the individual activity of all cardiac cells. During sinus rhythm, cardiac cells behave as a set of hourglasses, or more precisely, and analogously, as monostable multivibrators. They all operate at the same frequency, but their phases have a certain distribution. The time evolution of each oscillator in its own phase space can be represented as a set of overlapping orbits with the same period if the sinus rhythm is at a constant rate. The stability of any particular orbit depends on its current phase and on the phases of all oscillators that are at such spatial distances that their influence can act as a perturbation. Cardiac arrhythmogenesis is actually very complex, and this is certainly a simplistic view, but following these general ideas and making parallels with non-linear dynamics, it is possible to draw certain conclusions that aim to be independent of the nature of the dynamical system that is targeted for control. The activity of each cardiac cell is ultimately driven, through its neighbor, cardiac pacemaker and the conduction system. Collectively, these cardiac cells are controlled by the intrinsic distributed control system, referred to as the cardiac control system or the intrinsic control system. When this system fails, without intervention death inevitably results.

Ventricular fibrillation, the leading cause of death in the industrialized world, creates a chaotic* state in the heart through multiple unstable spiral waves rotating around their centers, termed phase singularities (PSs) in non-linear dynamics. These waves, which look like the arm of a spiral galaxy, are by nature electrical rotating waves. They prevent the heart from adequately pumping blood and lead to death if they are not terminated. Despite being extensively studied for decades, spiral waves are not easy to terminate, and at present the only practical means to

*In this dissertation, I frequently use the term "chaotic" as a description of generalized, unpredictable behavior that does not necessarily correspond to the rigorous mathematical definition of chaos, which I present later.

automatically stop VF is to deliver a single strong electric shock to the entire heart using defibrillators or with multiple low-energy shocks in a novel Low-Energy Anti-fibrillation Pacing (LEAP) technique[1]. Generally PSs act as organizing centers since they are anchoring spiral waves in the space around them, where their perturbation is the dominant influence. This may sound contrary to the common sense understanding that phase singularities chaotically create disorder and are often referred to as the driving factors for VF. PSs are organizing centers, but only in an area with limited radius, where the spiral wave is formed. In that area, perturbation of PSs is so dominant that any other perturbation that may originate from other PSs or from the cardiac control system is not strong enough to destabilize these orbits. The cardiac control system's inability to destabilize spiral waves explains why VF is a deadly cardiac arrhythmia. Spiral waves are highly self-organized dynamics and for their termination, a strong external perturbation shock must be delivered to the heart. A characteristic feature of spiral waves in excitable media is their strong stability against perturbations, for topological reasons[2]. If a low-energy shock is used, then a single shock cannot terminate the spiral waves – one of the reasons the LEAP technique uses multiple low-energy shocks, which eventually capture the entire heart.

As the influence of the PS falls with distance, there is an area in which the arm of the associated spiral wave ends. The reason for this is that in the area or "border zone" between the spiral wave and the rest of the cardiac tissue, phase space orbits of the associated oscillators are constantly perturbed from many different sources without any source being dominant. These sources can include multiple nearby PSs as well as perturbation from some nearby orbits that are still driven by the cardiac control system, and that also can be perturbed to a certain extent from some other PSs. Altogether, perturbations in the border zone from multiple sources and their complex mutual dependence create a situation in which the perturbation appears to be random. This in effect will mean that orbits of the cardiac cells in this area will exhibit what resemble chaotic behavior, or in other words, these orbits will be highly unstable and unpredictable. It is important to note that the dynamics of any area are mutually influential. The border zone, with its chaotic behavior area, also interacts with the nearby PS and may be able to destabilize it

along with its associated spiral waves in such a way that the spiral waves can break into multiple spiral waves confined to a smaller area. The reasoning above may explain why in the development of VF, spiral waves break into multiple ones with a smaller radius, due to the interaction with the chaos in the border zone and the PS. More and more PSs will have associated spiral waves of smaller radius that are more stable than spiral waves of greater radius, and therefore the number of PSs will reach a balance with the chaos in the border zones. Another limiting factor is interaction between PSs, since through these interactions PSs can terminate each other.

Now, since the intrinsic control system is not able to terminate the spiral waves with its small perturbation, the questions are how can small perturbations affect the chaotic dynamic in the boundary zone, and how will synchronized activity in the border zone affect the spiral wave? In order to answer these questions, it is necessary to understand the stability of the spiral waves. Ideally, in a homogenous media without boundaries, the spiral wave is stable so that its core (vortex) remains fixed. In every real excitable media, this is often not the case and the spiral wave can drift in time in response to the perturbations. Drifts types can be:

- resonant drift, occurring in response to time-dependent perturbation with a period close to the period of the spiral wave,
- inhomogeneity induced drift, which occurs when properties of the system vary in space,
- anisotropy induced drift, which occurs when properties of the system differ in different directions,
- boundary induced drift, observed in bounded media when the core of the spiral wave is close to the boundary, and
- drift due to interaction of spiral waves with each other when their own periods are approximately equal and cores are near to each other
- intrinsic drift, which occurs due to internal instabilities.

Resonant drift is of particular interest as the reentrant cardiac arrhythmia is related to the presence of the spiral waves, and it is natural to use resonant drift to drive vortices out of the cardiac tissue. The phenomenon of resonant drift of the spiral wave vortices was described by Davydov *et al.*[4] and Agladze *et al.*[5] and consists of directed motion of the spiral wave vortex when the spiral wave is perturbed by a spatially uniform and periodic external perturbation of the appropriate frequency. In a numerical study, Biktashev *et al.*[6] studied a feedback control method to induce resonant drift of the spiral waves. Their feedback mechanism consisted of a recording site within a spiral wave area that acts as a trigger each time the wavefront of the spiral wave arrives at the recording site. On each trigger signal, a perturbation is delivered to the whole excitable media globally at varying time delays. Their theoretical study was performed in a 2D excitable media and demonstrates that the threshold for termination of the spiral waves is an order of magnitude lower than the threshold in the case of a single defibrillation shock. This theoretical study is significant in the manner by which perturbation affects the spiral waves.

One other mechanism of spiral wave suppression is based on the observations that the spiral waves associated with VF are often anchored or pinned to anatomical obstacles in the heart. Such spiral waves can be very stable and it would be difficult to induce resonant drift as described above. When an electrical field is applied to tissue with an inexcitable obstacle, a virtual electrode is formed where a region neighboring one side of the obstacle is depolarized, while the other is hyperpolarized. Depending on the orientation of the virtual electrode with respect to the wavefront of the spiral wave, a new wave can be generated at the obstacle and thus inside the reentrant circuit, resulting in unpinning of the spiral wave[7]. In a similar study Ripplinger *et al*[8]. suggested that by inducing virtual electrodes a 20-fold reduction in energy could be achieved compared with conventional high-energy defibrillation, and that the unpinning methods by inducing virtual electrodes may be more effective than antitachycardia pacing.

It is important to note that the chaotic system is highly sensitive to the initial conditions, that is, it exhibits the butterfly effect, so it is certain that the chaotic dynamic of the border zone can be affected only by using perturbations that are so small that they cannot affect the dynamic

of the spiral wave, yet are strong enough to overshadow the perturbation in the border zone from the nearby PS. Ideally, precisely timed perturbation shocks are delivered so that the dynamic in the border zone is altered within a certain time interval. In the phase space of each cell this will mean that their periodic unstable and chaotic orbits will be "corrected" at their certain phase, and through multiple corrections orbits will be stabilized. As time evolves, through the interaction of mutual orbits, activity in the border zone will be synchronized and organized forcefully by means of external control that delivers a train of small perturbation shocks. It is to emphasize that external control is applied via continuous feedback, which is virtually zero most of the time and only at certain moment perturbation shocks will be delivered. Therefore external control is continuous although it looks as a train of small perturbation shocks. Through mutual dependence the border zone will interact with other areas, such as the spiral wave and other chaotic border zones, but in reality this interaction is actually unidirectional. Namely, if an external perturbation can be used to drive and stabilize the border zone, the orbits in the border zone will became insensitive to any other perturbation, and then the controlled activity of the border zone will be able to significantly affect the dynamic in the adjacent uncontrolled area. The hypothesis is that these perturbations through interactions will eventually restore synchronous activity across the entire cardiac tissue. Viewed from the macroscopic perspective this means that any complex VF, in which orbit periods are random, will be converted through external small perturbations to some more organized pattern, more like monomorphic ventricular tachycardia (MVT). The hypothesis is also that once the external perturbation control is turned off, MVT will spontaneously be converted to the sinus rhythm, since it is unable to sustain itself without external control and the "amount of chaos" in any remaining area is not big enough to spread again across the entire heart.

To understand cardiac control, it is useful to step back and examine more general classes of control problems. Here it can be shown that the methods that are based on feedback control are the most efficient and effective means of cardiac control.

Aspects of Control Theory

For any dynamical system the term "control" is associated with the idea of performing actions in order to achieve a desired system behavior. While control theory is one of the central subjects in engineering and has been explored by mathematicians and engineers for over a century, the idea of chaos control was introduced only in 1990, by Ott *et al.*[9] To understand why chaos control attracted such great interest among physicists, we must examine the properties of chaotic systems and concepts of control from an engineering perspective, such as stability, controllability and observability, and flexibility of a given dynamical system. The idea is to use the same concepts and control strategies from engineering and to draw parallels with the sophisticated control strategies embedded in biological systems to devise a control system that is optimized for biological systems.

Stability can be defined with a question: What happens with the system after a long period of time? To answer this question we must first choose a set of dynamical systems with certain characteristics, and of particular interest are systems with states that are periodically changing in time. In phase space their evolution in time is represented as closed trajectories that will be further referred to as orbits. In this case the question can be reformulated: Do small changes in the initial conditions (perturbations) lead to similar behavior, so that all future orbits will be close enough to each other? If the answer is yes, then such an orbit is called stable, and stability means that trajectories do not change significantly under small (based on some criteria) perturbations. Biological systems are specific in that due to their non-linear properties, stability is not the same along their periodic orbit. At certain phases along the orbit, phase space states can be quite sensitive to small perturbations, while at other phases the states can be practically insensitive. Also, for biological systems such as the heart, it is characteristic that the emergence of statistically defined properties of a system as a whole is a result of interaction between numerous cardiac cells, and in that case stability of the system as a whole depends on these interactions. During normal sinus rhythm, synchronous activity of cardiac cells can be

represented as a periodic orbit in the multidimensional phase space that takes into account all cardiac cells. As mentioned, these orbits are highly stable, and they resist all kinds of perturbations during a lifetime so that a system (heart) operates properly inside well-defined conditions. This implies that various control strategies have been embedded in the heart, and since the heart has the ability to monitor its own output and regulate itself in order to perform properly, intrinsic cardiac control must be implemented in the form of feedback.

Controllability and observability of the system are related to the possibility of controlling and stabilizing the system. Controllability denotes the ability to move the system in its phase space using allowable manipulations in order to achieve stabilization or optimal control. Observability is related to the possibility of observing the state of a system. Observation is often done with certain measurement techniques, and if the state is not observable, then a control system will not be able to determine its behavior. Altogether, this means that it is desirable to have a system such that all of its states are both controllable and observable, including undesirable states of a system.

Flexibility is a distinct and almost unique property of biological control systems in comparison to manmade control systems. This property, as will be explained, is of crucial importance. The whole strategy of control is to determine first the current state of the system, and if that state differs from the desired state, then to apply control in order to move the system in its phase space toward the desired point. In a manmade system this movement is often along a straight trajectory that connects the current state and the desired state, and it is often necessary for the movement to happen in a time interval as short as possible. In biological systems, flexibility allows that it is not necessary to drive the system to the desired state immediately or directly. Nature has its own reasons why trajectories are not direct. Direct driving often requires many times more energy than if the system is first allowed to fluctuate, and then the change of its dynamics is performed with small perturbations over a certain period of time. Through multiple small perturbations each sequential periodic orbit will more and more closely approximate the desired state or orbit. In this way the desired state is achieved through an

asymptotical approach trajectory constructed as a drift of multiple orbit revolutions. This is the choice of Nature, since in biological systems control strategies are optimized on efficacy and efficiency. An example is a strong external electrical defibrillation shock during VF where released energies can be hundreds of times greater than the energy needed by the heart to make a single beat (~ 1 J for a human heart). These strong shocks are driving the heart directly from its current state in VF to the desired state, which explains why it is necessary to release a large amount of energy. This raises a question: Can control be achieved based on the properties of the biological system primarily, such as flexibility, so that the desired state is approached asymptotically with multiple perturbations rather than directly?

As mentioned before, the natural cardiac control system is not able to terminate VF. From the aspect of control theory this means that the cardiac control system does not have any more ultimate observability and controllability in VF since it is not designed to operate under such conditions. In other words, the substrate (heart) becomes different and that ultimately limits the ability of the cardiac control system to operate effectively in a "new" system. Substrate differences are mainly from physiological abnormalities in the heart such as regional ischemia, cardiac damage, inherited heart defects, scars from cardiac surgery, fibrosis with aging, etc. Altogether this means that the same concepts regarding flexibility, controllability and observability remain, and that the same strategies as those of Nature can be used even in VF, although the control must be external.

Putting everything together, we hypothesize that control can be achieved through small energy perturbations in the border zone that exhibits chaotic behavior. Due to flexibility, control can be achieved through multiple small perturbations delivered within a certain time interval with precise timing. Since these shocks are not driving the system to the desired state/orbit directly, calling them "perturbation shocks" will distinguish them from the commercial single shock defibrillators that will be referred to as "defibrillation shocks."

Definition of a Chaotic System and Meaning of Chaotic Orbits

In common usage, chaos means "a state of disorder." However, in chaos theory, the term is defined more precisely. For a dynamical system to be chaotic, it must have the following properties: it must be sensitive to initial conditions, it must be topological mixing, and its periodic orbits must be dense.

Sensitivity to initial conditions means that each two states in a chaotic system that are arbitrarily close will evolve in time with significantly different trajectories. In other words, this means that if we start with only a finite amount of information about the system, then beyond a certain time the system will no longer be predicable. It is notable that this happens even in the deterministic dynamical systems, thus their deterministic nature does not make them predictable[10]. Sensitivity to initial conditions is characterized by the Lyapunov exponent. Quantitatively, two trajectories in the phase space with initial separation δZ_0 diverge as:

$$|\delta Z(t)| \approx e^{\lambda t}|\delta Z_0| \,, \qquad (1)$$

where λ is the Lyapunov exponent. A positive Lyapunov exponent is usually taken as an indication that the system is chaotic.

Topological mixing means that evolution of the system over time is such that any given open region of its phase space will eventually overlap with any other region of its phase space. Since the phase space is of finite size, this usually means that the phase space will become thoroughly mixed together after a fairly short time. Here, "mixing" is really meant to correspond to the standard intuition: the mixing of colored dyes or fluids is an example of a chaotic system. Topological mixing is a necessary condition for determination of a chaotic dynamic, as sensitivity on initial conditions is not sufficient.

Density of periodic orbits means that every point in the phase space is approached arbitrarily closely by periodic orbits, and it is one of the fundamental properties of a chaotic

system. This is contrary to the common sense notion that a chaotic system does not have periodic orbits at all, but periodicity in chaos theory has a slightly different meaning, as in a dynamic system an orbit isn't what we typically think. Here an orbit is just sets of points, paths through the phase space. Orbits may never repeat, but we still call them orbits. For example, we can describe the path in phase space of a leaf falling down to the ground as an orbit. This orbit obviously cannot repeat, and naturally an orbit that repeats is called a periodic orbit. For every dynamic system, we can divide its phase space into a collection of subspaces made distinct by the property that if at any point in time the state of the system is in one partition, it will never enter a state in some other partition. These partitions are called orbits. An example can be made with planetary orbits. Planets don't really travel around the sun in smooth elliptical paths – they wobble. They're pulled by their own moons, and by other bodies also orbiting the sun. In a complex gravitational system like the solar system, the orbits are complex paths. They might never repeat, but they're still orbits. The solar system never passes through exactly the same state twice. There's no point in time at which everything will be exactly the same. But the solar system and most chaotic systems are nearly periodic, or in other words the exact same state will never occur twice, but it will come arbitrarily close. A dynamical system with dense orbits is one that has a lot of different orbits which are all closely tangled up. Making even the tiniest change in the state of the system will shift the system into an entirely different orbit, one which may be dramatically different. In a typical pendulum, a small nudge will change its swing, increasing or decreasing the amplitude of its swing. If the pendulum is ideal, a small nudge will permanently change its orbit. Even the tiniest perturbation will create a permanent change. Concerning chaos, we can think of the orbits in terms of an attractor. In many cases chaotic behavior is found only in a subset of phase space, and most interesting cases arise when the chaotic behavior takes place if this subset is invariant to dynamic evolution. This subset is called a basin of attraction or simply an attractor. Figuratively, an attractor is a black hole in the phase space of a system, which is surrounded by a basin. Within the basin, the time evolution of a dynamic system is trapped in periodic orbits, circling around the attractor forever, unable to escape. These orbits

can be nearly periodic most of the time, but even the tiniest change can change the dynamic into an entirely different orbit, as orbits are densely tangled up around the attractor.

Concepts behind Chaos Control

The concepts behind chaos control are based on the dynamical characteristics presented above. Sensitive dependence on the initial conditions of a chaotic system implies that chaotic trajectories are also extremely sensitive to the effect of perturbation. As orbits are dense, this implies that there is an infinite variety of behaviors embedded in a chaotic dynamic as an infinite number of periodic orbits. Orbits are unstable, and a small perturbation will grow exponentially in time, resulting in a completely different orbit; therefore, any future orbits are possible with small perturbations. The idea is that small perturbations can be used to stabilize chaotic behavior in periodic orbits and to direct trajectories to a desired state[11]. This reasoning about chaos control is exploited in the Ott, Grebogi and Yorke (OGY) methods of chaos control[9].

The OGY method was one of the pioneering works related to chaos control that spawned hundreds of publications in the last two decades. The main idea behind the OGY method is the observation that a chaotic system has an infinite number of unstable period orbits as a chaos invariant set. Based on the ergodic theorem, any chaotic trajectory must pass close to the desired periodic behavior and then at that moment a small perturbation can be applied. This small perturbation is enough to stabilize the system in the desired periodic behavior. The OGY method has been experimentally demonstrated, including studies of cardiac control. In such experiments Garfinkell *et al.*[12] analyzed developing chaos in real time and then subsequently applied small control perturbations. Their strategy has been used to stabilize cardiac arrhythmias induced by the drug *ouabain* in the rabbit ventricle. By administering electrical stimuli to the heart at irregular times determined by chaos theory, the arrhythmia was converted to periodic beating. One of the key limitations of this method is that the dynamic of the system must be known a priori, and success depends on delivery of precise timing stimuli.

Delayed Feedback Control Algorithm

Introduction

Time-delayed feedback control is a well-known practical method for stabilizing unstable periodic orbits embedded in the chaotic attractors. The method is based on applying a feedback perturbation proportional to the deviation of the current state of the system from its state one period in the past, so that the control signal vanishes when the stabilization of the targeted orbit is achieved[13].

The delayed feedback control method[14] was introduced in 1992 and is one of the most active research fields in non-linear dynamics. The significance of this method is that DFC is reference-free, meaning that it allows us to treat the controlled system as a black box; no exact knowledge of the system's evolution equations is needed. Also, this method allows a noninvasive stabilization of unstable periodic orbits (UPOs) of a dynamical system, through the system's accessible parameters, in the sense that the control signal vanishes when the targeted orbit is reached. Once stabilization is achieved, the feedback signal is still present but its perturbation "strength" goes to zero, and that is why the DFC algorithm can be referred to as a continuous feedback control.

Analytical Treatment of the Delayed Feedback Control Algorithm

Consider a dynamic system which can be described by ordinary differential equations

$$\dot{\boldsymbol{x}}(t) = F(\boldsymbol{x}, p, t), \qquad (2)$$

where $\boldsymbol{x}$ defines the system variables and p is a scalar parameter available for external adjustment. We don't necessarily know these equations, but some scalar variable

$$y(t) = g(\boldsymbol{x}(\boldsymbol{t})) \qquad (3)$$

can be measured as the system output. Now, let's suppose that at $p = p_0 = 0$ the system has a UPO $\boldsymbol{x}_{UPO}$ that satisfies equation (2) and that $\boldsymbol{x}_{UPO}(t + T) = \boldsymbol{x}_{UPO}(t)$, where T is the period of

the UPO. It has been demonstrated using a standard method of embedded delay that a large number of distinct UPOs on a chaotic attractor can be identified from one scalar variable[15]. Applying this method to our system, we can determine from an experimentally measured signal $y(t)$ various periodic signals corresponding to different UPOs, including the one with the period T. Now we can introduce the perturbation $p(t)$ in the form of:

$$p(t) = K[y(t) - y(t - T)]. \qquad (4)$$

If the stabilization is successful, the feedback perturbation $p(t)$vanishes. Another convenience of the DFC algorithm is that DFC uses output $y(t - T)$ as the reference signal and the necessity of the UPO reconstruction is avoided. In other words, the DFC algorithm treats the dynamic system as a black box, and this is its main advantage. The block diagram of the method is presented in Figure 3.1.

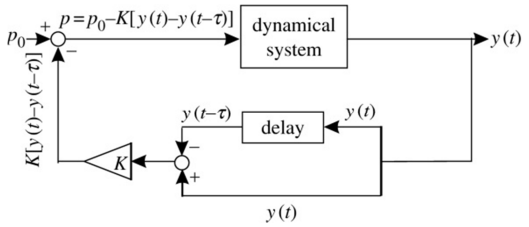

Figure 3.1. Block diagram of the delayed feedback control method. *y(t)* is an output variable; *p*, a control parameter; p_0, its value at which the dynamical system has an unstable periodic orbit with a period τ; and *K*, the feedback gain.
Pyragas K Phil. Trans. R. Soc. A 2006;364:2309-2334

Applications of the DFC Algorithm

Successful implementation of the DFC algorithm was mostly utilized in theoretical models from many different fields, including electronics, mechanics, optics, and chemistry, and particularly in cardiac systems. Hall *et al.*[16] showed that the DFC control method was able to suppress a cardiac arrhythmia that is the alternans rhythm in a piece of a dissected rabbit heart. Their control algorithm was adapted to drifting system parameters during alternans. However, they did not explore the DFC method on the whole heart and neither was it their goal to control VF. Bleich *et al.*[17] utilized the DFC method in a simple numerical experiment on Fitzhugh-Nagumo

equations, demonstrating that the DFC methods can stabilize irregular behavior in a paced excitable oscillator. The method is robust against slow variations in the pacing rate and requires no information about the desired orbit other than period, which is determined directly by the observation of the pacing signal. Rappel *et al.*[18] used the DFC method for stabilization of the spiral waves in the Beeler-Reuter model of cardiac tissue in order to prevent spiral wave breakup. Control is based on applying a feedback current at a discrete set of control points during the repolarizing phase of the action potential. None of these studies was implemented during VF, and, moreover, they were theoretical studies using a relatively simplistic 2D model of excitable media.

Beside control of cardiac dynamics, the DFC algorithm has also been implemented in economic models[19,20] and chaotic satellite altitude control[21], and Roseblum and Pikovsky have considered the possibility of its use in suppression of pathological brain rhythms[22,23].

The DFC method is popular in experimental investigations, but its theory has not been developed extensively. Systems with a time delay are often hard to handle if dynamics take place in infinite-dimensional phase spaces, as in the case of the heart that is additionally spatially extended system. The linear and non-linear investigation of such systems is usually performed numerically rather than analytically, and mechanisms of stabilization are hard to understand. Most investigations into the theory of the DFC are devoted to the stabilization of the unstable periodic orbits embedded in the chaotic attractors of low-dimensional systems, usually up to three-dimensional systems.

Proportional-Integral-Derivative Control Algorithm

Introduction

The Proportional-Integral-Derivative (PID) controller is the most common form of feedback controller. It was an essential element of early governors and became the standard tool when control processes emerged in the middle of the 20th century. In the absence of any

knowledge of the underlying process, a PID controller has been historically considered as the best controller. PID controllers are often standalone systems and are often combined with logic, and they are mostly utilized in transportation and manufacturing. Over the decades realization of the PID controller followed development of technology, from mechanics, electronics tubes, and microprocessors, on which almost all PID controllers are based nowadays. The PID controller is a generic loop feedback mechanism that calculates an "error" value as the difference between a measured process variable and a desired set point. The controller attempts to minimize the error by adjusting the process control inputs.

Algorithm of the PID Controller

The PID algorithm in textbooks is described as

$$u(t) = K\left(e(t) + \frac{1}{T_i}\int_0^t e(\tau)d\tau + T_d\frac{de(t)}{dt}\right) \quad (5)$$

$$e(t) = r - y\ , \quad (6)$$

where y is the measured process variable, r is the reference variable, e is the control error, and u is the control signal. The controller parameters are proportional gain K, integral time T_i, and derivative time T_d. The algorithm itself involves three separate terms: the proportional, the integral, and the derivative, denoted as P, I, D. These terms can be interpreted in the time domain as: P depends on the present error, I on the accumulation of the past errors, and D is a prediction of the future errors. The control signal is the weighted sum of these three terms. A block diagram of a PID controller is presented in Figure 3.2.

In practical realizations of a PID controller, it is not necessary for all three terms to be present. Often the proportional term is sufficient, and such a controller is called a P controller. PI controllers are fairly common since derivative action is sensitive to the measurement noise, whereas absence of an integral term may prevent the system from reaching its target value due to the control action. Namely, with only proportional control, there is always a steady state error in the proportional control. The error will decrease with gain increase, but that may induce oscillations, as the controller will constantly overshoot and undershoot the targeted state. With

the integral term, a steady state error disappears, but a transfer function of a feedback controller becomes of a second order without dissipative term. With low values of T_i, the tendency for

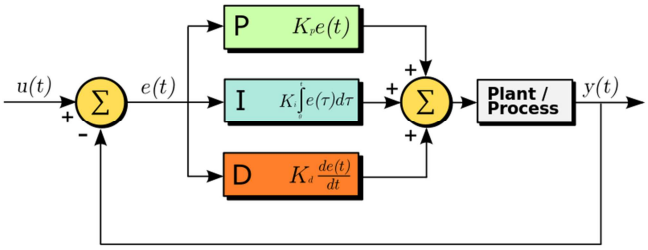

Figure 3.2. A block diagram of a PID controller.
http://en.wikipedia.org/wiki/File:PID_en.svg

oscillation increases as the strength of integral action decreases. For this reason a derivative term acts as a damper, increasing with the larger derivative time T_d.

The PID control algorithm has been used in numerous applications as stated above, but as far as we know it has not been used in cardiac control.

Control of Spatiotemporal Chaos and Spiral Turbulence in Cardiac Electrical Activity

The heart is a complex non-linear system that sustains life through pumping blood in the circulatory system. This is achieved via propagation of electrical waves through the heart that sequentially stimulate the cells of the heart. Disruption of this electrical pattern leads to cardiac arrhythmias and possibly VF. As each cardiac cell can be simplified as a two-state system, comprising a stable resting state and a metastable excited state, the heart as a whole belongs to the special class of systems referred to as excitable media. The heart is made of a large number of cells, resulting in a high-dimensional dynamic system that can display chaotic behavior. Excitable media have a distinct property of interacting waves, which mutually annihilate on colliding, and this is due to the fact that the excitation wavefront is followed by a region where all cells are in the refractory or recovery period, and cannot be stimulated by another excitation

wavefront. Some more complex interactions of excitation wavefronts are the genesis for spatiotemporal chaos resulting in spatial patterns that are commonly referred to as reentrant excitations in 1D, spiral waves in 2D and scroll waves in 3D. These waves are formed when the excitation wavefront is broken as the wave propagates across partially recovered tissue or encounters an inexcitable obstacle. The free ends of the wavefront gradually curl around an obstacle to form spiral waves. Once spiral waves are formed, they became self-sustained sources of high-frequency excitation, and the cardiac control system is usually not able to terminate them. If the spiral wave is unstable it may break up, resulting in the creation of multiple smaller spiral waves. Mechanisms for breakup can be multiple, and the most common are when the spiral wave collides with itself and breaks up spontaneously[24]. A wavefront can have a free end only at an inexcitable boundary or at a phase singularity. Hence the breaking up of a wavefront creates two free ends and a pair of opposite chirality (phase singularities)

Based on the reasoning above, cardiac control can be viewed as controlling spatiotemporal chaos in excitable media where the response to a control signal is not proportional to the signal strength because of the existence of a threshold. Regions that have not recovered from a previous excitation or where the control signal is below the threshold will not be affected by the control algorithm. In excitable media, control of chaos has a different focus, which is elimination of all activity rather than stabilization of unstable periodic behavior. The DFC and PID algorithms presented here aim to stabilize unstable periodic behavior, and that may present a problem, as the occurring VF is a fatal cardiac arrhythmia. Therefore, the goal is to terminate, not control it.

At present, the only practical means to treat VF involves very strong electrical shocks across the heart, either externally or internally. The principle of operation of the devices that deliver these shocks is to overwhelm the natural cardiac dynamic, to drive all regions of the heart to the resting state simultaneously; however, these methods may cause damage to portions of the cardiac tissue which subsequently results in scars that will increase the probability of future arrhythmias. Therefore, devising a low-power control method for spatiotemporal chaos in

excitable media is of crucial importance. Low-power atrial defibrillation might allow defibrillation of conscious patients.

All control methods that have been proposed for terminating spatiotemporal chaos in excitable media to date can be classified into three types: global control, if every region of the media is subjected to the signal; local control, if the control signal is applied only to a small localized region; and nonlocal multisite local control, if perturbations are applied simultaneously to a number of a spatially distant regions.

Global Control

The first attempt to control chaotic behavior in excitable media was to stabilize cardiac arrhythmia in a piece of tissue from a rabbit heart[12], as mentioned above, using a proportional perturbation feedback control (PPF). This method for cardiac control is derived from the originally proposed chaos control[9] where the desired unstable periodic orbit was stabilized using small perturbations. In later studies the PPF method was used to control atrial fibrillation in a human heart[25]**.** However, the effectiveness of PPF control methods has been questioned, especially in experimental attempts in feedback control to terminate fibrillation by applying a control stimulus at a single spatial location[26].

In theoretical studies of excitable media, global control was more successful in the numerical simulations where control stimuli are applied throughout the system. In those theoretical models the dynamic is typically described by a so-called fast variable and a slow variable. For cardiac cells, the fast variable is often associated with the transmembrane potential, while the slow variable represents an effective membrane conductance that replaces the complexity of different ion channels. Of the several models that support wave break of the spiral waves, the Panfilov[27] model was mostly used in theoretical studies of cardiac control. Osipov *et al.*[28] have shown that weak impulses can be used to change values of the slow variable at the front and back of the traveling wave, which leads to different wave-front and wave-back conduction velocities. This effect can destabilize the traveling wave, resulting in a transition to

the resting state. Their approach is based on the point that the traveling waves in excitable media can be separated into fast and slow motions. Gray[29] has studied the termination of a spiral wave breakup using short and long duration pulses that are applied to the fast variable. This study concluded that short pulses affected only the fast variable, while the long-duration pulses affected fast and slow variables and were more efficient in terms of the energy in termination of spatiotemporal chaos. Control signals added to the fast variable can also be periodic[30] as a sinusoidal function, in which case the critical amplitude of the control signal has been found to be a function of the signal frequency.

Conventional defibrillation can also be viewed as a global control, where a large amplitude control signal is used to synchronize that phase of activity at all points. This can be achieved by either exciting a previously unexcited region or slowing the recovery of already excited regions. From the phase space perspective, excitation of the previously unexcited region can be viewed as advancing the phase, while slowing recovery of the already excited region can be viewed as delaying the phase[31].

Some other global control schemes have proposed applying sinusoidal perturbations to the parameter controlling the excitation threshold, as suggested by Alonso *et al.*[32] The aim of their study was controlling scroll wave turbulence in 3D excitable media. Successful control depends on the relation between the control frequency and the spiral wave rotation frequency. If the control frequency is higher than the spiral wave frequency, turbulence suppression is achieved. The explanation of the undelaying mechanism is that control changes the tension in between filaments (the line joining phase singularities around which the scroll wave rotates) to become positive. This result in expansion of the scroll wave filaments, rather than their shrinking and collapsing, and ultimately leads to elimination of spatiotemporal chaotic activity. In a later study Alonso *et al.*[33] used perturbation by Gaussian noise, which also resulted in suppression of scroll wave turbulence.

Nonglobal Multisite Local Control

These control methods apply control signals only at certain points across the heart, and two control methods are used currently: control over a mesh and control over an 1D array of points.

The essential idea of the control scheme over a mesh is that the domain can be divided into electrically disconnected regions by creating boundaries consisting of recovering cells between these regions. These boundaries are created by external control by triggering excitation from a network of lines. In the case of 2D excitable media, the domain is divided into blocks that have to be small enough that the spiral wave cannot form inside the block. This network effectively stimulates nonconducting boundary conditions and absorbs spiral waves formed inside some particular blocks. This control method is studied by Sinha *et al.*[34] and has been applied to multiple excitable media models, including Panfilov and Luo-Rudy models. The idea behind this model comes from the well-known fact that small mammals do not get VF spontaneously[35] and was verified in swine ventricular tissue, where its mass was decreased gradually[36].

In control over an array of points, the points are arranged in a regular array. Such methods are proposed by Rappel *et al.*[18] for applying a DFC control scheme. However, this scheme does not control spatiotemporal chaos, as its aim is prevention of instabilities leading to the spiral wave breakup. In the method proposed by Sinha *et al.*[37], the authors have used an array of control points to terminate spatiotemporal chaos in the Panfilov model. The control points are placed at the distance d apart along a regular array and are not activated simultaneously, but the control point at one corner of the system is stimulated first, followed by the successive stimulation of the neighboring control points. This process is repeated after several particularly chosen intervals. Each time a stimulating traveling wave is created, and it has been shown that a simulating traveling wave is much more effective in control of spatiotemporal chaos than the simultaneous activation of all control points. The traveling wave allows the control

signal to engage all high-frequency sources of excitation in the spiral turbulence regime, ultimately resulting in a complete elimination of chaos.

Local Control of Spatiotemporal Chaos

In the local control of spatiotemporal chaos, control is applied only to a small localized region in the spatially extended system. All contemporary local control methods use overdrive pacing, generating a series of waves with a frequency higher than any of the existing excitations in the spiral turbulent state. In the area that is controlled, control signals dominate, establishing waves that over time will extend into the surrounding area. Therefore, through local control synchronicity is expanded gradually until the dynamic is synchronized across the entire heart. The time to achieve global control depends on the frequency difference between the control stimulation and dominant frequency in the chaotic activity. Control will be achieved faster if the difference is greater (control signal frequency smaller than dominant frequency in chaotic rhythm).

Stamp *et al.*[38] used low-amplitude, high frequency pacing using a series of pulses to terminate spiral turbulence in spatiotemporal chaos, but with only limited success. Some other methods with a periodic stimulation protocol proved to be successful in chaos control when applied to the Panfilov model. The idea behind these methods is a periodic alternation between positive and negative stimulation that shortens the recovery period around the region of control stimulation, and thus allows the generation of very high-frequency waves that would not be possible using positive stimulation alone. This idea has been studied more generally using biphasic pacing[39] where periodic waves emerging from the stimulation region gradually impose control over the regions exhibiting chaos.

In the local control scheme proposed by Zhang *et al.*[40] the excitation threshold in the model is perturbed in the same way as proposed by Alonso *et al.*[32], but this local control scheme is an analog of the original proposed global control scheme[32]. As in other methods we have discussed, local stimulation creates high-frequency waves that through propagation into AN

excitable medium will suppress the spiral waves. This control scheme perturbs the excitation threshold to the point that regions in the resting state can be spontaneously excited, resulting in generation of very high-frequency waves.

Conclusions

The majority of control methods in cardiac dynamics, and excitable media in general, involve applying perturbations either globally or over spatially extended control points. In most practical situations, it is not feasible to implement multisite control methods. Local control has the advantage of being easily and readily implemented. However, the problem with most contemporary local control methods is that they use very high-frequency waves to overdrive chaos. These waves are unstable and may break up during propagation, resulting in reinitiating the spiral waves even after the original chaotic activity has been terminated. In cardiac tissue, the problem is exacerbated by the existence of inhomogeneities that make the proposed local control methods more vulnerable. It is known that high-frequency pacing interacts with nonconducting obstacles, resulting in wave breaks and subsequent genesis of spatiotemporal chaos[41].

Based on the discussion above, the goal is to search for local control methods for terminating spatiotemporal chaos that can be implemented using low power and that are capable of terminating chaotic dynamics. The impact of such control methods will be enormous, in that they will be both efficient and effective in cardiac defibrillation.

Non-linear control methods for cardiac dynamics clearly show potential, but successful application of such approaches in termination of VF in the human heart is still lacking. Implantable cardioverter defibrillators (ICD) attempt to terminate an arrhythmia once it is initiated. Once an arrhythmia is detected, the ICD will deliver antiarrhythmic pacing, and if that fails, the ICD will revert to its high-energy defibrillation mode. A preferable strategy would be to have a device that prevents arrhythmias from occurring in the first place. That can be achieved

by recognizing and stopping precursor events. During VF there may be many different spiral waves present in the ventricles, and control methods based on the local stimuli would likely require recording from multiple sites. However, given a control method that is able to recognize the onset of VF, local control would still be efficient in rapid termination of VF.

Based on the reasoning in this chapter, in our experimental cardiac control studies we used two control methods, DFC and PID, as a local control of spatiotemporal chaos via continuous feedback control. In order to test these methods experimentally, we needed to develop some challenging instrumentation that is presented in the following chapters. This instrumentation included a high-current transconductance amplifier and a feedback controller that drives the transconductance amplifier and monitors electrical activity on the surface of the heart.

References

1. Luther, S. *et al.* Low-energy control of electrical turbulence in the heart. *Nature* **475**, 235–9 (2011).

2. DAVYDOV, V., ZYKOV, V. & MIKHAILOV, A. Kinematics of Autowave Patterns in Excitable Media. *USPEKHI FIZICHESKIKH NAUK* **161**, 45–86 (1991).

3. Ideker, R. E. & Rogers, J. M. Human ventricular fibrillation: wandering wavelets, mother rotors, or both? *Circulation* **114**, 530–2 (2006).

4. DAVYDOV, V., ZYKOV, V., MIKHAJLOV, A. & BRAZHNIK, P. Drift and Resonance of Spiral Waves in Active Media. *USPEKHI FIZICHESKIKH NAUK* **161**, 45–86 (1991).

5. AGLADZE, K., DAVYDOV, V. & MIKHAILOV, A. Observation of a Helical-wave Resonance in an Excitable Distributed Medium. *JETP LETTERS* **45**, 767–770 (1987).

6. Biktashev, V. N. & Holden, A. V Design principles of a low voltage cardiac defibrillator based on the effect of feedback resonant drift. *Journal of theoretical biology* **169**, 101–12 (1994).

7. Takagi, S. *et al.* Unpinning and Removal of a Rotating Wave in Cardiac Muscle. *Physical Review Letters* **93**, 058101 (2004).

8. Ripplinger, C. M., Krinsky, V. I., Nikolski, V. P. & Efimov, I. R. Mechanisms of unpinning and termination of ventricular tachycardia. *American journal of physiology. Heart and circulatory physiology* **291**, H184–92 (2006).

9. Ott, E., Grebogi, C. & Yorke, J. Controlling chaos. *Physical Review Letters* **64**, 1196–1199 (1990).

10. Werndl, C. What Are the New Implications of Chaos for Unpredictability? *The British Journal for the Philosophy of Science* **60**, 195–220 (2009).

11. Shinbrot, T. *et al.* Using the sensitive dependence of chaos (the "'butterfly effect'") to direct trajectories in an experimental chaotic system. *Physical Review Letters* **68**, 2863–2866 (1992).

12. Garfinkel, A., Spano, M., Ditto, W. & Weiss, J. Controlling cardiac chaos. *Science* **257**, 1230–1235 (1992).

13. Pyragas, K. Delayed feedback control of chaos. *Philosophical transactions. Series A, Mathematical, physical, and engineering sciences* **364**, 2309–34 (2006).

14. Pyragas, K. Continuous control of chaos by self-controlling feedback. *Physics Letters A* **170**, 421–428 (1992).

15. Lathrop, D. & Kostelich, E. Characterization of an experimental strange attractor by periodic orbits. *Physical Review A* **40**, 4028–4031 (1989).

16. Hall, K. *et al.* Dynamic Control of Cardiac Alternans. *Physical Review Letters* **78**, 4518–4521 (1997).

17. BLEICH, M. E. & SOCOLAR, J. E. S. Delayed Feedback Control of a Paced Excitable Oscillator. *International Journal of Bifurcation and Chaos* **10**, 603–609 (2000).

18. Rappel, W.-J., Fenton, F. & Karma, A. Spatiotemporal Control of Wave Instabilities in Cardiac Tissue. *Physical Review Letters* **83**, 456–459 (1999).

19. Hołyst, J. A., Żebrowska, M. & Urbanowicz, K. Observations of deterministic chaos in financial time series by recurrence plots, can one control chaotic economy? *The European Physical Journal B* **20**, 531–535 (2001).

20. Holyst, J. & Urbanowicz, K. Chaos control in economical model by time-delayed feedback method. *IZVESTIYA VYSSHIKH UCHEBNYKH ZAVEDENII RADIOFIZIKA* **31**, 574–582 (1988).

21. Tsui, A. P. M. & Jones, A. J. The control of higher dimensional chaos: comparative results for the chaotic satellite attitude control problem. *Physica D: Nonlinear Phenomena* **135**, 41–62 (2000).

22. Rosenblum, M. & Pikovsky, A. Controlling Synchronization in an Ensemble of Globally Coupled Oscillators. *Physical Review Letters* **92**, (2004).

23. Rosenblum, M. & Pikovsky, A. Delayed feedback control of collective synchrony: An approach to suppression of pathological brain rhythms. *Physical Review E* **70**, 041904 (2004).

24. Fenton, F. H., Cherry, E. M., Hastings, H. M. & Evans, S. J. Real-time computer simulations of excitable media: java as a scientific language and as a wrapper for c and fortran programs. *Biosystems* **64**, 73–96 (2002).

25. DITTO, W. L. *et al.* Control of Human Atrial Fibrillation. *International Journal of Bifurcation and Chaos* **10**, 593–601 (2000).

26. Gauthier, D. J. *et al.* Progress toward controlling in vivo fibrillating sheep atria using a nonlinear-dynamics-based closed-loop feedback method. *Chaos (Woodbury, N.Y.)* **12**, 952–961 (2002).

27. Panfilov, A. & Hogeweg, P. Spiral breakup in a modified FitzHugh-Nagumo model. *Physics Letters A* **176**, 295–299 (1993).

28. Osipov, G. & Collins, J. Using weak impulses to suppress traveling waves in excitable media. *Physical Review E* **60**, 54–57 (1999).

29. Gray, R. A. Termination of spiral wave breakup in a Fitzhugh-Nagumo model via short and long duration stimuli. *Chaos (Woodbury, N.Y.)* **12**, 941–951 (2002).

30. Sakaguchi, H. & Fujimoto, T. Elimination of spiral chaos by periodic force for the Aliev-Panfilov model. *Physical Review E* **67**, 067202 (2003).

31. Gray, R. A. & Chattipakorn, N. Termination of spiral waves during cardiac fibrillation via shock-induced phase resetting. *Proceedings of the National Academy of Sciences of the United States of America* **102**, 4672–7 (2005).

32. Alonso, S., Sagués, F. & Mikhailov, A. S. Taming Winfree turbulence of scroll waves in excitable media. *Science (New York, N.Y.)* **299**, 1722–5 (2003).

33. Alonso, S., Sancho, J. & Sagués, F. Suppression of scroll wave turbulence by noise. *Physical Review E* **70**, 067201 (2004).

34. Sinha, S., Pande, A. & Pandit, R. Defibrillation via the Elimination of Spiral Turbulence in a Model for Ventricular Fibrillation. *Physical Review Letters* **86**, 3678–3681 (2001).

35. Winfree, A. T. *When Time Breaks Down: The Three-Dimensional Dynamics of Electrochemical Waves and Cardiac Arrhythmias*. 340 (Princeton Univ Pr: Princeton, 1987).

36. Kim, Y. H. *et al.* Spatiotemporal complexity of ventricular fibrillation revealed by tissue mass reduction in isolated swine right ventricle. Further evidence for the quasiperiodic route to chaos hypothesis. *The Journal of clinical investigation* **100**, 2486–500 (1997).

37. Sridhar, S. & Sinha, S. Controlling spatiotemporal chaos in excitable media using an array of control points. *EPL (Europhysics Letters)* **81**, 50002 (2008).

38. Stamp, A. T., Osipov, G. V. & Collins, J. J. Suppressing arrhythmias in cardiac models using overdrive pacing and calcium channel blockers. *Chaos (Woodbury, N.Y.)* **12**, 931–940 (2002).

39. Zhang, H., Hu, B. & Hu, G. Suppression of spiral waves and spatiotemporal chaos by generating target waves in excitable media. *Physical Review E* **68**, 026134 (2003).

40. Zhang, H., Cao, Z., Wu, N.-J., Ying, H.-P. & Hu, G. Suppress Winfree Turbulence by Local Forcing Excitable Systems. *Physical Review Letters* **94**, 188301 (2005).

41. Panfilov, A. V & Keener, J. P. Effects of high frequency stimulation on cardiac tissue with an inexcitable obstacle. *Journal of theoretical biology* **163**, 439–48 (1993).

CHAPTER IV

HIGH POWER BIPOLAR CURRENT SOURCE WITH FLOATING AND REAL-TIME ARBITRARY WAVEFORM OUTPUT IN EXCESS OF A 1 KHZ BANDWIDTH[1]

Summary

We have developed a custom-made , arbitrary waveform voltage to current converter (V2CC) with an output that is isolated from the Earth ground, capable of delivering up to 1 A continuously and up to 5 A into a 40 Ω load for >500 ms in a pulsed regime. For currents lower than 5 A, the load resistance can be higher, so that the product *Current* x *Resistance* <200 V. The voltage on the output of a V2CC is limited maximally to ±220 V, the bandwidth is in excess of 1 kHz, and the timing accuracy is better than 10 μs. A set of precautionary measures is implemented that keeps the output disconnected through reed relays and H-bridge MOSFETs. The V2CC is designed to be used in *ex vivo* cardiac experiments, but is suitable for a wide variety of settings that require an arbitrary waveform high current source. It is not designed for human use.

Introduction

Active current sources can be designed in many different ways, depending on the particular applications and requirements, and all active current sources can be divided into two groups, those with a negative feedback and those without. Current sources without negative feedback are usually simpler and are designed with discrete components to be constant and unipolar current sources or sinks, such as current mirrors. If the current source is required to be

[1] Coauthors of this chapter are Mark Holcomb, Ron Reiserer and John Wikswo

bipolar and to serve as a transconductance amplifier, then a design with operational amplifiers (op-amps) is the traditional approach. For this purpose, a simple current source can be built by placing a load in the feedback loop of an op-amp. However, op-amps are designed as voltage sources and have very limited output current capacity. A very small number of op-amps have output current capacity greater than 50 mA and can output voltages above ±40 V. Power op-amps are traditionally designed with an additional integrated output stage that acts as a current gain, but they are limited by power dissipation capabilities. Examples are the high voltage power op-amps produced by Apex™ Microtechnology (Tucson, AZ) that can have an output voltage in the range of hundreds of volts, but the safe operating area limits their current capacity at the same time so that it is usually below 100 mA.

To overcome these limits, current gain is often designed as an additional stage controlled by the op-amp. For unipolar current sources, the gate of a MOSFET is controlled by the op-amp while negative feedback is implemented by sensing a voltage across the sense resistor placed in the source of the power MOSFET. The source of the current is in a drain of a MOSFET and this type of a current source is more accurately called a current sink.

Based on this reasoning, we designed a bipolar current source that uses a low voltage (±12 V) op-amp that controls the gate-source voltage of a power MOSFET through negative feedback implemented by the sense resistor placed at the source of a power MOSFET as in Figure 4.1. The op-amp and the MOSFET together resemble a unipolar transconductance amplifier. In the drain of a MOSFET that acts as a current sink, we placed a fast switching H-bridge controlled by the microcontroller that determines the polarity across the load connected to the H-bridge. In this setup, an arbitrary bipolar voltage input waveform is first processed so that its absolute value is fed into the transconductance amplifier, and simultaneously the polarity as a digital value is fed into a microcontroller that within 10 μs is able to change the H-bridge polarity whenever the input voltage crosses zero. Current produced through the load with this setup is bipolar and proportional to the input voltage with the proportionality constant g_m of 5A/5V=1 S.

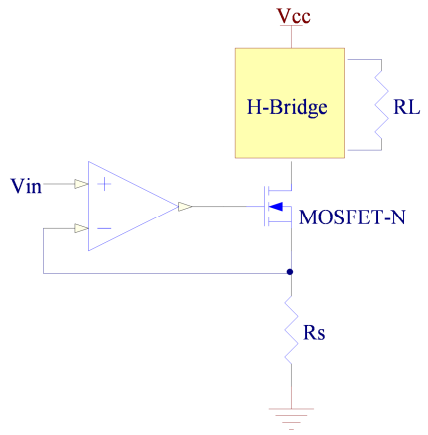

Figure 4.1. Traditional unipolar current source with an op-amp.

Specific Design Requirements and Safety Considerations

The design of the V2CC is bounded by the intended application in *ex vivo* cardiac experiments. The requirements and the technical specifications are as follows:

1) Output Current:
    a. Constant ±5 A output current for at least 500 ms at a duty cycle of 10%, rise time from 0 to 5 A of no less than 100 μs for load resistances below 40 Ω measured at the output of a V2CC.
    b. Gain is fixed at 1 S, meaning that the full output is 5 A for an input of 5 V. Lower currents will be sustained for longer intervals or longer duty cycles with continuous current for currents lower than 1 A into load resitances < 200 Ω.
    c. For currents lower than 5 A, load resistance can be higher, limited by the product Current x Resistance < 200 V in both polarities.
2) Output Voltage: Voltage range must be limited by the protection circuitry and a power supply. A range from -200 V to +200 V must be guaranteed.

3) Output Current: The V2CC should consist of a transconductance amplifier with built-in negative feedback that controls the output, such that the output current is independent of load resistance variations within the operating voltage specified above.
4) Frequency Bandwidth: The V2CC should be capable of producing arbitrary current waveforms in the frequency bandwidth from DC to 1 kHz with non-linearities and distortions less than 1%.
5) Voltage/Current Protections:
    a. In the power supply circuitry that supplies the output stage, there must be an over-current protection that limits the output current to a maximum of 5 A. If the over-current protection is activated, then the output of the V2CC will be disconnected and visual/audible signals will be generated, indicating the over-current state of the V2CC. Normal functioning can be restored after a reset button is pushed or when the defibrillator is powered off /on.
    b. For currents greater than 1 A, the V2CC can only work in a pulsed regime. Power dissipation factors across the power MOSFET dictate that only a pulsed regime is possible and time limits are imposed by the magnitude of a current. If these time limits are exceeded, protection will be activated, the output of the V2CC disconnected, and visual/audible signals generated. Also, if the voltage of a power supply to the transconductance amplifier exceeds the designed limit range, voltage protection will be activated, the output of the V2CC will be disconnected, and visual/audible signals will be generated.
6) Safety: A mechanical relay must ensure that the output terminals are always disconnected unless there is a special control signal present at the additional digital input. Due to slow response of mechanical relays (~30 ms), the output also can be disconnected through the solid state H-Bridge in ~ 10 μs unless there is a special input control signal present at the additional digital input.

7) Monitoring Circuitry: Voltages, current, and temperatures should be constantly monitored across different units in the V2CC. If these parameters are out of their predefined range, control logic will disconnect the output and render the V2CC in standby mode. LED indicators along with the LCD display and audible signals show various statuses of the V2CC as well as the error messages and the voltage and temperature values of the different modules in the V2CC.
8) Current/Voltage Measurements/Sensing at the Current Source Terminals:
    a) The current sense signal must be isolated from the V2CC output and float with respect to the Earth ground. The signal should be rescaled so that 5 V represents 200 V and -5 V represents -200 V. A standard BNC connector should be placed on the front panel.
    b) The current sense signal must be isolated from the output and floats in respect to the Earth ground. The signal is rescaled so that 5 V represents 5 A and -5 V represents -5 A. A standard BNC connector should be placed on the front panel.
9) Analog Input: The V2CC requires an analog BNC input connector for input of arbitrary waveforms (±5 V). The input must be buffered so that the input impedance is minimally 10 KΩ and it is isolated from the Earth ground and the transconductance amplifier.

V2CC Design Layout

The layout of the V2CC is depicted as a block schematic in Figure 4.2. The central component is a microcontroller that is responsible for normal and proper operation of the V2CC, by monitoring analog voltages and temperatures, reading certain digital lines, and setting certain digital lines that control various V2CC blocks. The microcontroller also controls the LCD and one of the LEDs on the front panel, which provide information about the current V2CC status. In a situation where monitored values are outside their safe operating range, the microcontroller will power off the high voltage supply, disconnect the V2CC current output, and generate an error

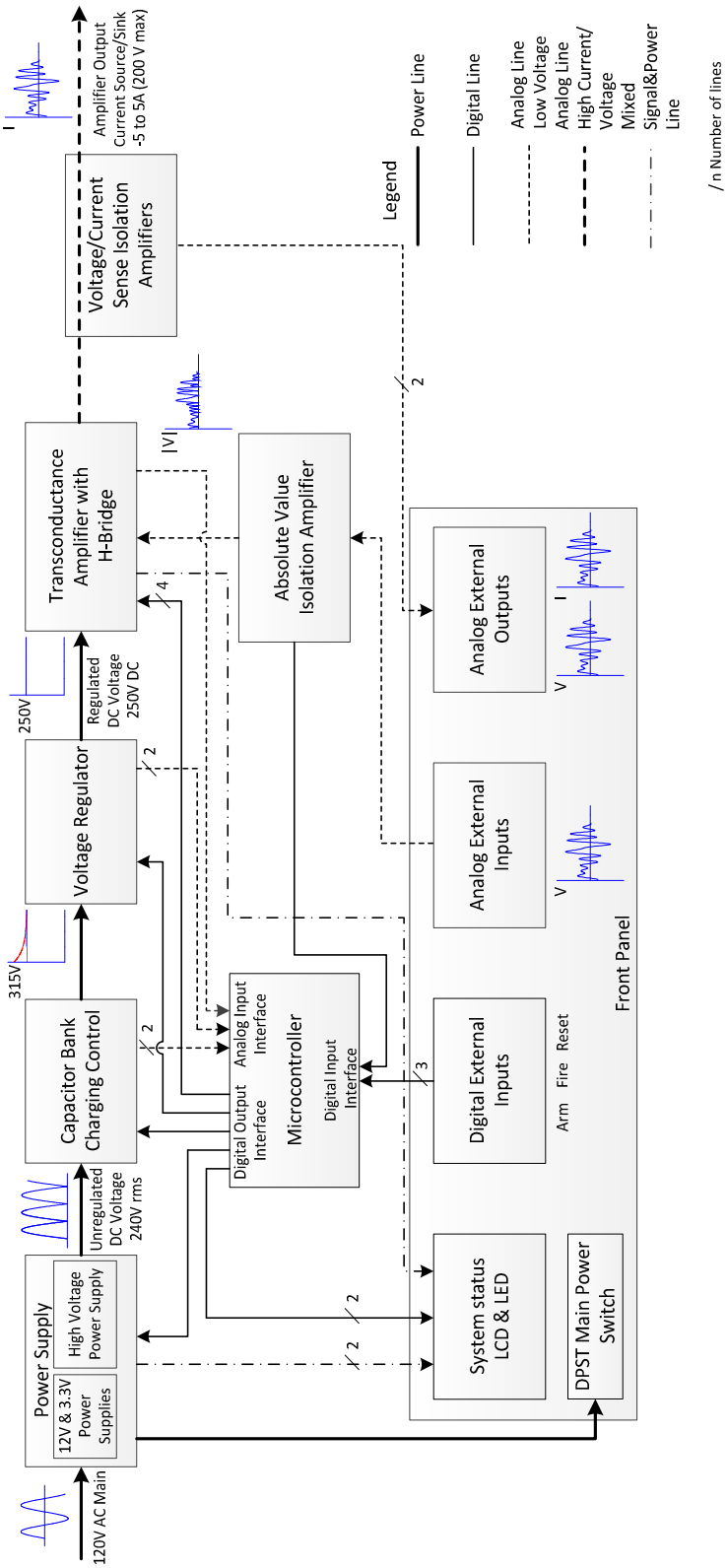

Figure 4.2. Block schematic of the voltage to current converter (V2CC).

report on the LCD. Normal operation can be resumed with a press of the reset button. A capacitor bank with a capacitance of 40,000 μF is necessary by design in order to produce 500 ms long, 5 A pulses into a 40 Ω load, and also to provide fast current rise on the V2CC output for high current demands. The capacitor charging control sets the charging current for the capacitor bank, while the voltage regulator regulates its output voltage to be 250 V, whenever the voltage across the capacitor bank is greater than 252 V and varies either because of discharging or charging the capacitor bank. The transconductance amplifier and H-Bridge form together a bipolar current source powered with a constant voltage source from the voltage regulator. Output current from the V2CC is proportional to the input waveform signal, and output current and voltage are sensed by the isolation amplifiers and monitored as analog representatives on the front panel.

Front Panel

The front panel consists of inputs and outputs for the user, and also displays the current status of the V2CC with LCD and LEDs, as shown in Figure 4.3.

- Inputs
    - "Input Waveform 1 V/A" is an analog input to the transconductance amplifier. 1V on the input will correspond to 1A on the V2CC output.
    - "*Arm*" is a digital active-low input to the microcontroller. It serves to activate reed relays that otherwise keep both sides of the V2CC output disconnected.
    - "*Fire*" is a digital active-low input to the microcontroller. It serves to activate the H-bridge that otherwise keeps both its output sides disconnected through power MOSFETs.
    - When the "Main Power Switch DPST" is turned on, only low voltage power supplies of 12 V and 3.3 V will be present inside the V2CC.
    - "Reset" is a push button that when pressed resets the microcontroller.
- Outputs

- "V2CC output" is the bipolar current source; 1 A on the output corresponds to a 1 V input waveform.
- "Voltage Monitor 1V/40V" is an analog output where 1 V corresponds to 40 V on the V2CC output.
- "Current Monitor 1V/1A" is an analog output where 1 V corresponds to 1 A on the V2CC output.

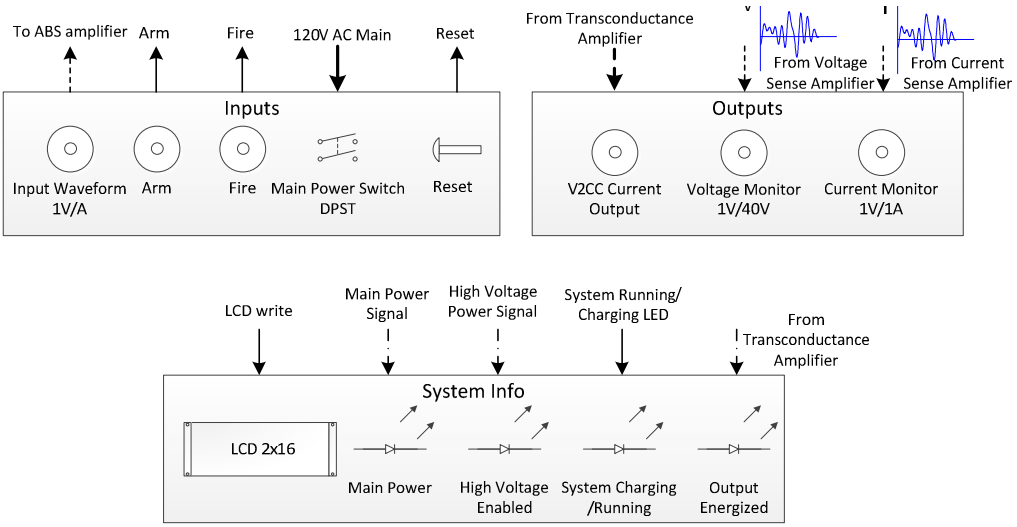

- System Info
  - "LCD" displays system status messages. It consists of 2 rows, each 16 characters long, and each character is coded in ASCII.
  - "Main Power LED" turns on when the main power switch is on. It is directly powered from the AC main and the microcontroller does not control its state.
  - "High Voltage Enabled LED" turns on when high voltage power supply is enabled and the secondary of the 120/240 V transformer is energized. It is directly powered from the DC voltage of 240 V_{rms} and the microcontroller does not control its state.

- "System charging/running LED" is controlled by the microcontroller and turns on when the microcontroller enables the high voltage power supply.
- "Output energized LED" turns on when output reed relays are energized. The microcontroller does not have control of its state.
- All Inputs/outputs Input Waveform, *Arm*, *Fire*, V2CC current output, Voltage and Current Monitor are isolated from each other and are floating, that is, not referenced to the Earth ground.

Power Supply Unit

The power supply consists of a 120/240 V 250 VA isolation transformer and two low voltage isolated power supplies of 12 V and 3.3 V. Their operation is provided from a line voltage of 110-140 V AC, 50/60 Hz, as seen in Figure 4.4. The microcontroller is powered by a 3.3 V power supply while all other electronics are powered with a 12 V power supply. The first stage includes an EMI filter with a fuse and a DPST main power switch (located on the front panel). Low voltage power supplies are connected directly to the input stage while the 120/240 V transformer is connected over the DPST solid state relay controlled by the microcontroller. A digital active-high *START* signal enables solid state DPST relay. The output of the Bridge Rectifier block serves as the high voltage power supply and provides an unregulated, rectified DC voltage of 240 V_{rms}

Capacitor Bank Charging Unit

The main purpose of the capacitor bank charging unit, as shown in Figure 4.5, is to set the charging current for the capacitor bank that consists of four 10,000 μF capacitors connected in a parallel arrangement totaling 40,000 μF. Their parallel setup minimizes equivalent series resistance and equivalent series inductance in order to provide fast current rise on the V2CC output. Capacitance of this value cannot be charged directly from the high voltage power supply since the inrush current can exceed 30 A and the charging circuitry sets the current to be 1 A. With a power supply that provides unregulated DC voltage of 240 V_{rms}, the upper limit across

capacitors is set to be 315 V, which is lower than the theoretical maximum of ~338 V. For voltages up to 250 V, the charging current is constant, while above 250 V, the charging current falls exponentially since charging is done with the rectified AC sinusoidal voltage and it takes approximately 4.5 s for the voltage across the capacitor bank to rise from 250 V to 305 V. The voltage across the capacitor bank (V Cap analog line) and the temperature of the heatsink attached to the capacitor charging circuitry (Temp1 analog line) are monitored by the microcontroller. As a safety measure, a pair of normally closed solid-state relays (crowbar relays) is implemented in order to discharge capacitors when no power is present within 60 s. The status of the crowbar relays is controlled with the *START* signal, and they are disenabled when the *START* signal is active.

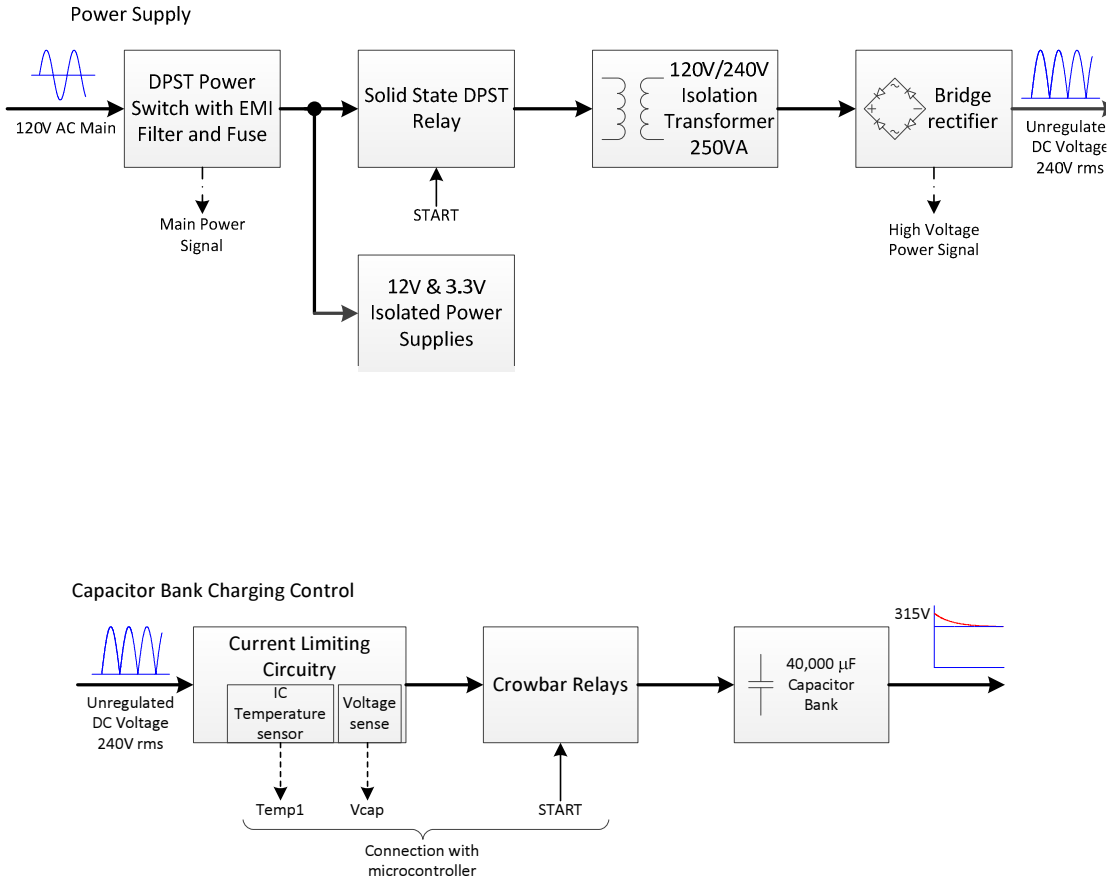

Figure 4.5. Block schematic of the Capacitor Bank Charging Unit.

Voltage Regulator

The voltage regulator outputs a constant DC voltage of 250 V, providing power for the transconductance amplifier and H–Bridge, as shown in Figure 4.6. The purpose of the voltage regulator is to hold its output voltage constant at 250 V while at the same time the capacitor bank rapidly discharges with currents up to 5 A. The difference between the minimal voltage regulator input voltage and voltage across the capacitor bank defines the maximal duration of the current that can be output from the V2CC. The minimal input voltage on the voltage regulator is 252 V, and with a current of 5 A it takes at least 500 ms for the capacitor bank to discharge from 305 V to 252 V, since capacitors are also charged at the same time. The charging time of 4.5 s from 250 V to 305 V sets the maximal duty cycle of 10 % at 5 A. The duty cycle increases with lower currents and is 100% for currents ≤1 A. Load resistance for a current of 5 A is maximally 40 Ω, while for currents lower than 5 A it can be higher, but limited by the product *Current* x *Resistance* ≤ 200 V in both polarities. Also, for currents lower than 5 A, pulse duration can be longer and is continuous for currents ≤1 A. For protection, the voltage regulator has current-limiting circuitry that limits the output current to 5 A, as well as short circuit protection that is activated whenever output of the voltage regulators falls below 200 V, in which case the output current from the voltage regulator drops to zero. These protective mechanisms are implemented due to high power dissipation across the linear regulator that can reach 325 W during normal operations. The voltage at the output of the voltage regulator (V Reg analog line) and the temperature of the heatsink attached to the voltage regulator (Temp2 analog line) are monitored by the microcontroller. The voltage regulator is only operative when the *START* signal is active; otherwise the output of the voltage regulator is in the state of high impedance with respect to the voltage regulator input.

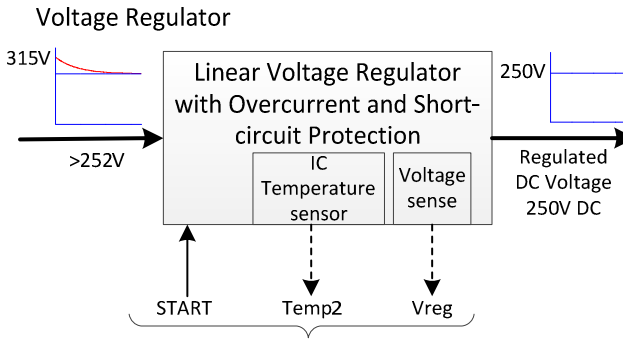

Figure 4.6. Voltage Regulator.

Transconductance Amplifier with the H-Bridge

The transconductance amplifier is designed as a current sink and therefore is unipolar (Figure 4.7a). It sinks current proportional to the input voltage signal originating from the ABS isolation amplifier. In order to provide bipolar operation, the H-Bridge circuitry is placed in series with the transconductance amplifier. Polarity across the H-Bridge output is controlled with the microcontroller, which provides adequate timing diagrams. The time required to switch polarity across the H-Bridge alone is about 1 μs, but the actual total time to switch polarity in the V2CC when the input waveform changes its sign is actually higher and takes up to 10 μs. (This will be explained in the section describing the Microcontroller unit.) The output of the H-Bridge is in series with mechanical reed relays that serve as a safety mechanism by keeping V2CC output disconnected. Operation of the reed relays is controlled with the digital active-high *RR Enable* line that is set by the microcontroller. When *RR Enable* is active both reed relays will be energized. *RR Status* is a digital active-high line monitored by the microcontroller that represents the current status of reed relays and serves as a safety measure. Gates of the MOSFETs in the H-Bridge are driven with gate control circuitry that consists of a gate driver powered with the isolated integrated switching power supply (Figure 4.7b). When the input digital signal *H-Bridge+* or *H-Bridge-* is active-high, the corresponding pair of gate drivers will provide instantly 15 V between the gate and the source of the corresponding pair of MOSFETs, creating a low impedance path between their drain and source. In this way one side of the output will be connected to the line

coming from the voltage regulator and the other side of the output will be connected to the sink of the transconductance amplifier. The temperature of the heatsink attached to the transconductance amplifier is monitored through the analog line Temp3 by the microcontroller.

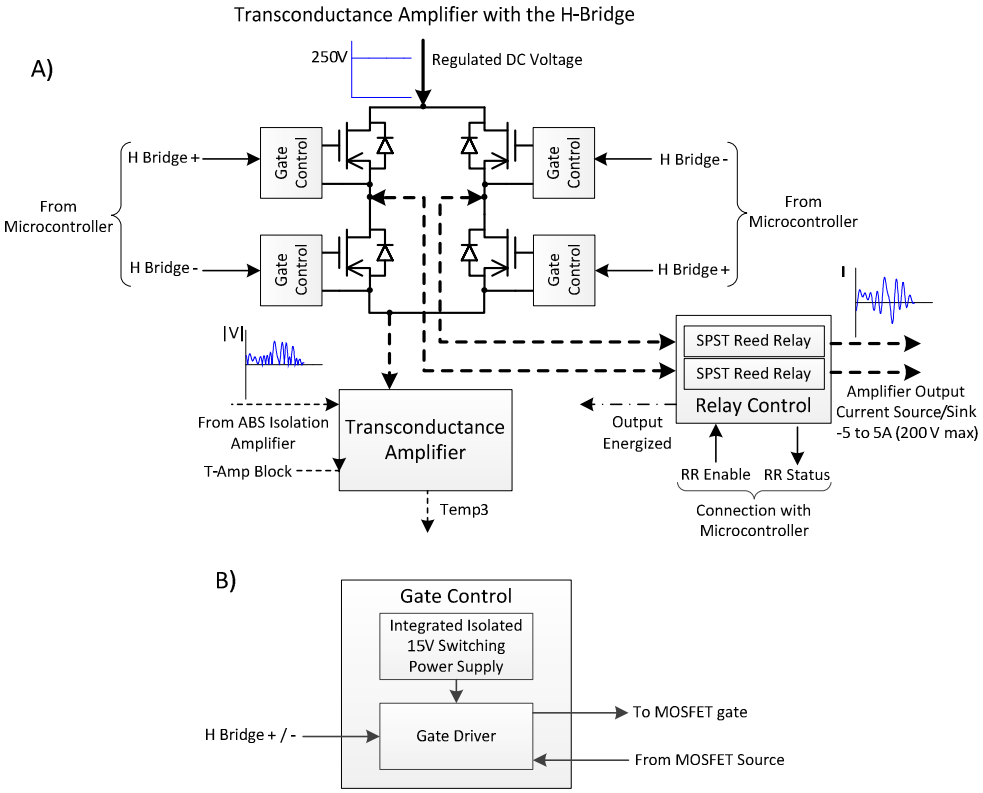

Figure 4.7. (a) Block schematics of the Transconductance Amplifier with the H-Bridge. (b) Block schematic of the Gate Driver.

Absolute Value Isolation Amplifier (ABS amplifier)

The absolute value isolation amplifier consists of an input and output stage connected by means of a digital isolator (Figure 4.8A). Conditioning electronics in the input stage accept an external waveform signal in the range of ±5 V and drive the 16-bit 100 Ksps A/D converter. The input stage is powered with ±12 V integrated and isolated switching power supplies in order to provide electrical isolation for the input signal from the rest of the V2CC circuitry. The output stage consists of a 16-bit 100 Ksps D/A converter and conditioning analog electronics. Only the first 15-bits representing the absolute value of the input signal are fed into the D/A converter,

while the MSB bit representing the sign of the input signal serves as an external interrupt for the microcontroller as a digital line named Sign. When Sign is digital 1, it indicates that the input signal waveform is currently negative, while digital 0 indicates that the input waveform is positive. Conditioning electronics in both stages have implemented analog filters designed as single pole low pass filters with a -3dB cut-off at 3 KHz.

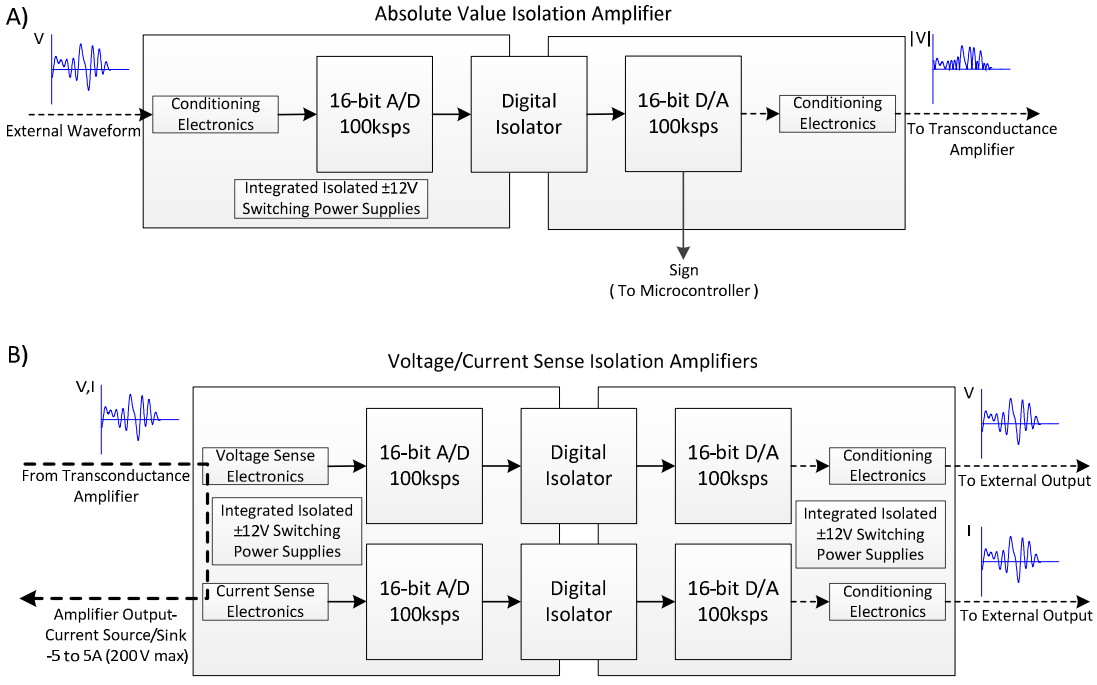

Figure 4.8. (a) Block schematics of the Absolute Value Isolation Amplifier. (b) Block schematics of the Voltage/Current Sense Isolation Amplifier.

Current/Voltage Sense Isolation Amplifiers

Current and voltage sense isolation amplifiers are designed in the same way as the ABS isolation amplifier (Figure 4.8B). The output voltage from the voltage sense isolation amplifier is scaled so that 1 V represents 40 V on the V2CC output, while 1 V from the current sense isolation amplifier output represents 1 A on the V2CC output. Voltage/current sense electronics in both stages have implemented analog filters designed as single pole low pass filters with a -3dB cut-off at 3 KHz. Both stages also have implemented ±12 V integrated and isolated switching power

supplies. They are necessary in the input stage since voltage and current on the V2CC output are on the high side, while on the output stage they provide isolation for the output signals from the rest of the V2CC circuitry.

Microcontroller Unit

The microcontroller unit is designed with the 8 MHz MSP430F169 Texas Instruments microcontroller. Using a microcontroller has multiple advantages. Replacing control logic with a microcontroller provides flexibility, since it is easier and more practical to change a line of code than to redesign a printed circuit board during design iterations. Also, nowadays, discrete control logic can be much more expensive than an approach with a microcontroller. The role of a microcontroller is to assure that the V2CC works properly and to provide the user with helpful messages representing the current status of the V2CC.

Table 4.1 Truth table of all digital control signals

Control Signal	Active High/Low
Arm	Low
Fire	Low
Reset	High
START	High
RR Enable	High
RR Status	Low
H-Bridge-	High
H-Bridge+	High
T-Amp Block	Low

All microcontroller inputs and outputs are divided into four sections: analog input section, digital input section, digital output section and a serial port communication.

The analog input section consists of five analog inputs, *Temp1*, *Temp2*, *Temp3*, *V Cap* and *V Reg*. They respectively correspond to heatsink temperature of the capacitor charging circuitry, heatsink temperature of the voltage regulator, heatsink temperature of the transconductance amplifier, voltage across the capacitor bank and voltage at the output of the

voltage regulator. These analog inputs are sampled with a rate of 1 Ksps. This sampling rate is particularly chosen so that the validity of the output voltage and current is time resolved with an accuracy of 1 ms.

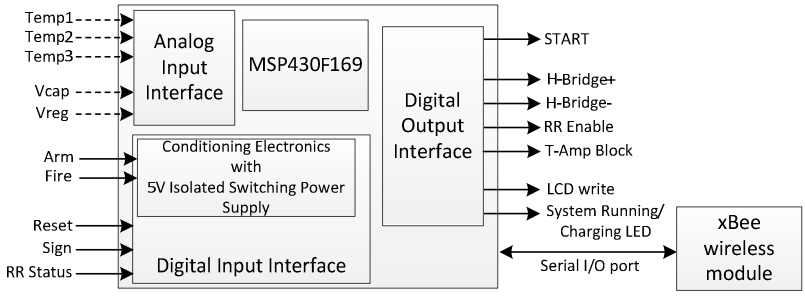

Figure 4.9. Block schematics of the Microcontroller Unit.

The digital output section can be divided into 3 subsections. The first consists only of a *START* signal and controls the high voltage power. When *START* is active, the solid state relay in the voltage supply block is activated, crowbar relays across the capacitor bank are disenabled and output of the voltage regulator is enabled. The second subsection controls the transconductance amplifier with H-Bridge block. With active-high digital lines *H-Bridge+* and *H-Bridge–*, the microcontroller sets the polarity at the H-Bridge output; active-high *RR Enable* energizes output reed relays; active-high T-Amp Block enables the transconductance amplifier; and its purpose is to shut-down the transconductance amplifier when polarity across the H-Bridge is being switched, since at that moment the load is disconnected from the H-Bridge. In the third subsection are control lines that control the LCD on the front panel and "System Running/Charging LED" on the front panel.

The digital input section can be divided into two subsections. The first represents user-controlled digital signals from the front panel: *Arm*, *Fire* and *Reset*. *Arm* and *Fire* are TTL active-low signals processed with level shifter electronics that shift TTL levels down to 3.3 V, and that are powered with the 5 V isolated switching power supply in order to isolate these two inputs from the rest of the V2CC circuitry. When *Arm* is active low, the microcontroller will enable output reed relays by activating *RR Enable*, but only if all other relevant parameters are within their

specified range. *Fire* serves as a mask for digital outputs *H-Bridge–* and *H-Bridge+* and sets them both as inactive when *Fire* is inactive. If *Arm* is inactive, the active *Fire* signal will be ignored. Both *Fire* and *Arm* serve as a safety mechanism so that output of the V2CC is electrically connected only when needed. For this purpose mechanical reed relays are implemented that enable the user to safely configure any setup driven with the V2CC current source. Since mechanical relays have a slow switching time (50 ms with the reed relays used in this design), and because we required a response time of 1 ms to connect the output of the V2CC, we added an additional user input named *Fire* that controls the MOSFETs of the H-Bridge as solid state relays. In this way when *Arm* is active and *Fire* inactive, output of the V2CC is still disconnected through high impedance MOSFETs, and active *Fire* will activate the output in less than 1 ms.

The second subsection consists of two digital signals generated automatically from other V2CC blocks: *Sign* and *RR Status*. *RR Status* is monitored in the same way as 5 analog signals; it is read every 1 ms. Its active high value means that reed relays are energized, and it serves as a safety measure so that the microcontroller can detect a failure when output reed relays are energized, but *RR Enable* is inactive and vice versa. Sign is a digital input that serves as a trigger for interrupt routine whenever it changes its value, either 0→1 or 1→0. Based on its value, the microcontroller will generate adequate timing diagrams for *H-Bridge+* and *H-Bridge–* digital lines, but these lines, as mentioned before, are masked with the *Fire* signal and will remain inactive if both *Arm* and *Fire* are inactive. Since the input waveform is sampled at a rate of 100 Ksps, it can take up to 10 μs for a *Sign* interrupt to appear when input waveform changes its sign. Processing of the *Sign* interrupt takes additionally up to 5 μs until the polarity across the H-Bridge is finally changed.

Serial port communication serves for debugging purposes. With a pair of wireless XBee modules, the microcontroller communicates with the PC. One XBee module is connected to the serial port of the microcontroller while other XBee module is connected to the PC. Communication is done through a simple terminal protocol using ASCII code. When microcontroller reads that the

"q" key is pressed on the PC side, it will send values of all analog and digital signals to the I/O port that will be subsequently displayed in the PC terminal window.

Theory of Operation

"Theory of operation" is described in terms of the algorithm for the microcontroller as shown in Figure 4.10. Operation of the microcontroller can be divided into 3 working modes, "Startup Mode," "Charging Mode," "Running Mode" and a special "Error Mode." This section provides a conceptual design for the algorithm. The actual coding may differ in specific details, but it performs as outlined below.

Error Mode

The microcontroller can enter in the "Error Mode" from any of the three working modes. In this mode the microcontroller inactivates all its digital outputs, displays a specific message on the LCD and stops any further code execution. The first line of the LCD displays the name of a mode and the second nature of an error. The only way that the microcontroller can exit the "Error Mode" is when the reset button is pressed or if the V2CC is powered off and powered on sequentially.

Startup Mode

After the power switch is turned on, the microcontroller executes commands from the "Startup Mode," as presented in Figure 4.10a. It sets all digital outputs as inactive, sets Timer A to generate interrupts every 1 ms, sets Timer B to generate interrupts every 500 ms and sets Timer C to countdown from 120 s (step 2). The purpose of the Timer A interrupts is to execute a special routine in which all relevant parameters for the current working mode are being checked to ensure proper operation of the V2CC. The purpose of the Timer B interrupts, which have a lower priority than the Timer A interrupts, is to update the LCD within the interrupt routine. The

purpose of Timer C is to allow 120 s for all five analog signals (*Vcap, Vreg, Temp1, Temp2* and *Temp3*) to fall into the predefined range, if they are not already there. Also, the microcontroller initializes and sets an auxiliary variable named *Exit* to zero, which represents a return value of the Timer A interrupt routine.

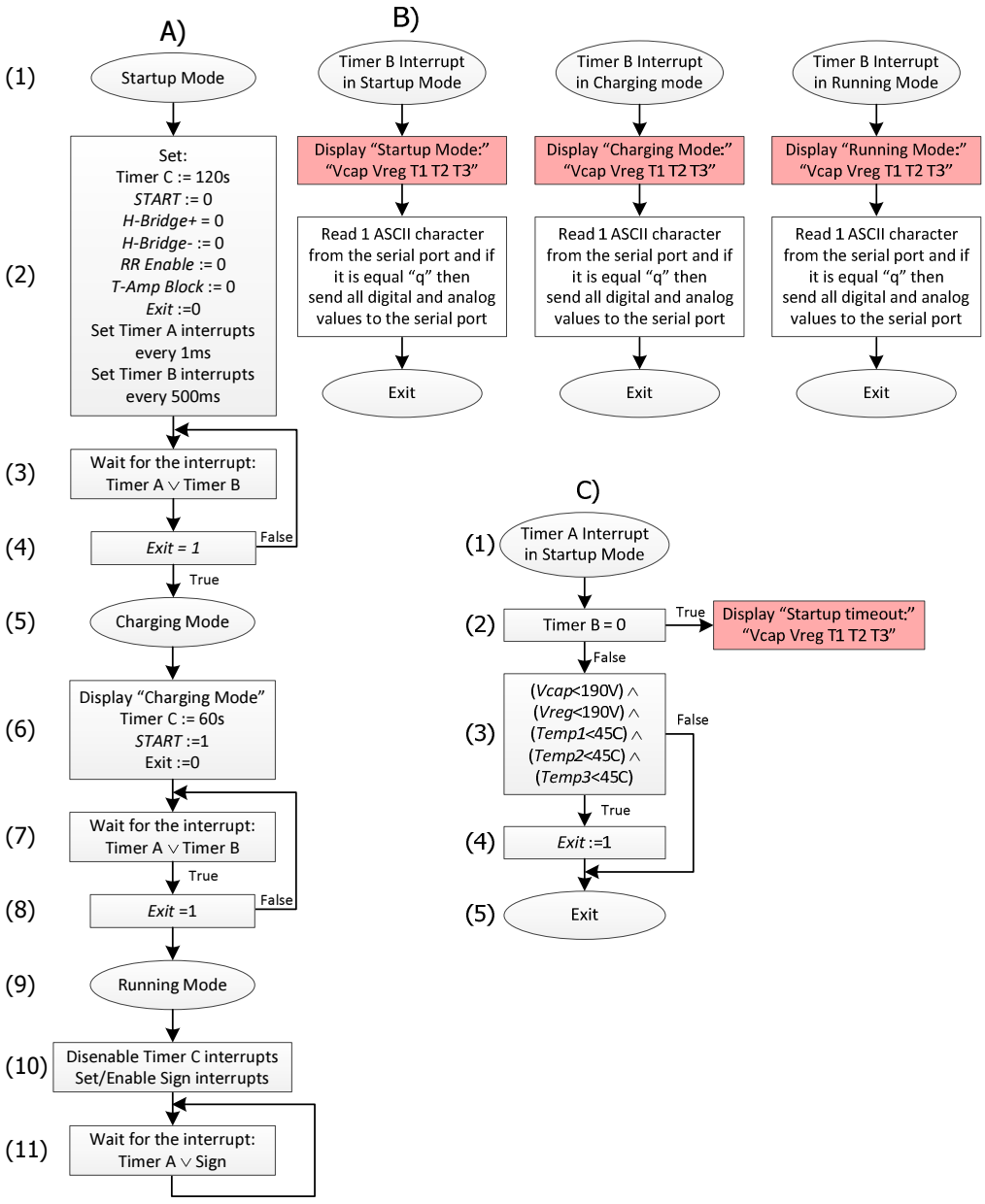

Figure 4.10. (A) Algorithm for the main code, (B) timer B interrupt routine in different working modes, (C) timer A interrupt routine in Startup Mode, (D) timer A interrupt routine in Charging Mode, (E) Timer A interrupt routine in Running mode, (F) Sign interrupt routine. All shaded boxes terminate program execution and require reset or restart.

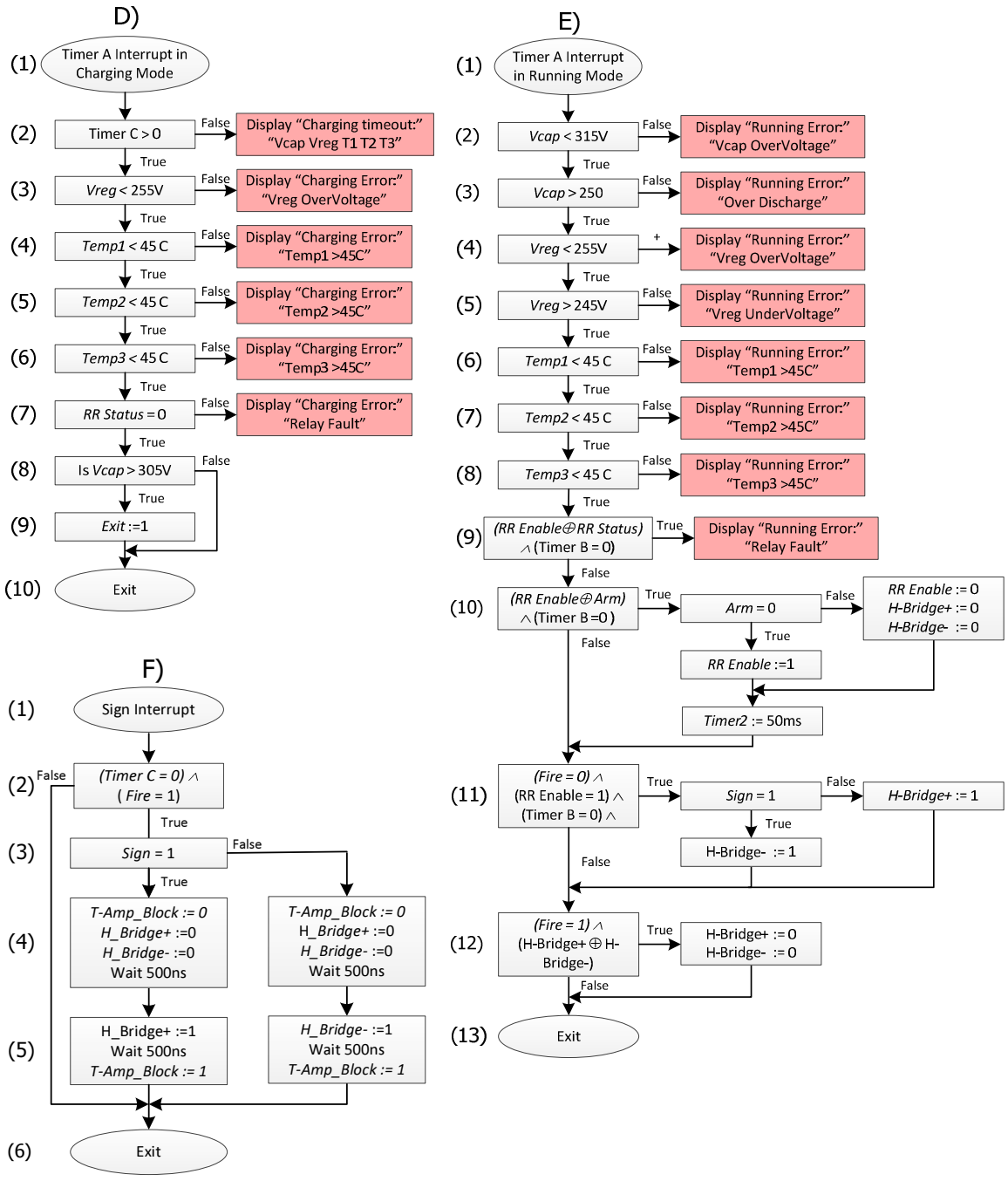

Figure 4.10. continued.

The Timer B interrupt routine differs among working modes (Figure 4.10B). As noted, the main purpose of this routine is to update the LCD so that its first line displays the current working mode while the second line displays values of all 5 analog signals: *Vcap*, *Vreg*, *Temp1, Temp2,*

and *Temp3,* respectively. Also, in this routine, microcontroller reads 1 ASCII character from the serial port and if the value of the character is "q" then values off all analog and digital signals will be sent to the serial port.

After all initial settings are performed, the microcontroller will wait for the interrupt requests either from Timer A or from Timer B (Figure 4.10, step 3). At that moment, only low voltages are present inside the unit (12 V and 3.3 V power supplies) and the microcontroller will "power up" the high voltage power supply when it determines that all relevant parameters are within their predefined safe operating range. This check is performed in the "Timer A Interrupt in Startup Mode" routine, as presented in Figure 4.10C. If all relevant values are within their predefined range (*Vcap<190 V, Vreg<190 V, Temp1<45 °C, Temp2< 45 °C* and *Temp3 < 45 °C*), the interrupt routine will return an *Exit* value of 1 and the microcontroller will proceed into the "Charging Mode." If any of these values is outside of its predefined range, and at the same time Timer B is greater than zero, the microcontroller will wait for the next Timer A or B interrupt. Otherwise, if Timer B is equal to zero, an error report "Startup Timeout" will be displayed and the microcontroller will enter into the "Error Mode" and halt any firther code execution until reset.

Charging Mode

Continuing along Figure 4.10A, we see that in the "Charging Mode," the microcontroller activates the *START* signal*,* sets *Exit* to 0 and sets Timer C to countdown from 60 s (step 6). The purpose of Timer C is to wait maximally 60 s for the capacitors to be charged to 305 V. Charging requires about 15 s and during this time the microcontroller waits for an interrupt either from Timer A or from Timer B. As in the "Startup Mode," the Timer A interrupt routine has the same purpose to perform checks of all the relevant V2CC parameters, although the algorithm itself is slightly different. In the same manner, the Timer B interrupt routine (Figure 4.10 B) updates the LCD. In the "Timer A Interrupt in Charging Mode" routine (Figure 4.10 D) the microcontroller performs the following checks: Timer C has to be greater than 0, otherwise an error "Charging Timeout" will be displayed on the LCD; *Vreg* has to be lower than 255 V, otherwise an error

"Vreg OverVoltage" will be displayed; each of the three temperature signals has to be lower than 45 °C, otherwise an error indicating which temperature signal caused an error will be displayed; and the *RR Status* signal has to be inactive, otherwise an error "Relay Fault" will be displayed. In each case when the error message is displayed, the microcontroller enters the "Error Mode". As can be inferred from the algorithm, in the "Charging Mode" the input signals *Fire* and *Arm* are not being processed and therefore the output of the V2CC remains inactive. When the voltage across the capacitor bank reaches 305V, the interrupt routine will return an *Exit* value of 1 (Figure 4.10D (9)). That is the necessary condition for a microcontroller to enter into the "Running Mode;" otherwise it will wait again for the Timer A/B interrupt.

Running Mode

In the "Running Mode," the microcontroller first disenables the Timer C interrupts (Figure 4.9A (10)), sets and enables external interrupts from the *Sign* digital line and waits for an interrupt to be generated either from Timer A, Timer B or from the *Sign* (step 11). Timer A and Timer B interrupts have the same purpose, and as in the previous working modes thus the algorithm is different. The *Sign* interrupt makes the microcontroller process the sign routine in order to change the polarity across the H-Bridge. A *Sign* interrupt request has the highest priority. Timer C in the Running Mode has a special purpose and is used only inside the Timer A interrupt routine. It represents the time that it takes for the reed relays to close or open when the *RR Enable* signal becomes active or inactive, respectively, so that the *RR Enable* and *RR Status* signals have the same values afterwards. Without the Timer C delay, reading the *RR Status* signal and comparing it with the actual value of the *RR Enable* signal will cause false errors.

- In the "Timer A Interrupt in Running Mode" routine (Figure3.9C) the following checks are performed:
    - *Vcap* has to be lower than 315 V and greater than 250 V, otherwise an error "Vcap OverVoltage" or "Over Discharge" will be displayed, respectively.

- *Vreg* has to be lower than 255 V and greater than 245 V, otherwise an error "Vreg OverVoltage" or "Vreg UnderVoltage" will be displayed.
- The temperature from each of the three temperature sensors must be lower than 45 °C, otherwise an error will be displayed indicating which particular temperature signal caused an error.
- *RR Enable* and *RR Status* need to have the same values when Timer C = 0. For this purpose the exclusive or function will be true if *RR Enable* and *RR Status* have different values, and if additionally Timer C = 0, the error "Relay Fault" will be displayed (step 9).
- Processing of the *Arm* signal (step 10) only takes place if at the same time its value differs from the current status of the *RR Enable* signal and only if at the same time Timer B = 0. When these conditions are met it means that there was a change in the value of the *Arm* signal from the previous interrupt cycle. If *Arm* is active, the microcontroller will set active *RR Enable* and will set Timer C to countdown from 50 ms. If *Arm* is inactive, *RR Enable, H-Bridge+ and H-Bridge-* will be inactivated, and Timer C set to countdown from 50 ms. Inactivating the H-Bridge ensures that it is disenabled regardless of the status of the *Fire* signal when *Arm* isn't active.
- When the *Fire signal* becomes active (step 11), the polarity across the H-Bridge will be set, but only if reed relays are already energized (*RR Enable* = 1) and there is no transition process on the reed relays (*Timer B* = 0). These conditions ensure that reed relays are energized and that enabling the H-Bridge will instantly make the output current on the V2CC valid. When these conditions are met, polarity on the H-bridge will be set accordingly to the value of the *Sign* input, where *Sign* value of 1 indicates that the input waveform has negative polarity.

- When the *Fire* signal becomes inactive (step 12), at the same time one of the two signals *H-Bridge–* or *H-Bridge+* is still active, which is an indication that the *Fire* signal changed its value from active to inactive in comparison to the previous interrupt cycle. In that case, both signals *H-Bridge+* and *H-Bridge–* will be inactivated. This ensures that H-Bridge is disenabled as fast as possible without checking which H-bridge polarity lines should be inactivated to save CPU time.

- The "Sign interrupt" routine (Figure 3.9F):
  - The "Sign interrupt" routine will only be fully processed if *Fire* is active and Timer C = 0 (step 2). This ensures that reed relays have been activated and that the polarity across the H-Bridge has been set previously, otherwise there is no need to further process the routine.
  - If the above conditions are met, the polarity across the H-Bridge will be set accordingly to the value of the *Sign* (step 3). First, the transconductance amplifier and the H-Bridge are disabled (step 4) and code execution is paused for 500 ns, since the H-Bridge and its polarity controlling circuits need a certain time to respond, mainly due to the gate-source capacitances of the H-Bridge MOSFETs. Checking the *Sign* value is performed before the inactivation of the H-Bridge since it is desirable to switch the polarity across the H-Bridge as fast as possible. Otherwise, if the H-Bridge is first inactivated and then a value of the *Sign* is checked, it will create unnecessary longer time intervals during which the H-Bridge is inactivated.
  - According to the value of the *Sign* (step 5), either *H-Bridge+* or *H-Bridge-* will be set as active, code will be paused for 500 ns to allow polarity across the H-Bridge to be set, and *T-Amp Block* will be inactivated.

How to Apply a Shock From the Output:

- V2CC must be in the Running mode.
- Set external input *Arm* as active to activate reed relays.
- Set external input *Fire* as active to enable the H-Bridge. Note that minimally 50 ms has to pass in order for the reed relays to be closed and any further changes of the *Fire* signal will be ignored within these 50 ms.
- After the H-Bridge is activated, V2CC output current will be proportional to the input waveform that is fed into the V2CC.

LCD Messages:

LCD messages representing working modes and certain errors in different modes are represented in Figure 4.11. The first line of the LCD shows the working mode, except in the error mode, when particular error messages will be displayed. The second line of the display shows the values of 5 analog signals. From left to right they are: voltage across the main capacitor bank, voltage on the output of the voltage regulator, temperature of the heatsink in the capacitor charging block, temperature of the heatsink in the voltage regulator block and temperature of the heatsink in the amplifier block. In the upper right corner of the LCD, a Timer C time is displayed that is active in the startup and the charging modes.

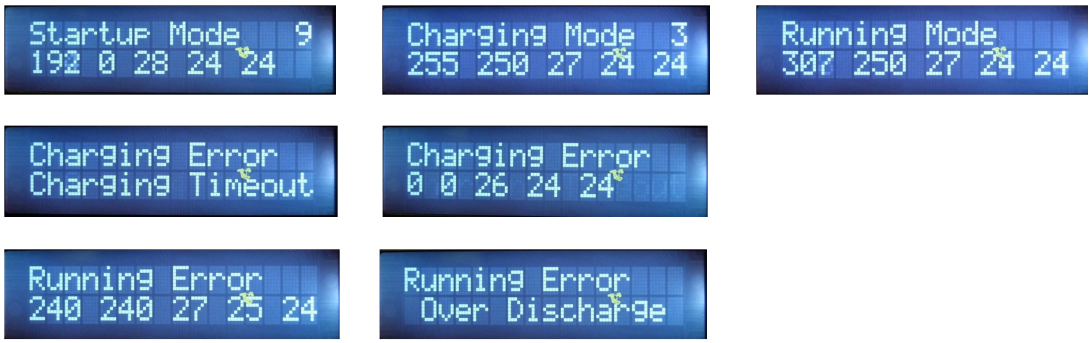

Figure 4.11. Various LCD messages represented as a screenshoots.

Conclusion

Shock duration is limited by the voltage across the main capacitor bank. With the 120V AC main, the internal voltage across the main capacitor bank will reach above the 305 V necessary for the 500 ms long, 5 A current shocks. If longer shocks are needed, the 120V AC main power supply can be increased to 140V AC using an autotransformer. In this case, the voltage across the main capacitor bank will reach 315 V, allowing longer shock durations.

As with any high-voltage capacitor-energy storage device, the V2CC is capable of causing injury or death. The V2CC design we present may not address all possible failure modes, and hence this device should be used with extreme caution. The design of this device is not certified by any individual or organization nor is the system intended for use on human subjects. The authors do not accept any responsibility for injury or death that might occur as a result of proper or improper use of this device. Given these caveats, the system we have developed is robust and well suited for a wide variety of experiments including but not limited to cardiac defibrillators.

Acknowledgment

This work is supported in part by FDA contract, NIH Grant R01 HL58241-11 through the American Recovery and Reinvestment Act of 2009, and the Vanderbilt Institute for Integrative Biosystems Research and Education (VIIBRE). We appreciate numerous suggestions by Dr. Richard Gray. We thank Allison Price for editorial assistance.

Various Current Waveforms on the V2CC output

The following figures represent various waveforms at the current output of the V2CC. The analog waveform input of the V2CC was driven by the signal generator, set to output sine, triangle and square waveforms. The amplitude was set to 50 mA, 500 mA, 5 A, while the frequency was set to 10 Hz, 100 Hz, and 1 KHz. Current was delivered into a 40 Ω load and waveforms were recorded with 8-bit Yokogava DL1540 digital scope.

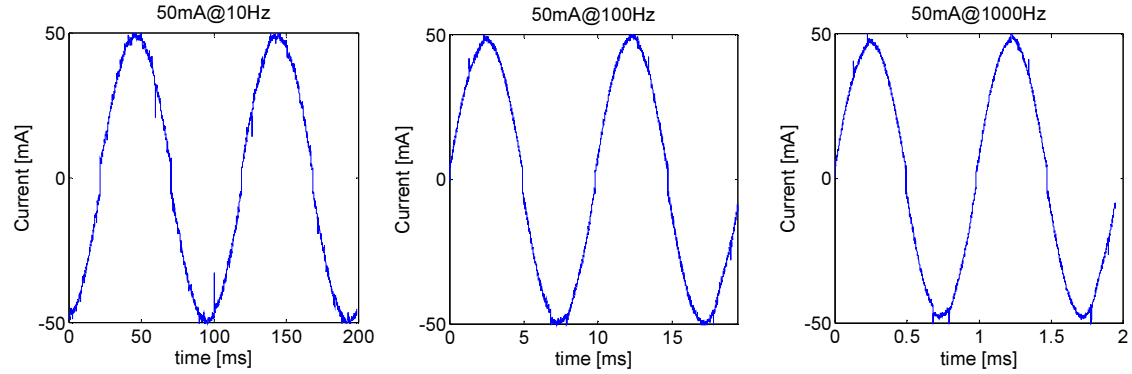

Figure 4.12. Sinusoidal waveforms on the V2CC output at different frequencies. The input of the V2CC was driven with the signal generator with a sine wave amplitude of 50 mA.

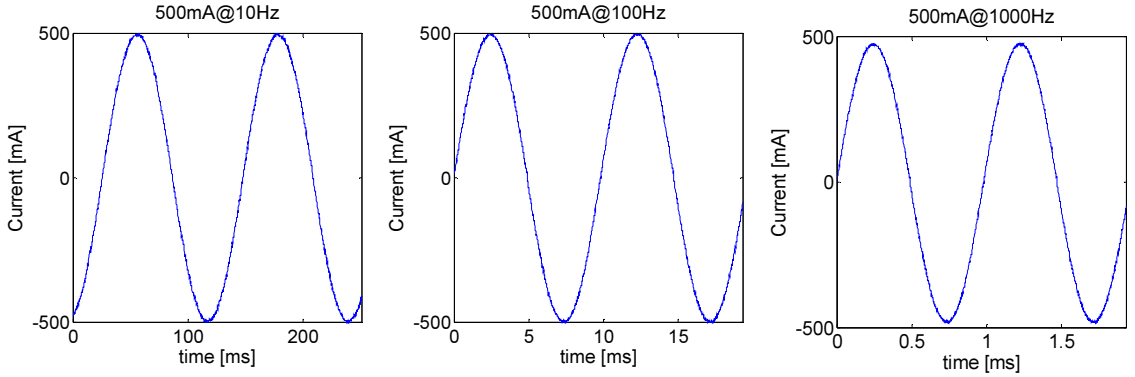

Figure 4.13. Sinusoidal waveforms on the V2CC output at different frequencies. Input of the V2CC was driven with the signal generator with a sine wave amplitude of 500 mA.

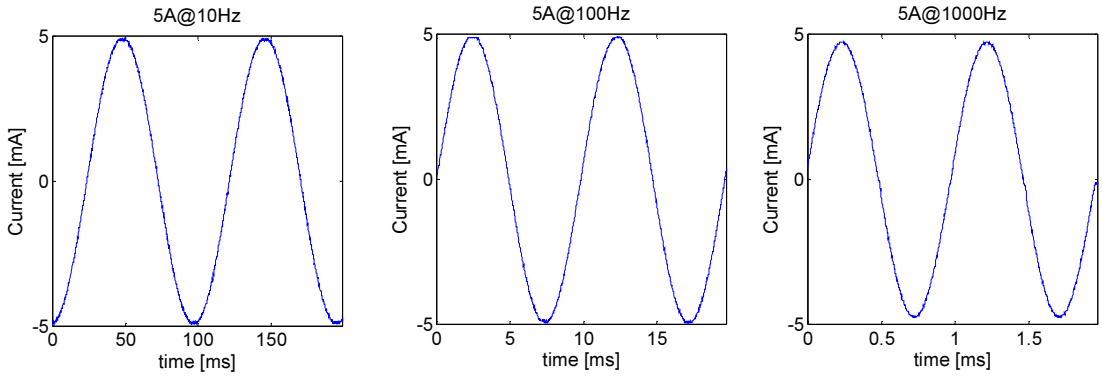

Figure 4.14. Sinusoidal waveforms on the V2CC output at different frequencies. The input of the V2CC was driven with the signal generator a sine wave amplitude of 5 A.

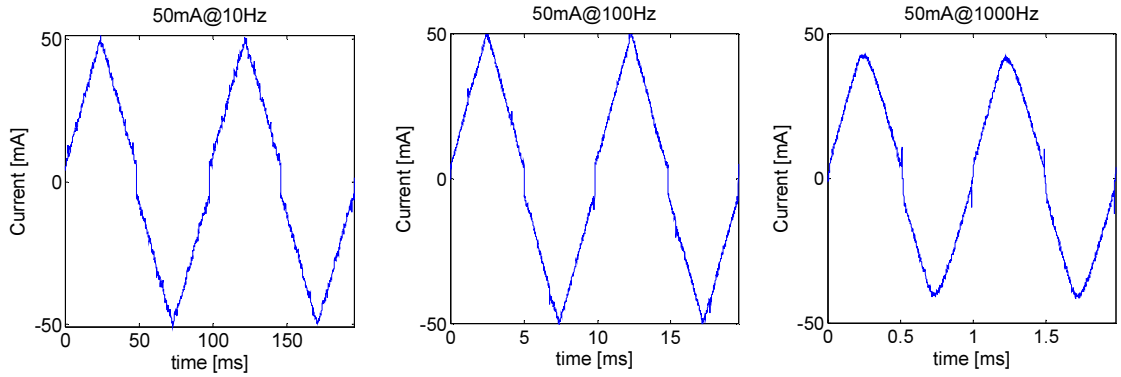

Figure 4.15. Triangular waveforms on on the V2CC output at different frequencies. The input of the V2CC was driven with the signal generator with an amplitude of 500 mA.

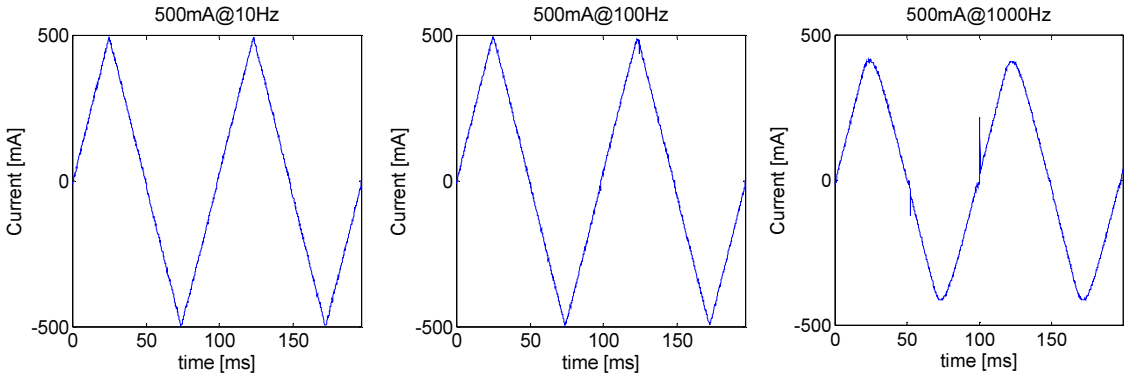

Figure 4.16. Triangular waveforms on on the V2CC output at different frequencies. The input of the V2CC was driven with the signal generator with an amplitude of 500 mA.

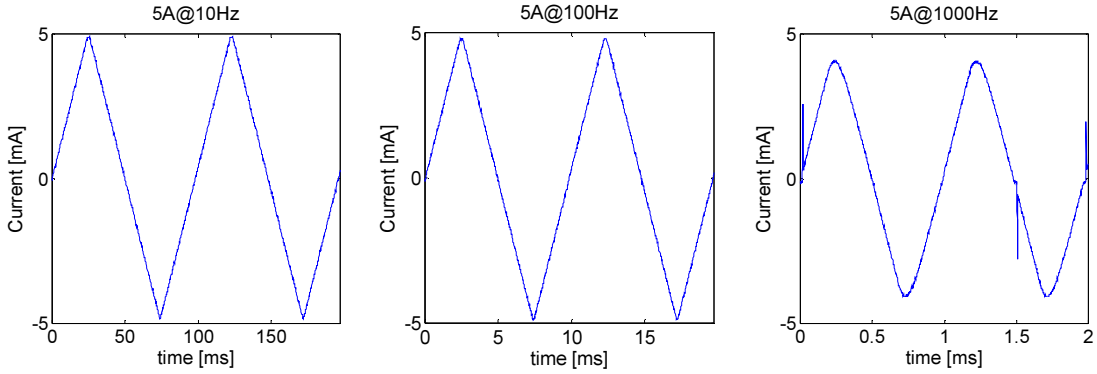

Figure 4.17. Triangular waveforms on the V2CC output at different frequencies. The input of the V2CC was driven with the signal generator with an amplitude of 500 mA.

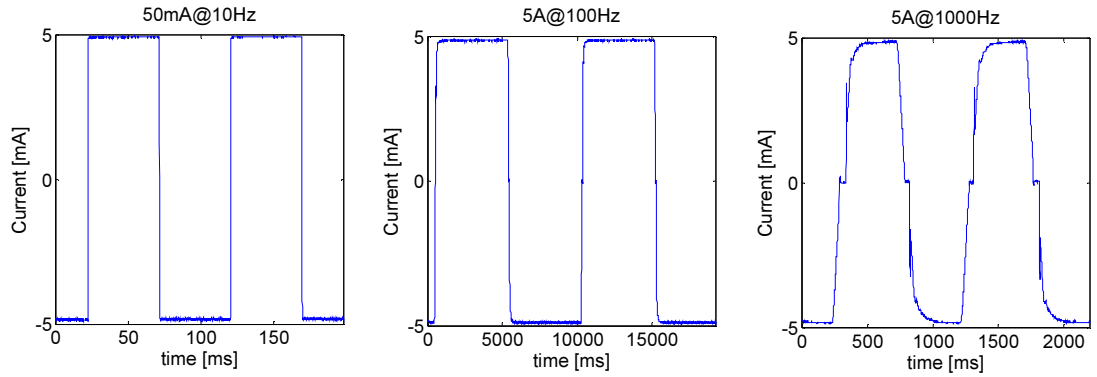

Figure 4.18. Square waveforms on on the V2CC output at different frequencies. The input of the V2CC was driven with the signal generator with an amplitude of 5 A.

Photos of the V2CC

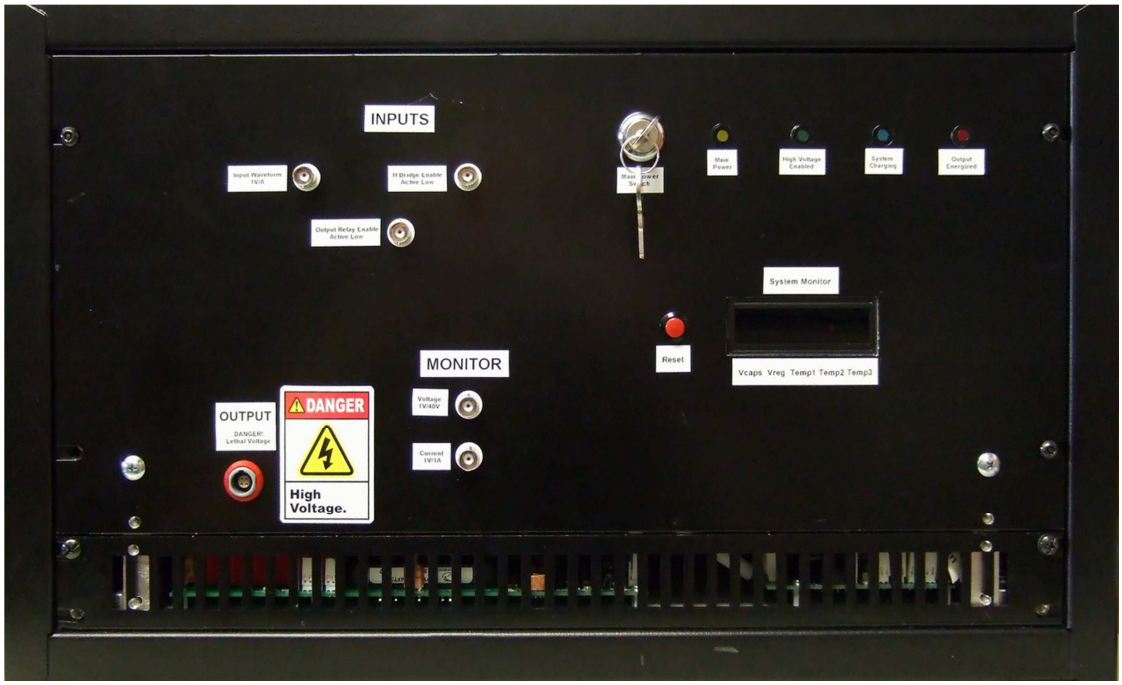

Figure 4.19A. V2CC front panel.

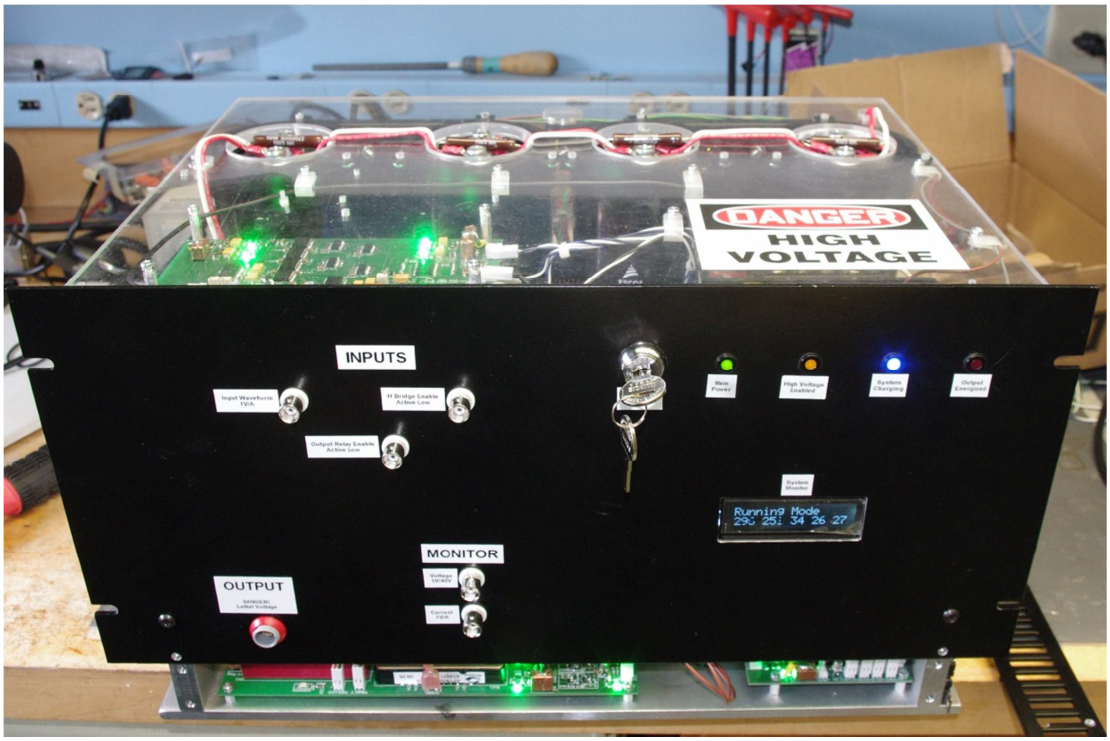

Figure 4.19B. V2CC unit removed from the chassis.

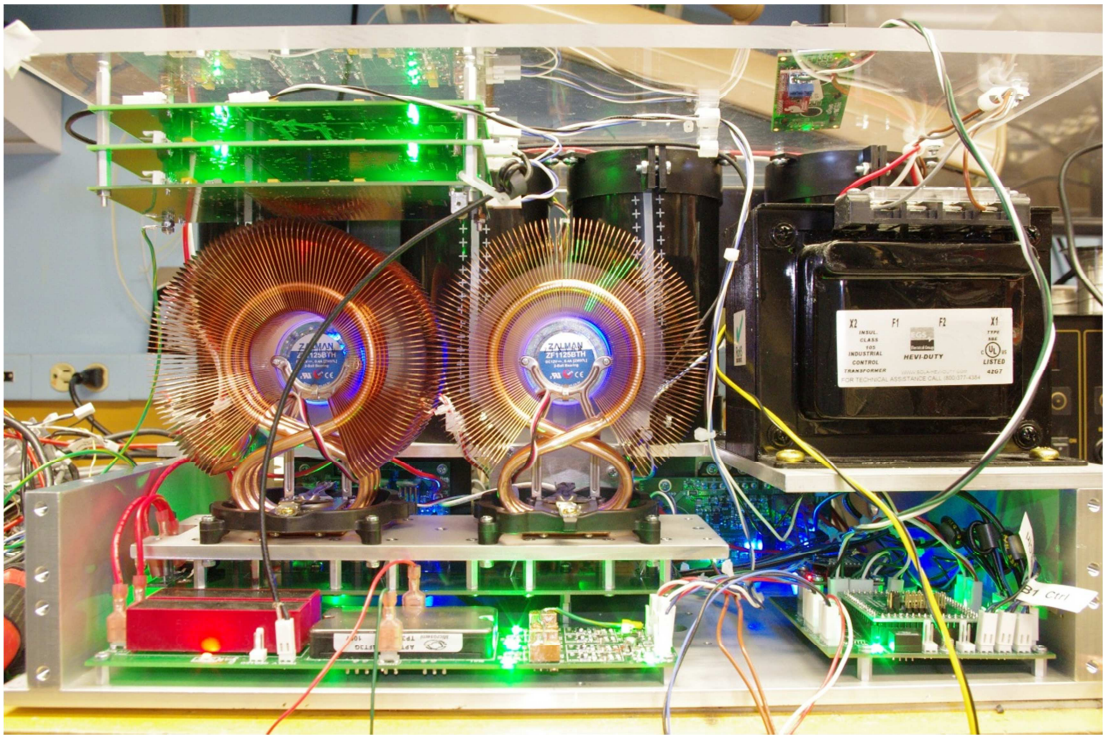

Figure 4.19C. V2CC without the Front Panel and chassis (front view).

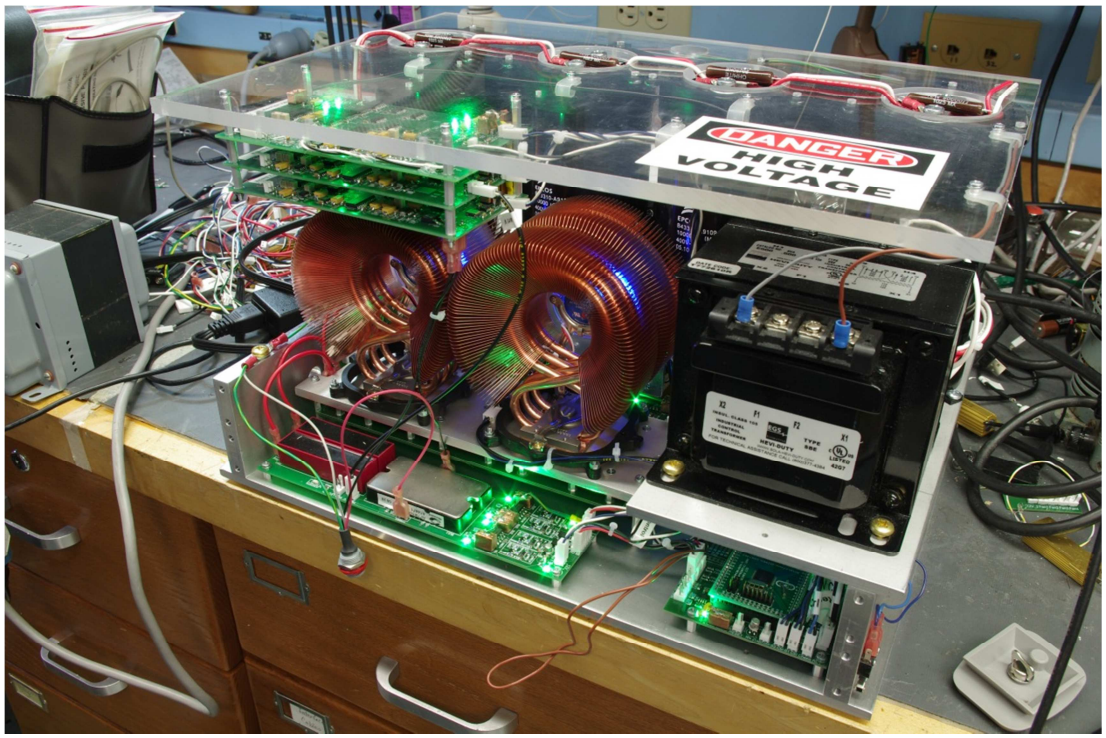

Figure 4.19D. V2CC without the Front Panel and chassis (side view).

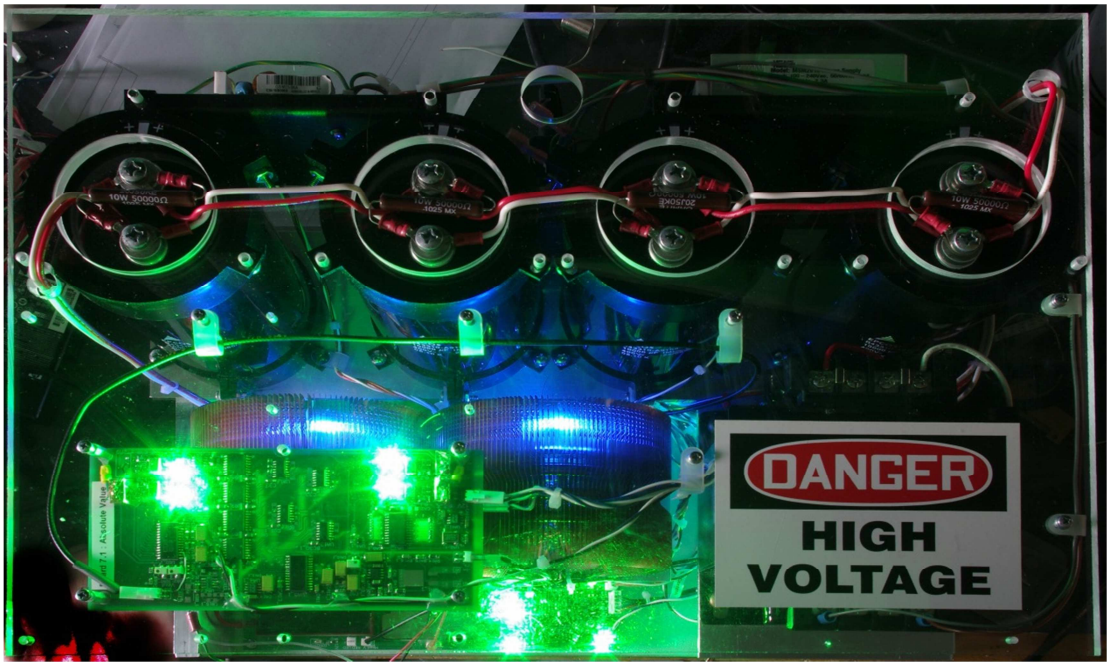

Figure 4.19E. V2CC without the Front Panel and chassis (top view).

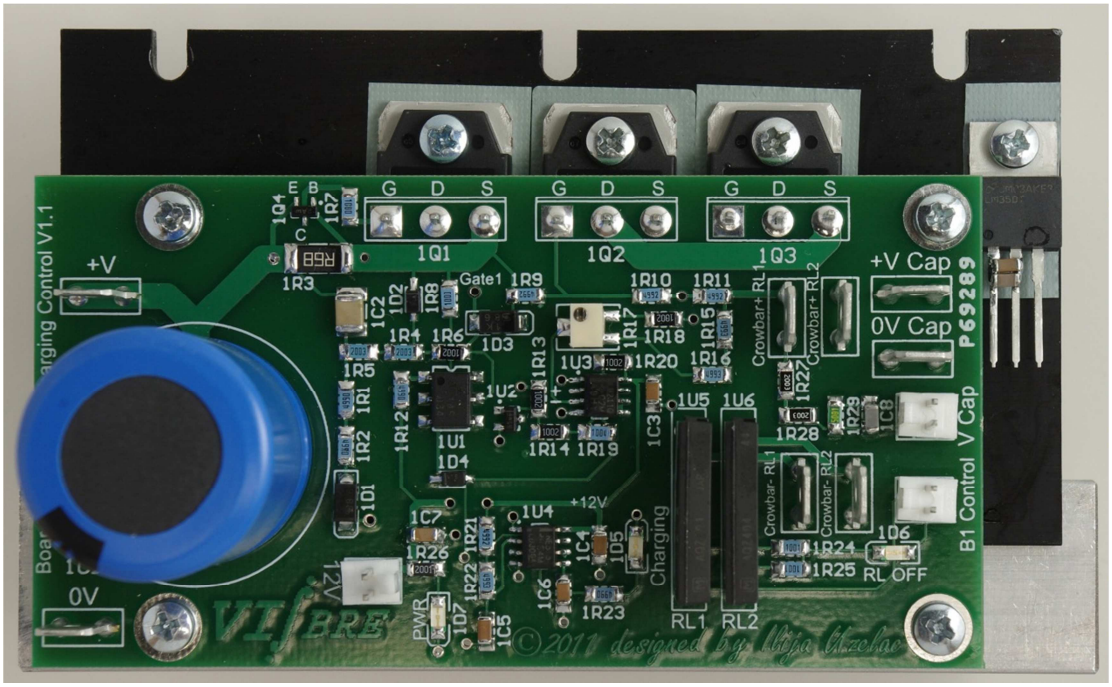

Figure 4.19F. Capacitor Block Charging Unit.

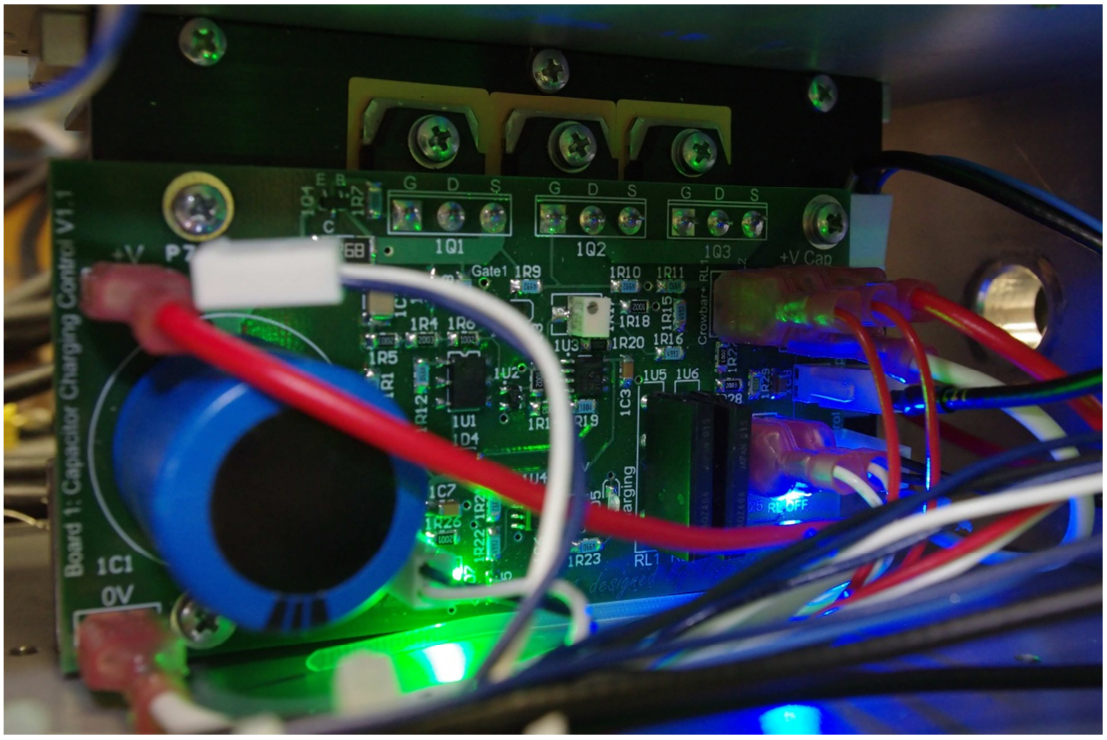

Figure 4.19G. Capacitor Charging Unit assembled in the V2CC.

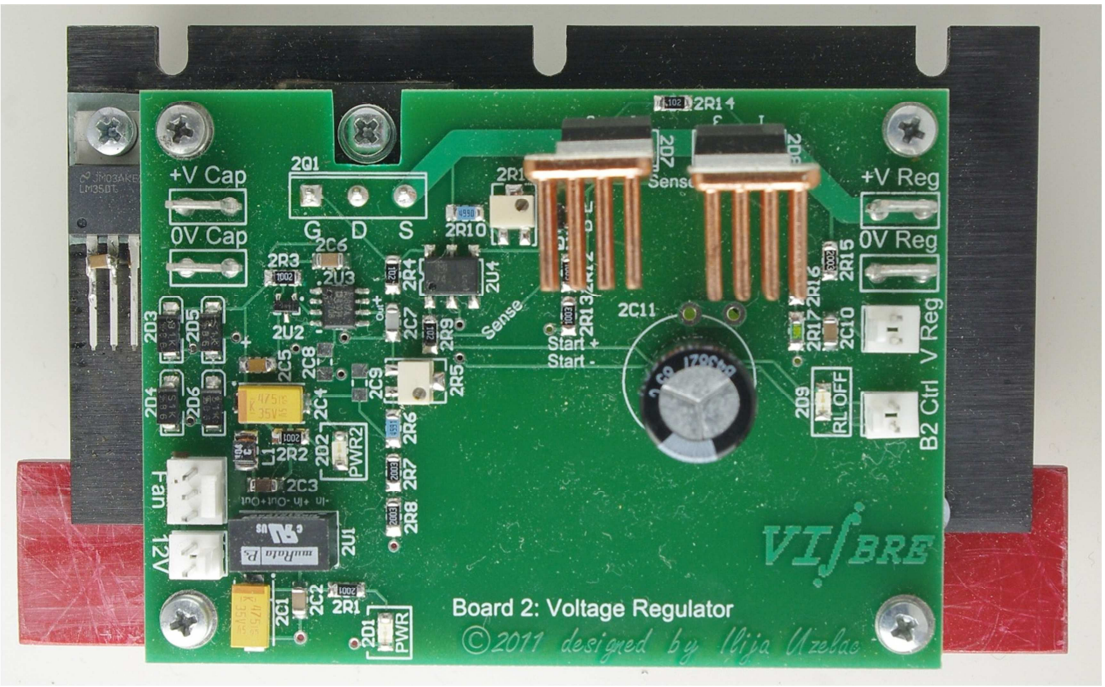

Figure 4.19H. Voltage Regulator.

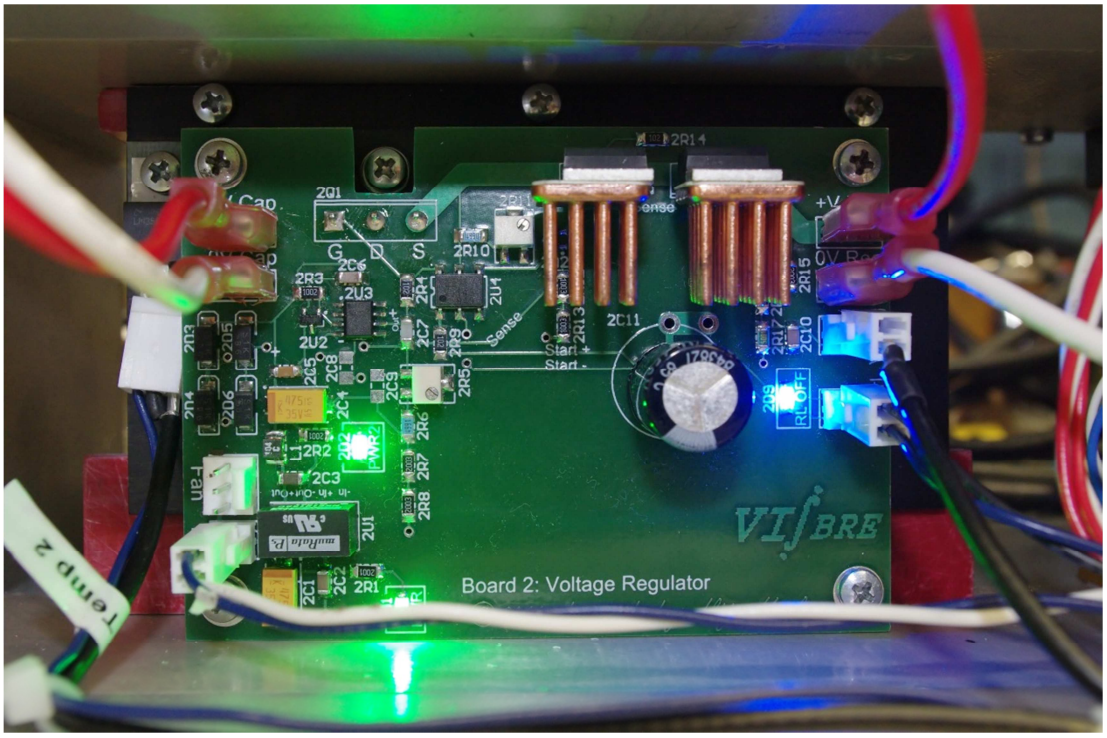

Figure 4.19I. Voltage Regulator assembled in the V2CC.

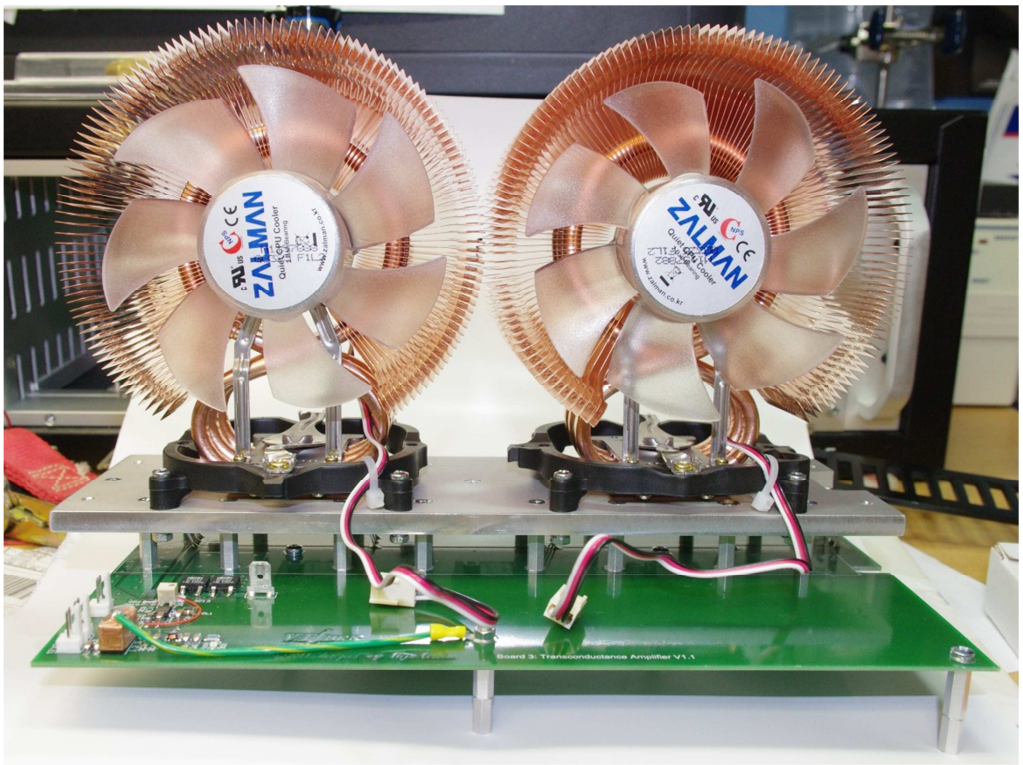

Figure 4.19J. Transconductance Amplifier.

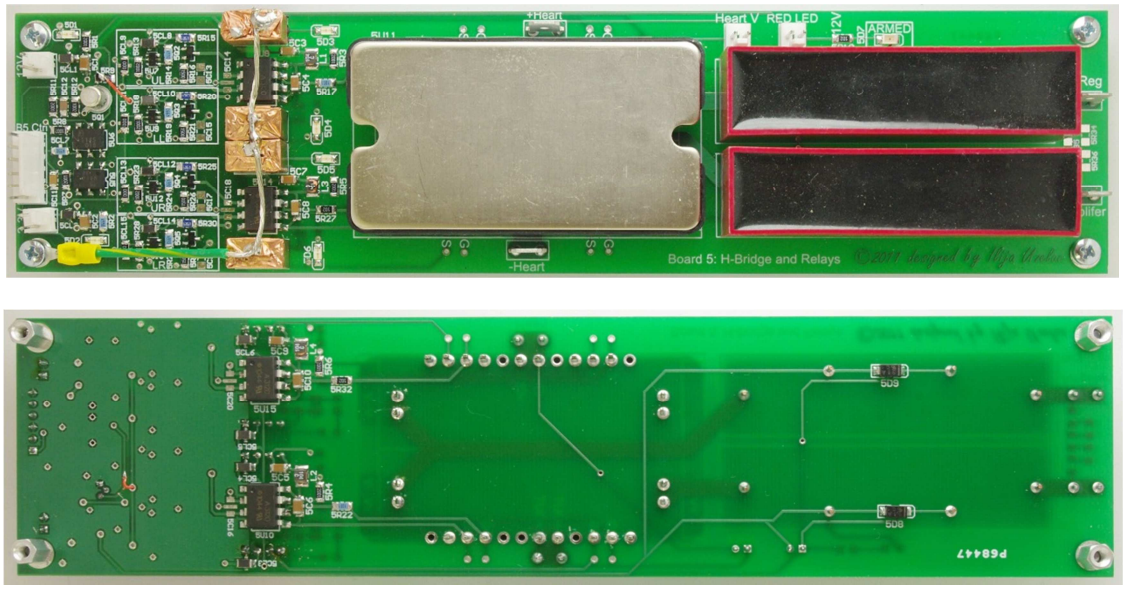

Figure 4.19K. Board with H-Bridge and reed relays.

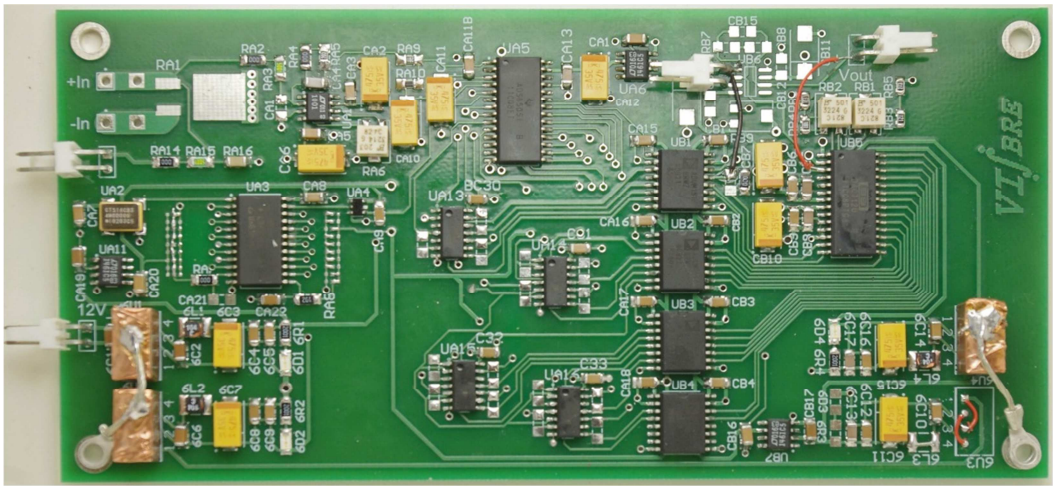

Figure 4.19L. Absolute Value Isolation Amplifier.

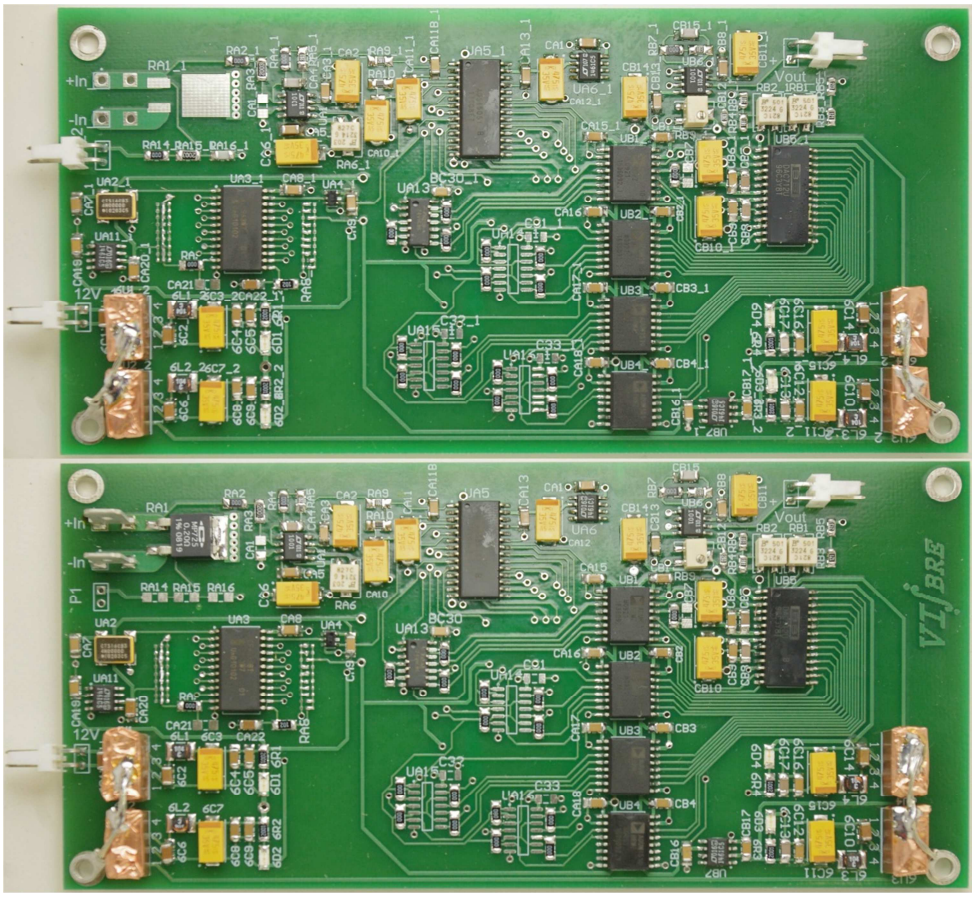

Figure 4.19M Voltage/Current Sense Isolation Amplifiers (upper/lower).

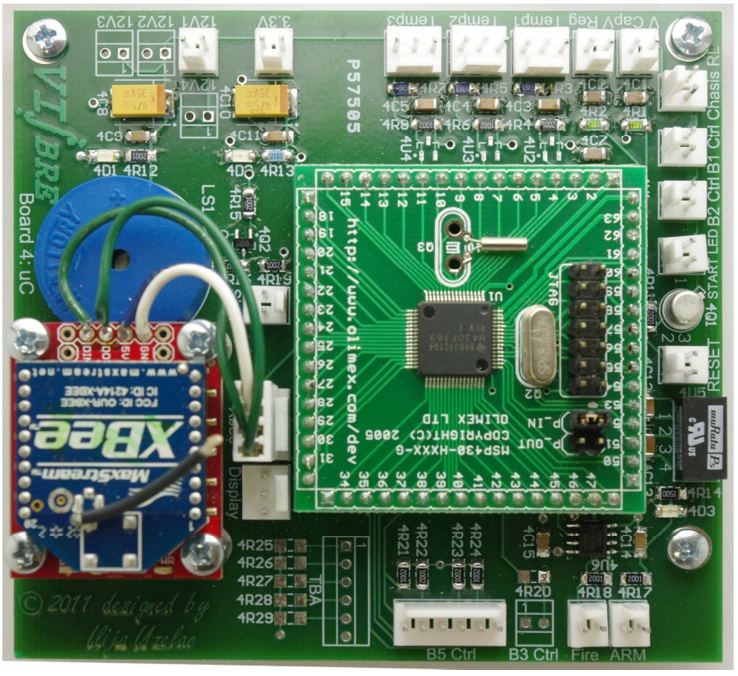

Figure 4.19N. Microcontroller Unit.

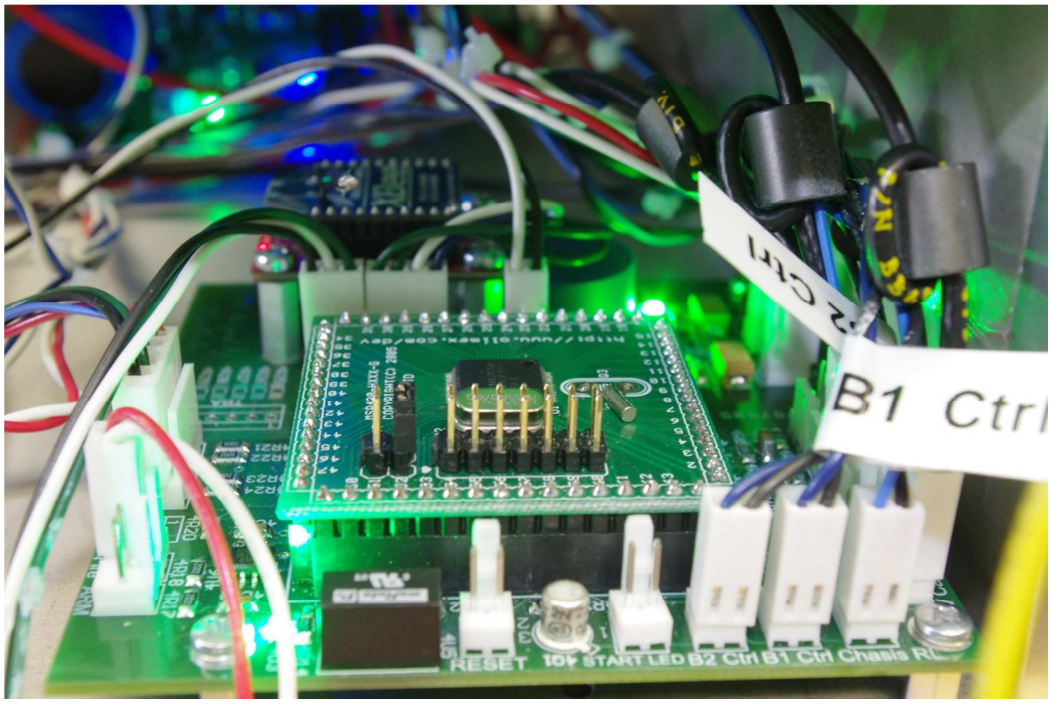

Figure 4.19O. Microcontroller Unit assembled in the V2CC.

CHAPTER V

EMBEDDED SYSTEM FOR FEEDBACK CONTROL*

Summary

The theory of cardiac control is presented in Chapter III, and two continuous feedback control methods are described: Delayed Feedback Control (DFC), and Proportional-Integrative-Derivative (PID) control. This chapter describes a practical implementation of these two control methods with the development of a Feedback Controller that is designed as an embedded system. Both control methods utilize the same hardware, and by simple reprogramming of the Feedback Controller, control methods can be easily switched. A feedback signal is calculated in real time from the emitted florescence from the surface of the isolated rabbit hearts stained with the photometric dyes and supported in a Langendorff perfusion apparatus, as described in the Methods section of Chapter II. Emitted fluorescence light is guided with the optical fibers towards the two photodiodes that are connected to the low noise transimpedance amplifiers. The resulting voltage signals are analog filtered, DC decoupled, digitized, and processed with the 16 MHz/16-bit MSP430F2618 microcontroller. The Microcontroller calculates the feedback signal, based on the specific control algorithm, and sends the feedback signal to the analog input of the V2CC, which is described in Chapter IV. Additionally, the microcontroller controls the *FIRE* and *ARM* inputs of the V2CC, and samples voltage and current outputs of the V2CC. Through a USB port it communicates with the PC where custom software that is different for each control method has additional control over the microcontroller, setting certain control parameters and providing the ability to store sampled analog values to the PC memory storage.

*Coauthors of this chapter are Mark Holcomb and John Wikswo

Introduction

Continuous feedback control methods, DFC and PID algorithms, are described in detail in Chapter III. For practical implementation of these methods, it is necessary to develop a control system that has the ability to observe the current state of the system and deliver the feedback control signal to the system, accordingly to the particular control algorithm. In our experimental setups, the dynamic systems targeted for control are the isolated rabbit heart in the Langendorff perfusion apparatus.

The electrical activity of the heart is usually mapped with the Di-4-Anneps voltage-sensitive florescent dye bound to the cardiac cell membranes with the chromophore end inside the phospholipid bilayer of the membrane. When excited with a green laser (532 nm), the emission spectrum is above 550 nm and any positive rise in the trans-membrane potential has associated with it a small red shift in the emission spectrum. With a band-pass filter in the red spectrum this shift will be seen as a decrease in the fluorescence intensity that is less than 10% of the baseline fluorescence. Our design goal was to have a dynamic range of at least 10-bits, meaning that we needed to resolve an intensity change as small as 1/10,000 of the baseline fluorescence. The emitted fluorescence light is guided towards a pair of photodiodes by two optical fibers facing opposite sides of the heart, and these two signals represent the local electrical activity on each side of the heart. In our design of the photodiode amplifier we used Hamamatsu S6428-01 photodiodes that have built in film filters with the spectral response shown in Figure 5.1. In our preliminary measurements we observed that with the baseline fluorescence, the photodiode current peak is around 100 nA. This means that our photodiode amplifier needs to be able to resolve currents as small as 10 pA. In terms of a bandwidth we set our design goals to have a bandwidth of 1.5 kHz.

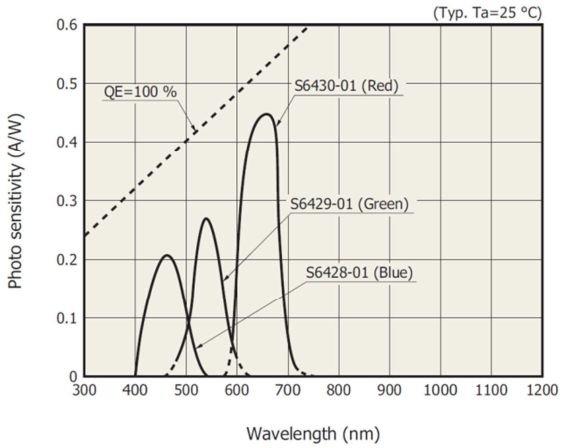

Figure 5.1. Spectral response of the Hamamatsu S6430-01 photodiode.

A transimpedance amplifier is traditionally designed with a single operational amplifier, whose gain is proportional to the value of the feedback resistor in Figure 5.2. The limitations of this design are mostly in the terms of the bandwidth and noise of the op-amp. The main sources of noise are the op-amp input voltage and current noise that follow a 1/f noise characteristic. Also, the choice of an op-amp with a low bias current is essential, because if the bias current is greater than the photodiode current, the signal from the photodiode will not be "visible". The influence of the bias current can be easily eliminated with the choice of the proper op-amp. In our photodiode amplifier design we used ultra-low bias-current op-amp LMP7721 (Texas Instruments) that has the maximal input bias current of a 20 fA at 25 °C.

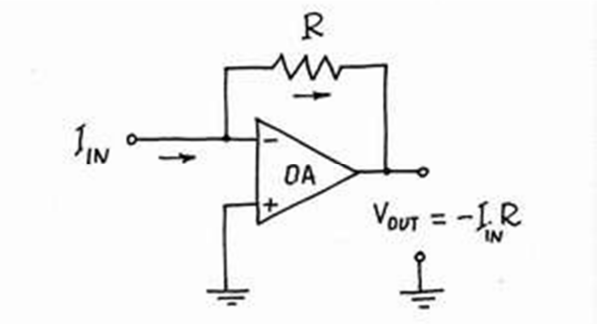

Figure 5.2. A traditional design of a transimpedance amplifier.

The input voltage noise of the op-amp along with the input voltage offset can be modeled as a voltage source between an op-amp inputs and this voltage source serves as limiting factor in the bandwidth of the transimpedance amplifier shown in Figure 5.1. Since any photodiode has a certain capacitance, a transimpedance amplifier will act as a voltage amplifier for the modeled voltage source with the gain of R/X_c, where R is the feedback resistor in the transimpedance amplifier, and X_c is the reactance of the photodiode capacitance. As the impedance of the photodiode falls with increasing as frequency, this means that the gain for the modeled voltage source "explodes" at high frequencies. To solve this problem, a traditional photodiode amplifier has a capacitance added across the feedback resistor that will create a pole in the transfer function, therefore canceling the zero introduced by the photodiode capacitance, Figure 5.3.

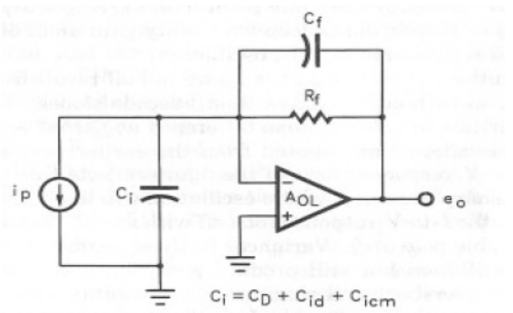

Figure 5.3. A traditional design of a photodiode amplifier. The photodiode is modeled as the current source in parallel with the photodiode capacitance[1].

The capacitance of large photodiodes can often exceed 100 pF. The Hamamatsu diode that we used has a capacitance of 200 pF, and therefore capacitance across the feedback resistor needs to be at least 200 pF. As the LMP7721 op-amp uses ±2.75 V power supply, and as the peak of baseline fluorescence current was observed to be around 100 nA, it follows that a resistance of the feedback resistor needs to be less than 27.5 MΩ. Our choice was the feedback resistor of 22 MΩ that sets the gain to 22 mV/nA. A transfer function of the photodiode amplifier in Figure 5.3 is given by:

$$\frac{R}{1 + jwRC}$$

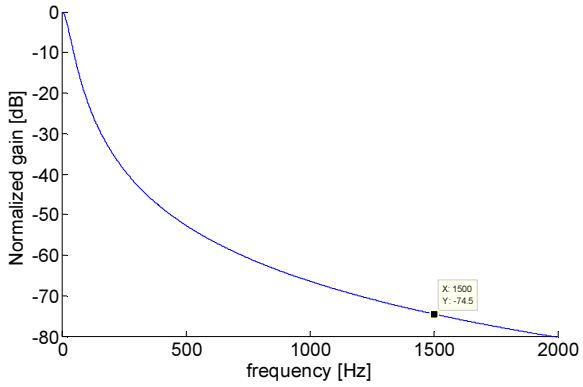

Figure 5.4. Plot of the transfer function (1). R=22 MΩ, C= 200 pF

For given values of *R* and *C,* the transfer function is plotted in Figure 5.4. At 1.5 kHz we see that the gain falls to -75 dB while our design goal was no more than a -3 dB. This indicated that we need to use a photodiode with a smaller area. One of the design golden rules is that it is better to use smaller area photodiode to limit its capacitance and to use a collimating lens instead, to increase signal to noise ratio, rather than increase the size of a photodiode. As our design was limited by the choice of the photodiode we needed to find solution to the problem in some other ways. One way is to polarize diode with the reverse potential that will increase the width of the depleted P-N junction in the photodiode and decrease the capacitance, but reverse potential increases drastically the dark current of the photodiode and therefore this was eliminated as the solution. One other solution is to keep the voltage across the photodiode constant, regardless of the photodiode current, and this is called the photodiode bootstrapping. In that way the effective voltage source between the op-amp inputs defined above as the noise, does not change the voltage across the photodiode capacitance. It sees theoretically only the impedance of the photodiode that is in the GΩ range and therefore does not produce any noise offset at the op-amp output. A detailed schematic of the photodiode amplifier is presented in Figure 5.5. Bootstrapping is achieved by N-type Enhanced-JFET Q1A. It acts as a current source

and is powered from a precise and multiple-stage actively filtered power supplies providing 4 and -2 V respectively. As the JFET acts as a current source and as variations of the potential on its gate due to the modeled voltage source across an op-amp input are very small, there will be the same variations of the potential on the source of the JFET. As the gate and the source are across the photodiode, this means that the photodiode is held at a constant potential. Practically the JFET has gate input capacitance that that is ~3 pF and this capacitance will be seen by the modeled voltage across the op-amp input; therefore we used capacitance of 4.7 pF across the feedback resistor. Both capacitances set the attenuation in the bandwidth of -3.4dB at 1.5 kHz.

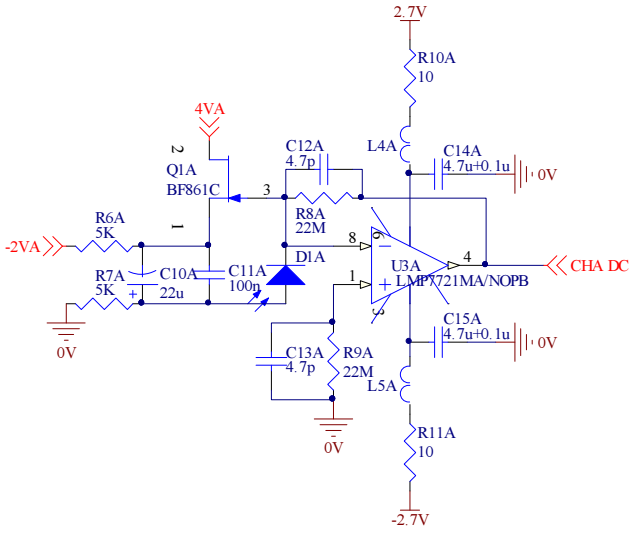

Figure 5.5. Detailed schematic of the photodiode amplifier.

Theory of Operation

For a simple analysis the Feedback Controller is divided into three sections: analog signal processing, digital signal processing, and the PC control program.

- In the analog section, there are six input analog signals (Ch A/B DC, Ch A/B AC and V2CC voltage and current sense) and two output analog signals (control and voltage reference).

- In the digital section, the microcontroller performs A/D conversion on six analog input signals, generates one output analog signal, processes two internal input digital signals and generates two external digital signals, and communicates with the PC via a USB interface.
- The PC program controls and communicates with the microcontroller. It sends certain parameters to the microcontroller and has the ability to save all 7 digitized analog signals along with all relevant parameters.

The naming of signals as input or output is from perspective of the microcontroller. Many of the signals are intrinsic to the embedded system and those that serve for "communication" out of the embedded system are referred as external.

Analog Input Section:

A block diagram of the analog input section is presented in Figure 5.6. There are four analog signals, named as Ch A/B DC and Ch A/B AC.

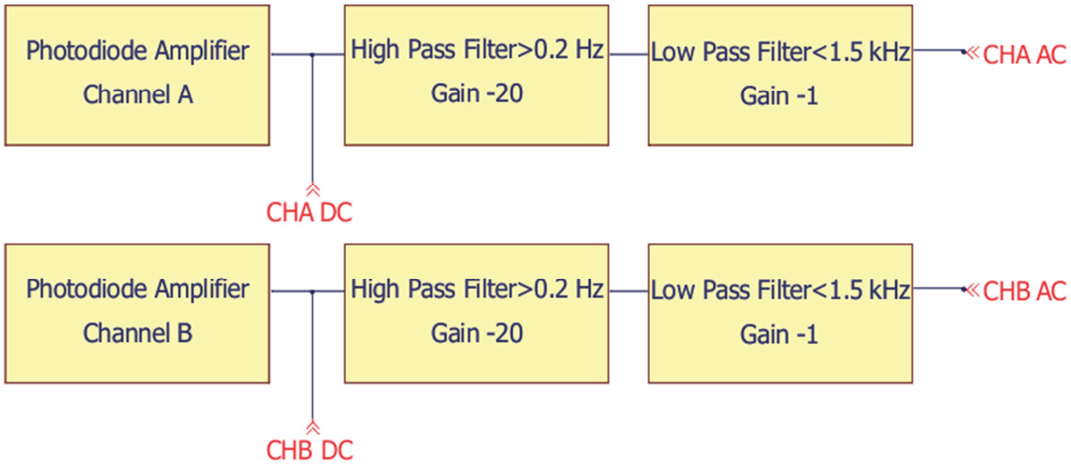

Figure 5.6. Block schematic of the analog input section. The outputs are in red.

The photodiode trans-conductance amplifier has a maximal output voltage of 2.68 V, noted as CHA/B DC. The signal from the photodiode amplifier that represents electrical activity on the surface of the heart is single-ended and unipolar and moreover we are interested only in the AC part that are the changes in fluorescence intensity. With the high pass filter, the AC

component is extracted and multiplied by a inverting gain of -20. The purpose of adding extra gain in the second stage is that the AC signal are less than 10% with respect to the baseline DC signal and they will be subsequently digitized with the 16-bit A/D. The high pass filter is designed as a second order active filter in the multiple-feedback-topology (MFT) with -3 dB cut-off at 0.2 Hz, Figure 5.7A. In the third stage, signals are filtered with the third order active MFT low pass filter with -3 dB at 1.5 kHz, as shown in Figure 5.7B. Filters in in MFT are designed with an inverting amplifier, hence gain is always negative. The transconductance amplifier also has a negative gain, and as the fluorescence signal decreases with an increase of the transmembrane potential, the CHA/B AC have positive action potential upstrokes and expected amplitudes are up to +5V.

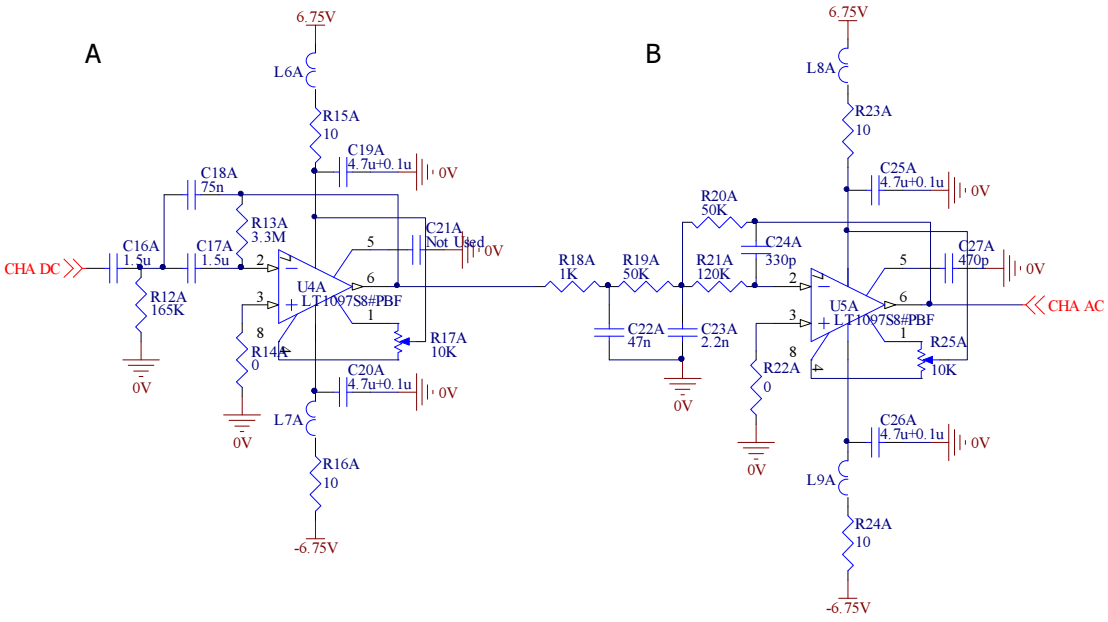

Figure 5.7. Detailed schematic of the active filters. A) MFT second order high pass filter. B) MFT third order active low-pass filter.

In the analog section there are additionally two analog external input signals that, named V sense and I sense. These analog signals represent voltage and current measurements, respectively, from the V2CC output.

In summary, the 6 analog input signals are as follows:

-CHA/B DC single-ended and unipolar, representing the total fluorescence signal in the range of [0,2.68] V, with a bandwidth of 1.5 kHz

-CHA/B AC single-ended and bipolar representing changes in the fluorescence in the range of [-5,5] V, with a bandwidth of 1.5 kHz

-V Sense, bipolar and differential, representing voltage measurements from the V2CC output, where 1 V=40 V on the V2CC output. The range is [-5,5] V and the bandwidth 1 kHz

-I Sense, bipolar and differential, representing current measurements from the V2CC output, where 1V=1A on the V2CC output. The range is [-5,5] V and bandwidth is 1 kHz

All analog signals are digitized with the LTC1859 16bit A/D convertor, with an input range of [-5,5] V for bipolar and [0,5] V for unipolar signals, as shown in Figure 5.8. Timing diagrams for the operation of the A/D and as well as the digital readout are serviced by the microcontroller that will be described in the Digital Section.

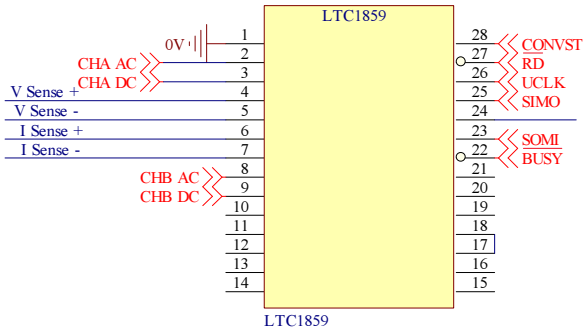

Figure 5.8. 16-bit A/D convertor.

Digital Section:

The central part of the digital section is organized around a MSP430F2618, 16MHz/16bit microcontroller, shown in Figure 5.9. The role of the microcontroller is to communicate with the A/D converter, communicate with the PC via a USB port and to communicate with the V2CC, sending to it two digitals and one analog signal. The summary of all MSP connection and their functions is given in Table 5.1.

- The microcontroller communicates with the A/D converter through the USCI_B0 port via 3wire SPI bus (SOMI, SIMO and UCLK digital lines) for a data readout, and 3 digital control lines (CONVST, $\overline{RD}$ and $\overline{BUSY}$) that provide necessary timing diagrams.
- Communication with the PC is through USCI_A0 port (Rx, Tx, RTS, CTS digital lines), configured as UART over the additional USB interface board (Sparkfun CP2102).
- There are 2 input digital signals named $\overline{Batt1\ Ind}$ and $\overline{Batt2\ Ind}$. When these signals are activated it is an indication that corresponding battery is discharged below the operating level.
- There are two external output digital signals named Arm and Fire that serve to enable the output stage of the external defibrillator box, *i.e.*, the reed relays and the H-Bridge.

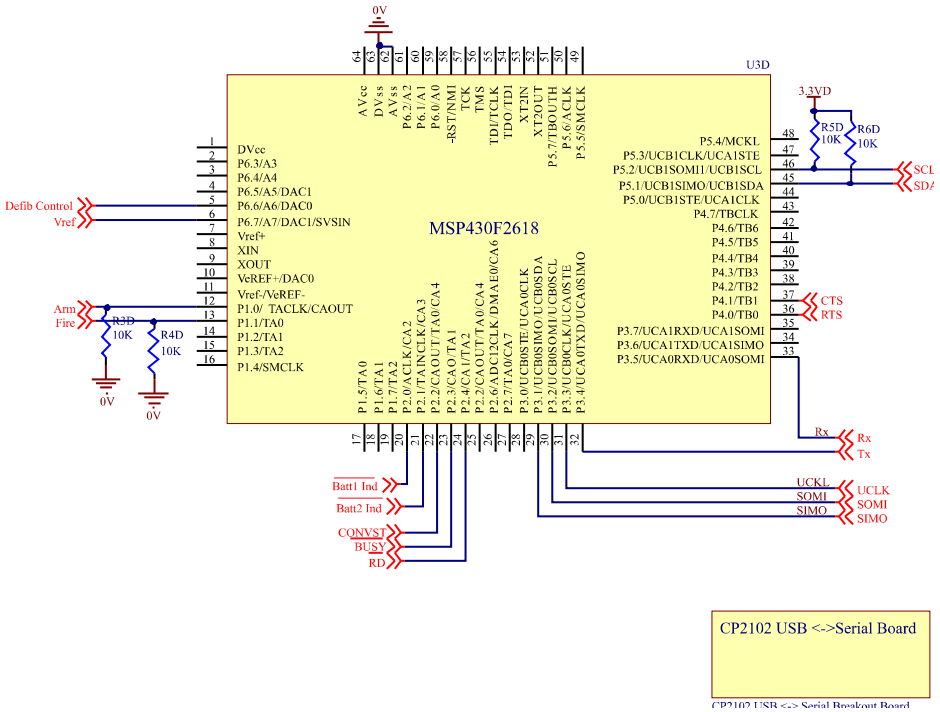

Figure 5.9. Connections for the MSP430F2618, 16MHz/16bit microcontroller.

Table 5.1. List of all MSP connections and functions.

Name	Pin	Dir	Type	Active High/Low
USCI_A0				
TX	P3.4	Out	Digital	N/A
RX	P3.5	In	Digital	N/A
RTS	4.0	Out	Digital	Low
CTS	4.1	In	Digital	Low
USCI_B0				
SIMO	3.1	Out	Digital	
SOMI	3.2	In	Digital	
UCLK	3.3	Out	Digital	
USCI_B1				
SDA	P5.1	bi	Digital	N/A
SCL	P5.2	bi	Digital	N/A
CONVST P2.2	Out	Digital		High
$\overline{\text{BUSY}}$	P2.3	In	Digital	Low
$\overline{\text{RD}}$	P2.4	Out	Digital	Low
Arm	P1.0	Out	Digital	Low
Fire	P1.1	Out	Digital	Low
$\overline{\text{Batt1 Ind}}$ P2.0	In	Digital		Low
$\overline{\text{Batt2 Ind}}$ *P2.1*	In	Digital		Low
Defib Signal	P6.6	Out	Analog	N/A
V Ref	P6.7	Out	Analog	N/A

Output Analog Section:

The output analog section the Feedback Controller generates the feedback signal that is used as the input waveform of the V2CC that delivers the perturbation shocks to the heart. The analog signal is first calculated in the microcontroller as the digital representative using specific feedback control method and then subsequently output as the unipolar analog signal using internal 12-bit DAC_0 D/A converter of the microcontroller. Another analog output signal from the microcontroller, Vref, is generated by the internal 12-bit DAC_1. It is needed to convert the unipolar Defib Control signal to bipolar, with the additional conditioning electronics shown in Figure 5.10 The upper op-amp shifts the unipolar signal to bipolar, while the lower op-amp serves as a buffer/driver for the coaxial cable. SCL and SDA are I2C bus signals on the USCI_B1

port of the microcontroller. Their purpose is to control the digital pot AD5241. The digital pot has 256 counts in the equidistant range from 0 to 10 KΩ. Its purpose is to control the gain of the analog output signal rather than performing software gain control prior the D/A. As the final output, the Debif Control signal is differential and bipolar in the range of [-5,5] V.

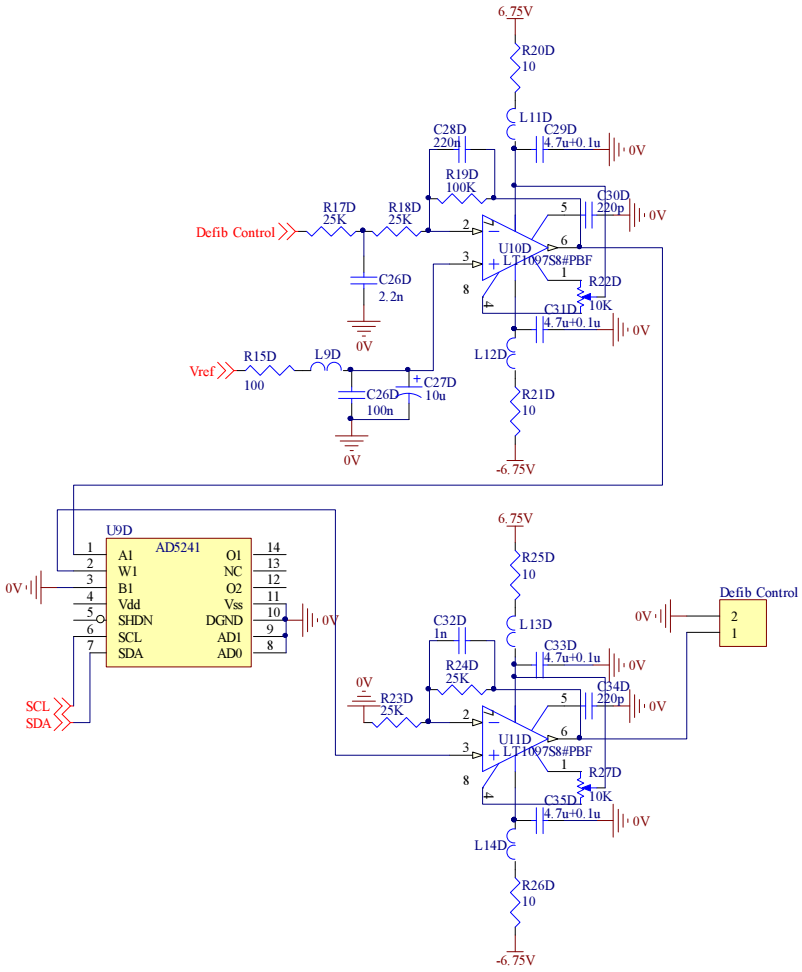

Figure 5.10. Output analog section.

Algorithm for the Microcontroller:

In the cardiac control feedback experiment we used two control methods, Delayed Feedback Control (DFC) in the temporal domain and Proportional-Integral-Derivative (PID) control from phase space. The detailed DFC algorithm is presented in Figure 5.11. As both algorithms mostly differ in the way how feedback signal is calculated, the algorithm for the PID control is summarized below.

The PID controller parameters have to be defined during regular sinus rhythm in a process of "calibration" as:

- Sample signals from the photodiodes representing electrical activity on the surface of the LV and RV, named A and B respectively, for a couple of seconds, and from the obtained samples, calculate the normalization multipliers for each signal separately.
- Normalize obtained sets of samples, and perform a linear regression $B = B(A)$ to determine the analytical form of the linear fit line, its slope m and intercept b.

$$B = m \cdot A + b,$$

$$m = \frac{\sum_k (A_k - \overline{A})(B_k - \overline{B})}{\sum_k (A_k - \overline{A})^2}$$

$$b = B - m * \overline{A}$$

- For each pair of samples(A_k, B_k), calculate the normal distance from a fit line.

$$d_k = \frac{B_k - m * A_k - b}{\sqrt{m^2 + 1}}, \; k=1..N$$

- Calculate the mean value D and standard deviation σ from the obtained set of distances.

$$D = \overline{d}$$

$$\sigma = std(d)$$

Empirically establish the threshold as a number of standard deviations. Once the initialization procedure is performed, VF is induced and the perturbation shock termed *DEFIB* is calculated in real time as follows:

- After each sampled pair (A_k, B_k), multiply samples with the normalization constants, and calculate the normal distance d_k from a fit line.
- If the distance is greater than the predefined threshold, apply a perturbation shock as:

$DEFIB_k = K_D\{ (d_k - DT) + \frac{1}{T_i} T \sum_{n=1}^{k} (d_n - DT) + T_d \frac{d_k - d_{k-1}}{T} \}$ $k \geq 2$, where $K_D, T_i, and\ T_d$ are user-defined parameters or weight factors for the PID controller configuration. T is the sampling time interval. DT is a distance threshold expressed in a number of standard deviations.

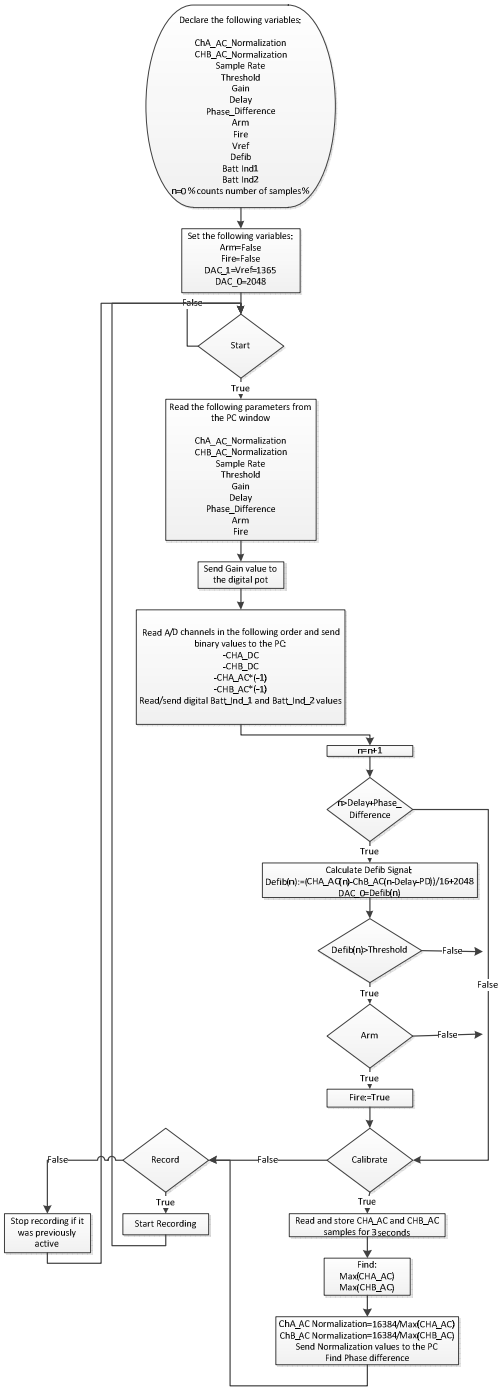

Figure 5.11. DFC algorithm for the microcontroller.

PC Control Program

The PC control program is different for both control methods, although many functions are the same. The main purpose of the control program is to set the necessary Feedback controller parameters and record digitized analog values to the PC memory storage along with the digital representative of the *Defib* signal and status of the *ARM* digital output signal. The analog values are: ChA/B DC, ChA/B AC, V_Sense, I_Sense. The sampling speed of the digitized analog valued can be choosen from the range of 500 sps to 4000 sps in the case of the DFC algorithm and in the range of 500 sps to 2000 sps in the case of the PID algorithm.

PC Control Program for the DFC Feedback Controller

The PC control program for the DFC Feedback Controller is presented in Figure 5.12.

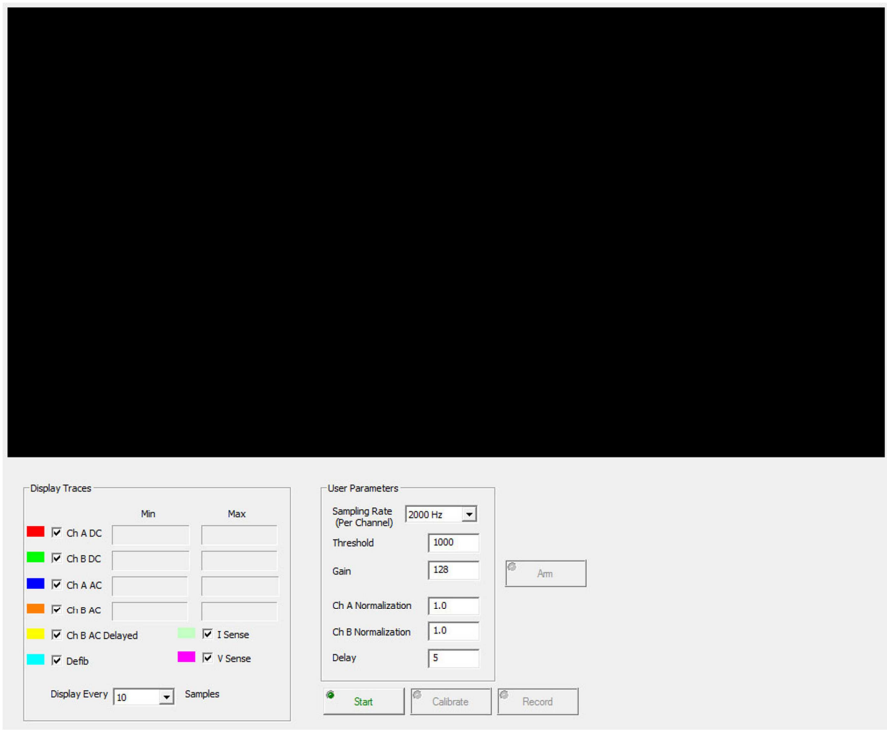

Figure 5.12.Screenshoot of the control program for the DFC Feedback Controller.

In the subpanel Display Traces, all six analog values along with the *I_Sense* and *V_Sense, Defib* signal and its delayed version can be selected to be displayed as traces in the upper black window. Their minimal and maximal values are displayed in the corresponding boxes on the right, for the duration of one trace. In the pull-down menu at the bottom the user has the ability to select that every n-th sample is actually displayed in the trace window.

In the subpanel User Parameters, user has the ability to select the sampling rate, set the threshold for the calculation of the *Defib* signal, set the gain for the digital potentiometer in the analog output section, set the normalization scale factors for both channels, and set the value for the delay. The normalization factor is calculated automatically during the calibration mode, but the user has the ability to adjust them additionally.

On a press of the Start button, the control program reads all analog values and displays then in the trace window. The Calibrate button is only active if the start button is pressed. On the press of the Calibrate button, the microcontroller samples ChA/B AC analog values for couple of second to determine the normalization constants. The Record button is only active if the Start button is pressed, and on press of the Record button, the PC program saves to the PC storage all variables listed above. The ARM button serves to generate active digital output from the Feedback Controller that controls the ARM digital input of the V2CC. On a press of the ARM button, the V2CC reed relays will be activated

PC Control Program for the PID Feedback Controller

The PC control program for the PID Feedback controller is presented in Figure 5.13. It shares many common features with the control program for the DFC Feedback Controller so only differences will be emphasized.

In the User Parameters subpanel, besides the normalization scale factors the user has the additional ability to offset both signals.

- AB samples indicates that the microcontroller should take a certain number of consecutive samples at the sampling rate of 32 ksps and average them to lower the digitization noise.
- Cal Rep roughly represents twice the number of seconds of the duration of the calibration procedure.
- Battery 1 and Battery 2 are indicators of the level of the batteries.
- VSense to Defib is used for debugging and when active, any analog signal present on the VSense analog input will be forwarded to the Defib output
- Fit Parameters subpanel displays values of the linear fitting when the Fit button is pressed.
- In the PID parameters subpanel user has ability to enter the parameters for the PID controller.
- The window on the right represents in real time the 2D phase space as Ch B vs Ch A. The width of the red stripe represents the standard deviation (sigma) of the linear fit line.

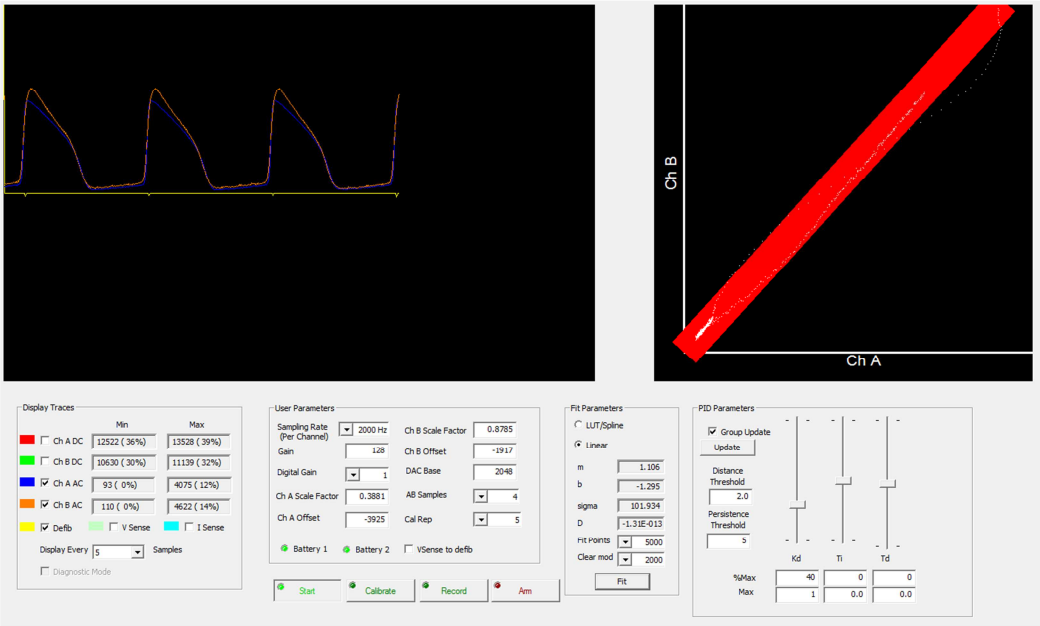

Figure 5.13.Screenshoot of the control program for the PID Feedback Controller.

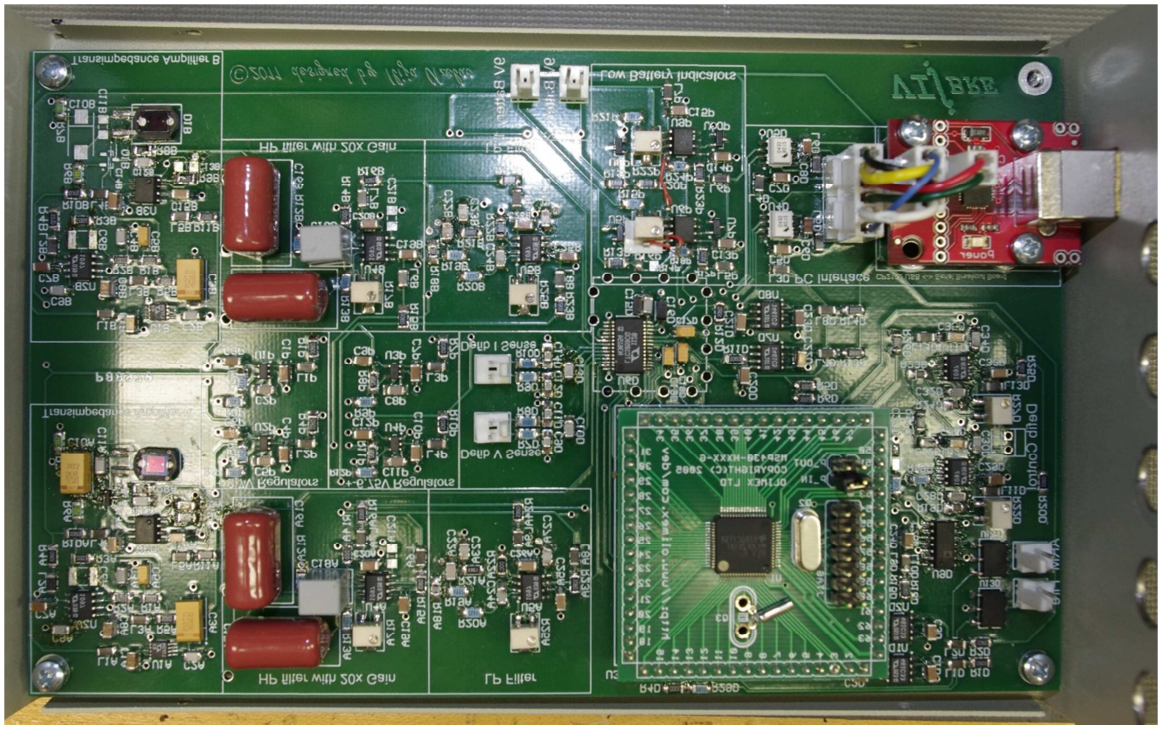

Figure 5.14. Photo of the Feedback Controller.

References

1. Graeme, J. *Photodiode Amplifiers: OP AMP Solutions*. (McGraw-Hill: 1995)

CHAPTER VI

STABILIZATION OF CHAOTIC SPIRAL WAVES DURING CARDIAC VENTRICULAR FIBRILLATION WITH DELAYED FEEDBACK CONTROL*

Summary

In a phase space, ventricular fibrillation (VF) can be represented as closed loop trajectories with different and unpredictable future orbit periods, and we therefore refer to these orbits as random and unstable. Since the heart is a real dynamic system, these orbit periods are naturally limited to a certain range and moreover have a non-uniform distribution. The non-uniform distribution means that some orbit periods are more preferable or naturally supported by the system than others. Therefore, cardiac dynamic can never be fully chaotic since fully chaotic dynamic will have a random distribution of orbit periods. In this chapter we studied how unstable orbit periods during VF can be stabilized with external continuous feedback control. As a method of external control we utilize external continuous delayed feedback control (DFC), described in the Methods section of Chapter III. With DFC, "random" orbit periods during VF can be stabilized in a way such that DFC supports the existence of only particular orbit periods while other orbit periods are suppressed. From the theory of DFC, the embedded time delay is defined as a delay through the feedback controller that should match the orbit period targeted for stabilization. In reality we have observed that there is an additional delay through the system due to the finite conduction velocity in the heart and the time scale in which the feedback system operates. In our terminology, we refer to delay through the feedback control as the external delay and delay to the system itself as the intrinsic delay. Due to intrinsic delay, in our experiments we had to use a shorter external delay than the orbit period targeted for stabilization.

* Coauthors of this chapter are Mark Holcomb, Richard Gray and John Wikswo

Our continuous feedback control is using a feedback controller, presented in Chapter V, which is programmed as a DFC controller. The DFC controller calculates in real time feedback control signal that is the current state of the system minus the state of the system delayed with the predefined delay. A continuous feedback control signal, in the form of a series of defibrillation shocks, was delivered inside the ventricles of a rabbit to create perturbation current shocks, delivered with the V2CC, which is described in Chapter IV.

The experiments were performed on isolated rabbit hearts in Langendorff perfusion, and the optimal external delay was determined experimentally rather than being derived from the dynamics of the VF. Also, the feedback gain, *i.e.,* the strength of the feedback perturbation shock was adjusted from experiment to experiment empirically to achieve the minimal feedback gain that led to stabilized VF. We have observed that stabilization of VF works best when the external delay is set between 100-105 ms. DFC methods treat the system as a black box and no further knowledge of the system is needed, but through practical implementation of DFC algorithms we were able to study certain aspects of cardiac control. From these studies we constructed many hypotheses and gained a better understanding of how VF can be controlled and converted from a dynamic that appears to be chaotic to one that is organized. This understanding gives us a clear direction and raises many important questions that will be answered in proposed future experiments. Also, through a better understanding of cardiac control and by exploring the limitations of the current implementation of the DFC method, we see how to improve DFC algorithms in future experiments.

Introduction

The theory of cardiac control is presented in Chapter III. Here, however, we will summarize the general concepts and main points of cardiac control theory.

During VF, the cardiac dynamic exhibits chaotic behavior due to the presence of spiral waves in the heart's electrical activity. Despite being studied extensively, spiral waves are not

easy to terminate. At present the only practical means to automatically stop VF is to deliver a single, strong electric shock to the entire heart using defibrillators or to deliver multiple low-energy shocks in a novel Low-Energy Anti-fibrillation Pacing (LEAP) technique[1]. The spiral wave has at its center an entity known as a phase singularity (PS), which acts as an organizing center in the area that surrounds it, where the spiral wave is formed. (Phase singularity theory is presented in Chapter I, while its role in VF and cardiac control is discussed in Chapter III.) It is important to remember that in the border zone areas between the spiral waves and the rest of the heart, the cardiac dynamic tends to be chaotic during VF. These areas are targeted for cardiac control with low energy perturbation shocks.

Currently, there is a lack of systematic and unifying study that would connect detection of phase singularities and the associated chaotic dynamic with the optimal shape, amplitude, timing and duration of defibrillation shocks, or, as in our study, perturbation shocks. Moreover, the mechanisms by which defibrillation shocks terminate VF are currently not well understood. Our defibrillation approach considers the heart as a dynamic system that exhibits spatiotemporal chaotic behavior in VF. With the phase space approach and by using methods from control theory, we aim to arrive at a better understanding of cardiac control that would ultimately lead to novel defibrillation methods. Our ultimate goal is to achieve global control of spatiotemporal chaos through local control with only small perturbations of the system.

On making the transition from theory to implementation, we were faced with certain practical obstacles, and one of them was that the DFC method treats the dynamical system as a point or a system without any spatial dimension, while in reality that is not often the case. The heart exhibits spatial dimensions, and as a consequence any perturbation of the system takes time to propagate from the perturbed area to the area that is being monitored by the feedback control system. In other words, perturbation of the system is not immediately observable, and as a consequence there is an additional delay that we refer to as intrinsic delay. DFC theory states that the total delay through the system represents the period of the orbit targeted for stabilization. Therefore, due to intrinsic delay we had to set the external delay smaller than the

period of the orbit that is targeted for stabilization, so that the sum of delay through the feedback controller and intrinsic delay equals the period of the orbit targeted for stabilization. From the perspective of chaos control theory, we are trying to control chaos that exhibits spatial-temporal dimensions, and that is a special class of chaos control.

Methods

New Zealand White rabbits' hearts were isolated and experiments were performed in a Langendorff perfusion system, as described in the Methods section of Chapter II, and shown in Figure 6.1. Hearts were stained with voltage-sensitive dyes (Di-4-Anneps), and fluorescence was excited by a Xenon arc lamp. Light was filtered through an excitation filter (530-540 nm). Two optical fibers were placed on the opposite sides of the heart, facing the LV and RV to collect emitted fluorescence from the heart's surface and to quide light towards the photodiodes with band-pass filters of 600-700 nm in the Feedback Controller as shown in Figure 6.2. The Feedback

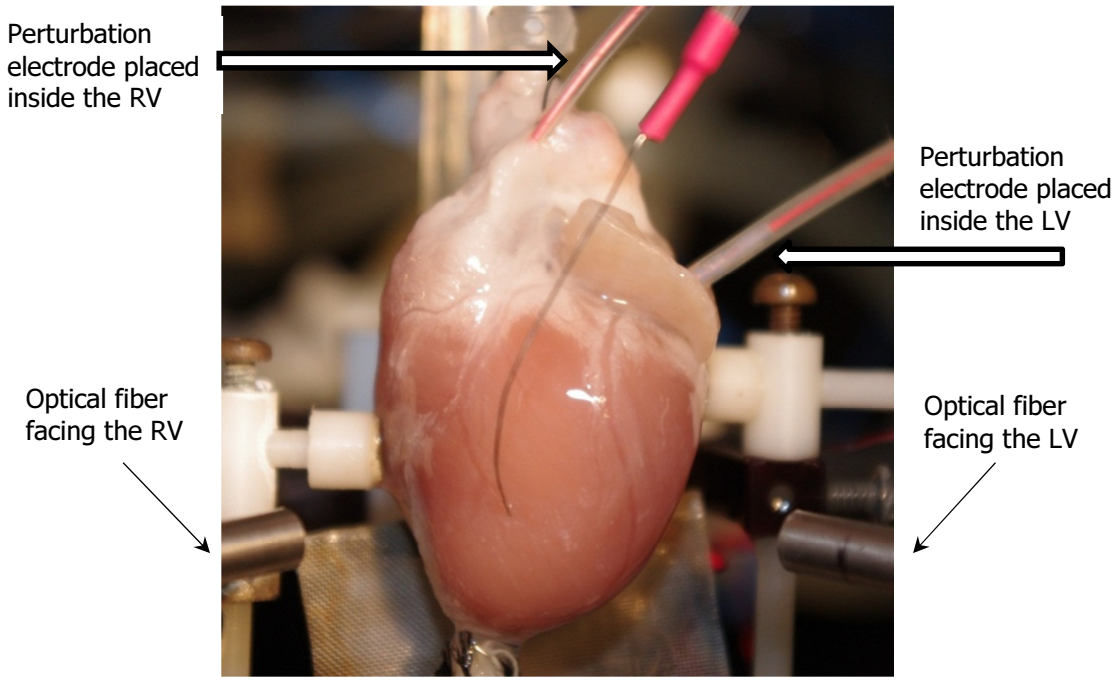

Figure 6.1. Isolated rabbit heart in Langendorff perfusion, with perturbation electrodes inserted into the LV and RV and optical fiber facing the LV and RV.

Controller is described in Chapter V and consists of a microcontroller that processes these optical signals in real time and sends a calculated feedback control signal to the V2CC (Chapter IV), which in turns delivers the perturbation shocks to the heart in the form of an electrical current. In our experimental setups we used coil electrodes in both the RV and LV.

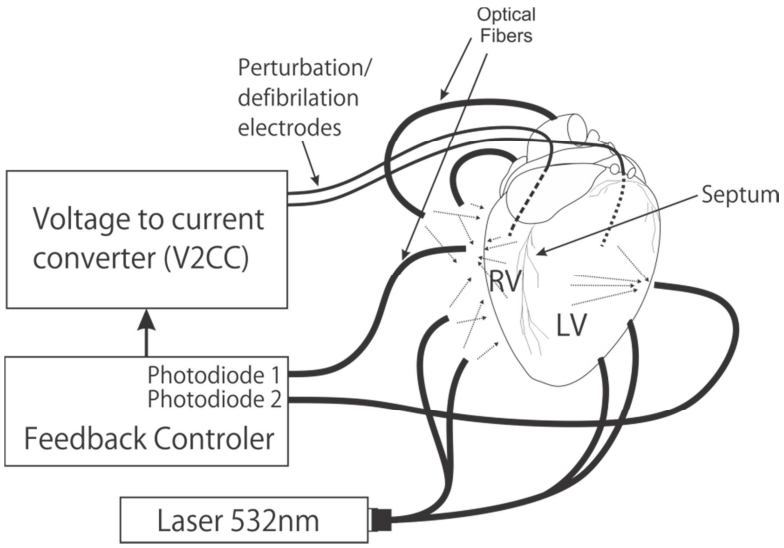

Figure 6.2. Feedback control system.

The DFC method is discussed in detail in Chapter III. Briefly, the algorithm of DFC is as follows:

- Two photodiode signals are subtracted from each other, resulting in an external signal $y(t)$ of a chaotic system (representing the cardiac dynamic in VF)
- The signal $y(t)$ minus its delayed version $y(t-\tau)$ is fed into the V2CC, which delivers the perturbation shock in the form of the electrical current to the heart.

The algorithm for the feedback controller is presented in detail in Chapter V. Briefly, DFC controller parameters have to be defined during regular sinus rhythm in a process of calibration. Signals from the photodiodes representing electrical activity on the surface of the LV and RV, named A and B respectively, are sampled for a couple of seconds, and from the obtained samples, calculated are the normalization multipliers for each signal.

After calibration, VF was induced by train of pacing stimuli varying between 80 and 110 ms, or by 40 Hz AC current of 50 mA, delivered to the heart as current with the V2CC, driven by the wave form generator. Along with optical traces, analog values representing voltage and current delivered to the heart were sampled as well. All analog values were sampled at 4 Ksps and recorded during sinus rhythm and during applied control for subsequent analysis.

The DFC controller communicates via USB protocol with the custom PC software, described in detail in Chapter V. Briefly, custom PC software allows visualization in time domain of the optical traces. The user has ability to enter manually the delay time (external delay or embedded time) and the threshold, and to record the following signals: Electrical activity from the LV, electrical activity from the RV, the *DEFIB* feedback signal, and current and voltage signals from the V2CC output. The reed relays of the V2CC were controlled manually via the Arm button in the control program. The PID controller additionally controlled the *FIRE* input of the V2CC, setting it to "active" whenever the calculated feedback signals exceeds the user defined threshold.

External delay was empirically determined from our experiments as a delay upon which the feedback control system was able to stabilize VF. Feedback gain, that is, the strength of the perturbation shocks, was empirically obtained as the minimal gain needed for the applied control to achieve stabilization. It is important to emphasize that any subsequently induced VF on the same heart may not necessarily exhibit the same pattern as previously induced VF, and that creates difficulties in repeating experiments in order to retest certain control parameters. Therefore, successful VF control is best described as a probability to achieve stabilization under defined conditions. Nonetheless, this does not limit the DFC method; rather, it is an indication that experimental procedures are imperfect since we are using a relatively simplistic and rigid algorithm. Moreover, experiments can differ due to other variables such as placement of the perturbation electrodes and their size and shape; placement of optical fibers and defining the size of the area that will be monitored by optical fibers; the heart itself; and any limitations of the analog and digital electronics due to laser, sensor or amplifier noise.

Results

In the DFC control experiments, 11 New Zeeland white rabbits were used. We recorded optical traces that represent cardiac electrical activity on the surface of the heart, from the LV and RV, and subsequently processed them to study the cardiac dynamic during various selected intervals. These intervals include induced VF, applied feedback control, and eventually restored sinus rhythm. Intervals with the applied feedback control can be further divided into the following subintervals: control with no VF stabilization, control with achieved VF stabilization, and control with loss of VF stabilization. These particular subintervals are not necessarily present in every control experiment, with the exception of the first subinterval of control with no VF stabilization. Sinus rhythm interval was always present if it was preceded with stabilized VF.

Herein we present and analyze optical traces in the time and space domain, as well as in the frequency domain. During applied control, we calculated the energy and the instantaneous power delivered to the heart. The sampling rate was 4 ksps, while delay through the feedback controller and strength of the perturbation shock were varied in each experiment as unknown parameters that were experimentally determined. We now present four control experiments with external delays of 100, 105, 110 and 90 ms, respectively, from the sixth heart. These external delays are the major parameters upon which the ability of the feedback system to stabilize VF depends.

Figures 6.3-6.7 represent a successful control experiment with the external delay of 100 ms where feedback control was applied twice. In the first attempt shown in Figure 6.3A, VF was stabilized, but stabilization was not sustained and was subsequently lost. In the second attempt on the same heart (Figure 6.3C), stabilization was achieved, although it was not perfectly stable and was even transiently lost. Nevertheless, feedback control was turned off at the moment when stabilization was achieved, and, as was hypothesized in Chapter III, sinus rhythm resumed, without further intervention. Panels (B) and (D) show a zoomed-in view of the transition from

unstable-to-stable VF during applied control. In both cases it can be observed that transition was gradual with asymptotical envelopes. Panel (E) shows the transition into sinus rhythm when control was turned off. During this transition it was always observed that a stable sinus rhythm was preceded by a couple of faster beats. In Figure 6.4 the phase space is constructed as a 2D space as RV vs LV. Panel (A) shows the first unsuccessful control attempt , and Panel (B) shows the second successful control attempt. Figure 6.5 represents orbit periods of the corresponding phase space trajectories from Figure 6.4. Fourier spectra are presented in Figure 6.6 and normalized to the highest peak that occurred during the second control attempt. Panels (A), (B) and (C) represent the first control attempt and panels (D) and (E) represent the second control attempt. In Figure 6.7, panels (A) and (C) represent instantaneous power delivered to the heart, while panels (B) and (D) represent delivered energy over time in the first and second control attempts, respectively.

The second and equally successful feedback control experiment, with a feedback delay of 105 ms in the same manner as the first experiment, is presented in Figures 6.8-6.12. Before control was applied, the heart was in sustained VF, although that interval was not recorded. Control was terminated during stabilized VF and termination led to sinus rhythm.

Figures 6.13-6.17 present the third and partially successful feedback control experiment with a feedback delay of 110 ms, again in the same manner as the first experiment. Before control was applied, the heart was in sustained VF, although that interval was not recorded. VF was stabilized, but stabilization was subsequently lost. Control was terminated during unstable VF that led into complex monomorphic ventricular tachycardia (MVT). This experiment was partially successful since, although VF was stabilized, stabilization was lost.

The fourth and unsuccessful control experiment, with a feedback delay of 90 ms, is represented in Figures 6.18-6.21. VF was not stabilized despite applying control for a much longer time interval than in the first three experiments. As in the second and third experiments, before the control was applied the heart was in sustained VF, although that interval was not recorded.

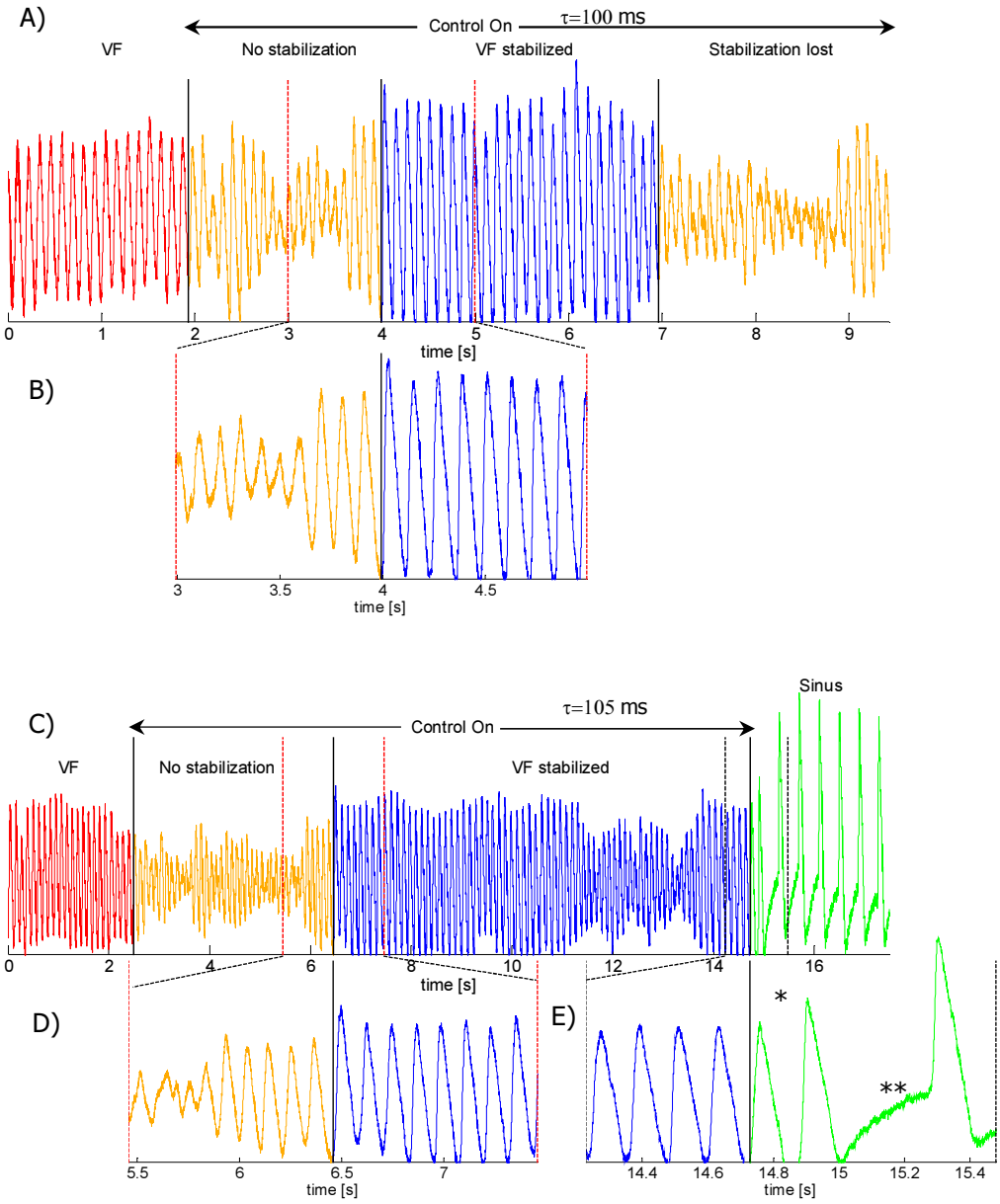

Figure 6.3. Traces representing electrical activity from the LV in the first control experiment. A) Activity during VF and when control was applied for the first time. VF was stabilized and then stabilization was lost. B) Detail of region showing transition from unstable to stable VF while control was on. C) A second attempt, where activity during VF was successful and VF stabilized, that led to sinus rhythm after control was terminated. D) Detail of region showing the transition from unstable to stable VF while control was on. E) Detail of region showing transition from stabilized VF to sinus after control was terminated. * indicates the appearance of two faster sinus pulses until sinus rhythm stabilizes. ** indicates resting potential that appears as the integrated DC signal as a result of DC decoupling with a 1 Hz high pass filter.

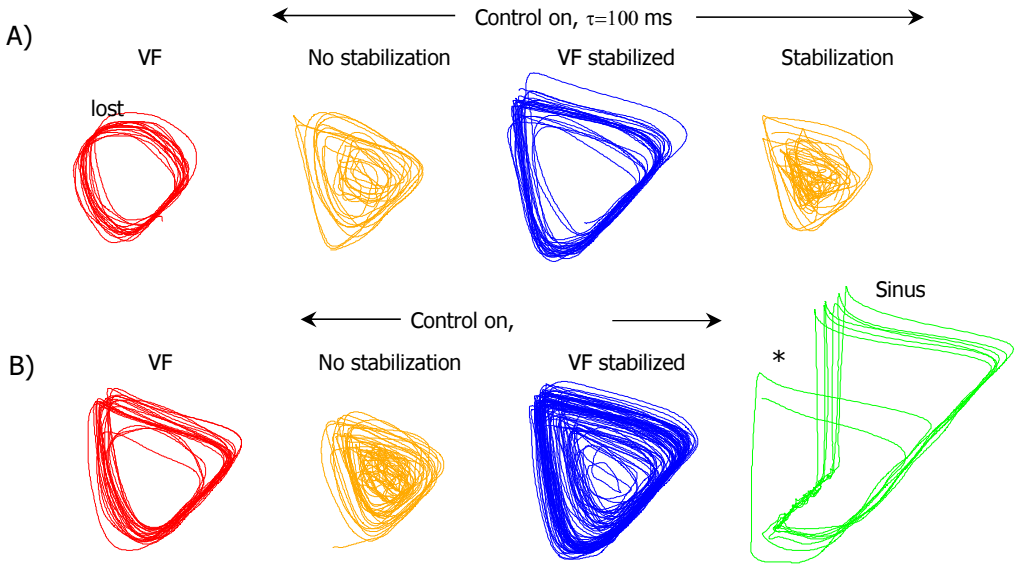

Figure 6.4. Phase space trajectories LV in the first control experiment. Panel (A) represents the first control attempt and panel (B) represents the second control attempt that led to sinus rhythm after control was turned off. * indicates smaller phase space orbits as a transition from faster to stable sinus rhythm after control was terminated.

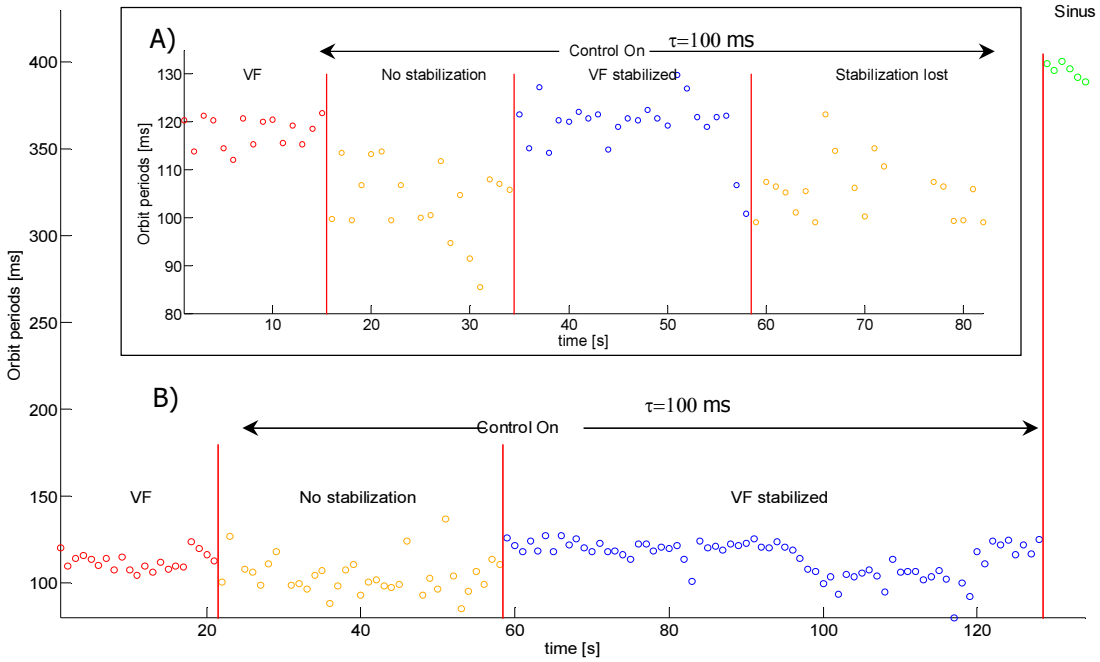

Figure 6.5. Orbit periods during VF and during applied control during two different control attempts in the first control experiment. Inset (A) is the first control attempt with loss of stabilization. B) Second control attempt that led to sinus rhythm after control was turned off. Note that the sinus period at the end was almost four times larger than that for the immediately preceding stabilized VF.

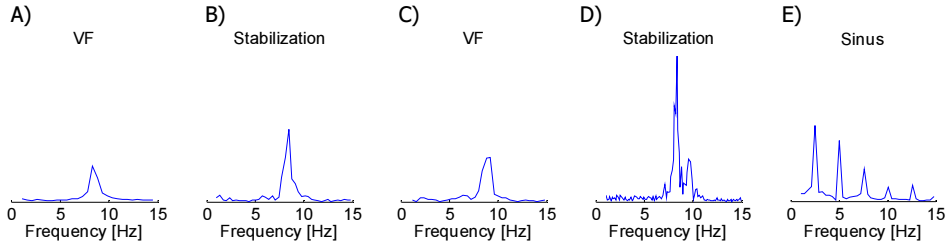

Figure 6.6. Frequency spectra of the signal from the left photodiode representing electrical activity from the LV in the first control experiment. A) During VF. B) During first stabilization. C) During VF after first stabilization was lost. D) During second stabilization. E) During restored sinus.

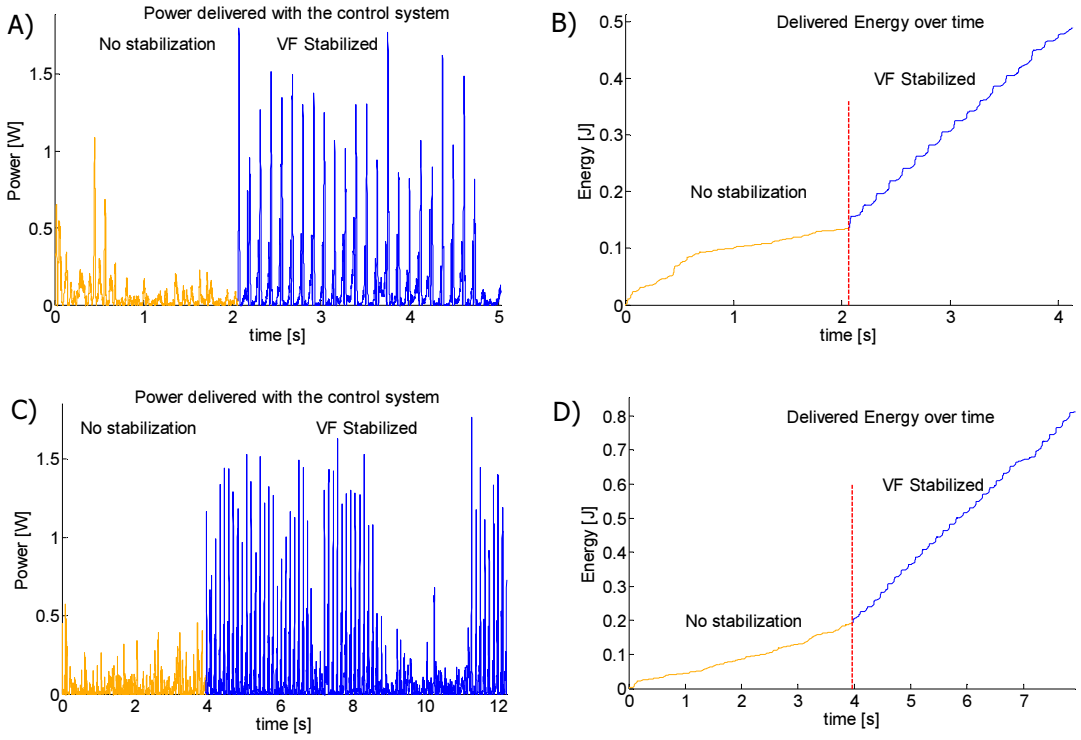

Figure 6.7. Power and delivered energy over time with the control system in the first control experiment. A) Power during first control attempt and during stabilization with total energy presented in panel (B). Panels (C) and (D) are power and delivered energy

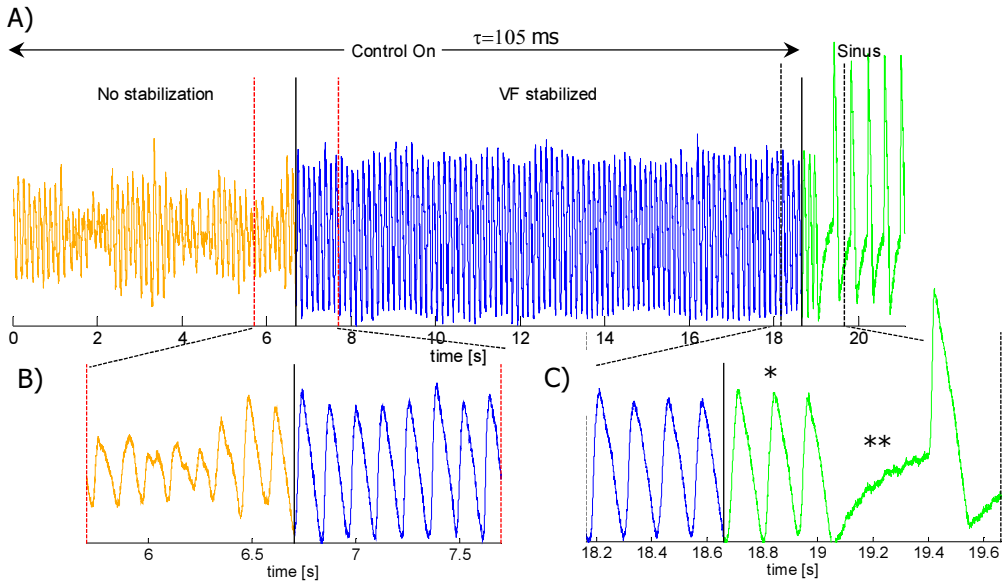

Figure 6.8. Traces representing electrical activity from the LV during the second experiment on the same heart as in Figures 6.1-6.5, but at a later time. A) Activity when control was successful and VF stabilized that led to sinus rhythm after control was terminated. B) Zoomed-in view of region showing transition from unstable to stable VF while control was on. C) Zoomed-in view of region showing transition from stabilized VF to sinus after control was terminated. * indicates appearance of three faster sinus pulses until sinus rhythm stabilizes. ** indicates resting potential that appears as the integrated DC signal as a result of DC decoupling with a 1 Hz high pass filter.

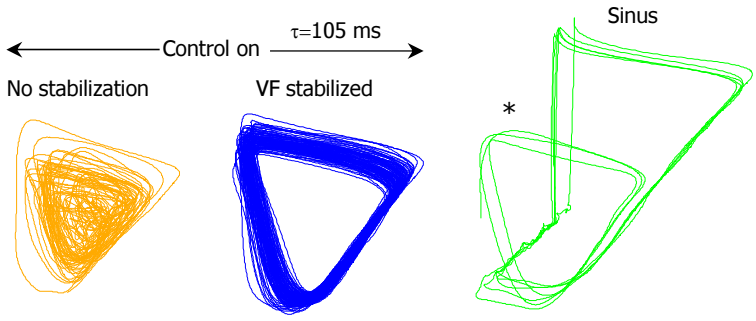

Figure 6.9. Phase space trajectories during control and during restored sinus rhythm in the second control experiment. * indicates smaller phase space orbits as a transition from faster to stable sinus rhythm after control was terminated.

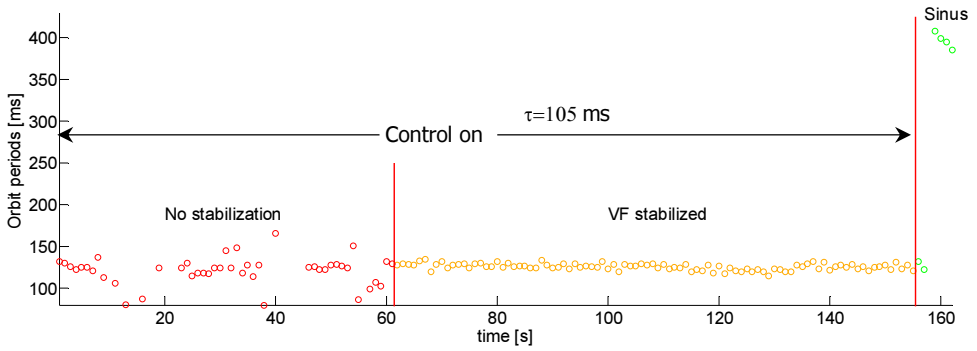

Figure 6.10. Orbit periods during applied control with sinus outcome after control was turned off in the second control experiment. Note that the sinus period at the end was almost four times larger than that for the immediately preceding stabilized VF.

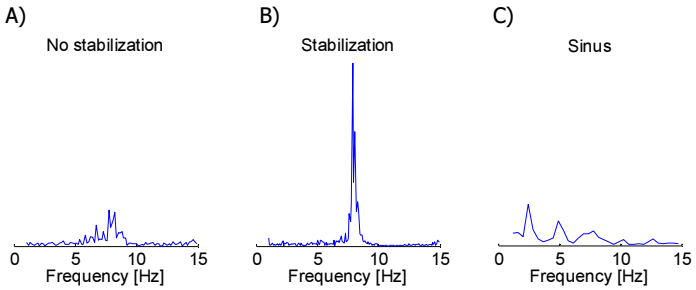

Figure 6.11. Frequency spectra of the signal from the left photodiode representing electrical activity from the LV in the second control experiment. A) During applied control with no stabilization. B) During applied control with stabilization. C) During applied control and lost stabilization.

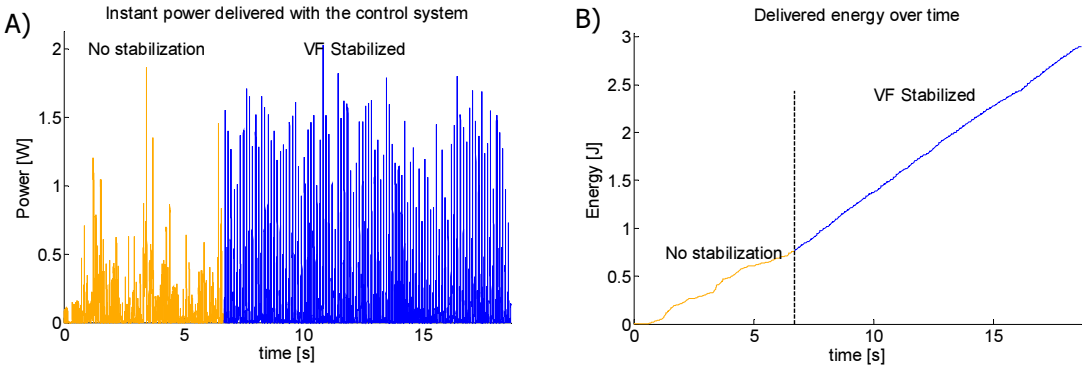

Figure 6.12. Power and delivered energy over time with the control system in the second control experiment. A) Power delivered with the control system. B) Delivered energy over time.

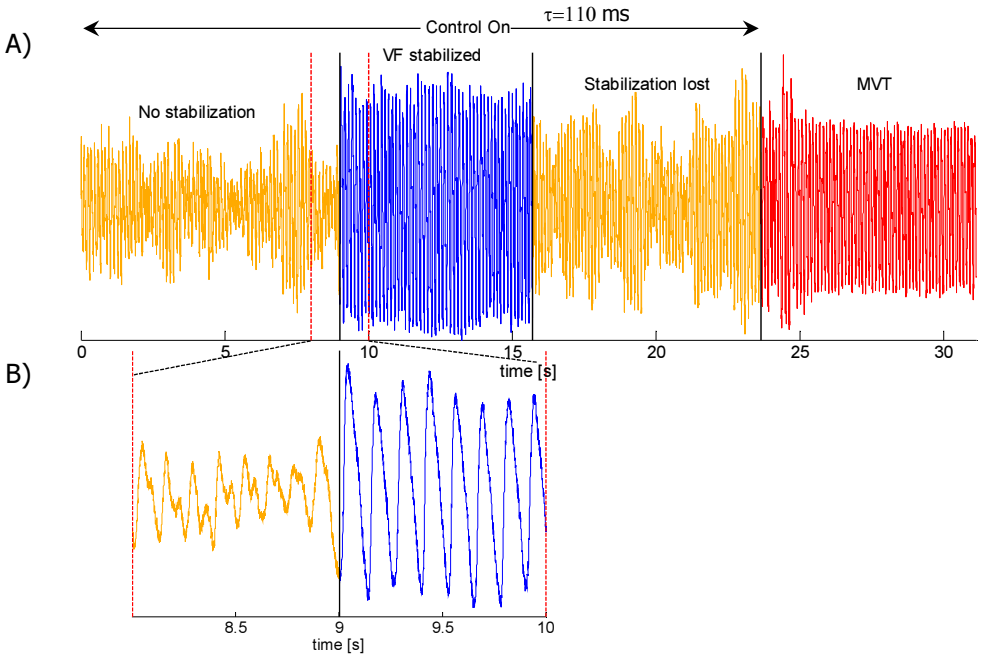

Figure 6.13. Traces representing electrical activity from the LV, during the third experiment on the same heart as in Figures 6.1-6.10. A) Activity when control was applied, VF stabilized and then stabilization was lost. The termination of control led to a monomorphic ventricular tachycardia (MVT). B) Zoomed-in view of region showing transition from unstable to stable VF while control was on.

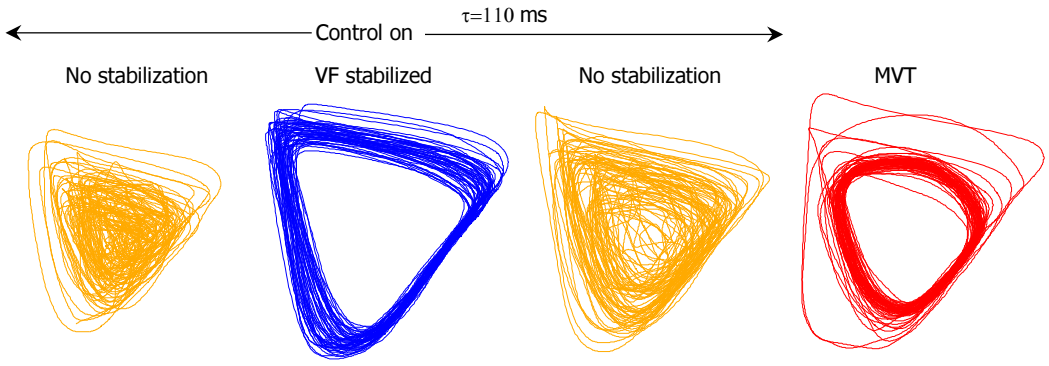

Figure 6.14. Phase space trajectories during control and during MVT after control was terminated in the third control experiment.

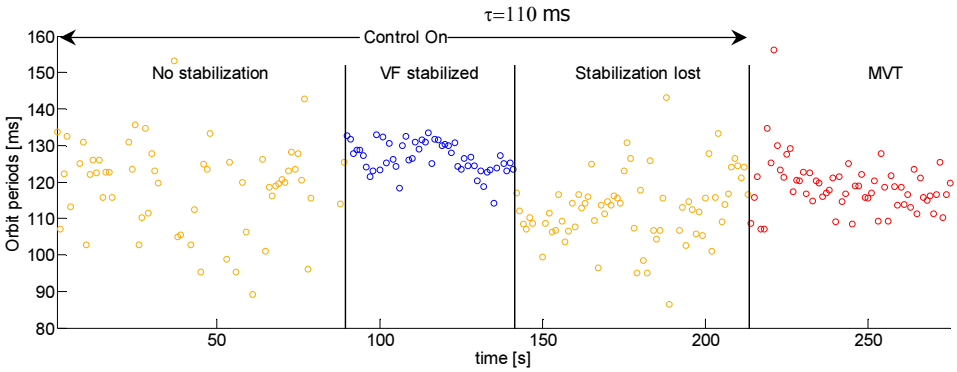

Figure 6.15. Orbit periods during applied control with and during MVT after control was terminated in the third control experiment.

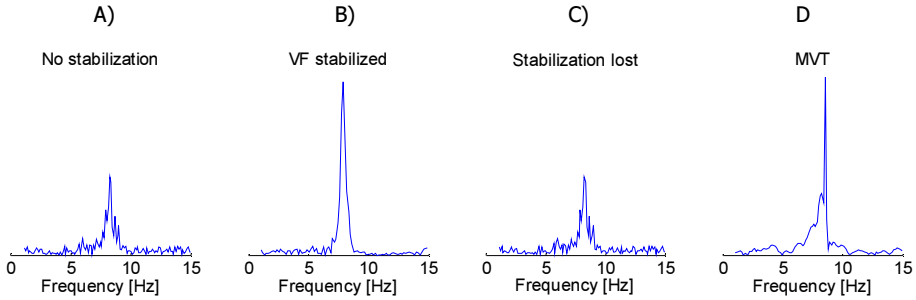

Figure 6.16. Frequency spectra of the signal from the left photodiode representing electrical activity from the LV in the third control experiment. A) During applied control with no stabilization. B) During applied control with stabilization. C) During applied control and lost stabilization.

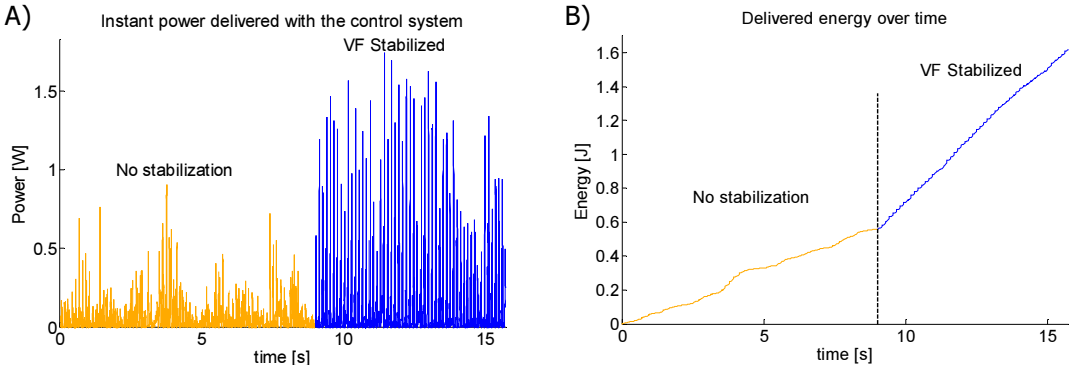

Figure 6.17. Power and delivered energy over time with the control system in the third control experiment. A) Power delivered with the control system. B) Delivered energy over time.

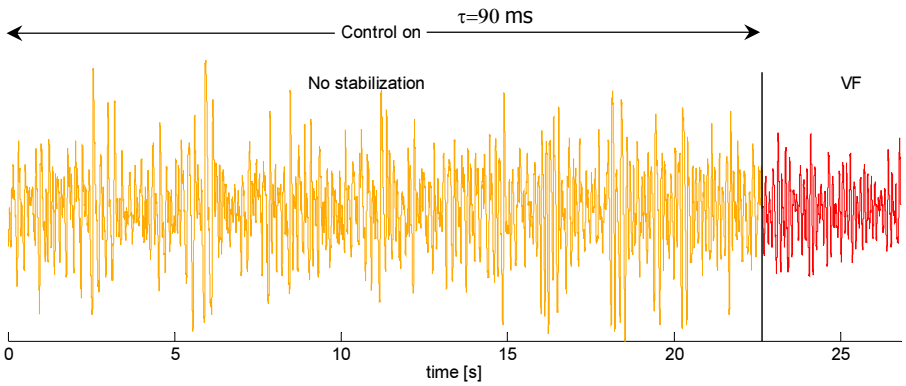

Figure 6.18. Traces representing electrical activity from the LV during the fourth experiment on the same heart. Control was applied but VF stabilization was not achieved even after 20 seconds. VF continues after control was terminated.

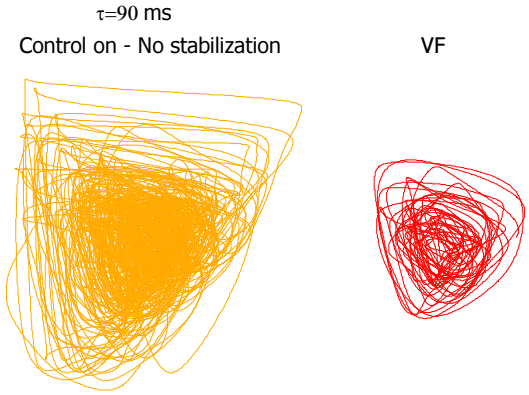

Figure 6.19. Phase space trajectories during applied control and during VF after control was terminated in the fourth control experiment.

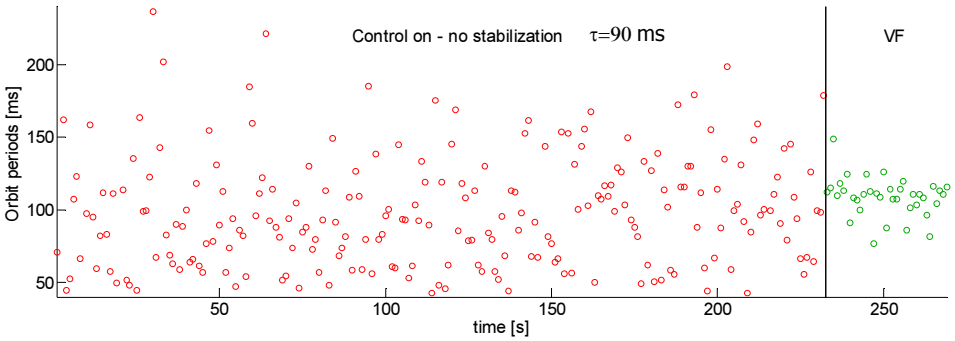

Figure 6.20. Orbit periods during applied control with and during VF after control was terminated in the fourth control experiment.

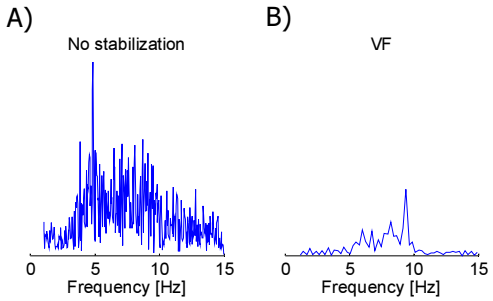

Figure 6.21. Frequency spectra of the signal from the left photodiode representing electrical activity from the LV in the fourth control experiment. A) During applied control with no stabilization. B) During VF with no controlled applied.

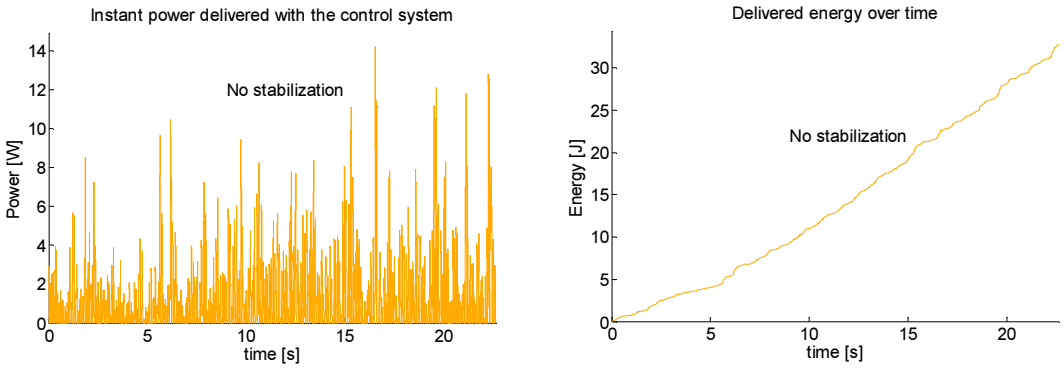

Figure 6.22. Power and delivered energy over time with the control system in the fourth control experiment. A) Power delivered with the control system. B) Delivered energy over time.

Discussion

In the Results section we presented four experiments with different external feedback delays ranging from 90-110 ms. The central idea of DFC is to apply feedback control during VF so that only certain orbit periods that are naturally supported by the system are allowed to exist, while others are suppressed by the control system.

The theory of chaos control with embedded feedback delay states that the delay through the feedback control system must be the same as the period of the orbit that is targeted for stabilization. In our work we observed that this is not the case due to certain additional factors. Three out of four presented experiments were successful with the external delay of 100, 105 and

110 ms. Our criteria for detection of stabilized VF is done upon observation that orbit periods or amplitudes of the traces in time domain are not varying over time in comparison to the prior time when variations are significant. Panels (A) and (B) in Figure 6.3 show stabilization with the external delay of 100 ms, and, in both cases, orbits of 120 ms were stabilized and allowable by the feedback system, while other orbit periods were suppressed. For the external delay of 105 ms, stabilization was greatest for orbits of 125 ms, as shown in Figure 6.8. For the external delay of 110 ms, stabilization was greatest for orbits close to 130 ms, as shown in Figure 6.13. This difference between the external delay and the period of stabilized orbits indicates that there is an additional delay in the system. This difference is constant in all three cases of 20 ms, and we conclude that it must be related to either intracardiac propagation delay or the analog and digital electronics (feedback processing unit and the V2CC). The delay due to electronics can be at most couple of ms, so it appears that the additional delay is due to propagation delay between perturbation electrodes and the areas on the surface of the heart that are being monitored with the photodiodes. Perturbation shocks have low energy and are delivered to the endocardium of the ventricles. Since the areas that are being monitored with the photodiodes are on the epicardium and, moreover, not necessarily adjacent to the perturbation electrodes, it certainly takes some time for excitation to travel along the spatial distances that separate the perturbation electrodes and monitored area. With a longitudinal conduction velocity of 76 cm/s and transverse conduction velocity of 26 cm/s in the rabbit heart, the delay of 10 ms would correspond to a spatial distance of 7.6 mm longitudinally and 2.6 mm transversally[1]**.** These spatial distances are within reasonable ranges in our experimental setups, and we conclude that the spatial dimension must play a role in the overall extra delay of 20 ms.

In time domain plots we observed certain transitional patterns when control was successful (presented in Figures 6.3, 6.8 and 6.13) and will discuss these patterns in more details. Understanding of transition from unstable-to-stable VF and transition from stabilized VF to sinus rhythm aim to provide a better understanding of cardiac control and the underlying dynamic during VF and stabilized VF.

Transition from Unstable VF to Stabilized VF under External Feedback Control

In every transition from unstable VF to stabilized VF, we observed that immediately before the occurrence of stabilized VF, the traces had minimal amplitude and were random or chaotic following asymptotic transition into stabilized VF. This asymptotic transition supports the reasoning in Chapter III where we hypothesized that the global control with the local perturbations is established as expanding synchronicity through dominant perturbations from the areas controlled by external feedback control to the surrounding areas that exhibit chaotic behavior. During VF, multiple spiral waves are surrounded with the chaotic areas and are in balance through mutual perturbations that define the number and radius of the spiral waves. If somehow the chaotic dynamic in these surrounding areas becomes organized, they will no longer perturb spiral waves in a random way and through organized perturbations will certainly affect the dynamic of the spiral waves. In other words, the balance between these surrounding areas and the spiral waves will be shifted in favor of the dynamic of the surrounding areas, which will impose their dynamic not only on the adjacent spiral waves but also on any other adjacent areas that exhibit a different dynamic. We hypothesize this as a mechanism of successful cardiac control. With the external control system, the dynamic of a certain area that exhibits chaotic behavior is constantly perturbed until a specific organized dynamic is achieved. From that moment on, the dynamic in this area is driven with the external control system, and, through a series of perturbations, the dynamic in the surrounding areas will be gradually changed. Ultimately, global control through local perturbation will be reached. This gradual process is shown in Figures 6.3B, 6.3D, 6.8B and 6.13B as the asymptotical transition from unstable VF into stabilized VF.

As mentioned above, during the transition from unstable-to-stable VF there is a time interval when traces appear chaotic. We observed this pattern in each experiment that resulted in a stabilized VF, and we explain this as a phenomenon due to VF not being fully chaotic, because the perturbations that certain areas impose on some other areas are not fully random, and that

means that there is some dominant perturbation. This dominant perturbation, as elaborated in Chapter III, can be from the intrinsic cardiac system, from some organized dynamic in the surrounding area, and from nearby spiral waves. If this is the case, then additional small perturbations with the external control system must "compete" with the underlying dominant perturbation. Through this competition any additional perturbation certainly increases chaotic behavior, as shown with orbit periods in Figures 6.3A and 6.3B, when control was applied without achieved stabilization in comparison to the orbit periods in the preceding VF. The greater the amount of chaos, the easier will it be for an external perturbation to overpower any other non-random perturbation. Therefore, once complete chaos is established, its duration will be for only a short term, since a system that exhibits chaos is extremely sensitive to any perturbation and, moreover, the external perturbation is not random and from that moment on becomes dominant. As stated in Chapter III, when a system exhibits chaos it is extremely sensitive to even a small perturbation, meaning that its future states are unpredictable. This, in other words, means that the system allows and supports any future state equally among all possible states and that with adequate perturbation it can be driven to any desired state. The presence of chaos is observed in Figures 6.3B, 6.3D, 6.8B and 6.13B as the appearance of small and random amplitudes. DFC theory applies to a system that is fully chaotic and on first approach does not seem suitable for cardiac control, wherein VF is never true chaos. This does not mean that the method is not applicable to cardiac control, since, if external perturbations are able to create full chaos first, they will then be able to control it. This is exactly what happens, and it explains why transition to stabilized VF is through occurrence of full chaos first as a necessary condition. From the last experiment, with feedback delay of 90 ms, we show that complete chaos was definitely reached if we look at any of the Figures 6.18-6.21, but stabilization of VF was never reached. This leads us to conclude that creation of full chaos is a necessary, but not sufficient, condition. There are other conditions necessary for transition into stabilized VF, and one of them is certainly the value of external delay. We cannot set this delay to support those orbit periods that are not supported by the system itself. We targeted a feedback delay of 90 ms to stabilize orbit periods of 110 ms,

and it seems that these orbit periods are not supported by the heart as readily as are longer orbit periods. As a final conclusion we assert that in order to establish control, any memory or visible pattern during VF first must be terminated. This approach of stabilization through external perturbation control is comparable to the asymptotic control evident in many biological control systems.

Transition from Stabilized VF into Sinus at the Termination of External Control

In our experiments we have observed that if control was terminated while VF was stabilized, it then led to sinus rhythm (2 of 2 trials), as shown in Figures 6.1C and 6.6A. This supports our reasoning in the previous chapter where we hypothesized that stabilized VF can only be supported with external control and that upon its termination, the dynamic of the system must change with the following outcomes: degradation into VF, transition into some complex MVT, or transition into sinus rhythm. From our experiments, we observed sinus outcome. As we elaborated in Chapter IV, during stabilized VF the number and size of the areas with remaining chaotic behavior are suppressed to the minimum or are nonexistent. From traces in Figures 6.1C and 6.6A, orbit periods do not appear ultimately stable, and we hypothesize that this is due to additional perturbations other than those from the external control system. In order to test and study this hypothesis, further experiments must be devised. Nevertheless, since sinus outcome is definite upon termination of the external control, this means that all remaining areas with chaotic behavior cannot perturb the surrounding areas having an organized dynamic in order to expand chaos. It is the other way around: areas of chaotic behavior are overwhelmed with the perturbations from surrounding areas having an organized dynamic. One of the possible reasons why there are areas with a chaotic dynamic even during stabilized VF is that these areas cannot follow a fast and organized dynamic to be established in the rest of the heart. After control is terminated, the cardiac intrinsic control system becomes dominant and imposes a dynamic that is naturally supported across the entire heart, and hence sinus rhythm will be restored. Figures 6.3E and 6.8C show the transition into sinus rhythm after control was terminated and, as pointed

out, this transition was always accompanied with a few faster beats followed by normal sinus rhythm. We hypothesize that this transition is most probably from the remaining rotor or rotors during stabilized VF. These rotors are supported with the external control system and cannot exist when external control is terminated; however, they may exhibit a couple of full revolutions before they disappear. One other possibility is that this transition constitutes some intrinsic property of the cardiac control system due to different cardiac properties, such as the change of conduction velocity in VF and the time required to accommodate the conduction velocity with a slower pacing rate.

In Figures 6.3A and 6.13A, control was terminated at the moment when stabilization was lost and this led to VF and complex MVT, respectively. Based on the reasoning above, the loss of VF stabilization means that external perturbation was overwhelmed with some dominant perturbations that together will increase the number and size of the areas with chaotic behavior. When control is terminated, the perturbation from these chaotic areas remains dominant and the subsequent cardiac dynamic will be determined by these dominant perturbations, not the intrinsic cardiac control system. Therefore, in this situation, termination of control did not led to sinus rhythm.

Analysis in the Frequency Domain

Fourier spectra of optical traces are shown in Figures 6.6, 6.11, 6.16, and 6.21. In each figure peaks are normalized to the highest peak that always occurred during VF stabilization. By comparing heights and widths of the peaks during control without stabilization and stabilized VF, we see that external feedback control clearly suppresses certain frequencies, or, in other words, orbit periods, and allows only certain frequencies to exist. In Figure 6.6D, the Fourier spectrum has two peaks, consistent with the optical trace from Figure 6.3C, where we see that during the second control attempt stabilization was transiently lost.

Instantaneous Power and Delivered Energy with the Control System

Instantaneous power and delivered energy with the control system are presented in Figures 6.7, 6.12, 6.17, and 6.22. Delivered power and energies in cases when control was successful were very small. With single shock defibrillation, typical energies needed to defibrillate the entire rabbit heart in far-field stimulation, are in the range of few Joules and delivered in typical time intervals of 5 ms. This means that the instantaneous delivered power for standard defibrillation can be over 100 W. In our DFC experiments, the total delivered energy is on the order of a Joule for the entire control that can last over 10 s, and instantaneous power is only a few watts.

In Figure 6.7D, the small increasing steps in total energy reflect the energy delivered per pulse, and these energies are only a fraction of a Joule (~50 mJ). Such small energies are an indication that the control system is not delivering defibrillation shocks, but perturbation shocks.

DFC theory predicts that once chaos is stabilized and controlled, energies needed to keep the dynamic organized should be lower than before the control was established. In our experiments we have always observed that instantaneous power is greater during stabilized VF than during unstable VF. However, we interpret this as a limitation of our implementation of a DFC algorithm that doesn't provide any contingent control over the strength of the perturbation shocks for different cardiac dynamics. We hypothesize that if we lowered the strength of the perturbation shocks manually after VF had been stabilized, VF would remain stabilized. We believe that the reason why the strength of the perturbation shocks is greater once VF is stabilized is due to the presence of an additional intracardiac delay. Namely, the feedback signal is calculated as the difference of the photodiode signals at the present time minus the same difference, but at a time τ earlier, which is shorter than the stabilized orbit period. In a typical scenario, stabilized VF is driven with electrodes inserted into ventricles, and, once the perturbation shock is delivered, it will certainly excite first either the LV or RV of the heart, depending on the polarity of the shock. As a consequence, the difference in activation time of the

LV and RV will create a non-zero difference in the timing of the peaks in the photodiode signals. If there is no intracardiac propagation delay, the difference in the present time will be subtracted with the same difference in the past time if there is no intracardiac propagation delay, and theoretically this difference (feedback control signal) will be zero. Due to intracardiac propagation delay, the difference in the past is subtracted at the time during plateau of the action potential and therefore the total feedback signal will not be zero even during achieved stabilization. Moreover, as optical signals represent integral activity in the areas that are monitored, synchronicity in the monitored areas will lead to a total increase of the signal averages over the monitored areas, and as a consequence leads to an increase in feedback signal. These two mechanisms explain why during stabilized VF, the power delivered with the control system is even greater than in the case when there is no stabilization.

Conclusions

In the DFC experiments we studied a local, single-site control of a global spatio-temporal dynamics. For an experiment to be successful, the biggest challenge was to minimize the phase difference in excitation of the LV and RV. This phase difference depends on the placement of the optical fibers, their distance from the heart, and size and location of the defibrillation electrodes with respect to the area that is being monitored. To address this problem we introduced a threshold that if exceeded is an indication that here is an irregular cardiac dynamic. As the patterns of induced VF differ from control experiment to control experiment and given the factors above, we find that establishing a statistic over the control experiments is not possible. Any statistic would be biased with many experimental variables as our control algorithm is not optimized with regard to these variables. Basically, we do not have the algorithm that will calculate an optimized feedback control signal based on the numerous experimental variables, but experiments we did through manual adjustments should serve as a guide and tell us how to optimize the algorithm and make it "smart". We tested principles and ideas, and confirmed them

many times through the experiments. Optimization is not part of that. Our performed experiments were designed for the purpose of gathering better understanding behind cardiac control and gaining a better understanding of how control algorithm should be improved.

From experiments with stabilized VF we observed that it always takes a certain time for VF to be stabilized and that the transition from unstable-to-stabilized VF is always through establishment of complete chaos and subsequent asymptotical approach to stabilized VF. We hypothesized the possible explanation in the Discussion section and we hope that our understanding of these transitions will lead to a better understanding of cardiac control, and further experiments are needed to be devise control paradigms that will address this transient pattern. We also hypothesize that if chaotic behavior is very prominent, the transition time from unstable-to-stabilized VF will be minimal and the highest on the case of MVT.

Transition from stabilized VF into sinus was accompanied with a couple of faster beats. We hypothesized a possible explanation in the Methods section above, but further experimental and theoretical studies are needed to address this pattern. Further imaging is needed to confirm the existence of any remaining rotor when control is terminated.

Since external delay is obtained empirically, improvement of the DFC implementation will be through automatic calculation of the optimal embedded delay time from the dynamic of VF that is targeted for stabilization. Additionally , we have used a relatively simple algorithm, and it will be interesting to test more complex algorithms, such as chaos control through extended feedback delay[2]**.**

As instantaneous delivered power is greater during stabilized VF than during unstable VF, further experiments should prove our hypothesis that stabilized VF can be controlled with lower power. With more advanced DFC algorithms this can tested as a demonstration that the feedback control system automatically decreases power once VF is stabilized.

All experiments were performed with a stiff feedback delay, meaning that it was not possible to change the external delay while control was applied. We propose future experiments with a non-stiff delay so that a feedback controller will have the ability to gradually change the

delay once VF is stabilized to a value that corresponds to the sinus rhythm. In this way stabilized VF will be gradually slowed down and "walked in" to sinus rhythm.

1. Reiter, M. J., Landers, M., Zetelaki, Z., Kirchhof, C. J. H. & Allessie, M. A. Electrophysiological Effects of Acute Dilatation in the Isolated Rabbit Heart : Cycle Length Dependent Effects on Ventricular Refractoriness and Conduction Velocity. *Circulation* **96**, 4050–4056 (1997).

2. Pyragas, K. Control of chaos via extended delay feedback. *Physics Letters A* **206**, 323–330 (1995).

CHAPTER VII

STABILIZATION OF CHAOTIC SPIRAL WAVES DURING CARDIAC VENTRICULAR FIBRILLATION WITH PROPORTIONAL-INTEGRAL-DERIVATIVE FEEDBACK CONTROLLER IN THE PHASE SPACE

Summary

Cardiac arrhythmias that lead to ventricular fibrillation (VF) arise from electrical spiral waves rotating within the heart with characteristic periods. A single drifting spiral wave often degenerates into multiple spiral waves, creating a chaotic appearance, or VF. As the number of wave sources increases, the degree of chaos in the electrical activity of the heart increases as well. Here we take an approach of detecting chaotic rhythms that is based on the miscorrelation between electrical activity of the left and right ventricles (LV and RV) in the phase space. The phase space is constructed as RV versus LV, and we have observed substantially different phase-space trajectories corresponding to the amount of chaos or irregularity in the electrical activity of the heart. For sinus rhythm, correlation between RV and LV is maximal, leading to phase-space trajectories that are, ideally, a straight line. When sinus rhythm is disrupted, correlation of the electrical activity between LV and RV decreases and phase space trajectories exhibit substantially different patterns depending upon the complexity of the cardiac dynamic. In the case of monomorphic ventricular tachycardia (MVT), phase space trajectories will appear as overlapping closed orbits with very small differences in their periods. In the case of VF, phase space orbits will appear to be random, creating phase space trajectories that cross each other without a visible organizational pattern. Our continuous feedback control presented in this chapter is based on a proportional-integral-derivative feedback (PID) controller that calculates in real time feedback control signal from the phase space considerations. Feedback control signals, in the form of a series of defibrillation shocks, were delivered inside the ventricles of a rabbit heart with a strength that is a function of the distance from the current state in the phase space to the

straight line fit obtained from the set of phase space states when the heart was in sinus rhythm. Typically, the energy of each defibrillation shock was up to a hundred times lower in comparison to the single "classic" defibrillation shocks needed to defibrillate the rabbit heart, and, moreover, the total energy delivered through the series of shocks was often of a magnitude lower than the energy of the single "classic" defibrillation shock. Defibrillation through a series of small energy shocks occurred as a gradual change in the dynamic of the heart. Based on this information, we refer to these shocks as perturbation shocks rather than defibrillation shocks. Our ultimate goal is to show that we can defibrillate the heart with a total energy that is an order of magnitude smaller than the "classic" single defibrillation shock. As was shown in Chapter VI, feedback control was used to stabilize unstable orbits during VF in order to achieve stable VF. Feedback control could target for stabilization only those orbit periods that were supported by the dynamic of VF. With the PID phase space feedback controller, stabilization was achieved by forcing the dynamic system back to "maintain" its phase space trajectories permissible only within the sinus dynamic.

Introduction

The theory of cardiac control is presented in Chapter III. Here, however, we will summarize the general concepts and main points of cardiac control theory.

During VF, the cardiac dynamic exhibits chaotic behavior due to the presence of spiral waves in the heart's electrical activity. Despite being studied extensively, spiral waves are not easy to terminate. At present the only practical means to automatically stop VF is to deliver a single, strong electric shock to the entire heart using defibrillators or to deliver multiple low-energy shocks in a novel Low-Energy Anti-fibrillation Pacing (LEAP) technique[1]. The spiral wave has at its center an entity known as the phase singularity (PS), which acts as an organizing center for the area that surrounds it, where the spiral wave is formed. (Phase singularity theory is presented in Chapter I, while its role in VF and cardiac control is discussed in Chapter III.) It is

important to remember that in the border zone areas between the spiral waves and the rest of the heart, the cardiac dynamic tends to be chaotic during VF. These areas are targeted for cardiac control with low energy perturbation shocks.

Currently, there is a lack of systematic and unifying study that would connect detection of phase singularities and the associated chaotic dynamic with the optimal shape, amplitude, timing and duration of defibrillation shocks, or, as in our study, perturbation shocks. Moreover, the mechanisms by which a defibrillation shock terminates VF are currently not well understood. Our defibrillation approach considers the heart as a dynamic system that exhibits spatiotemporal chaotic behavior in VF. With the phase space approach and by using methods from control theory, we aim to arrive at a better understanding of cardiac control that would ultimately lead to novel defibrillation methods. Our ultimate goal is to achieve global control of spatiotemporal chaos through local control with only small perturbations of the system.

Methods

New Zealand White rabbits' hearts were isolated and experiments were performed in a Langendorff perfusion system, as described in the Methods section of Chapter II, Figure 7.1. Hearts were stained with voltage-sensitive dyes (Di-4-Anneps), and fluorescence was excited by a green laser light (Coherent, 532nm). Two optical fibers were placed on the opposite sides of the heart, facing the LV and RV to collect emitted fluorescence from the heart's surface, and to guide light towards the photodiodes with band-pass filters of 600-700 nm in the Feedback Controller, Figure 7.2. The Feedback Controller is described in Chapter V and consists of a microcontroller that processes these optical signals in real time and sends a calculated feedback control signal to the voltage-to-current converter (V2CC, described in Chapter IV), which in turn delivers perturbation shocks to the heart in the form of an electrical current. In our experimental setups we had used coil electrodes inserted into the RV, while in the LV we used both coil and mesh electrodes. In comparison to the experimental setup with delayed feedback control, here

we additionally used collimating lenses attached to the fibers, as shown in Figure 7.1. With the collimating lenses we were able to observe cardiac electrical activity integrated over the larger areas to minimize unavoidable phase differences between excitation of the LV and RV during sinus rhythm as this is of great importance, as will be explained.

In order to better understand the control principles and ideas behind the PID control in phase space, Figures 7.3 and 7.4 present traces of the photodiode signals in the time and space domains, respectively. From these figures we can also gather a better understanding of the role of the phase difference in excitation between the RV and LV in order to devise a proper control algorithm.

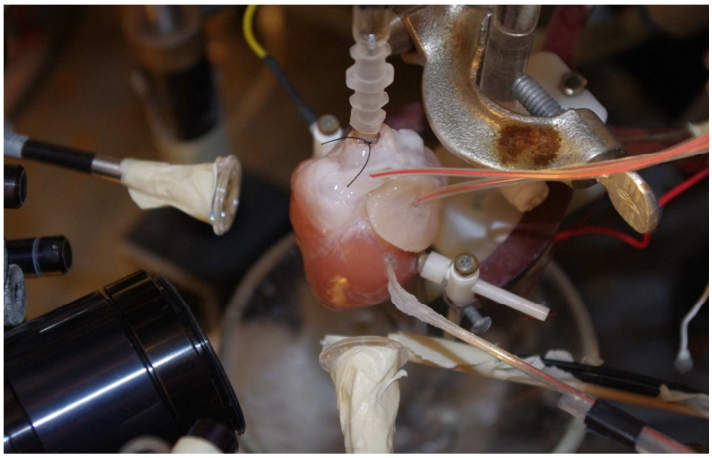

Figure 7.1. An isolated rabbit heart in Langendorff perfusion, with perturbation electrodes inserted into the LV and RV and optical fibers facing the LV and RV.

Figure 7.3 represents how the normalized transmembrane potentials are acquired from the opposite sides of the heart, V_1 and V_2 along their difference V_1-V_2. During regular/sinus rhythm, both signals are maximally correlated, in both amplitude and phase, resulting in a difference signal with much smaller amplitude than the optical signals themselves. During MVT correlation is partially lost and although signals can have the same amplitude, it is central to MVT that they have different phases, resulting in a larger difference signal than during sinus rhythm. In the case of VF, both optical signals are minimally correlated, resulting in a largest difference

signal. This example indicates that any irregularity in the cardiac dynamic will result in a loss of the excitation correlation between the LV and RV that is the basis of our defibrillation algorithm. Our novel defibrillation algorithm calculates LV minus RV not in the time domain, but in the phase space as a distance between the current state and the reference state, as will be explained.

Phase space trajectories of optical traces from LV and RV are noted as A and B, respectively, in Figure 7.4. During regular sinus rhythm, both signals are maximally correlated,

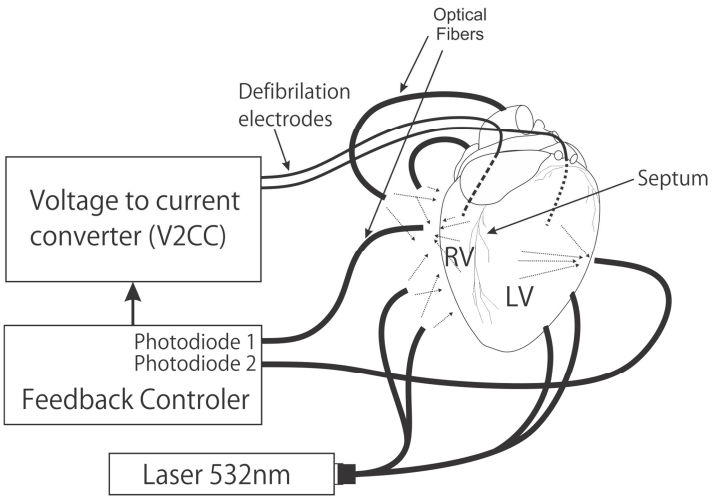

Figure 7.2. Experimental setup.

resulting in phase space trajectories that are centered along a diagonal line (represented with a blue line in both panels). Red trajectories in panel (A) of Figure 7.4 represent cardiac activity during MVT, while in panel (B) they represent cardiac activity during VF.

Ideally, a phase space trajectory during sinus rhythm should be centered in the area along a diagonal line with minimal width. In experiments, that is often not the case due to the following factors: phase difference in excitation between the LV and RV, placement of the optical fibers, size of the area monitored with optical fibers, and presence of any mechanical movement. It is important that these factors are optimized to minimize the width of the closed orbits during sinus rhythm since the width defines a rectangular area that serves as a decision threshold for application of the perturbation shocks. Namely, with the defined rectangular area during sinus

rhythm, as the system evolves in time, any phase space state occurring outside of the rectangular area is an indication that there is an irregularity in the cardiac dynamic, and an appropriate perturbation shock should be delivered. We calculate the perturbation shock as a function of the shortest distance from the current phase space state of the system to the line that is constructed by linear regression of the all the phase space states during sinus rhythm.

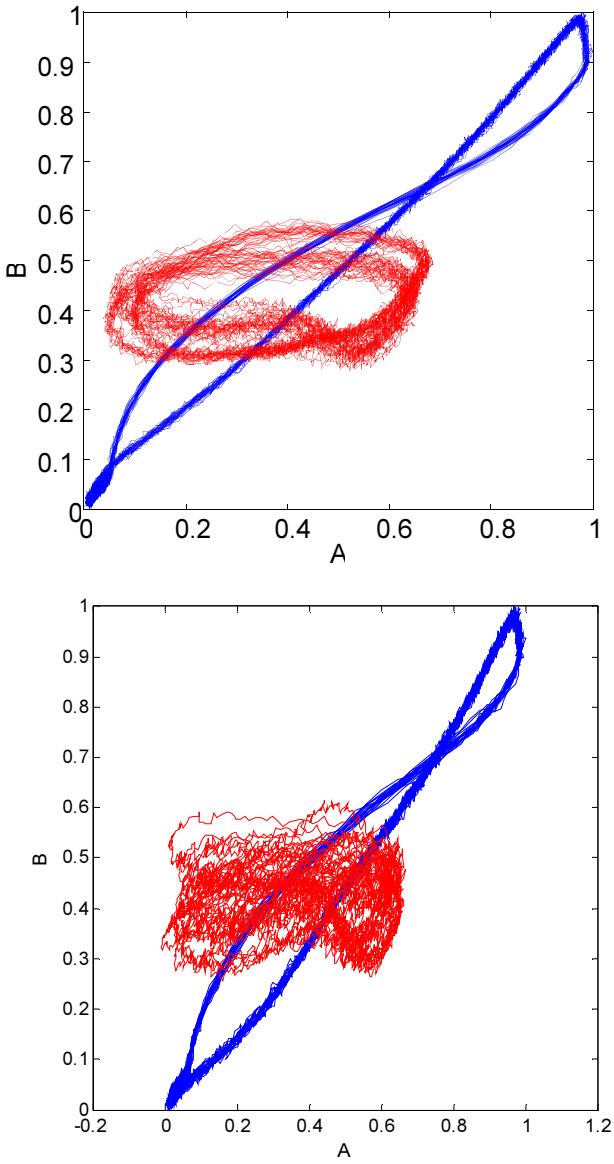

Figure 7.3. Phase space trajectories of electrical activity of the LV and RV as plotted as A versus B, respectively. Sinus rhythm is noted as blue trajectories. The red trajectory in panel (A) represents MVT, while the red trajectory in panel (B) represents VF.

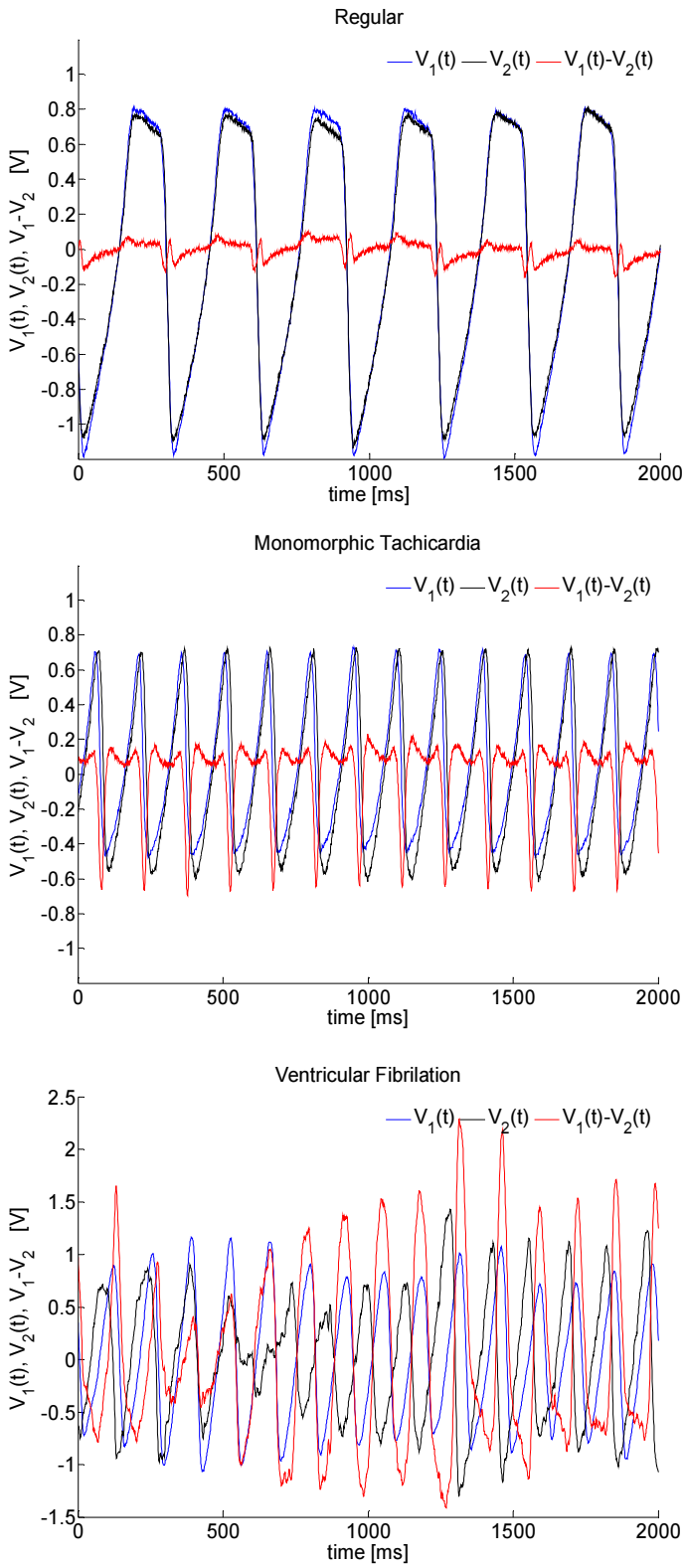

Figure 7.4. Time domain plots of electrical activity from the LV and RV plotted as V_1 and V_2, respectively.

Algorithm for Cardiac Control with PID Control in the Phase Space

The PID controller parameters have to be defined during regular sinus rhythm in a multisteo "calibration" process of as follows:

- Sample signals from the photodiodes representing electrical activity on the surface of the LV and RV, termed A and B respectively, for a couple of seconds, and from the obtained samples, calculate the normalization multipliers for each signal separately.
- Normalize the obtained sets of samples, and perform a linear regression $B = B(A)$ to determine the analytical form of the linear fit line, its slope m and intercept b

$$B = m \cdot A + b,$$

$$m = \frac{\sum_k (A_k - \overline{A})(B_k - \overline{B})}{\sum_k (A_k - \overline{A})^2}$$

$$b = B - m * \overline{A} \quad .$$

- For each pair of samples(A_k, B_k), calculate the normal distance from the fit line

$$d_k = \frac{B_k - m * A_k - b}{\sqrt{m^2 + 1}} \text{ , } k=1..N \text{ .}$$

- Calculate the mean value D and standard deviation σ from the obtained set of distances

$$D = \overline{d}$$

$$\sigma = std(d) \quad .$$

Once this is done, empirically establish the threshold as a number of standard deviations. Once the initialization procedure is performed, VF is induced and the perturbation shock wave form, termed *DEFIB*, is calculated in real time as follows:

- After each sampled pair (A_k, B_k), multiply samples with the normalization constants, and calculate the normal distance d_k from the fit line.
- If the distance is greater than the predefined threshold, apply a perturbation shock as the sum of proportional, integral and differential terms

$$DEFIB_k = K_D\{ (d_k - DT) + \frac{1}{T_i} T \sum_{n=1}^{k} (d_n - DT) + T_d \frac{d_k - d_{k-1}}{T} \} \quad k \geq 2,$$

where $K_{D,}T_{i,}\ and\ T_d$ are user-defined parameters or weight factors for the PID controller configuration. *T* is the sampling time interval. DT is a distance threshold expressed in a number of standard deviations. As the PID controller is already described in Chapter III, it will here be only briefly summarized. The proportional, the integral, and the derivative terms in the *DEFIB* equation are denoted as P, I, D, respectively. These terms can be interpreted in the time domain as: P represents a present error, I represents cumulative past errors, and D represents the predicted future errors. The control signal *DEFIB* is the weighted sum of these three terms.

Before feedback control experiments were performed, the PID controller was calibrated while the heart was in sinus rhythm. After calibration, additional parameters for the PID controller were entered manually in the control panel of the custom software that communicates with the feedback controller. These parameters are: strength of the perturbation shock, K_D; distance threshold (DT); and persistence threshold (PT) expressed in number of samples. These parameters were obtained empirically, and varied in experimental trials.

K_D was determined experimentally as the minimal value upon which delivered perturbation shocks were able to defibrillate the heart. DT was also obtained empirically, and we usually used values between 1 and 2. We observed that sometimes during MVT, due to a certain correlation between excitation of the LV and RV, the orbits of the phase space trajectories were smaller than in VF, and in order to defibrillate the heart in MVT we usually had to use DT values as low as 0.5, or to increase K_D. When DT values were set too low, then upon successful heart defibrillation the threshold was often exceeded even during sinus rhythm, and perturbation shocks were delivered to the heart unnecessarily. These shocks during restored sinus rhythm were caused by the phase difference in excitation between the LV and RV, and to neutralize the effect of the phase difference, PT was set to be at least equal to the phase difference determined empirically during calibration in sinus rhythm as the necessary minimal number of samples, so that *DEFIB* signal stays inactive.

After calibration, VF was induced by train of pacing stimuli varying between 80 and 110 ms, or by 40 Hz AC current of 50 mA, delivered to the heart as current with the V2CC, driven by

the wave form generator. Along with optical traces, analog values representing voltage and current delivered to the heart were sampled as well. All analog values were sampled at 2 Ksps and recorded during sinus rhythm and during applied control for subsequent analysis.

The PID controller communicates via a USB protocol with the custom PC software, described in detail in Chapter V. Briefly, custom PC software allows visualization of the optical traces in both the time and space domains. The user has the ability to enter manually the PID control parameters and record the following signals: electrical activity from the LV, electrical activity from the RV, the *DEFIB* feedback signal, and current and voltage signals from the V2CC output, as shown in Figure 7.5. The reed relays of the V2CC were controlled manually via the Arm button in the control program. The PID controller additionally controlled the *FIRE* input of the V2CC, setting it to "active" whenever the distance in the phase space exceeded the DT for the consecutive number of samples set by the PT parameter.

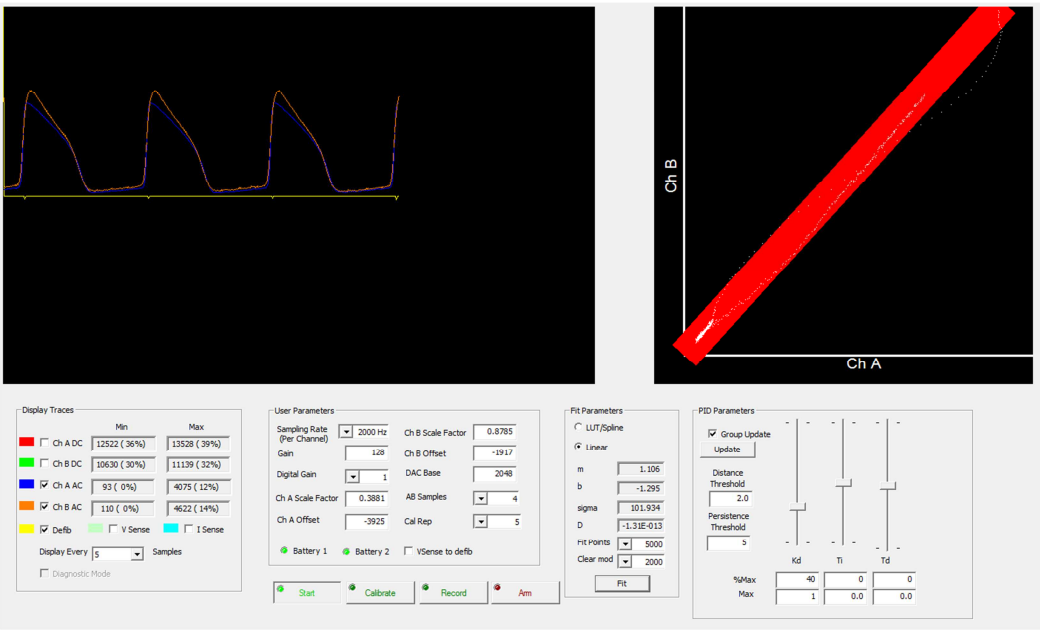

Figure 7.5. Screenshoot of the control program that communicates with the PID controller. Left window represents traces in the time domain that can be manually selected in the Display Traces control subpanel. Traces are: Channel A DC, Channel B DC, Channel A AC, Channel B AC, *DEFIB* signal, current on the V2CC output, and voltage on the V2CC output. Channel A represents electricaly activity on the surface of the LV, while Channel B represents electrical activity on the surface of the RV. The panel on the right represents phase space trajecotries as B vs A. The width of the red area represents distance threshold. PID control parameters can be entered in the PID Parameters subpanel.

Results

In the PID control experiment, a total of 10 New Zealand White rabbit's hearts were used. In the case of two of the rabbit hearts we were not able to induce VF, while with three of the rabbit hearts it was problematic to induce sustained VF, which thereby limited the number of control experiments. In the remaining five rabbit hearts, we were able to run up to 40 control experiments per heart. In all experiments we used only the proportional term.

We recorded optical traces that represent cardiac electrical activity on the surface of the heart, from the LV and RV, and subsequently processed them to study the cardiac dynamic during various intervals. These intervals include induced VF, applied feedback control, and restored sinus rhythm. Herein we present and analyze optical traces in the time and space domain. During applied control, we calculated the energy and the instantaneous power delivered to the heart.

Table 5.1 lists all control experiments with the heart number in the first column, The third and seventh heart are not listed as we were not able to induce VF. The second column represents the experiment number. Not all experiment number are listed, as some of them were only for recording of arrhythmias and various tests. The third column describes the type of the experiment and recordings with sinus rhythm are listed to indicate when calibrationwas performed, as the intensity of the fluorescence is gradually decreasing and therefore feedback gain K_D is effectively lower until next calibration is performed. In the case of the first seven hearts, K_D was calculated as the distance from the fit line without subtracting the threshold, therefore K_D is lower than in the experiments with the heart's numbers 8,9, and 10.

Figures 7.6-7.9 show the results obtained from four different experiments on the two different hearts. The results in Figures 7.6 and 7.7 are from the ninth heart (control experiments numbered as 15 and 17, respectively), while those presented in Figures 7.7 and 7.8 are from the tenth heart (control experiments numbered as 10 and 3 respectively). The experiment in Figure

7.9 was performed with the negative K_D multiplier to investigate how the PID control algorithm works when the feedback closed loops is positive. Time is plotted along the vertical axis; sinus rhythm is indicated in green; induced VF is represented in red; and blue traces indicate when the feedback control was applied. All four experiments represent successful defibrillation, and, upon observing that the perturbation shocks restored normal sinus rhythm, feedback control was terminated manually.

Panels (A) in Figures 7.6-7.9 are 3D plots of RV versus LV and time along the vertical axis. Panels (B) and (C) are projections of the 3D plots in panels (A) observed from a point that is perpendicular to the action potential upstroke in the RV-LV plane (diagonal) and a projection observed from a point in the RV-LV plane that looks into the tip of the action potential upstroke (diagonal), respectively. Panel (D) shows the transitions from induced cardiac arrhythmias when feedback control was applied (red-blue transition), and the transition from termination of the feedback control into sinus rhythm (blue-green transition). In each case, the duration of the traces is 500 ms before and after the transition. Panel (E) shows the normal distance in the phase space between the current phase space state and a fit line. Panel (F) shows the *DEFIB* signal that is computed from the normal distance in panel (E) after threshold and persistence parameters are applied. Panel (G) represents the defibrillation current in Amperes that is proportional to the *DEFIB* signal in panel (F).

Table 7.1. List of all PID control experiments with control parameters.

Heart No	Exp. trial No	Description	Kd	DT	PT	Note
1	1	Sinus-Calibration				
1	3	Stab. & Defib. - Yes	0.3	1	10	
1	4	Sinus-Calibration				
1	5	Stab. & Defib. - Yes	0.5	1	10	
1	6	Sinus-Calibration				
1	7	Stab. & Defib. - Yes	0.5			
1	8	Stab. & Defib. - Yes	1	1	10	
1	9	Sinus-Calibration				
1	10	Stab. & Defib. - Yes	1			
1	11	Sinus-Calibration				
1	12	Stab. & Defib. - Yes	0.25	1	10	
1	13	Stab. & Defib. - Yes	0.25	1	10	
2	3	Sinus-Calibration				
2	6	Stab. & Defib. -Yes	0.1	1	10	
2	7	Stab. & Defib. - No	0.1	1	10	
2	8	Stab. & Defib. - Yes	0.1	1	10	
2	9	Sinus-Calibration				
2	10	Stab. & Defib. -Yes	0.1	1	10	
2	11	Stab. & Defib. -Yes	0.05	1	10	
2	12	Stab. & Defib. - No	0.025	1	10	
2	13	Stab. & Defib. -Yes	0.05	1	10	
2	14	Stab. & Defib. - No	0.05	1	10	
2	15	Stab. & Defib. -Yes	0.1	1	10	
2	16	Stab. & Defib. - No	0.1	1	10	
2	18	Sinus-Calibration				
2	19	Stab. & Defib. -Yes	0.1	1	10	
2	20	Stab. & Defib. -Yes	0.2	1	10	
2	21	Stab. & Defib. -Yes	0.2	1	10	
2	25	Sinus-Calibration				
2	26	Stab. & Defib. - No	0.8	1	10	
2	27	Stab. & Defib. - No	0.8	1	10	
2	28	Sinus-Calibration				
2	29	Stab. & Defib. -Yes	0.8	1	10	
4	1	Sinus-Calibration				
4	3	Stab. & Defib. -Yes	-0.1	1	10	

4	4	Stab. & Defib. -No	0.1	1	10	
4	5	Stab. & Defib. -No	-0.2	1	10	
4	8	Sinus-Calibration				
4	9	Stab. & Defib. -No	-0.2	1	10	
4	10	Stab. & Defib. -No	-0.4	1	10	
4	11	Stab. & Defib. -No	-0.5	1	10	
4	12	Sinus-Calibration				
4	13	Stab. & Defib. -Yes	-0.4	1	10	
4	14	Stab. & Defib. -No	0.4	1	10	
4	15	Stab. & Defib. -No	-0.4	1	10	
4	16	Sinus-Calibration				
4	17	Stab. & Defib. -Yes	-0.6	1	10	
4	18	Stab. & Defib. -Yes	-0.8	1	10	
4	19	Stab. & Defib. -Yes	-0.8	1	20	
4	20	Stab. & Defib. -No	-0.8	2	20	
4	21	Sinus-Calibration				
4	22	Stab. & Defib. -Yes	-0.6	1	10	MVT present
4	23	Stab. & Defib. -Yes	-0.6	1	10	MVT present
4	24	Stab. & Defib. -No	-0.6	1	10	MVT present
4	25	Stab. & Defib. -No	-1	1	10	MVT present
4	26	Stab. & Defib. -No	-1	1	10	MVT present
4	27	Stab. & Defib. -Yes	-1	1	10	MVT present
5	2	Sinus-Calibration				
5	3	Stab. & Defib. -Yes	-0.3	1	10	
5	4	Stab. & Defib. -Yes	-0.3	1	10	
5	5	Stab. & Defib. -Yes	-0.5	1.5	10	
5	8	Sinus-Calibration				
5	9	Defibrilation - Yes	-2	1	10	Strong shocks-Defib. w/ VF control
5	10	Defibrilation - Yes	2	1	10	Strong shocks-Defib. w/ VF control
5	11	Defibrilation - Yes	1	1	10	Strong shocks-Defib. w/ VF control
6	0	Sinus-Calibration				
6	1	Stab. & Defib. -Yes	-0.1	1	10	
6	1-1	Stab. & Defib. -No	-0.05	1	10	
6	1-2	Stab. & Defib. -No	-0.1	1	10	
6	2	Sinus-Calibration				
6	3	Stab. & Defib. -Yes	0.1	1	10	
6	4	Stab. & Defib. -Yes	0.05	1	10	
6	5	Stab. & Defib. -Yes	0.05	1	10	

6	6	Sinus-Calibration				
6	7	Stab. & Defib. -Yes	0.05	1	10	
6	8	Stab. & Defib. -Yes	0.1	1	10	
6	9	Sinus-Calibration				
6	10	Stab. & Defib. -Yes	0.1	1	10	
6	11	Sinus-Calibration				
6	12	Stab. & Defib. -Yes	0.15	1	10	
6	13	Stab. & Defib. -No	0.15	1	10	
6	14	Stab. & Defib. -Yes	0.15	1	10	
6	16	Sinus-Calibration				
6	17	Stab. & Defib. -Yes	0.1	1	10	
6	17-1	Stab. & Defib. -No	0.1	1	10	
6	18	Stab. & Defib. -Yes	0.15	1	10	
6	19	Stab. & Defib. -Yes	0.2	1	10	
6	20	Stab. & Defib. -Yes	0.3	1	10	
6	21	Stab. & Defib. -Yes	0.2	1	10	
6	22	Stab. & Defib. -No	0.5	1	10	
6	23	Stab. & Defib. -No	0.25	1	10	
8	1	Sinus-Calibration				The mesh electrode inside the LV
8	2	Stab. & Defib. -Yes	5	1	10	
8	3	Stab. & Defib. -Yes	5	1	10	
8	4	Stab. & Defib. -Yes	5	1	10	
8	5	Stab. & Defib. -Yes	5	1	10	
8	6	Stab. & Defib. -Yes	5	1	10	
8	7	Stab. & Defib. -Yes	5	1	10	
8	8	Stab. & Defib. -Yes	3	1	10	
8	9	Stab. & Defib. -Yes	2	1	10	
8	10	Sinus-Calibration				
8	12	Stab. & Defib. -Yes	2	1	10	
8	13	Stab. & Defib. -Yes	4	1	10	
8	14	Stab. & Defib. -Yes	4	1	10	
8	15	Stab. & Defib. -Yes	4	1	10	
8	16	Stab. & Defib. -Yes	2	1	10	
8	17	Stab. & Defib. -Yes	3	1	10	
8	18	Stab. & Defib. -Yes	3	1	10	
8	20	Sinus-Calibration				
8	21	Stab. & Defib. -Yes	2	1	10	
8	22	Stab. & Defib. -Yes	2	1	10	
8	23	Stab. & Defib. -Yes	1	1	10	
9	6	Sinus-Calibration				The coil electrode

						inside the LV
9	7	Stab. & Defib. -No	0.5	1	30	
9	8	Stab. & Defib. -No	2	1	30	
9	9	Stab. & Defib. -No	5	1	30	
9	10	Stab. & Defib. -No	10	1	10	
9	11	Stab. & Defib. -No	10	0.5	10	
9	12	Stab. & Defib. -No	2	0.5	10	
9	13	Stab. & Defib. -Yes	5	0.5	10	
9	14	Sinus-Calibration				
9	15	Stab. & Defib. -Yes	2	1	10	
9	16	Sinus-Calibration				The mesh electrode inside the LV
9	17	Stab. & Defib. -Yes	1	1	30	
9	18	Stab. & Defib. -Yes	1	1	30	
9	19	Stab. & Defib. -Yes	1	0.5	10	Same VF pattern as in 17
9	19-1	Stab. & Defib. -No	1	0.5	30	Different VF pattern
9	19-2	Stab. & Defib. -No	2	0.5	30	VF with small with of trajectories
9	20	Stab. & Defib. -Yes	5	0.5	30	VF with small with of trajectories
9	21	Sinus-Calibration				VF with small with of trajectories
9	22	Stab. & Defib. -Yes	1	0.3	30	
9	23	Sinus-Calibration				
9	24	Stab. & Defib. -Yes	2	1	30	
9	25	Stab. & Defib. -Yes	1	1	30	
9	26	Stab. & Defib. -No	1	1	30	
9	27	Stab. & Defib. -No	1	1	30	
9	28	Stab. & Defib. -No	2	1	30	
9	29	Stab. & Defib. -Yes	4	1	30	
9	30	Sinus-Calibration				
9	31	Stab. & Defib. -Yes	1	0.3	5	
9	32	Stab. & Defib. -Yes	1	1	30	
9	33	Stab. & Defib. -Yes	1	1	30	
9	34	Sinus-Calibration				Same VF pattern as in 32
9	35	Stab. & Defib. -Yes	1	2	10	
9	36	Stab. & Defib. -Yes	1	1	30	
9	37	Stab. & Defib. -Yes	3	1	40	
9	38	Stab. & Defib. -Yes	4	1	50	
10	1	Sinus-Calibration				
10	1-1	Stab. & Defib. -No	0.2	2	10	

10	1-2	Stab. & Defib. -No	2	2	2
10	1-3	Stab. & Defib. -No	-2	2	2
10	1-4	Stab. & Defib. -No	-5	2	5
10	2	Stab. & Defib. -Yes	-10	1	5
10	3	Stab. & Defib. -Yes	-20	1	5
10	4	Sinus-Calibration			
10	5	Stab. & Defib. -Yes	2	1	20
10	6	Stab. & Defib. -Yes	2	1	20
10	7	Sinus-Calibration			
10	8	Stab. & Defib. -Yes	0.5	1	30
10	9	Sinus-Calibration			
10	10	Stab. & Defib. -Yes	0.5	1	30

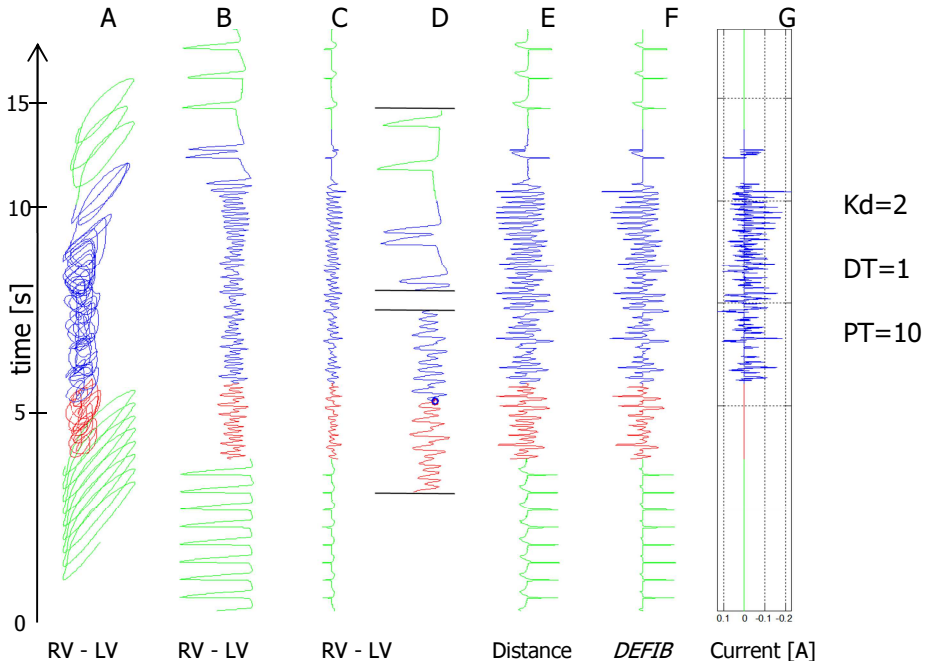

Figure 7.6. Optical traces representing electrical activity at the surface of the ninth heart during sinus (green), induced VF (red), applied feedback control (blue), and after termination of the feedback control (green). The seven columns are described in the text.

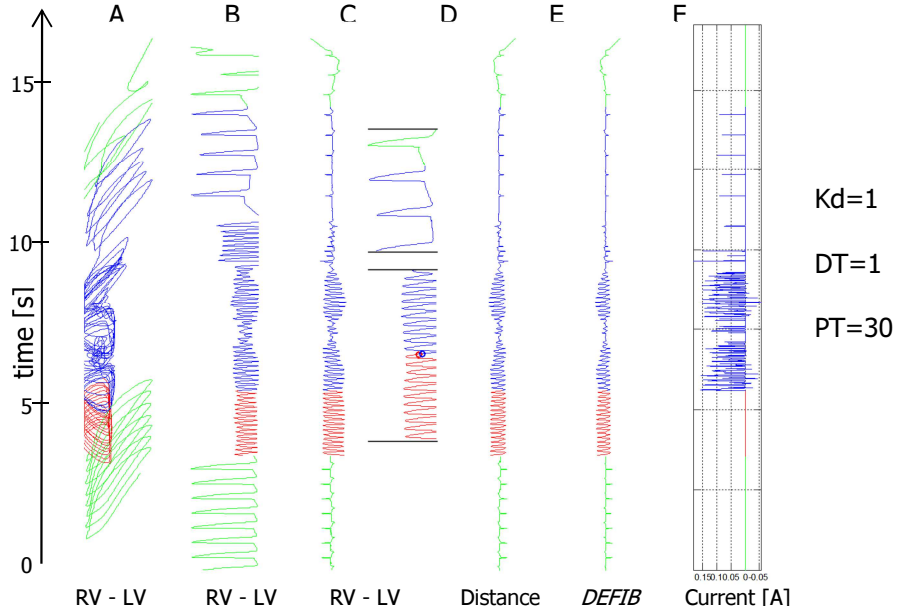

Figure 7.7. Optical traces representing electrical activity at the surface of the ninth heart during sinus (green), induced MVT (red), applied feedback control (blue), and after termination of the feedback control (green).

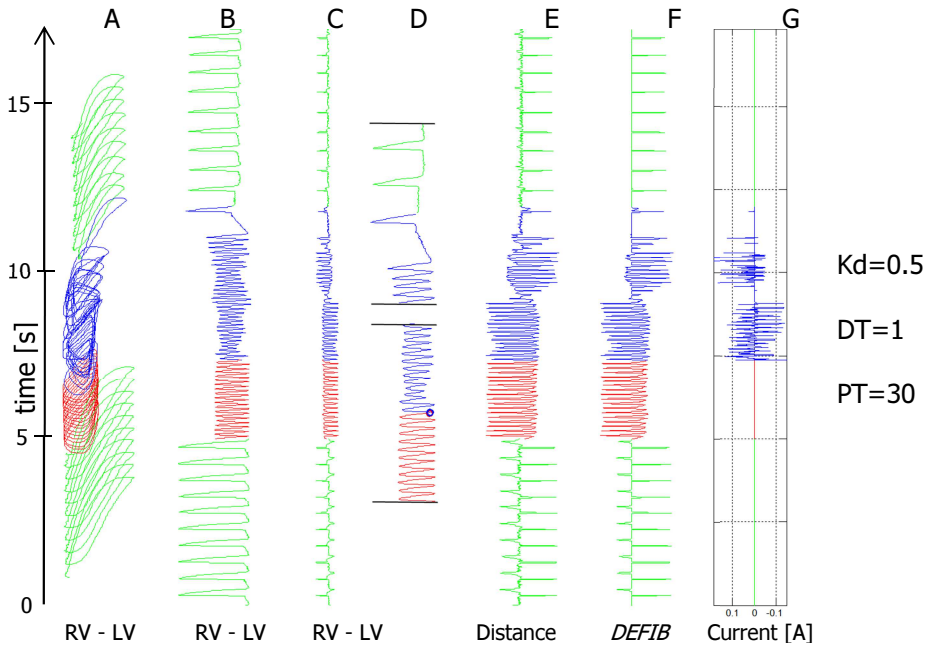

Figure 7.8. Optical traces representing electrical activity at the surface of the tenth heart during sinus (green), induced MVT (red), applied feedback control (blue), and after termination of the feedback control (green).

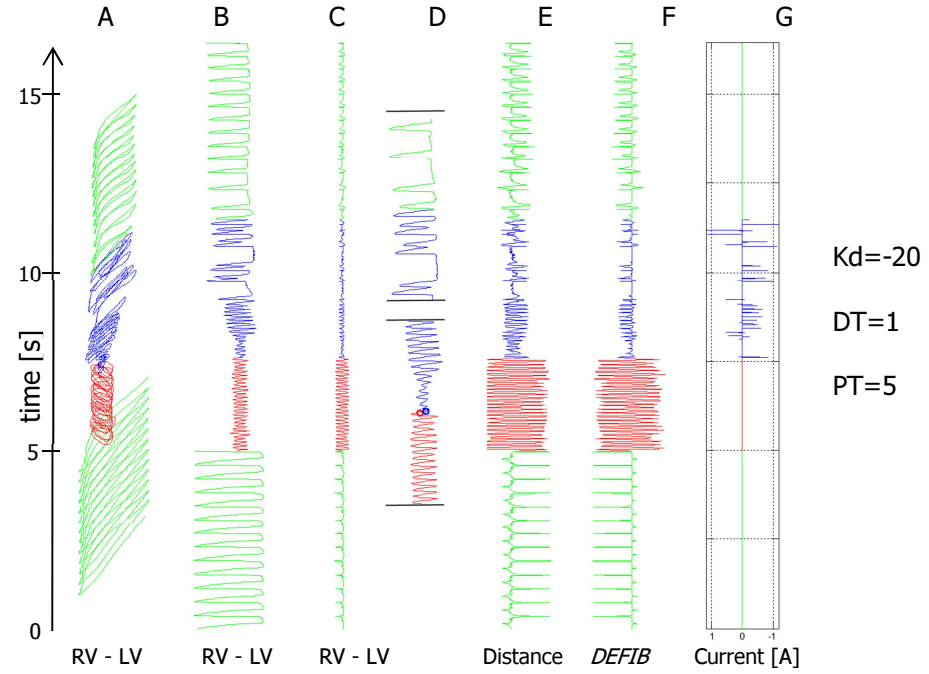

Figure 7.9. Optical traces representing electrical activity at the surface of the tenth heart during sinus (green), induced VF (red), applied feedback control (blue), and after termination of the feedback control (green). The K_D multiplier was negative.

Phase space trajectories of the experiments presented in Figures 7.6-7.9 are plotted in Figure 7.10. For each time interval representing sinus rhythm, induced arrhythmia, applied feedback control and restored sinus rhythm after termination of the feedback control, trajectories are plotted in separate subpanels. The color coding is the same as in Figures 7.6-7.9.

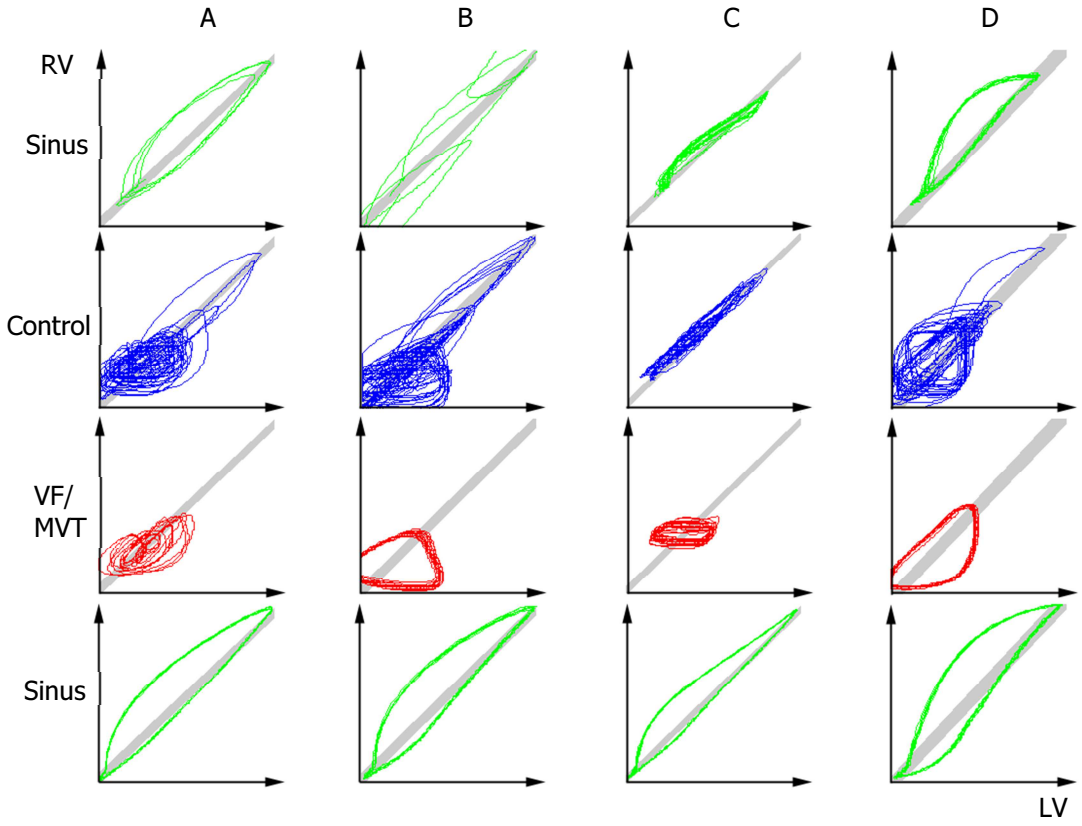

Figure 7.10. Phase space trajectories of the experiments presented in Figures 7.6-7.9, plotted as RV vs LV. The width of the gray shaded area represents threshold distances from the fit line. Panel (A) corresponds to the experiment presented in Figure 7.6. Panel (B) corresponds to the experiment presented in Figure 7.7. Panel (C) corresponds to the experiment presented in Figure 7.8. Panel (D) corresponds to the experiment presented in Figure 7.9.

Figures 7.11-7.14 represent the instantaneous power delivered with the control system and delivered energy over time for the control experiments shown in Figures 7.6-7.9.

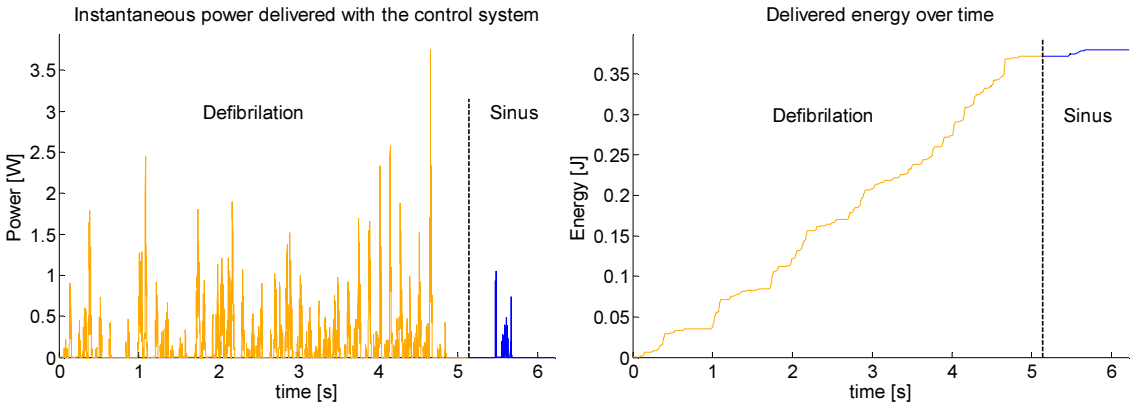

Figure 7.11. Instantaneous power delivered by the control system and integrated delivered energy over time for the experiment trial shown in Figure 7.6.

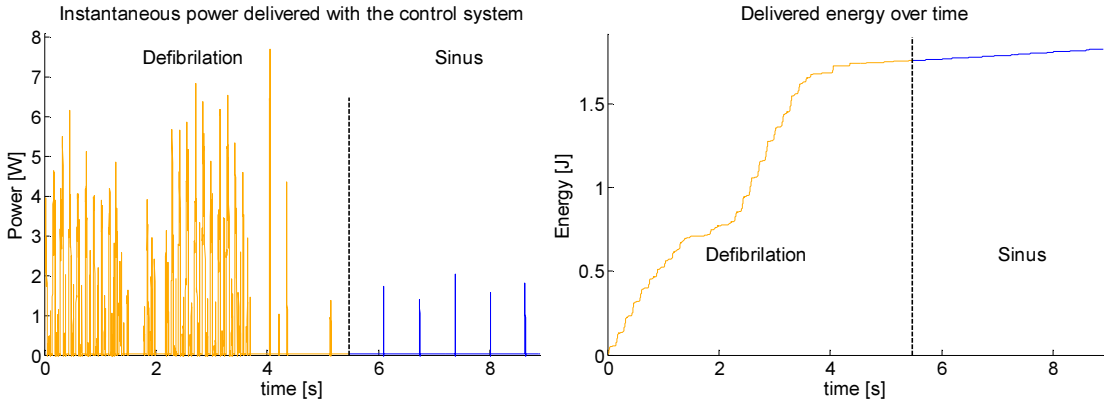

Figure 7.12. Instantaneous power delivered by the control system and integrated energy over time for the experiment trial shown in Figure 7.7.

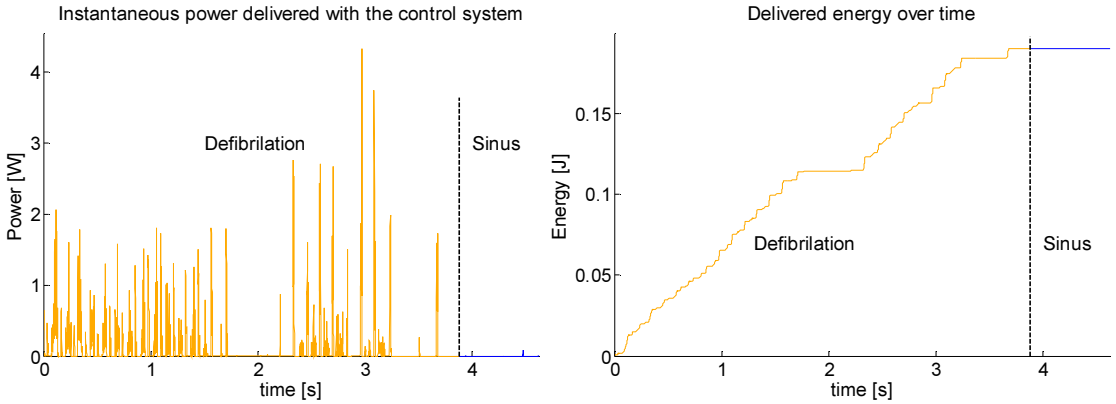

Figure 7.13. Instantaneous power delivered by the control system and integrated delivered energy over time for the experiment trial shown in Figure 7.8.

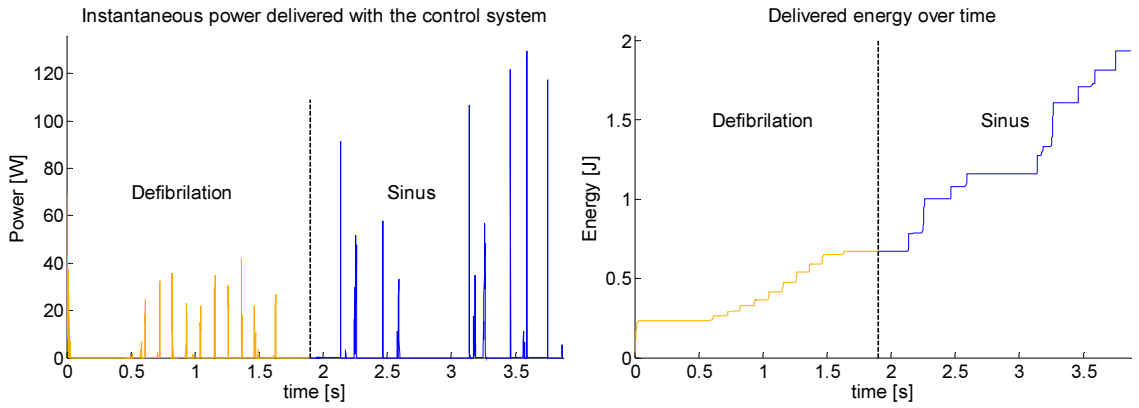

Figure 7.14 Instantaneous power delivered by the control system and integrated delivered energy over time for the experiment trial shown in Figure 7.9. Note that the feedback controler was set in a positive feedback configuration.

Discussion

In our experiments with the PID control algorithm, our initial task was to perform calibration during sinus rhythm and to minimize eccentricity of the closed loop trajectories during normal sinus rhythm. Minimization was often a challenging task due to the numerous interdependent experimental variables: the distance of the optical fibers from the heart; the location and size of the areas monitored with the optical fibers; and the presence of any mechanical movement of the heart. If the eccentricity of the closed loop trajectories during sinus rhythm was very small, setting the PID control parameters was straight forward; while if the eccentricity was very pronounced, setting the optimal PID control parameters was often a challenging task, as will be explained. The mutual dependence between DT and $K_{D,}$ can be easily explained, as perturbation shocks are proportional only to the portion of the distance in phase space that is above the DT; therefore, higher DT means necessarily higher $K_{D,}$ and vice versa.

After successful calibration, VF was induced and control was applied with standard initial control parameters that would be subsequently optimized, and they were: K_d=2; DT=1, and PT=10. If the control restored sinus rhythm, VF was induced again and the strength of the perturbation shock was lowered. We repeated this sequence until we crossed the threshold and

were unable to defibrillate the heart, assuming that the VF patterns were the same. In this process we were also adjusting PT so that there is no apparent perturbation shock once sinus rhythm is restored. The DT was adjusted based on the VF pattern. If phase space trajectories during VF were very narrow then DT had to be decreased to as low as 0.5, which was often the case with MVT. Having lower DT imposed a problem with unwanted perturbations during restored sinus rhythm and lower DT required larger PT.

Figure 7.6 shows one of the control experiments with initial tryout parameters that we did not consider as optimal for two reasons, although the instantaneous power and the total delivered energy in the corresponding Figure 7.11 are quite low. The first reason is that the feedback gain $K_{D,}$was 2 and we assumed that $K_{D,} = 1$ should also be successful as $K_{D,} = 1$ was the common value in most of the successful control experiments. The second reason is that the perturbation shocks were delivered even in restored sinus rhythm, panel (B) of Figure 7.6. This is no surprise if we observe panel (A) in Figure 7.10, as from phase space trajectories during sinus rhythm it is obvious that even in sinus rhythm, the trajectories are outside the gray shaded area. Noting that the boundaries of the gray shaded area represent location of the threshold, the PID controller will deliver a perturbation shock proportional to the instantaneous distance from the current phase space state to the edge of the gray shaded area, and this shock will be delivered even during restored sinus rhythm. This represented a serious problem in our experimental design and one which we tried to minimize through multiple solutions. Our initial solution was implementation of collimating lenses on the ends of the optical fibers to collect emitted fluorescence from a larger area. In that way, through averaging, differences in excitation between the LV and RV are minimized. Another solution was better placement of the optical fiber, until we observed that that the opening of the phase space trajectories during sinus rhythm was minimized. As a last solution, luckily, part of the trajectories outside the gray shaded area are only during depolarization and are very short in duration, therefore setting PT to the number of samples representing action potential upstroke duration is an easy solution if everything else fails.

In the subsequent control experiment, we lowered the feedback gain, $K_{D,} = 1$, and increased PT to 30 samples. As a result we didn't observe any perturbation shock during restored sinus rhythm, meaning that PT=30 was the optimal value. However, when we compared delivered energies in the corresponding figures, Figure 7.12 with Figure 7.11, it seemed contradictory that the lower feedback gain would result in a 5 times increase of the delivered energy. The contradiction is resolved if we look at the phase space trajectories, panels (A) and (B) in Figure 7.10, from which it is obvious that the VF pattern was completely different in these two experiments. In panel (B) that corresponds to the experiment in Figure 7.7; red phase space trajectories represent MVT and they are significantly wider than the red phase space trajectories in panel (A) that represent VF. Therefore, we were unable to repeat the experiment in Figure 7.6 to determine the optimal parameters, and, moreover, since in the experiment in Figure 7.7 phase space trajectories were very wide during MVT, feedback gain could be set probably as low as 0.2, as that is the ratio of the energies between these two experiments. Nevertheless, although the experiment in Figure 7.7 was successful it was certainly with highly unoptimized control parameters and we cannot conclude that defibrillation energy of over 1.5 J was really necessary to defibrillate the heart. It is reasonable to expect that the energy could be significantly lower.

The control experiments in Figures 7.8 and 7.9 are from another heart. Up to this point we had empirically observed that PT of 30 samples is usually the optimal value. That was proved true once again, as shown in panel (B) of Figure 7.8 where there is no indicated perturbation shock in the restored sinus rhythm. As the phase space trajectories in panel (C) of Figure 7.10 look similar to the phase space trajectories of the control experiment in Figure 7.6, panel (A) in Figure 7.10, in terms of a width of the closed loops we tried even lower feedback gain, K_d=0.5. Our control experiment was successful, being able to defibrillate the heart with even lower energies than in our experiment in Figure 7.6. This certainly proves that defibrillation in the control experiment, Figure 7.7, was with high, non-optimal parameters and raises the possibility that the control parameters in the control experiment in Figure 7.6 could be even further optimized.

The control experiment in Figure 7.9 is performed with reversed polarity across the defibrillation electrodes, which was achieved with the negative $K_{D,}$. This means that the feedback controller operates in a positive feedback loop, and we hypothesized that such a control experiment should deliver significantly higher instantaneous power and still be able to defibrillate the heart through a smaller number of high power shocks. Figure 7.14 shows that, with the positive feedback loop, instantaneous energies are an order of magnitude higher, although number of shocks is smaller, as expected.

Conclusions

In our experiment with the PID feedback controller, we showed that the heart can be defibrillated using a novel approach for cardiac control from phase space considerations. Methods of cardiac control, cardiac dynamic during VF, and how low energy perturbation shocks affect the cardiac dynamic are elaborated in the Discussion section in Chapter VI and in Chapter III. Briefly, in areas at the border of the spiral waves, the cardiac dynamic tends to be chaotic due to multiple perturbations. These perturbations have their origin from nearby spiral waves, the cardiac pacing intrinsic control system, and other nearby areas exhibiting complex dynamics. Low energy shocks act as an additional perturbation that, due to their low energy, cannot change the dynamic in the areas where spiral waves are formed. The main characteristic of the chaos dynamic is that future states are unpredictable and highly sensitive to initial conditions, or, in other words, perturbations. Therefore, if an external organized perturbation in areas with a chaotic dynamic becomes dominant, it will lead to an organized dynamic supported by the external control system. Over time, the organized dynamic from certain areas will, through constant organized perturbations, affect the dynamics of its surrounding areas, including the spiral waves. As the number of spiral waves and their radii depend on the degree of chaos in the border zone, any organized dynamic in the border zones will suppress spiral waves through organized and dominant perturbations. Ideally, synchronicity will be established across the entire

heart and will lead ultimately to sinus rhythm. It is important to note that the PID algorithm is designed to deliver a perturbation shock only when there is an irregularity in the cardiac dynamic. The feedback control signal is calibrated during sinus rhythm, establishing a threshold for a feedback signal. In that way, when sinus rhythm is restored, perturbation will be terminated automatically.

In all experiments with PID feedback control we used only a proportional term, while integral and derivate terms were not explored in any depth. While experiments with only a proportional term were successful with optimal parameters of the PID controller, we had numerous unsuccessful experiments due to non-optimal parameters. The most difficult were experiments with MVT, since MVT is characterized with a certain correlation in excitation of the LV and RV and distance threshold often needed to be set as low as 0.5. With such a low distance threshold, once the heart was defibrillated, perturbation shocks were still delivered to the heart. However, our control method is primarily designed to work with VF and it actually works better if VF is more chaotic. We hypothesize that if we had used the integral term, then even during MVT the distance thresholds could be set higher than 0.5. Although distances in that case would be below the threshold, integral term will sum them over time and threshold will be exceeded. From that moment on, perturbation shocks will be the same, as there is no integral term; the integral term is a slowly changing variable and behaves as an offset or adjustable DT accommodating to the feedback signal, so that the perturbation shock will be delivered at a later time. Therefore, we hypothesize that with the addition of an integral term, our defibrillation method would be successful even with less optimized parameters, thus an integral term will make it more robust. In certain experiments we observed that the strength of the delivered shock can became unusually and unnecessarily high, especially if the PT and DT are set to low. The derivative term represents rate of change, and we hypothesize that with the addition of a derivative term, any sudden rise in the amplitude of the perturbation shocks will be damped.

Our PID control algorithm is based on the distances from a linear fit line in the phase space, and it is often ineffective due to many non-idealities in experimental setup. A more

advanced and complex algorithm could be based on distances from a non-linear curve, such as could be parameterized by the use of splines. Also, in the linear regression performed on a set of samples during sinus rhythm, we treated all samples with the same weight factors, but most of the phase space points during sinus rhythm are clustered into two sets. The first set consists of states representing full repolarization, and it is close to the origin. The second set consists of states representing the plateau of action potential located in the upper right corner in the phase space. This is the reason why the gray area follows a line that connects minima and maxima in the phase space. In Figure 7.10D, during initial sinus rhythm, as mentioned in the Discussion section, trajectories are curved below the gray area. However, the slope of the linear fit line will not be affected significantly since the number of phase space points representing these curved trajectories is at least an order of magnitude smaller in comparison to the total number of phase space points. Adding weight factors to the phase space states for the linear regression fit would result in a fit line that is along the trajectory representing the rise of an action potential, and that fit line will be more suitable as a reference than the trajectory representing repolarization.

As mentioned above, one of the difficulties we faced during experiments was to achieve an optimal balance between the distance threshold, the shock strength, and the persistence, as variables are interdependent. Moreover, induced VF patterns are not necessarily the same from one VF to another VF and that presents additional challenges in setting the optimal PID control parameters. Also, the physiology of the isolated heart changes over time and the heart becomes ischemic over time. Due to photo-bleaching of the potentiometric dye, we could not run more than a few experiments, as the PID control parameters had to be recalibrated and this lowers the possibility of being able to repeat control experiments under the same conditions. In experiments this is quite contrary since, ideally, recalibration has to be done for each control experiment, as each recalibration introduces new control parameters and that makes repeating the control experiment, even with the same VF pattern, questionable. Additionally, from one heart to another, parameters that seem perfect for one heart can be different for another heart, as the locations of perturbation electrodes in respect to monitored area vary. In summary, we conclude

that in successful control experiments, control parameters do not necessarily mean that control parameters were optimal or that the perturbation current was ideally minimal. On the other hand, all unsuccessful experiments resulted from incorrectly set control parameters rather than failure on the part of control method.

Certain PID control parameters such as PT could be automatically determined during initialization. As PT corresponds to the phase space stated during action potential upstroke, PT should be equal to the number of samples that are outside of the gray shaded area.

Based on these considerations, we find that establishing a statistic over the control experiments is not possible. Any statistic would be biased with many experimental variables, as our control algorithm is not optimized on them. Basically, we do not yet have the algorithm that will calculate optimized feedback control signal based on the numerous experimental variables, as experiments we did through manual adjustments should serve as a guide and tell us how to optimize the algorithm and make it "smart". We tested principles and ideas, and confirmed them many times through the experiments. Optimization is not part of that.

CHAPTER VIII

FINAL WORDS

In the previous two chapters we presented the experimental study of two cardiac control methods based on continuous feedback via delivery of small, energy perturbation shocks. The mechanisms for both methods are based on the same principles behind chaos control and can be explained from the phase-space perspective, although with a substantially different approach. Delayed Feedback Control (DFC) and Proportional-Integral-Differential control (PID), deliver perturbation shocks proportional to the deviation from the periodic orbit that is targeted for stabilization. This consequentially means that the control methods (or in other words the Feedback Controller) must have a "memory" of the orbit that is targeted for stabilization. In the case of the DFC method, memory is inherited from the dynamic of ventricular fibrillation (VF). From many existing orbit periods during VF, DFC allows and supports only a particular (prior and user-defined) orbit period to exist, while other orbit periods are suppressed. In the case of PID control, the Feedback Controller has memorized the phase space orbits during sinus rhythm fitted to a line. Therefore, as the DFC method aims to stabilize VF, converting it to a monomorphic ventricular tachycardia (MVT), the PID method aims to convert VF to a normal sinus rhythm, and it can be used even to prevent the occurrence of VF.

The mechanisms of cardiac control are mostly observed from the perspective of chaos control theory, so our approach began with the description of a chaotic system, and, based on the rules that govern and describe any chaotic dynamic, we sought out parallels with the cardiac dynamic. The heart consists of numerous cardiac cells and its phase space is effectively infinite; moreover, it is has spatio-temporal complexity that increases the difficulty. Ideally, control should be created within that infinite-dimensional phase space, but that is not practically possible and currently not even theoretically feasible. Therefore, certain approximations must be made. Our

approximation is that the infinite-dimensional phase space of the cardiac dynamic can be embedded as a 2D phase space in the form of the electrical activity of the left ventricle (LV) versus that in the right ventricle (RV). As both control methods are purely derived from considerations in the 2D phase space defined as above, our understanding of the mechanisms of cardiac control is limited by the domain of control methods. Control mechanisms are well understood in the 2D embedded space; however, in real experiments control methods are not capable of "sensing" the actual complexity, just as bacteria on a flat dish are incapable of understanding of a 3rd dimension. Additionally, even if the phase space of the heart is 2D, a transition from the theoretical control model to a real dynamic system must include certain additional parameters or variables that are specific for the system. Moreover, both of our control methods are certainly simplified even from the perspective of control theory. Luckily for us, coupling between the cardiac cells actually lowers the dimensionality of the system, and, as we are monitoring certain areas of the ventricles, our 2D state space has embedded most of the higher dimensionality of the natural infinite-dimensional phase space. Therefore, our hypothesis is that even with the 2D state space approximation we would be able to quantify well enough the complex dynamic of the heart. Also, in our experimental studies we did not aim to fully quantify and statistically describe the control methods; our aims were to gain a better understanding of cardiac control through our experiments and to understand the role of the experimental variables when we develop more advanced DFC and PID control methods. The important variation here is that the control algorithms will not be based on the 2D embedded phase space theoretical studies, where the heart is treated as a black box, but will include many experimental variables. Such control methods seem more suitable for increased cardiac control and for an understanding of the heart's physiology in general.

We deliberately included certain experimental variables in both control methods, and one of them was the minimization of the phase difference of activation between the LV and the RV during sinus rhythm. In our experimental setups we addressed this manually by adjusting the distances between the optical fibers and the heart, and by adjusting the size and location of the

areas being monitored. In the case of the PID control method, we added LED collimators to increase the areas of the monitored surfaces. In both control methods, we have yet to explore the possibility of adjusting in real time the delay of one of the signals, either from the LV or from the RV, that precedes another. In certain DFC control experiments we tried to delay preceding signals manually, but without an automatic method for calculation of the phase difference of activation, manual adjustment was almost impossible. Certainly, calculation of the phase difference of activation can be based on the correlation between signals. Threshold was another experimental variable that was included in the PID control methods, but the threshold is not an independent variable because of its high correlation with the phase difference in activation. The threshold is defined as a distance equal to a chosen number of standard deviations or, in other words, it corresponds to a width of the phase space trajectories during normal sinus rhythm, which is directly related to the phase difference of activation. Therefore, introduction of the threshold was mainly our "way around" to minimize the activation phase differences. Persistence threshold was another experimental variable introduced in the PID control method, and it corresponds to the number of samples required for the feedback control signal to always stay below the valid defined threshold during normal sinus rhythm. In other words, it is equal to the number of phase space states that represent the action potential upstroke during sinus rhythm. A more advanced control method might have an automatic calculation of the persistence threshold. It is also valid to include persistence threshold in the DFC control method, but we did not implement that parameter.

Certainly there are other experimental variables to note, and one of them is the distance from the perturbation electrodes to the monitored areas with the optical fibers. From our experiments we have only gained a limited understanding of that variable, and only in the DFC control method did we hypothesize that finite conduction velocity plays a role in adding the extra delay through the system. Still, from the experiments we recognize the importance of this experimental variable, and we propose that further studies are necessary on the theoretical models that will reveal the role of spatio-temporal distances between the perturbation areas and

the monitored areas. We further recognize that theoretical models would allow us to better understand the role of the spatial dimension of the cardiac dynamic in general.

In both control methods we hypothesized the mechanism of VF control and defibrillation through organized perturbation of a chaotic dynamic that would over time recruit areas of the heart with synchronized activity; we further hypothesized that global control would be achieved through expansion of the organized dynamic to the whole heart. Without imaging of the electrical activity on the surface of the heart, it is not possible to confirm our hypothesis, and therefore future studies ideally should include imaging that will give us another perspective and may even reveal new control mechanisms.

As mentioned above, both control methods, even if all experimental variables are excluded, are limited by their construction to being non-ideal control methods from the perspective of control theory. In the case of the DFC approach, the approximation is that the necessary memory is based only on a single phase-space state at a chosen moment in the past. A system that is targeted for stabilization needs to have the embedded periodic orbit targeted for stabilization in the embedded 2D phase space. The DFC algorithm will use that embedded information to stabilize that particular orbit period. If such an orbit period is not embedded, then the DFC control algorithm is not able to establish the desired control and stabilization. This can certainly lead to a user error in trying to stabilize a non-existent orbit period, but as is shown in Chapter VI, certain existing orbit periods are more easily stabilized than others. Thus certain orbit periods are preferable to others due to their underlying cardiac dynamic, and this has been demonstrated as we observed that orbit periods during VF are not uniformly distributed. This can be for a purely physiological reason, but it is also due to the fact that certain orbit periods are more strongly embedded in the 2D phase space such that the DFC control is able to "extract" them with a higher signal-to-noise ratio. In this case "noise" does not have the traditional meaning but represents integral information from all other embedded orbit periods. We hypothesize that by adjusting the distance of the optical fibers, along with the size and location of the monitored area, we have introduced the experimental variable that not only influences

phase difference of activation during rhythm, as discussed above, but also the distribution of the orbit periods in VF. The supporting facts are found in our observations that during VF different areas of the ventricles may have a different dynamic, and this hypothesis can be addressed in a theoretical study that uses a model of the heart. From these experiments we understand the importance of having preferable orbit periods, and any future DFC method could have an automatic procedure of "extraction" of the preferable orbit during VF as the most frequent orbit period. Also, we hypothesize that we would be able to stabilize most of the other less probable orbits by inclusion of many more states from the past and not the single one as is currently used. This approach is used in the extended DFC method that is proven in theoretical experiments (not cardiac) to be more robust and efficient, but we have not yet explored the extended DFC method.

In the case of the PID control method, as we mentioned above, included more experimental variables than in the case of the DFC method by also considering the distance threshold and the persistence threshold. On the other hand, the PID control method has more approximations than the DFC control method. One of the approximations, as discussed in the Conclusion section in Chapter VII, was that we have not yet included the integral and the derivative terms. Also, memory in the PID control method is in the form of a straight fit line as an approximation of the sinus trajectory, and as such the fit line is not exactly a true representative of phase space trajectories during sinus rhythm, as in the case of the DFC method. From our experiments we understood the limitations of a linear fitting, and the more advanced PID control method should be based on the spline fitting that would approximate a phase space trajectory during sinus rhythm more closely. Ideally, distances should be calculated from the analytical line that represents only repolarization trajectories during normal sinus rhythm. Moreover, a more complex algorithm should recognize trajectories that represent action potential upstroke and should not deliver any perturbation shocks at that time.

In summary, we successfully tested ideas and principles that would yield a better understanding of the methods of cardiac control with the ultimate aim of understanding the

mechanisms of cardiac control and defibrillation. Identifying all possible experimental variables is of crucial importance and was one of the aims of our experimental study – to develop more robust, effective and efficient control algorithms that are optimized to the nature of the system targeted for control. Identification of all the experimental variables would reveal parallels between the mechanisms of cardiac control and control theory, or more generally chaos theory. That will allow us to better understand cardiac control in terms of chaos control and also bring to light the differences, but it will certainly lead us to a better understanding of the cardiac dynamic fitted and bounded in a well-defined theory of chaos control. Many of the mechanisms of how perturbation shock affects the dynamic of the heart and achieves stabilization of VF or restoration of sinus rhythm have already been hypothesized in the Discussion sections of both control methods chapters. Those hypotheses were based on the observation of the patterns during applied feedback control and derived from the general reasoning behind control of a chaotic system. Once we identify the role of all experimental variables, we can study the role of all of the system's dynamic variables that govern self-sustained chaos without being limited by the influence of certain experimental variables. Finally, increased understanding of how perturbation shocks terminate and control VF will allow us to devise a systematic and unifying study that connects detection of phase singularities, and eventually the associated VF, with the optimal shape, amplitude, timing and duration of a defibrillation shock.

APPENDIX A[1]

THE POTENTIAL OF DUAL CAMERA SYSTEMS FOR MULTIMODAL IMAGING OF CARDIAC ELECTROPHYSIOLOGY AND METABOLISM

Mark R. Holcomb

Department of Physics and Astronomy, Vanderbilt University

Present address: Department of Physics, Davidson College, Davidson, North Carolina 28035; Tel: 704-894-2077; E-mail: maholcomb@davidson.edu

Marcella C. Woods

Department of Biomedical Engineering, Vanderbilt University Nashville, Tennessee 37235-1631; Tel: 615-322-4419; Fax: 615-322-4977; E-Mail: marcella.woods@vanderbilt.edu

Ilija Uzelac

Department of Physics and Astronomy, Vanderbilt University Nashville, Tennessee 37235-1807; Tel: 615-343-4124; Fax: 615-322-4977; E-mail: ilija.uzelac@vanderbilt.edu

John P. Wikswo

Department of Physics and Astronomy; Department of Biomedical Engineering; Department of Molecular Physiology and Biophysics; Vanderbilt Institute for Integrative Biosystems Research and Education Vanderbilt University Nashville, Tennessee 37235-1807; Tel: 615-343-4124; Fax: 615-322-4977; E-mail: john.wikswo@vanderbilt.edu

Jonathan M. Gilligan

Department of Earth and Environmental Sciences, Vanderbilt University Nashville, Tennessee 37235-1805; Tel: 615-322-2420; Fax: 615-322-2138; E-mail: jonathan.gilligan@vanderbilt.edu

Veniamin Y. Sidorov

Department of Biomedical Engineering; Vanderbilt Institute for Integrative Biosystems Research

---

[1] This is a peer reviewed manuscript published in Exp Biol Med (Maywood). 2009 Dec;234(12):1.

and Education Vanderbilt University Nashville, Tennessee 37235-1631; Tel: 615-322-4419; Fax: 615-322-4977; E-Mail: v.sidorov@vanderbilt.edu

Abstract

Fluorescence imaging has become a common modality in cardiac electrodynamics. A single fluorescent parameter is most commonly measured. Given the growing emphasis on simultaneous imaging of more than one cardiac variable, we present an analysis of the potential of dual camera imaging, using as an example our straightforward dual camera system that allows simultaneous measurement of two dynamic quantities from the same region of the heart. The advantages of our system over others include an optional software camera calibration routine that eliminates the need for precise camera alignment. The system allows for rapid setup, dichroic image separation, dual-rate imaging, and high spatial resolution and is generally applicable to any two-camera measurement. This type of imaging system offers the potential for recording simultaneously not only transmembrane potential and intracellular calcium, two frequently measured quantities, but also other signals more directly related to myocardial metabolism, such as $[K^+]_e$, NADH, and reactive oxygen species, leading to the possibility of correlative multimodal cardiac imaging. We provide a compilation of dye and camera information critical to the design of dual camera systems and experiments.

Keywords: Epifluorescence imaging; cardiac transmembrane potential; intracellular calcium; electrophysiology; cardiac electrodynamics; cardiac metabolism; dual camera imaging; ratiometric imaging; multimodal cardiac imaging

Introduction

Fluorescence imaging has become the primary modality for studying the electrodynamics of isolated hearts. Typically a single dye is used, and by monitoring the intensity of the fluorescence, a dynamic quantity can be observed. Frequently measured parameters in cardiac electrophysiology are transmembrane potential (V_m) and intracellular calcium concentration ($[Ca^{2+}]_i$). Ideally, both are viewed simultaneously,[28] and there is a growing number of published reports of simultaneous V_m and $[Ca^{2+}]_i$ in cardiac tissue using different imaging methods. Dual photodiode arrays have been developed, but these systems require precise alignment because of the small number of pixels.[13,17,44] As an example of the growing number of V_m – $[Ca^{2+}]_i$ studies, Omichi *et al.*[58] reported a study on whole hearts that examined V_m and $[Ca^{2+}]_i$ dynamics during ventricular fibrillation. They employed two cameras with appropriate filters placed side-by-side that were manually aligned to view approximately the same area of the heart. A more recent study by Hwang *et al.*[33] examined simultaneous V_m and $[Ca^{2+}]_i$ dynamics during defibrillation in rabbit hearts. They used two CCD cameras with different perspectives and had to implant four cactus needles into the heart as registration markers for use in a software program to match the V_m and $[Ca^{2+}]_i$ pixels to the same location. This methodology, which cannot provide the single-optical path of our approach, also introduces potential error in the data, as heterogeneities inserted in tissue produce shock-induced changes in polarization.[43,73] Hoeker *et al.*[30] describe a multi-modal optical mapping system that uses a dichroic mirror to perform dual calcium–voltage[44] and ratiometric calcium optical mapping[34] in the same cardiac preparation and used it to study an animal model of heart failure. Chuck *et al.*[15] reported on V_m and $[Ca^{2+}]_i$ activity in embryonic hearts using two cameras interfaced with a fluorescence microscope. The system we have developed addresses a different set of technical issues than those that occur with microscope imaging of planar cultures, small hearts or restricted epicardial imaging at very high magnification.

The challenge of controlling and synchronizing multiple cameras can be addressed using individual frame grabbers and custom software,[9,20] or with a commercial camera controller designed to support two cameras (for example, the MiCAM02 Dual Camera System, Scimedia USA Ltd, Irvine, CA). The latter approach has been used recently to image V_m and $[Ca^{2+}]_i$ in the *in vivo* mouse brain,[5] although no details are provided regarding the dual camera optical configuration. While most recent reports use multiple cameras, it is also possible to use mirrors to project two or more separate images onto the focal plane of a single camera, as was done for monochrome panoramic imaging of the epicardial V_m distribution of a rabbit heart,[9] or for multicolor imaging with a microscope (Dual-View and Quad-View, MAG Biosystems, Tucson, AZ).

In this paper, we describe a very straightforward dual CCD camera system which permits simultaneous measurement of two dynamic quantities from the same region. Our system is unique for a number of reasons. It is designed for rapid setup and has high spatial resolution over a large field of view. It utilizes dichroic image separation so that image acquisition is through a single optical path which maximizes light detection efficiency, eliminates parallax, and simplifies alignment of the images. The system can also be used to provide two separate image magnifications or camera frame rates. The computer control system supports configuration files that readily allow changes in camera parameters or the hardware setup. In the Results section we present multiple demonstrations of the utility of this dual camera system. We also analyze various issues regarding selection of dyes and illumination wavelengths for dual imaging as applied to cardiac metabolic measurements. The flexibility and simplicity of a dual camera system should enable a broader application of multimodal cardiac imaging.

Dual Camera Setup

Our dual camera system, in the configuration for simultaneous V_m and $[Ca^{2+}]_i$ imaging, is shown in Fig. 1. The first optical element is a dichroic mirror (635 DCLP, Omega Optical), oriented at 45° with respect to both cameras, that reflects the $[Ca^{2+}]_i$ signal and transmits the V_m signal. The V_m camera uses a 710 nm long pass filter (25 mm round 710AELP, Omega Optical), and the $[Ca^{2+}]_i$ camera uses a 585 $\pm$ 20 nm band pass filter (25 mm round 585AF40, Omega Optical). Both cameras have a lens (25 mm 1 inch format C-mount, Navitar) to which the filters are attached by a custom connector. In this figure, the setup contains two Dalsa cameras for high spatial resolution imaging (DS-12-16K5H, 128 × 128 pixels, typically 487 frames/second), but with simple changes in the image acquisition control software, either one or both cameras can be replaced with a Redshirt CCD for high temporal resolution (CardioCCD-SMQ, Redshirt Imaging 26 ×26 pixels, 5000 frames/second). The cameras are supported by a pair of custom mounting plates[20] supported by a tilt and rotation stage (Newport P080N). A 6 mm thick aluminum base

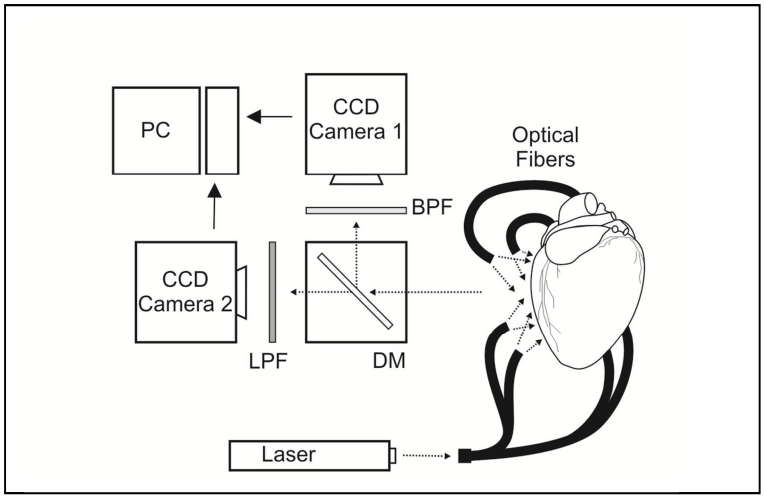

Figure 1. A diagram of our experimental setup configured for simultaneous recording of V_m and $[Ca^{2+}]_i$.

plate can accommodate various combinations of lenses and working distances. The entire system is mounted on a 20 cm × 20 cm lab jack that allows the height to be easily adjusted. A custom computer program controls all data acquisition, camera calibration, camera synchronization, laser illumination, and external stimuli.

Image Registration

For maximum usefulness, the images recorded by the cameras should correlate spatially as well as temporally. The Newport stages allow quick and accurate mechanical alignment. Because the translation stages are expensive, as are the custom machined parts, we developed an alternative to precise mechanical alignment using a numerical algorithm that allows fine image alignment with only very coarse mechanical alignment of the cameras. The breadth of image registration methods is reviewed elsewhere;[77] here we address those that have been applied to dual camera cardiac imaging and the simple approach we have adopted.

Direct placement of fiducial reference points on the heart that are visible in both cameras would permit a traditional image registration but interfere with the fluorescence data. Omichi *et al.*[58] reported placing a grid in the field of view to be used for image registration, with a positional accuracy of ±1 mm. However, in their approach, the two cameras view the heart from different perspectives, which invariably leads to less than ideal image registration. Therefore we chose a camera calibration technique which uses a stand-alone alignment grid of small points, each termed an alignment marker (AM). We used a backlit 35 mm photomask with a rectangular grid of translucent AMs containing 15 AMs in the horizontal direction and 11 AMs in the vertical direction. The size of the grid was matched to the field of view of both cameras for the magnification being used – the grid must be seen entirely and in focus by both cameras. The AMs were circular, with a diameter of approximately 0.15 mm so that the width of each AM will occupy two or three pixels using the 12 mm × 12 mm field of view we used in our experiments. The exact size of the AMs is not critical. A photomask is convenient but not necessary; we have

also used a simple grid made on a laser printer. The exact spacing of the AMs is also not critical since both cameras view the same grid and only their relative positions are used.

Were we to assume that light entering both cameras is paraxial and there is no difference in magnification due to unequal object distances or lenses, we could use a least-squares fit with corresponding alignment points to compute a global offset vector and rotation. We find that the generic method we have developed to correct for local distortions works well without the need for *a priori* assumptions regarding the sources of all distortions in the images. This is particularly important since the source of the largest distortions can change each time mechanical setup is altered. Our specific camera calibration implementation uses the rubber sheet transformation technique whose salient features are described by Gonzalez *et al.*[27] More sophisticated solutions to the general registration problem have been developed,[77] including using radial basis functions[77] or elastic registration.[3] The method we have chosen permits correction of distortions and at the same time is computationally simple enough to be applied in real-time. This allows the calibration to be integrated in the acquisition software.

The calibration procedure begins by recording one image with each camera, with the alignment grid in the field of view of both cameras. For each of the two images, we first identify the approximate location of each alignment mark (AM) in an image. To do this automatically we sort all pixels by intensity, while keeping their associated spatial coordinates. The brightest pixel is taken as the approximate location of one of the AMs. All pixels within a distance of five pixels from this pixel are removed from our search for other AMs, as the AM separation is about 10 pixels. With these nearby pixels removed from consideration, the brightest pixel remaining identifies the approximate location of another AM. We repeat this process of selection of the most intense pixel and removal of nearby pixels from the list until the approximate locations of all AMs are found.

Since the AMs are larger than one pixel, we next need to determine accurately the coordinates of the AM geometric centers. Because our AMs are less than two pixels in diameter,

we use the 3×3 set of pixels centered around each approximate AM location to determine a center-of-intensity of each AM given by

$$\vec{\mathbf{X}} = \frac{\sum_{i=x-1}^{x+1}\sum_{j=y-1}^{y+1} x_{ij}(I_{ij} - B)}{\sum_{i=x-1}^{x+1}\sum_{j=y-1}^{y+1} I_{ij}}, \qquad (1)$$

where $\vec{\mathbf{X}}$ is the calculated coordinates of the geometric center of the AM, I_{ij} is the intensity of the ij^{th} pixel, and B is the average background intensity of the entire image. In the case where (I_{ij}-B) gives a negative value, it is taken as zero. The approximate center of the AM, (x,y), in the previous step determines the limits of the summations. When the center-of-intensity has been computed for all AMs in both images, the resulting two tables of pairs of floating-point numbers listing the calculated geometric center of all AMs in the alignment grid form the completed correspondence map. We term each entry in a table an alignment point.

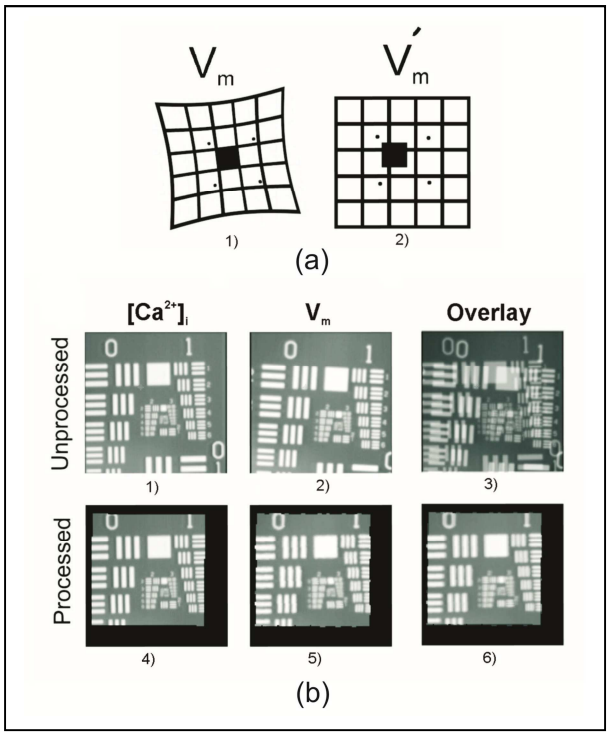

Figure 2. Image registration using the rubber sheet algorithm.

Were we to assume that there were no distortions between the two images, we could use a least-squares fit with corresponding alignment points to compute a global offset vector and rotation. However, because of distortions from the lenses and differences in magnification, we find it is better to use the alignment point correspondence map to identify and correct for local distortions. For our experiments, we arbitrarily choose to adjust the V_m image and leave the $[Ca^{2+}]_i$ image unchanged, although it does not matter which image is adjusted. For each of the 16,384 pixels in the V_m image, we locate the closest four V_m alignment points. As illustrated in Fig. 2(a) part 1, we use our knowledge of the grid geometry to locate the corresponding four alignment points in the $[Ca^{2+}]_i$ image, part 2, denoted V_m'. We compute the position of a V_m pixel in relation to the $[Ca^{2+}]_i$ image by calculating the location $\vec{\mathbf{X}}'$ in V_m', the processed V_m image, that corresponds to the location (*i,j*) given by

$$\vec{\mathbf{X}}' = \frac{\sum_{k=1}^{4} \vec{\mathbf{r}}'_k - (\vec{\mathbf{r}}_k - \vec{\mathbf{X}}_{ij})}{4}, \qquad (2)$$

where $\vec{\mathbf{X}}_{ij}$ is the original V_m pixel location, and $\vec{\mathbf{X}}'$ is the calculated corresponding point in the V_m' image. $\vec{\mathbf{r}}'_k$ and $\vec{\mathbf{r}}_k$ are alignment points in the $[Ca^{2+}]_i$ and V_m images, respectively.

Most pixels from the V_m image do not correspond to only one pixel in the V_m' image. Because of distortions, the fractional pixels mapped into a particular pixel in V_m' may not sum to unity. If *n* pixels from V_m partially map to pixel (*i,j*) in V_m' with percentages f_n, the intensity of the *ij*th pixel in V_m' is given by

$$I'_{ij} = \frac{\sum_{k=1}^{n} I_k f_k}{\sum_{k=1}^{n} f_k}. \qquad (3)$$

No processing is done on the $[Ca^{2+}]_i$ images other than to eliminate pixels that do not map to V_m'. At the end of this procedure a calibration file is saved that describes how to process the images from both cameras. An interactive program written in C allows the camera calibration to be accomplished very quickly. The same calibration file can be used repeatedly to process movies as long as the cameras are not moved with respect to each other.

To demonstrate our technique, the cameras were deliberately misaligned. After completing the calibration procedure just described, we placed a test target in front of the cameras. Images (1) and (2) in Fig. 2(b) are unprocessed and show the test target (USAF 1951 Res Target, Edmund Optics) as seen from both cameras. Image (3) is the combination of the raw images before processing, with one set to 50% transparency. Note there are significant translational and rotational differences in the two images. Images (4) and (5) were processed using the calibration data. Image (6) shows the combined processed images, with the same one set to 50% transparency; note the significant improvement in this overlay in comparison with the one in (3). In tests in which the cameras were better aligned, the positions of features in the images typically differ by no more than one pixel for the 128×128 pixel image. In the example shown in Fig. 2, the processed images differ by as much as two pixels. We believe that the large rotation in this example exposes the weakness of using only linear interpolation, although the results are still quite good.

A disadvantage of the software calibration is that all pixels in the CCD cameras are not utilized since the aligned images can only represent the intersection of what is seen by both cameras. This effect can be seen as the black borders in the processed images (4)-(6) in Fig. 2(b). A second disadvantage is that the calibration makes no allowance for surface curvature of the heart, which could affect the mapping of a single point on the heart to the two planar images which were aligned using a planar array of AMs. For the small field of view we typically use, however, this is not a significant problem, but it could be accounted for by using a non-planar alignment grid in the calibration procedure, for example a solid object with AMs.[9] The C source

code which accomplishes our camera calibration and applies it to images can be found at http://www.vanderbilt.edu/viibre/technologies.html.

Field Lens for Image Magnification

A field lens arrangement commonly used in these types of imaging studies is easily configured by attaching a positive achromatic lens (15 mm, Omega Optical) to the cubical mirror housing (NT56-265, Edmund, not shown in Fig. 1), such that the lens is now the first element in the dual camera system. We can magnify and narrow the field of view to be as small as 2 mm × 2 mm, which would be required to image, for example, a mouse heart. In adjusting the various parameters, we found that focusing the 25 mm lenses to infinity and adjusting the camera distance from the mirror-lens combination works best for controlling the field of view. Varying the distance between the entire system and the heart works best for adjusting focus. This configuration achieves a small field of view without losing a significant amount of light and preserves the shallow depth of field that is important in this type of imaging.

Spectral Overlap Estimation of RH-237 and Rhod-2AM

To estimate the spectral overlap between RH-237 and Rhod-2AM fluorescence, we followed two separate experimental protocols that we have published previously.[67] In the first protocol at the beginning of the experiment the heart was stained only with the V_m-sensitive dye RH-237 and both voltage and "calcium" images were recorded using the respective filters. The data acquired through the calcium filter represented the bleed-through of the voltage signal, which we termed the calcium error (error $[Ca^{2+}]_i$). Thereafter the Ca^{2+}-sensitive dye Rhod-2AM was administered, and data were acquired while the heart was continuously stimulated at a pacing rate of 300 ms. In the second experimental protocol only Rhod-2AM was used at first. In this situation, the "voltage" images represented the voltage error (error V_m). After collecting data, the heart was then stained with RH-237, the pacing protocol was repeated, and voltage and calcium fluorescence were recorded again. To calculate the error due to overlap of the voltage and

calcium spectra, the amplitude of the calcium transient error was normalized to the amplitude of $[Ca^{2+}]_i$:

$$\% \text{ error } [Ca^{2+}]_i = (\text{error } [Ca^{2+}]_i / [Ca^{2+}]_i) \times 100\%.$$

The error for voltage measurements was calculated as the amplitude of the voltage error normalized to the amplitude of the V_m signal:

$$\% \text{ error } V_m = (\text{error } V_m / V_m) \times 100\%.$$

Experimental Preparation

All experiments were conducted in accordance with the National Institutes of Health regulations for the ethical use of animals in research and were approved in advance by the Vanderbilt Institutional Animal Care and Use Committee. New Zealand white rabbits of either sex weighing 2.7 to 3.1 kg were used in the experiments. The detailed description of the heart preparation has been published previously.[68,74] The animals were preanesthetized with ketamine (50 mg/kg), heparinized (1,000 units), and anesthetized with sodium pentobarbital (60 mg/kg). The heart was quickly removed from the chest and mounted on a Langendorff apparatus for retrograde perfusion with oxygenated Tyrode's solution of the following composition (mM): 133 NaCl, 4 KCl, 2 $CaCl_2$, 1 $MgCl_2$, 1.5 NaH_2PO_4, 20 $NaHCO_3$, and 10 glucose. For experimental protocols where endocardial imaging was required, the right ventricle was isolated from rest of the rabbit heart, stretched across a Plexiglas frame, and cannulated via the right coronary artery.[37] All experiments utilized either a commercial current source (Bloom), custom USB-powered and -controlled stimulators,[31] or a custom high-voltage stimulator.[48]

Fluorescent Dye Staining

We have used our dual camera system in a variety of experimental protocols that demonstrate the capabilities of the approach. Unless otherwise noted, the excitation-contraction uncoupler 2,3-butanedione monoxime (BDM [Sigma-Aldrich, St. Louis, MO]) was added to the perfusate (15 mM) to eliminate contractile optical artifacts. For field-shock and trabecula experiments, the heart

or right ventricle preparation was placed in a bath; otherwise the heart was in air. The first experiments using this system were studies of simultaneous V_m and $[Ca^{2+}]_i$ on the anterior left ventricle of a Langendorff-perfused rabbit heart in response to unipolar cathodal and anodal stimulations.[67] In these experiments, the heart was first stained with the calcium-sensitive dye Rhod-2AM by delivering slowly 1 mL of the dye stock solution (0.5 mg/mL DMSO) via an injection port above the aorta. Thereafter, 10 μL of the voltage-sensitive dye RH-237 (1 mg/mL DMSO) was gradually administered through the same injection port. In other experiments in which V_m alone was imaged, the heart was either stained with RH-237 as described above or with another voltage-sensitive dye, di-4-ANEPPS (200 μL of stock solution with concentration of 0.5mg/mL DMSO). Ratiometry experiments utilized RH-237 without an excitation-contraction uncoupler. Hearts were loaded with dihydroethidium (DHE), an indicator of reactive oxygen species (ROS), by recirculating Tyrode's solution containing 6.34μM DHE in the perfusion system for 20 minutes, followed by a washout period of 25 minutes with standard Tyrode's solution. In all experiments the fluorescent dyes were excited by 532 nm laser light (Verdi, Coherent, Santa Clara, CA), although it is also possible to use other light sources, including light emitting diodes.[19,20,39]

Fluorophore Emission Spectra

To compare the emission spectra of DHE as a reporter of ROS, Rhod-2 AM as an indicator of $[Ca^{2+}]_i$, and di-4-ANEPPS and RH-237 as indicators of V_m, we used 532 nm laser light for excitation. A USB2000 miniature fiber optic spectrometer (Ocean Optics, FL, USA) was used to record the fluorescence spectra of the different probes. The spectrometer comprises optical elements coupled with a 2048-element linear silicon CCD array detector which is responsive from 200 to 1100 nm.

NADH Imaging

While not yet imaged in dual camera mode, in anticipation of multimodal cardiac imaging (MCI), we have demonstrated that these cameras can also be utilized to image ischemia-related

changes in the concentration of reduced nicotinamide adenine dinucleotide (NADH), which plays a critical role in the mitochondrial generation of ATP. NADH is autofluorescent – it absorbs light in the ultraviolet range of 320-380 nm and emits fluorescence between 420-480 nm. The oxidized form (NAD^+), however, does not absorb light in the 320-380 nm range. Thus imaging NADH gives a measure of the redox state of the mitochondria.[51] To spatiotemporally measure NADH, light from a mercury lamp (Nikon) was passed through a 365±5 nm band pass filter and directed onto the surface of the isolated heart via a dichroic mirror. The emitted light was band pass filtered at 470±20 nm before being collected by a CCD camera. The heart was immobilized mechanically, and an excitation-contraction uncoupler was not used.

Results

Estimation of spectral overlap of RH-237 and Rhod-2AM

Figures 3(a) and 3(b) demonstrate the fluorescence recordings when hearts were stained with either RH-237 or Rhod-2AM, respectively.[68] No prominent RH-237 fluorescence bleeding through the band pass filter is observed in Fig. 3(a) (lower trace). The mean % error of $[Ca^{2+}]_i$ was 3.97 $\pm$ 1.66 (3 hearts). If the heart was stained only with Rhod-2AM (Fig. 3(b)), slight leakage of $[Ca^{2+}]_i$ fluorescence through the long pass filter is observed (lower trace). The mean % error of V_m was 4.45 $\pm$ 1.94 (3 hearts).

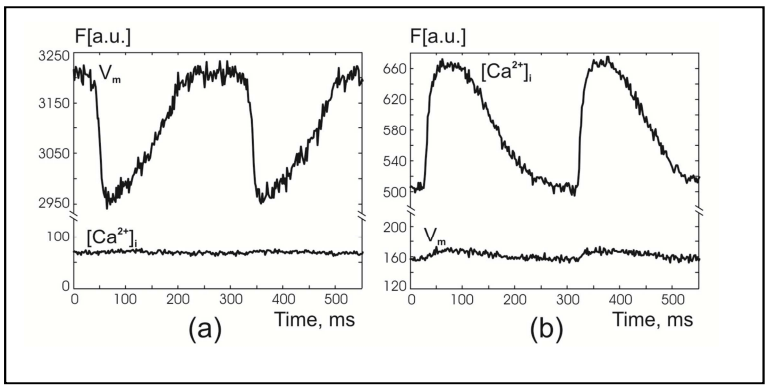

Figure 3. Changes in fluorescence recorded at one pixel when the heart was only stained with either RH-237 (a) or Rhod-2 AM (b) alone. (Reprinted from Sidorov, et al.67 with permission).

Dual V_m and $[Ca^{2+}]_i$ Imaging

Figure 4 shows the V_m and $[Ca^{2+}]_i$ responses to a strong systolic stimulus (S2) applied to an isolated rabbit heart. A detailed discussion of these data is beyond the scope of this paper and is presented elsewhere,[67] but the figure does show the ability to distinguish the detailed spatiotemporal relationship of the two signals. Briefly, it is well established that V_m leads $[Ca^{2+}]_i$ during normal pacing (S1 stimulation), as shown in Fig. 4(a). Fig. 4(b) clearly demonstrates the interesting feature that upon termination of the S2 stimulus, the $[Ca^{2+}]_i$ distribution correlates spatially with the virtual-electrode V_m polarization pattern for an S1-S2 coupling interval of 90 ms, although as shown by the color bars, the magnitude of the peak-to-peak excursion in the $[Ca^{2+}]_i$ signal is smaller than the peak-to-peak difference observed in V_m (also evident for the single pixel time traces shown in Fig. 4(a)).

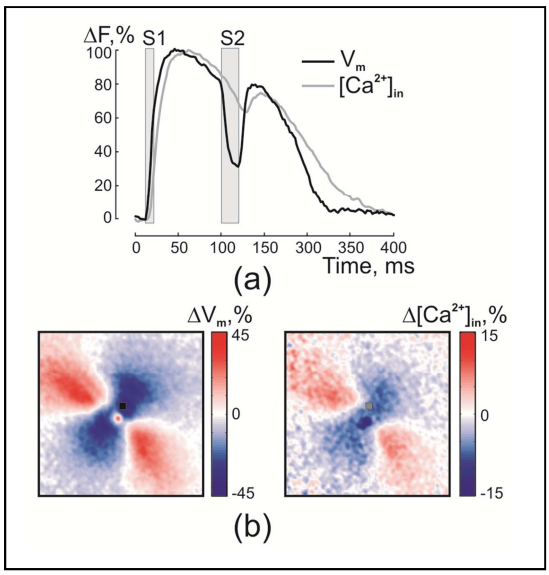

Figure 4**.**The voltage and calcium responses to anodal stimulation for a 12 mm × 12 mm field of view of the epicardium of an isolated rabbit heart.

One of the important applications of the dual camera system is the study of the V_m and $[Ca^{2+}]_i$ relationship during an arrhythmia. Figure 5 displays an example of the spatiotemporal dynamics of V_m and $[Ca^{2+}]_i$ during reentry initiated in the isolated right ventricle of a rabbit heart.

The analyzed interval corresponds to the time segment when the stationary rotor located inside the white square of the image in Fig. 5(a) drives the arrhythmia. The snapshots of V_m and $[Ca^{2+}]_i$ distributions and an activation map of one complete rotation are shown in Fig. 5(b). Figure 5(c) demonstrates the ability of dual camera imaging of V_m and $[Ca^{2+}]_i$ to quantify the instantaneous phase of the heart, without having to rely on time-delay embedding.[13,28] To create the V_m versus $[Ca^{2+}]_i$ phase map in the left panel of Fig. 5(c), we calculated the phase angle as $\arctan([Ca^{2+}]_i/V_m)$. On the right of panel (c), the phase-space trajectory[8,28] is shown for the black pixel in the phase map. The change in the shape, size, and center of the trajectories reflects the onset of the higher-frequency reentrant arrhythmia following S2.

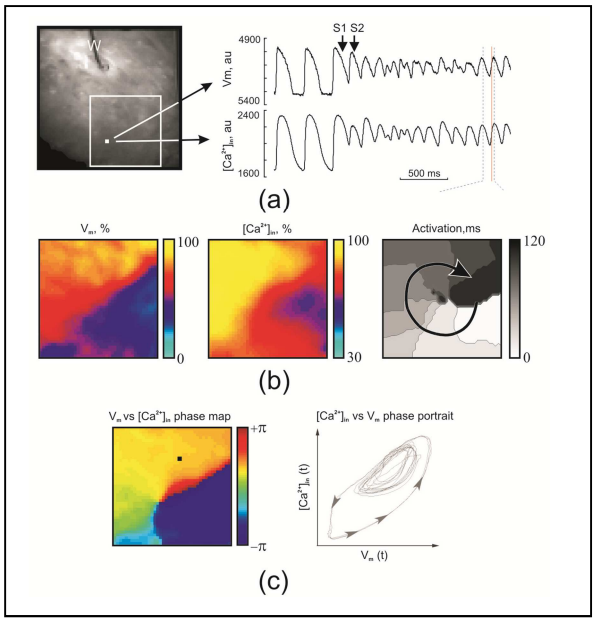

Figure 5**.** The voltage and calcium dynamics in the isolated right ventricle preparation.

Field Lens Magnification of Trabecula

As a demonstration of the ability of the system to capture high-resolution dual images using the field lens arrangement, Fig. 6 shows a 5 × 5 mm^2 image of a trabecula from an isolated right ventricle of a rabbit heart. The V_m and $[Ca^{2+}]_i$ traces in panel (a) illustrate the tissue

response during continuous pacing (S1) and uniform field shock (S2, 20 V/cm, S1-S2 interval of 70 ms) at opposite ends of the trabecula. Figure 6(b) illustrates the effect of field polarity (-30 V/cm and +30 V/cm, S1-S2 interval of 100 ms) on tissue response at one location. By using an opaque piece of black paper to shield the trabecula from the underlying tissue,[2] we avoided contamination of the images by the fluorescence of the underlying tissue. The field-induced polarization is clearly seen in optical traces from opposite ends of the trabecula, showing opposite polarities of shock-induced changes in V_m.

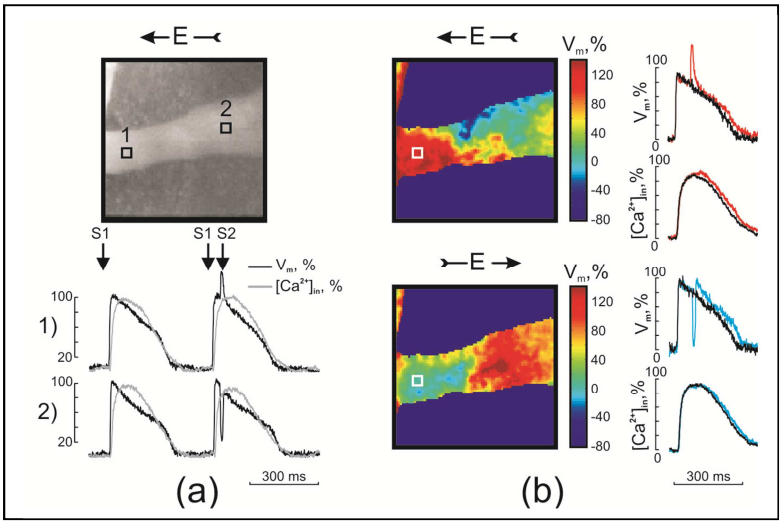

Figure 6. The response of a right ventricular trabecula to field stimulation.

:

This system can also be configured for different types of experiments. For example, it is an ideal setup for ratiometric imaging of V_m, in which only the filters need to be changed.[38] Figure 7 demonstrates optical signals acquired with a 610 ± 30 nm band pass filter (Fig. 7(a)) and 710 nm long pass filter (Fig. 7(b)). The short/long wave fluorescence ratio significantly reduces the motion artifact (Fig. 7(c)).[40,41] To quantify the motion amplitude, horizontal and vertical time-space plots of fluorescence intensity were created (Fig. 8). The motion waves are evident in the space derivative maps in Fig. 8. The crest positions of the motion waves show motion deflections occurring at the spatial scale of less than 2 mm. We anticipate the ease of acquiring ratiometric measurements with this system will be particularly important in metabolic

imaging experiments since the use of contraction blockers can result in a large reduction of cardiac metabolic demand, and, hence, it is important to develop practical techniques to reduce motion artifact.

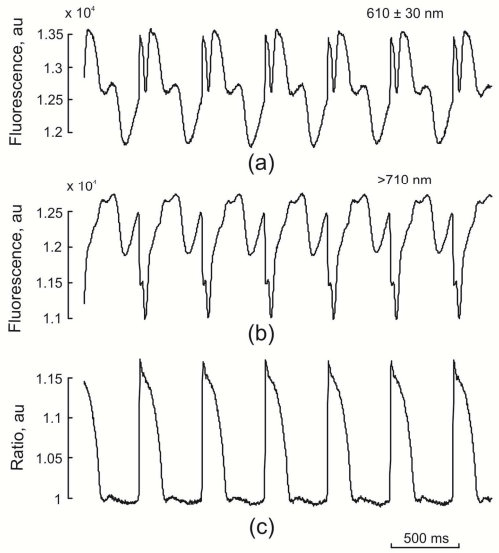

Figure 7. Ratiometric measurement of optical action potential.

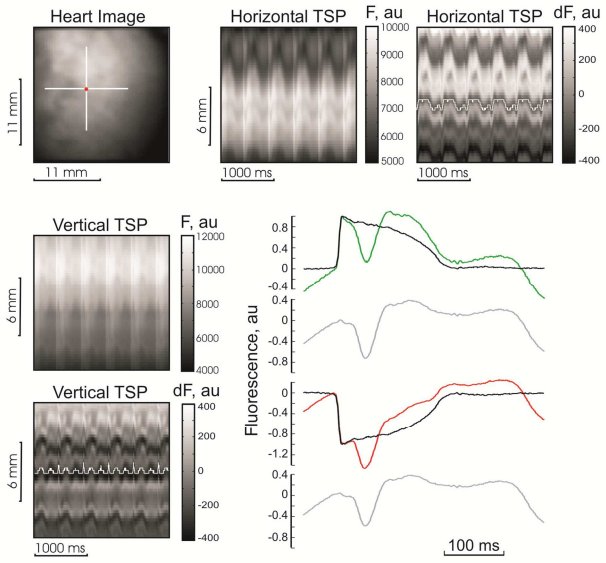

Figure 8. Motion amplitude quantification in the ratiometric determination of V_m.

Dual-rate Imaging

We have also used this system with one low-resolution, high-speed camera running at 5000 frames/second (26 ×26 pixels, CardioCCD-SMQ, Redshirt Imaging) and one high-spatial resolution camera (DS-12-16K5H, 128 × 128 pixels, 487 frames/second, Dalsa) in a field shock study.[74] In this case the heart was stained with only a voltage dye (di-4-ANEPPS), and both cameras used the same long pass filters (>607 nm). The dichroic mirror was replaced with a 70% transmission/30% reflection beam splitter which allowed both cameras to view the same activity. Figures 9(a) and (b) show the whole heart as acquired with the Redshirt and Dalsa CCDs, respectively. Comparing the high temporal resolution Redshirt fluorescence data in Fig. 9(c) with the high spatial resolution Dalsa data in Fig. 9(d) reveals how much activation information is lost in the Dalsa data. Prominent positive polarization of the right ventricle and negative polarization of the left ventricle are apparent in panel (c), whereas in panel (d) this left/right disparity is reduced to a single frame. Simultaneous acquisition with a Dalsa and a Redshirt CCD is a powerful combination that allows analyses of both high spatial and high temporal information of the same imaging parameter.

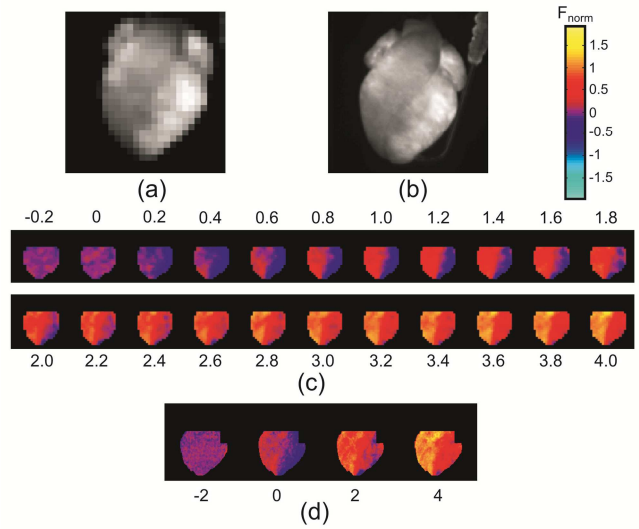

Figure 9. Whole heart field stimulation data acquired simultaneously with high temporal and high spatial resolutions using the dual camera system.

Other Fluorescent Parameters

This dual camera setup can additionally be used for imaging of $[K^+]_e$ (Guy Salama, Personal Communication), NADH,[21,51] and ROS[36,47] by changing only the optical filters and possibly the excitation source from those used for V_m and $[Ca^{2+}]_i$. Dihydroethidium (DHE) is a membrane-permeable dye that is oxidized preferentially by O^{2-} to form ethidium when inside the cells, which then stains the cell nuclei, emitting a red fluorescence that reports the ROS concentration. Given that spectra of fluorescent dyes are reported in various media, Fig. 10 allows comparison of the emission spectra of DHE, Rhod-2 AM, di-4-ANEPPS, and RH-237 as measured in an isolated rabbit heart. With our two-camera system, we can readily image two quantities simultaneously, consistent with the various excitation/emission wavelengths presented in Table 1.

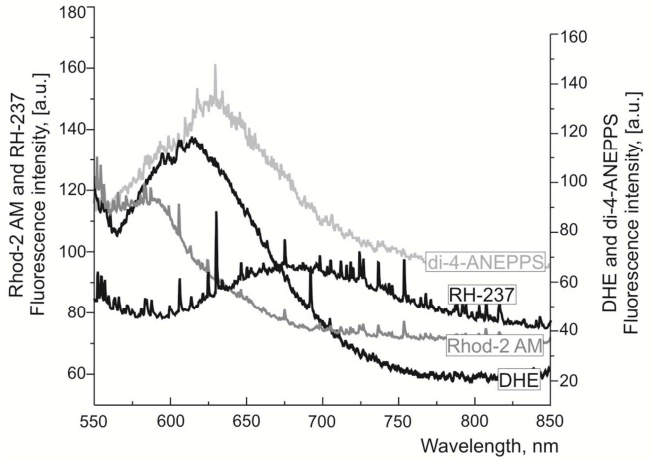

Figure 10. A comparison of the emission spectra measured from a rabbit heart for DHE as a reporter of ROS, Rhod-2 AM as an indicator of $[Ca^{2+}]_i$, and di-4-ANEPPS and RH-237 as indicators of V_m.

Figure 11 provides a demonstration of the type of results that can be obtained with CCD imaging of NADH changes with ischemia and reperfusion, albeit without dual camera imaging. After 30 minutes of global anoxia, the autofluorescence is markedly brighter, indicating an

increase in NADH. After reperfusion with oxygenated perfusate, NADH autofluorescence quickly decreases. These results correlate well with previous investigations.[51,70] Because the autofluorescent spectra of NADH do not overlap with the spectra of many of the other optical probes we consider, it is possible to image NADH and $[Ca^{2+}]_i$[7] and NADH and V_m[65] in the same heart. We must note that Mayevsky and Rogatsky[51] review the difficulties encountered with NADH imaging in blood-perfused hearts because the absorption/emission spectra of hemoglobin overlap those of NADH. Our ability to image multiple metabolic variables will allow us to assess the magnitude of the metabolic compromises of non-blood perfusion.

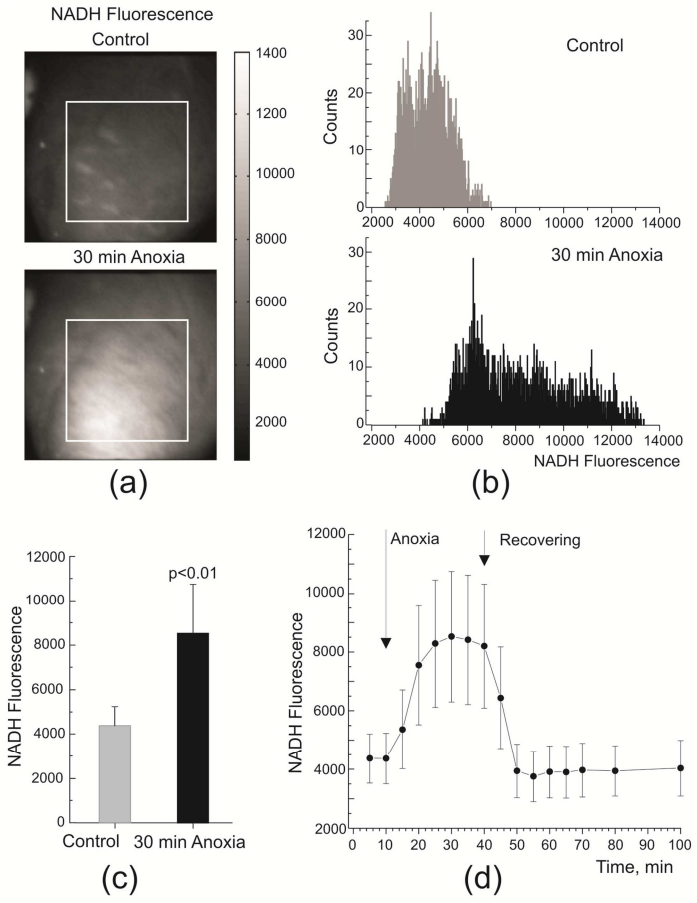

Figure 11. NADH autofluorescence in a Langendorff-perfused rabbit heart under normal conditions (95% O_2 and 5% CO_2) (control) and after 30 minutes of global anoxia (95%N_2, 5%CO_2).

Discussion

Research in cardiac electrophysiology (CEP) tends to focus at two divergent spatial scales – that of the ion channel and the whole heart. Patch-clamp studies of the molecular cardiology of voltage-gated ion channels have the goal of identifying targets for antiarrhythmic drugs and enabling and motivating the development of numerical models of the cardiac action potential in the whole heart. Studies of the whole heart, most recently using fluorescent imaging of the transmembrane potential and intracellular calcium, are directed towards validation of these models, identification of the macroscopic mechanisms of cardiac reentry and fibrillation, and the response of the heart to pacing and defibrillation shocks. Despite these efforts, reentrant cardiac arrhythmias, sudden cardiac death (SCD), and congestive heart failure remain difficult to treat.[35,42,56] The efficacy of many antiarrhythmic drugs has been questioned, in part because of patient-specific pharmacogenetics.[10,29,57,59,63,66] Hence, the prophylactic treatment of choice for SCD remains the implantable cardioverter/defibrillator (ICD). While the ICD has reduced mortality or morbidity in selected populations,[4,11,16,52,54,55] its prophylactic application in a variety of cardiac disorders has yet to be demonstrated. The challenge in developing new treatments for cardiac disease is to understand the spatiotemporal complexity of ischemic heart disease and heart failure, which can best be addressed with new multimodal measurements and integrated mathematical models. One might ask whether optical measurements of voltage or calcium alone are sufficient for this task. Obviously, the ability of two-camera systems, such as the one we report, to record both variables simultaneously is a step forward.

Looking beyond voltage and calcium, the larger issue is the extent to which other signals are relevant. It is becoming increasingly appreciated that metabolic factors play a role in SCD through their tight interrelationship with CEP,[18,66] and that identification of these factors will strengthen our mechanistic understanding of rate-dependent cardiac remodeling, heart failure, and fatal arrhythmias, as well as lead to new therapies.[71] However, few scientists working on the

measurement and modeling of whole-heart CEP have the tools needed to correlate recordings of spatiotemporal patterns of cardiac activity with measures of metabolism that may affect, or even define, arrhythmogenic substrates.

There is extensive literature on the metabolism of the entire heart and individual cardiomyocytes; there is also a recent growing interest in the quantitative relationships between cardiac metabolism and the ischemic action potential. Recent studies have shown that the ROS associated with ischemia also produce lipid peroxidation products that have a direct effect on ion channel conductances, thereby producing a previously unrecognized coupling between CEP and metabolism.[6,25] What is missing is the ability to correlate spatial patterns of metabolism with those of electrical activity associated with spatial heterogeneities (*e.g.,* regional ischemia), and potentially fatal arrhythmias – an ability that would enable the testing of hypotheses regarding metabolic interventions to reduce the risk of fatal arrhythmias. Hence there is a need to implement technological innovations that will allow the integration of state-of-the-art electrophysiological imaging of the isolated rabbit heart with optical imaging of the metabolism associated with both regional ischemia and tachycardia, *i.e.,* to create correlative MCI.

While the two-camera system we describe in this report is directed towards V_m and $[Ca^{2+}]_i$, in our analysis we conclude that it should be possible to use this system to record additional variables that are more directly related to myocardial metabolism, and hence the two-camera approach is a first step towards MCI. We have already shown that superconducting quantum interference device (SQUID) imaging of action and injury currents can be correlated spatially with $V_m(t)$.[23,24,32] Additional methodologies might include positron emission tomography (PET),[12,45,69] single photon emission computed tomography (SPECT),[26,53] or magnetic resonance imaging (MRI) and its associated spectroscopies,[22] although there are technological hurdles that must be surmounted to achieve simultaneous optical imaging with these technologies, with those for SQUID and MRI far greater than for PET or SPECT.

The challenges of the optical approaches to MCI are related to overlap of the emission spectra of the various dyes and tissue autofluorescence, as illustrated in Fig. 12. There are

several possible ways that these might be addressed, ranging from development of new dyes, [49,50,64] careful selection of narrow-band excitation and filters, and spectral deconvolution.[76] The use of rapid switching of different illumination wavelengths gated to individual image frames for high-frame-rate, *i.e.,* time-domain multiplexing of multiple metabolic signals, is useful if the excitation spectra do not overlap. The ability of an acousto-optic modulator to control high-speed illumination of the heart has already been demonstrated for older, low-speed CCD cameras.[46,72] An alternative would be to use LEDs of different colors whose pulsed excitation is interleaved and synchronized with the camera frames. Because LEDs have a rise time of microseconds, this approach would be possible as long as each color LED was excited for a sufficiently long train of pulses that it could reach the thermal equilibrium appropriate for the chosen LED duty cycle. The next step will be to apply one of these techniques to multimodal metabolic imaging using modern, high-speed cameras[14] to interleave different metabolic images in a high-speed movie.

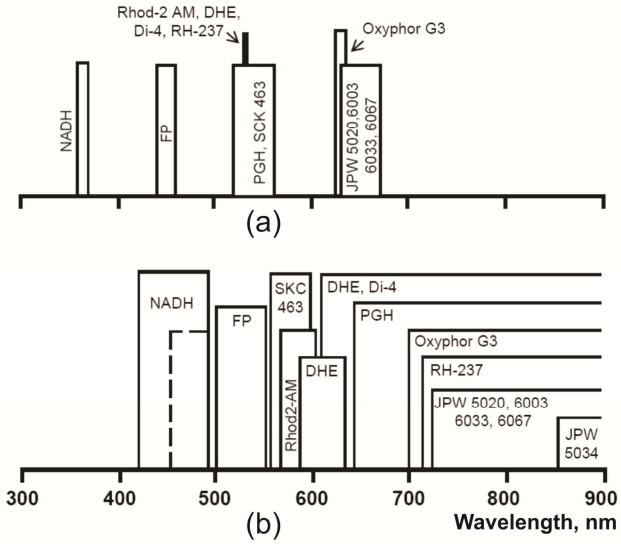

Figure 12. A schematic representation of (a) the excitation and (b) the emission wavelength bands for optical probes that can be used in multimodal cardiac imaging from the data in Table I.

The dual imaging of NADH and either $[Ca^{2+}]_i$, V_m, or ROS is particularly appealing, since NADH is an important coenzyme that is critical to the synthesis of ATP and provides a measure of

intracellular reduction potential. NADH is a main electron donor for the respiratory chain. Oxidation of NADH is coupled to the phosphorylation of ADP in the production of ATP. Because NADH is autofluorescent, absorbing 320-380 nm and emitting between 420-490 nm, and oxidized NAD^+ is not in these wavelength ranges, it is possible to use fluorescence imaging of NADH as a measure of the metabolic oxidation-reduction state.[51] As mitochondrial dysfunction is known to be involved in many diseases, such as Alzheimer's and ischemia, measuring NADH is greatly important. In the ATP-demanding heart, most of the consumed energy is for contraction. Hypoxic and ischemic conditions block the electron transport chain and cause NADH accumulation because oxygen levels are insufficient to continue oxidative phosphorylation. Thus NADH imaging is useful to investigate cardiac ischemia and ischemia/reperfusion.[1,36,47,62,70,75]

Ranji *et al.* [60] used a fiber-optic coupled, rotating-filter, time-interleaved fluorimeter to measure both NADH and flavoprotein (FP) autofluorescence during normal perfusion, regional ischemia (coronary artery ligation), and then reperfusion in the open-chest rabbit heart to assess the myocardial redox ratio, $Redox\ Ratio = FP/(FP + NADH)$, and hence myocyte apoptosis. In measurements of the isolated rabbit heart, this measurement was supplemented by the measurement of microvascular oxygen with the phosphorescent oxygen probe, Oxyphor G3, that was dissolved into the blood plasma.[61] Together, these three measurements may provide a measurement of intracellular and intravascular metabolic loads suitable for use in the cardiac operating room. Additionally, the development of new infrared voltage-sensitive dyes may relieve some of the spectral crowding evident in Fig. 12 and also allow imaging V_m in blood-perfused hearts and deep into the myocardium.[49,50,64] The excitation and emission wavelengths for these fluorescent indicators are shown in Table 1 and Fig. 12.

The measurement of more than one cardiac variable at a time will provide the ability to study the connections between CEP and metabolism. In the dual camera system we have described, simultaneous recording of NADH and V_m can be achieved by using two illumination sources. Figure 13 shows the diagram of the optical setup when a mercury lamp (365±5 nm) and a laser (532 nm) illuminate the heart to excite the autofluorescence of NADH and fluorescence of

di-4-ANNEPS. The second dichroic mirror splits the autofluorescence of NADH and the voltage dye fluorescence. To accomplish the concurrent recording of ROS (DHE) and V_m (Rh-237) one light source is sufficient (Table 1, Figure 12). The possibility of using a second light source for excitation of the new long-wavelength potentiometric dyes[64] in simultaneous measurements of ROS and V_m also exists.

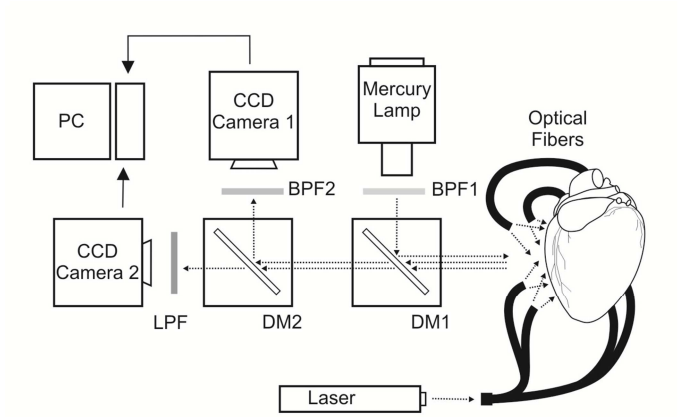

Figure 13. A schematic diagram of the optical setup for simultaneous V_m and NADH recording.

Most CCD cameras are optimized to detect visible light, and their sensitivity falls off rapidly at wavelengths longer than 800 nm. The spectral response of our Dalsa and Redshirt cameras, along with a popular 16×16 Hamamatsu photodiode array (PDA) and a Horiba camera with an near infrared (NIR) optimized deep depletion CCD, are shown in Figure 14. As indicated, the manufacturers use different units to describe spectral response, but the qualitative performance in the NIR can be inferred from the plots.

The Redshirt and Dalsa cameras have a significant response well into the NIR, although both fall off rapidly. The use of the Redshirt gain feature (3dB to 30 dB available) was demonstrated in the ratiometric example and could be used to compensate for lower sensitivity when using IR dyes. Dual-rate imaging could also be used with or without gain to make low-noise recordings of a slow metabolic variable in the NIR. For example, the Redshirt can run as slow as 30 frames/second. The longer integration times at lower frame rates greatly improve

SNR. Even when using dual-rate imaging, if both cameras use the same spatial resolution, our calibration method could still be used.

It is important to realize that typically the changes in metabolic variables are slow relative to either V_m or $[Ca^{2+}]$. If electromechanical uncouplers are not applied, the fast changes in the metabolic optical signal will signify the motion deflections, and therefore can be used for motion-correction of V_m or $[Ca^{2+}]$ from the fluorescence recordings. It has been demonstrated that utilizing the"silent" part of the spectrum insensitive to fast changes in $[Ca^{2+}]_i$ and V_m as the numerator in ratiometry is efficient in reducing motion artifacts in both quantities.[40]

The rapid change of illumination sources and filters within a motorized filter wheel would allow determination of multiple interleaved images, particularly if they involve different time scales.

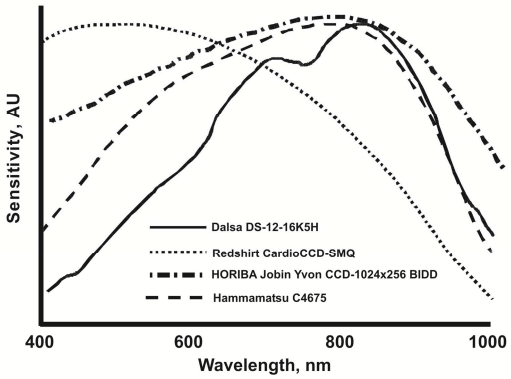

Figure 14. The spectral response of CCD cameras and PDA .

The use of a dual camera system with either a PET or SPECT system would allow measurement of glucose or oxygen uptake simultaneously with whatever optical measurements were desired. The metabolic information gained by multimodal imaging can be complemented by a number of key metabolic variables that can be measured biochemically in the cardiac effluent or with electrodes, but discussion of our ongoing efforts in this area is beyond the scope of this paper.

In conclusion it should be emphasized that such cardiac disturbances as hyperkalemia, anoxia, and "energy starvation" of the myocardium, all of which can be viewed as metabolic disorders with CEP manifestations, can be produced by (or perhaps be the result of) regional ischemia from coronary artery disease, tachycardia-induced remodeling, or congestive heart failure. The development of metabolic therapies for CEP abnormalities requires simultaneous observation of CEP and metabolism, and a mechanistic understanding of the relationship between the two. Our analysis of the potential for dual camera systems and the simple implementation that we report are our first steps towards advancing our understanding of "electrometabolic" cardiac disorders and their clinical treatment. Our review of related efforts to extend the optical measurements of myocardial function suggests that this is a rich field worthy of expanded research.

Acknowledgements

This work was supported in part by the National Institutes of Health (R01-HL58241), the Vanderbilt Institute for Integrative Biosystems Research and Education (VIIBRE), the American Heart Association (0635037N), and the Simons Center for Systems Biology at the Institute for Advanced Study. We thank Richard Gray for productive discussions.

References

1. F. G. Akar, M. A. Aon, G. F. Tomaselli, and B. O'Rourke, "The mitochondrial origin of postischemic arrhythmias," *J. Clin. Invest.* **115**(12), 3527-3535 (2005).
2. A. Al Khadra, V. Nikolski, and I. R. Efimov, "The role of electroporation in defibrillation," *Circ. Res.* **87**(9), 797-804 (2000).
3. R. Bajcsy and S. Kovacic, "Multiresolution Elastic Matching," *Comput. Vision Graph.* **46**(1), 1-21 (1989).
4. G. H. Bardy, K. L. Lee, D. B. Mark, J. E. Poole, D. L. Packer, R. Boineau, M. Domanski, C. Troutman, J. Anderson, G. Johnson, S. E. McNulty, N. Clapp-Channing, L. D. Davidson-Ray, E. S. Fraulo, D. P. Fishbein, R. M. Luceri, and J. H. Ip, "Amiodarone or an implantable cardioverter-defibrillator for congestive heart failure," *N. Engl. J. Med.* **352**(3), 225-237 (2005).
5. T. Berger, A. Borgdorff, S. Crochet, F. B. Neubauer, S. Lefort, B. Fauvet, I. Ferezou, A. Carleton, H. R. Luscher, and C. C. H. Petersen, "Combined voltage and calcium epifluorescence imaging in vitro and in vivo reveals subthreshold and suprathreshold dynamics of mouse barrel cortex," *J. Neurophysiol.* **97**(5), 3751-3762 (2007).
6. C. J. Brame, O. Boutaud, S. S. Davies, T. Yang, J. A. Oates, D. Roden, and L. J. Roberts, II, "Modification of Proteins by Isoketal-containing Oxidized Phospholipids," *J. Biol. Chem.* **279**(14), 13447-13451 (2004).
7. R. Brandes and D. M. Bers, "Simultaneous measurements of mitochondrial NADH and Ca2+ during increased work in intact rat heart trabeculae," *Biophys. J.* **83**(2), 587-604 (2002).
8. M.-A. Bray, R. R. Aliev, and J. P. Wikswo, Jr., "Use of topological charge to determine filament location in a numerical model of scroll wave activity," *IEEE Trans. Biomed. Eng.* **49**(10), 1086-1093 (2002).

9. M.-A. Bray, S.-F. Lin, and J. P. Wikswo, Jr., "Three-dimensional surface reconstruction and fluorescent visualization of cardiac activation," *IEEE Trans. Biomed. Eng.* **47**(10), 1382-1391 (2000).
10. B. Brendorp, O. D. Pedersen, C. Torp-Pedersen, N. Sahebzadah, and L. Kober, "A benefit-risk assessment of class III antiarrhythmic agents," *Drug Safety* **25**(12), 847-865 (2002).
11. A. E. Buxton, K. L. Lee, L. DiCarlo, D. S. Echt, J. D. Fisher, S. Greer, M. E. Josephson, D. Packer, E. N. Prystowsky, and M. Talajic, "Nonsustained ventricular tachycardia in coronary artery disease: Relation to inducible sustained ventricular tachycardia," *Ann. Intern. Med.* **125**(1), 35-39 (1996).
12. C. Casali, J. F. Obadia, E. Canet, K. Bendjelid, X. AndreFouet, D. Revel, and M. F. Janier, "Design of an isolated pig heart preparation for positron emission tomography and magnetic resonance imaging," *Invest. Radiol.* **32**(11), 713-720 (1997).
13. B. R. Choi and G. Salama, "Simultaneous maps of optical action potentials and calcium transients in guinea-pig hearts: mechanisms underlying concordant alternans," *J. Physiol.* **529, pt.1**, 171-188 (2000).
14. B. R. Choi, W. Jang, and G. Salama, "Spatially discordant voltage alternans cause wavebreaks in ventricular fibrillation," *Heart Rhythm* **4**(8), 1057-1068 (2007).
15. E. T. Chuck, K. Meyers, D. France, T. L. Creazzo, and G. E. Morley, "Transitions in ventricular activation revealed by two-dimensional optical mapping," *Anatomical Record Part A-Discoveries in Molecular Cellular and Evolutionary Biology* **280A**(2), 990-1000 (2004).
16. S. J. Connolly, M. Gent, R. S. Roberts, P. Dorian, D. Roy, R. S. Sheldon, L. B. Mitchell, M. S. Green, G. J. Klein, and B. O'Brien, "Canadian implantable defibrillator study (CIDS) - A randomized trial of the implantable cardioverter defibrillator against amiodarone," *Circulation* **101**(11), 1297-1302 (2000).

17. I. R. Efimov, V. P. Nikolski, and G. Salama, "Optical imaging of the heart," *Circ. Res.* **95**(1), 21-33 (2004).

18. P. T. Ellinor, D. J. Milan, and C. A. MacRae, "Metabolic gene defects and rick of arrhythmia," *Heart and Metabolism* **33**, 9-12 (2006).

19. E. Entcheva, Y. Kostov, E. Tchernev, and L. Tung, "Fluorescence imaging of electrical activity in cardiac cells using an all-solid-state system," *IEEE Trans. Biomed. Eng.* **51**(2), 333-341 (2004).

20. D. W. Evertson, M. R. Holcomb, M. Eames, M. Bray, V. Y. Sidorov, J. Xu, H. Wingard, H. M. Dobrovolny, M. C. Woods, D. J. Gauthier, and J. P. Wikswo, "High-resolution high-speed panoramic cardiac imaging system," *IEEE Trans. Biomed. Eng.* **55**(3), 1241-1243 (2008).

21. C. C. Fjeld, W. T. Birdsong, and R. H. Goodman, "Differential binding of NAD+ and NADH allows the transcriptional corepressor carboxyl-terminal binding protein to serve as a metabolic sensor," *PNAS* **100**(16), 9202-9207 (2003).

22. U. Flogel, C. Jacoby, A. Godecke, and J. Schrader, "In vivo 2D mapping of impaired murine cardiac energetics in NO-induced heart failure," *Magn. Reson. Med.* **57**(1), 50-58 (2007).

23. L. E. Fong, J. R. Holzer, K. McBride, E. A. Lima, F. Baudenbacher, and M. Radparvar, "High-resolution imaging of cardiac biomagnetic fields using a low-transition-temperature superconducting quantum interference device microscope," *Appl. Phys. Lett.* **84**(16), 3190-3192 (2004).

24. L. E. Fong, J. R. Holzer, K. K. McBride, E. A. Lima, F. Baudenbacher, and M. Radparvar, "High-resolution room-temperature sample scanning superconducting quantum interference device microscope configurable for geological and biomagnetic applications," *Rev. Sci. Instrum.* **76**(5), 053703 (2005).

25. K. Fukuda, S. S. Davies, T. Nakajima, B. H. Ong, S. Kupershmidt, J. Fessel, V. Amarnath, M. E. Anderson, P. A. Boyden, P. C. Viswanathan, L. J. Roberts, and J. R. Balser,

"Oxidative mediated lipid peroxidation recapitulates proarrhythmic effects on cardiac sodium channels," *Circ. Res.* **97**(12), 1262-1269 (2005).

26. R. J. Gillies, "In vivo molecular imaging," *J. Cell. Biochem.*, 231-238 (2002).
27. R. C. Gonzalez and R. E. Woods, *Digital image processing*, Addison-Wesley, Reading (1993).
28. R. A. Gray, A. Iyer, M.-A. Bray, and J. P. Wikswo, "Voltage-calcium state-space dynamics during initiation of reentry," *Heart Rhythm* **3**(2), 247-248 (2006).
29. H. L. Greene, D. M. Roden, R. J. Katz, R. L. Woosley, D. M. Salerno, and R. W. Henthorn, "The Cardiac-Arrhythmia Suppression Trial: first CAST...then CAST-II," *J. Am. Coll. Cardiol.* **19**(5), 894-898 (1992).
30. G. S. Hoeker, R. P. Katra, and K. R. Laurita, "Imaging cellular calcium dysfunction in the heart using multi-modal optical mapping," in Proceedings of the 28th IEEE EMBS Annual International Conference, IEEE, (2006), pp. 571-575.
31. M. R. Holcomb, R. Y. Bekele, E. A. Lima, and J. P. Wikswo, "USB-powered and -controlled isolated constant-current physiological stimulator," *Submitted* (2008).
32. J. R. Holzer, L. E. Fong, V. Y. Sidorov, J. P. Wikswo, Jr., and F. Baudenbacher, "High resolution magnetic images of planar wave fronts reveal bidomain properties of cardiac tissue," *Biophys. J.* **87**(6), 4326-4332 (2004).
33. G. S. Hwang, H. Hayashi, L. Tang, M. Ogawa, H. Hernandez, A. Y. Tan, H. Li, H. S. Karagueuzian, J. N. Weiss, S. F. Lin, and P. S. Chen, "Intracellular Calcium and Vulnerability to Fibrillation and Defibrillation in Langendorff-Perfused Rabbit Ventricles," *Circulation* **114**(24), 2595-2603 (2006).
34. R. P. Katra, E. Pruvot, and K. R. Laurita, "Intracellular calcium handling heterogeneities in intact guinea pig hearts," *Am J Physiol Heart Circ Physiol* **286**(2), H648-H656 (2004).
35. A. M. Katz, *Heart failure: pathophysiology, molecular biology, and clinical management*, Lippincott Williams & Wilkins, Philadelphia (2000).

36. L. G. Kevin, A. K. S. Camara, M. L. Riess, E. Novalija, and D. F. Stowe, "Ischemic preconditioning alters real-time measure of O-2 radicals in intact hearts with ischemia and reperfusion," *Am. J. Physiol. Heart* **284**(2), H566-H574 (2003).

37. Y.-H. Kim, A. Garfinkel, T. Ikeda, T.-J. Wu, C. A. Athill, J. N. Weiss, H. S. Karagueuzian, and P.-S. Chen, "Spatiotemporal complexity of ventricular fibrillation revealed by tissue mass reduction in isolated swine right ventricle. Further evidence for the quasiperiodic route to chaos hypothesis," *J. Clin. Invest.* **100**(10), 2486-2500 (1997).

38. S. B. Knisley, R. K. Justice, W. Kong, and P. L. Johnson, "Ratiometry of transmembrane voltage-sensitive fluorescent dye emission in hearts," *Am. J. Physiol. Heart* **279**(3), H1421-H1433 (2000).

39. I. Kodama, I. Sakuma, N. Shibata, S. B. Knisley, R. Niwa, and H. Honjo, "Regional differences in arrhythmogenic aftereffects of high intensity DC stimulation in the ventricles," *PACE* **23**(5), 807-817 (2000).

40. W. Kong, G. P. Walcott, W. M. Smith, P. L. Johnson, and S. B. Knisley, "Emission ratiometry for simultaneous calcium and action potential measurements with coloaded dyes in rabbit hearts: Reduction of motion and drift," *J. Cardiovasc. Electrophysiol.* **14**(1), 76-82 (2003).

41. W. Kong, P. L. Johnson, and S. B. Knisley, "Reduction of motion artifacts and photobleaching during multiwavelength ratiometric optical recording of action potentials and intracellular calcium transients in rabbit hearts," *PACE* **23**(4) 608 (2000).

42. R. E. Lane, M. R. Cowie, and A. W. C. Chow, "Prediction and prevention of sudden cardiac death in heart failure," *Heart* **91**(5), 674-680 (2005).

43. D. M. Langrill and B. J. Roth, "The effect of plunge electrodes during electrical stimulation of cardiac tissue," *IEEE Trans. Biomed. Eng.* **48**(10), 1207-1211 (2001).

44. K. R. Laurita and A. Singal, "Mapping action potentials and calcium transients simultaneously from the intact heart," *Am. J. Physiol. Heart* **280**(5), H2053-H2060 (2001).

45. R. Lecomte, E. Croteau, M. E. Gauthier, M. Archambault, A. Aliaga, J. Rousseau, J. Cadorette, J. D. Leroux, M. D. Lepage, F. Benard, and M. Bentourkia, "Cardiac PET imaging of blood flow, metabolism, and function in normal and infarcted rats," *IEEE Trans. Nucl. Sci.* **51**(3), 696-704 (2004).

46. S.-F. Lin, R. A. Abbas, and J. P. Wikswo, Jr., "High-resolution high-speed synchronous epifluorescence imaging of cardiac activation," *Rev. Sci. Instrum.* **68**(1), 213-217 (1997).

47. L. S. Lu, Y. B. Liu, C. W. Sun, L. C. Lin, M. J. Su, and C. C. Wu, "Optical mapping of myocardial reactive oxygen species production throughout the reperfusion of global ischemia," *J. Biomed. Opt.* **11**(2), 021012 (2006).

48. D. N. Mashburn, S. J. Hinkson, M. C. Woods, J. M. Gilligan, M. R. Holcomb, and J. P. Wikswo, "A high-voltage cardiac stimulator for field shocks of a whole heart in a bath," *Rev. Sci. Instrum.* **78**, 104302 (2007).

49. A. Matiukas, B. G. Mitrea, A. M. Pertsov, J. P. Wuskell, M. D. Wei, J. Watras, A. C. Millard, and L. M. Loew, "New near-infrared optical probes of cardiac electrical activity," *Am. J. Physiol. Heart* **290**(6), H2633-H2643 (2006).

50. A. Matiukas, B. G. Mitrea, M. Qin, A. M. Pertsov, A. G. Shvedko, M. D. Warren, A. V. Zaitsev, J. P. Wuskell, M. d. Wei, J. Watras, and L. M. Loew, "Near-infrared voltage-sensitive fluorescent dyes optimized for optical mapping in blood-perfused myocardium," *Heart Rhythm* **4**(11), 1441-1451 (2007).

51. A. Mayevsky and G. G. Rogatsky, "Mitochondrial function in vivo evaluated by NADH fluorescence: from animal models to human studies," *Am. J. Physiol. Cell* **292**(2), C615-C640 (2007).

52. J. McAnulty, B. Halperin, J. Kron, G. Larsen, M. Raitt, R. Swenson, R. Florek, C. Marchant, M. Hamlin, G. Heywood, P. Friedman, W. Stevenson, M. Swat, L. Ganz, M. Sweeney, J. Shea, J. Steinberg et al., "A comparison of antiarrhythmic-drug therapy with implantable defibrillators in patients resuscitated from near-fatal ventricular arrhythmias," *N. Engl. J. Med.* **337**(22), 1576-1583 (1997).

53. E. R. McVeigh, "Emerging imaging techniques," *Circ. Res.* **98**(7), 879-886 (2006).

54. A. J. Moss, W. Zareba, W. J. Hall, H. Klein, D. J. Wilber, D. S. Cannom, J. P. Daubert, S. L. Higgins, M. W. Brown, and M. L. Andrews, "Prophylactic implantation of a defibrillator in patients with myocardial infarction and reduced ejection fraction," *N. Engl. J. Med.* **346**(12), 877-883 (2002).

55. A. J. Moss, J. Hall, D. S. Cannom, J. P. Daubert, S. L. Higgins, H. Klein, J. H. Levine, S. Saksena, A. L. Waldo, D. Wilber, M. W. Brown, and M. Heo, "Improved survival with an implanted defibrillator in patients with coronary disease at high risk for ventricular arrhythmia," *N. Engl. J. Med.* **335**(26), 1933-1940 (1996).

56. R. J. Myerburg, K. M. Kessler, and A. Castellanos, "Sudden cardiac death - structure, function, and time-dependence of risk," *Circulation* **85**(1), 2-10 (1992).

57. R. J. Myerburg, R. Mitrani, A. Interian, and A. Castellanos, "Interpretation of outcomes of antiarrhythmic clinical trials - Design features and population impact," *Circulation* **97**(15), 1514-1521 (1998).

58. C. Omichi, S. T. Lamp, S. F. Lin, J. Z. Yang, A. Baher, S. M. Zhou, M. Attin, M. H. Lee, H. S. Karagueuzian, B. Kogan, Z. L. Qu, A. Garfinkel, P. S. Chen, and J. N. Weiss, "Intracellular Ca dynamics in ventricular fibrillation," *Am. J. Physiol. Heart* **286**(5), H1836-H1844 (2004).

59. E. N. Prystowsky, S. Freeland, N. A. Branyas, D. P. Rardon, R. I. Fogel, B. J. Padanilam, and J. S. Rippy, "Clinical experience with dofetilide in the treatment of patients with atrial fibrillation," *J. Cardiovasc. Electrophysiol.* **14**(s12), S287-S290 (2003).

60. M. Ranji, S. Kanemoto, M. Matsubara, M. A. Grosso, J. H. Gorman, R. C. Gorman, D. L. Jaggard, and B. Chance, "Fluorescence spectroscopy and imaging of myocardial apoptosis," *J. Biomed. Opt.* **11**(6), 064036 (2006).

61. M. Ranji, D. L. Jaggard, S. V. Apreleva, S. A. Vinogradov, and B. Chance, "Simultaneous fluorometry and phosphorometry of Langendorff perfused rat heart: ex vivo animal studies," *Opt. Lett.* **31**(20), 2995-2997 (2006).

62. M. L. Riess, A. K. S. Camara, Q. Chen, E. Novalija, S. S. Rhodes, and D. F. Stowe, "Altered NADH and improved function by anesthetic and ischemic preconditioning in guinea pig intact hearts," *Am J Physiol Heart Circ Physiol* **283**(1), H53-H60 (2002).

63. D. M. Roden, "CAST: Implications for the use of antiarrhythmic agents in the setting of ischemic heart disease," *Coron. Artery Dis.* **2**(6), 723-729 (1991).

64. G. Salama, B. R. Choi, G. Azour, M. Lavasani, V. Tumbev, B. M. Salzberg, M. J. Patrick, L. A. Ernst, and A. S. Waggoner, "Properties of new, long-wavelength, voltage-sensitive dyes in the heart," *J. Membr. Biol.* **208**(2), 125-140 (2005).

65. G. Salama, R. Lombardi, and J. Elson, "Maps of optical action-potentials and NADH fluorescence in intact working hearts," *Am. J. Physiol.* **252**(2), H384-H394 (1987).

66. M. Shah, F. G. Akar, and G. F. Tomaselli, "Molecular basis of arrhythmias," *Circulation* **112**(16), 2517-2529 (2005).

67. V. Y. Sidorov, M. R. Holcomb, M. C. Woods, R. A. Gray, and J. P. Wikswo, "Effects of unipolar stimulation on voltage and calcium distributions in the isolated rabbit heart," *Basic Research in Cardiology* **In press** (2008).

68. V. Y. Sidorov, M. C. Woods, and J. P. Wikswo, "Effects of elevated extracellular potassium on the stimulation mechanism of diastolic cardiac tissue," *Biophys. J.* **84**(5), 3470-3479 (2003).

69. L. Stegger, A. N. Hoffmeier, K. P. Schafers, S. Hermann, O. Schober, M. A. Schafers, and G. Theilmeier, "Accurate noninvasive measurement of infarct size in mice with high-resolution PET," *Journal of Nuclear Medicine* **47**(11), 1837-1844 (2006).

70. J. D. Stoner, M. G. Angelos, and T. L. Clanton, "Myocardial contractile function during postischemic low-flow reperfusion: critical thresholds of NADH and O-2 delivery," *Am. J. Physiol. Heart* **286**(1), H375-H380 (2004).

71. H. Taegtmeyer, "Cardiac metabolism as a target for the treatment of heart failure," *Circulation* **110**(8), 894-896 (2004).

72. J. P. Wikswo, Jr., S.-F. Lin, and R. A. Abbas, "Virtual electrodes in cardiac tissue: a common mechanism for anodal and cathodal stimulation," *Biophys. J.* **69**(6), 2195-2210 (1995).

73. M. C. Woods, V. Y. Sidorov, M. R. Holcomb, D. L. Beaudoin, B. J. Roth, and J. P. Wikswo, "Virtual electrode effects around an artificial heterogeneity during field stimulation of cardiac tissue," *Heart Rhythm* **3**(6), 751-752 (2006).

74. M. C. Woods, "Field stimulation of the diastolic rabbit heart: The role of shock strength and duration on epicardial activation and propagation," in *The response of the cardiac bidomain of electrical stimulation, PhD Dissertation,* Vanderbilt University, 109-138 (2005).

75. X. Zhu, L. Zuo, A. J. Cardounel, J. L. Zweier, and G. He, "Characterization of in vivo tissue redox status, oxygenation, and formation of reactive oxygen species in postischemic myocardium," *Antioxid. Redox. Signal.* **9**(4), 447-455 (2007).

76. T. Zimmermann, J. Rietdorf, and R. Pepperkok, "Spectral imaging and its applications in live cell microscopy," *FEBS Lett.* **546**(1), 87-92 (2003).

77. B. Zitova and J. Flusser, "Image registration methods: a survey," *Image Vision Comput.* **21**(11), 977-1000 (2003).

Table 1. Excitation and Emission Parameters for Correlative Multimodal Cardiac Imaging						
Optical Probe	Measured Parameter	Excitation Maximum [nm]	Recommended Excitation [nm]	Emission Maximum [nm]	Recommended Emission Collection [nm]	References
Dihydroethidium (DHE) (oxidized to ethidium)	ROS (O_2^-)	518	532	605	>607	Invitrogen
					605±25	Invitrogen
Rhod-2 AM	$[Ca^{2+}]_i$	550	532	571	585±20	Invitrogen
Di-4-ANEPPS	V_m	488	532	605	>607	Invitrogen
RH 237	V_m	506	532	687	>710	Invitrogen
Autofluorescence of nicotinamide adenine dinucleotide (NADH)	[NADH]	340	365±5 (filtered Hg lamp)	455	470±20	[21]
					455±35	[61]
Autofluorescence of Flavoprotein (FP)	[FP]	436	450±10 estimated	530	525±25	[61]
Luminescence of Oxyphor G3	Microvascular $[O_2]$	635	635±10 estimated	810	>695	[61]
SKC 463	$[K^+]_e$		540±20	575	575±20	Guy Salama, Personal Communication

JPW 6003, 6033, 6067, 5020	V_m	various	650±20		>720	[49,50]
JPW 5034	V_m		650±20		>850	[49]
PGH	V_m		540±20		>640	[64]

Figure Captions

Fig. 1. A diagram of our experimental setup configured for simultaneous recording of V_m and $[Ca^{2+}]_i$. Laser light (532 nm) is delivered to the heart with optical fibers. The dichroic mirror (DM) reflects short-wave (<635 nm) and passes long-wave emitted fluorescence. The band pass (BPF) and long pass (LPF) Omega Optical filters are used to image Ca^{2+} and V_m fluorescence, respectively, with two DALSA CCD cameras (128x128 pixels, 490 frames/second). Use of different dyes, illumination and detection wavelengths would enable imaging of other quantities, such as ROS or NADH.

Fig. 2. Image registration using the rubber sheet algorithm. (a) Pixel mapping. Left: V_m image; right: V_m' image. A single highlighted pixel in the V_m image with its four closest alignment points (left) is mapped to the image grid V_m' (right) using the corresponding alignment points in the $[Ca^{2+}]_i$ image. (b) Demonstration of numerical alignment of two-camera images. 1) and 2) Unprocessed images from both cameras. 3) Overlay of intentionally misaligned, unprocessed images. 4) and 5) Processed images. 6) Overlay of the processed images. The field of view is approximately 12 mm × 12 mm.

Fig. 3. Changes in fluorescence recorded at one pixel when the heart was only stained with either RH-237 (a) or Rhod-2 AM (b) alone. (Reprinted from Sidorov, *et al.*[67] with permission).

Fig. 4. The voltage and calcium responses to anodal stimulation for a 12 mm × 12 mm field of view of the epicardium of an isolated rabbit heart. The S2 stimulus was 20 ms in duration and 20 mA in amplitude and was delivered at an S1-S2 interval of 90 ms. The optical data were first

preprocessed by applying a spatial 8 × 8 Gaussian filter and a 3-point mean temporal filter, then normalized on a pixel-by-pixel basis, and are presented as the percentage of highest change in fluorescence. (a) Action potential (black trace) and calcium transient (gray trace) extracted from the same pixel (black and gray squares in (b)) at the central hyperpolarized area. (b) Voltage and calcium distributions at the end of S2. To display net voltage (ΔV_m) and calcium $[\Delta Ca^{2+}]_i$ displacements due to S2, the previous response was subtracted from the S2 response. (Adapted from Sidorov *et al.*,[67] with permission).

Fig. 5. The voltage and calcium dynamics in the isolated right ventricle preparation. (a) The arrhythmia was initiated by two premature stimuli (S1, S2) delivered via a wire electrode (W). The image size is 22 x 22 mm^2. During the last 400 ms the stationary rotor with its center located inside the white square drives the arrhythmia. Two traces represent RH 237 and Rhod-2 AM fluorescence. (b) and (c) demonstrate data analyses from the open white square in (a). The left and middle panels of (b) show the spatial distributions of V_m and $[Ca^{2+}]_i$ for the 2314 ms time point, indicated by the red line in the temporal traces in (a). The activation map on the right shows one complete rotation with time resolution of 15 ms. The left panel of (c) shows the V_m versus $[Ca^{2+}]_i$ phase map at 2314 ms, while the right panel of (c) is the phase-space trajectory over time for the black pixel in the phase map for the entire duration of recording, 2,468 ms (at 1000 frames/second).

Fig. 6. The response of a right ventricular trabecula to field stimulation. Two high-speed Redshirt CCD cameras were used to acquire the data. An achromatic lens was added to the dual camera system to obtain the small 5 x 5 mm^2 field of view shown in the top image. The preparation was stained with RH 237 and Rhod-2 AM to image V_m and $[Ca^{2+}]_i$, respectively, using filters as described in the text. (a) The trabecula response to field shock of 10 ms duration and 20 V/cm strength at an S1-S2 interval of 70 ms. The time traces 1) and 2) show the averaged responses from the areas depicted by the "1" and "2" squares in the image. (b) The V_m distribution during negative and positive field stimulation of 30 V/cm at a coupling interval of 100 ms. The averaged traces from one square (white) illustrate the tissue responses as a function of shock polarity. The

traces from the virtual cathode (red) and virtual anode (blue) are superimposed on the optical signals recorded when only the S1 field shock was applied. The optical data were preprocessed with a spatial 5 × 5 Gaussian filter and normalized. The arrow above the image indicates electric field direction. The spatial and temporal resolutions are 80 x 80 pixels and 1000 frames/second, respectively.

Fig. 7. Ratiometric measurement of optical action potential. The heart was stained with RH-237 and illuminated with laser light (532 nm). To split the emission light, we utilized a beam splitter with 70% reflectance and 30% transmission. Two high-speed Redshirt CCD cameras were used to image: (a) short- (610 ± 30 nm) and (b) long-wave (>710 nm) fluorescence. (c) The ratio of short- (a) to long-wave (b) fluorescence. The data were filtered with a spatial 5 × 5 Gaussian filter and a five-point mean temporal filter. The spatial and temporal resolutions were 80 x 80 pixels and 1000 frames/second, respectively. The gain for the camera recording short-wave fluorescence was 10 dB, and for the camera recording the long-wave signal the gain was 3 dB.

Fig. 8. Motion amplitude quantification in the ratiometric determination of V_m. Time-space plots were created along horizontal and vertical white lines centered at the pixel of interest (red dot). To estimate the extent of motion deflections, the time-space plots were differentiated along the space axis. The white curved lines in horizontal and vertical differentiated time-space plots represent crest positions of motion waves in the vicinity of the red pixel. The time traces are 400-ms intervals of the traces from Fig. 7 showing short-wave (green) fluorescence (Fig. 7(a)) and long-wave (red) fluorescence (Fig. 7(b)) with superimposed short/long ratiometric (black) signals (Fig. 7(c)). The upper and lower gray traces are results of subtractions of the green and black signals and of the red and black traces, respectively, and, hence, depict traces that reflect the motion without the V_m signal.

Fig. 9. Whole heart field stimulation data acquired simultaneously with high temporal and high spatial resolutions using the dual camera system. The heart was stained with di-4-ANEPPS to image V_m. Raw images of the whole heart were acquired with (a) Redshirt CCD (26 x 26 pixels, 5000 frames/second) and with (b) Dalsa CCD (128 x 128 pixels, 487 frames/second). In both (a)

and (b) the scale is approximately 50 x 50 mm^2. The insulated bipolar electrode used to pace the heart near the apex can be seen in the right of (b). False color fluorescence (c) Redshirt and (d) Dalsa data reveal the spatiotemporal response of the heart to diastolic field stimulation of 50 V/cm strength and 8 ms duration. The numbers above or below each frame represent the time in [ms] since the field shock onset. The fluorescence data were normalized (F_{norm}) according to the paced beat preceding the field shock. Pixels corresponding to atrial tissue were digitally removed from the images in (c) and (d).

Fig. 10. A comparison of the emission spectra measured from a rabbit heart for DHE as a reporter of ROS, Rhod-2 AM as an indicator of $[Ca^{2+}]_i$, and di-4-ANEPPS and RH-237 as indicators of V_m.

Fig. 11. NADH autofluorescence in a Langendorff-perfused rabbit heart under normal conditions (95% O_2 and 5% CO_2) (control) and after 30 minutes of global anoxia (95%N_2, 5%CO_2). (a) Images of the 22 x 22 mm^2 (80 x 80 pixels) field of view. (b) Pixel intensity histogram. (c) Histogram integrals demonstrating a statistically significant increase in NADH during anoxia. (d) NADH autofluorescence over the course of the experiment, including control, 30 minutes of global anoxia, and reperfusion.

Fig. 12. A schematic representation of (a) the excitation and (b) the emission wavelength bands for optical probes that can be used in multimodal cardiac imaging from the data in Table I. Rhod-2 AM, DHE, Di-4, and RH-237 are all excited by a 532 nm laser line. The width of the rectangles represents the approximate full-width at half maximum of the excitation spectra or the common choices in emission filters. Long-pass filters are open-ended on the right. The heights of the rectangles have no significance other than to aid in data visualization. These data may not always reflect the shift in wavelengths that can occur when the dye is in tissue instead of a solvent.

Fig. 13. A schematic diagram of the optical setup for simultaneous V_m and NADH recording. The four fibers direct laser light (532 nm) on the heart to excite di-4-ANEPPS fluorescence. Light from the mercury lamp is passed through a band pass filter (BPF1, 365±5 nm) and directed to the heart by means of dichroic mirror 1 (DM1), which reflects light below 400 nm and transmits it

above 400 nm (400DCLP, Chroma). The second dichroic mirror (DM2) operates at longer wavelengths to reflect light under 565 nm and transmit above 565 nm (565DCXR, Chroma). The NADH autofluorescence, excited with ultraviolet light from the mercury lamp, passes through DM1 and is reflected by DM2 to CCD camera 1 equipped with a band pass filter (BPF2, 470±20 nm). The emitted V_m fluorescence passes through the two dichroic mirrors and the long pass filter (LPF, >607 nm) before collection with CCD camera 2.

Fig. 14. The spectral response of CCD cameras and PDA. The Dalsa DS-12-16K5H (www.dalsa.com) is given in digital number/(nJ/cm2), the Redshirt CardioCCD-SMQ (www.redshirtimaging.com) and HORIBA Jobin Yvon CCD-1024x256 BIDD (www.jobinyvon.com) are given in quantum efficiency, and the Hamamatsu C4675 (www.hamamatsu.com) in photosensitivity A/W. The figure was created using the datasheets found at the URLs shown.

APPENDIX B

DIASTOLIC FIELD STIMULATION: THE ROLE OF SHOCK DURATION IN EPICARDIAL ACTIVATION AND PROPAGATION*

Marcella C. Woods, PhD,* Ilija Uzelac, MSc,† Mark R. Holcomb, PhD,‡ John P. Wikswo, PhD,* †§¶
Veniamin Y. Sidorov, PhD*§

*Department of Biomedical Engineering, Vanderbilt University, Nashville, Tennessee;
†Department of Physics and Astronomy, Vanderbilt University, Nashville, Tennessee;
‡Department of Physics, Susquehanna University, Selinsgrove, Pennsylvania;
§Vanderbilt Institute for Integrative Biosystems Research and Education, Vanderbilt University, Nashville, Tennessee;
¶Department of Molecular Physiology and Biophysics, Vanderbilt University, Nashville, Tennessee

Keywords – diastolic stimulation, virtual electrodes, hyperpolarization, optical mapping

Corresponding author

Dr. Veniamin Y. Sidorov

Department of Biomedical Engineering

Vanderbilt University,

Box 1807, Station B

Nashville, TN 37240

Email: v.sidorov@vanderbilt.edu

Tel: 615-322-4419

Fax: 615-322-4977

*This is a manuscript submitted for a journal publication

Abstract

Detailed knowledge of tissue response to both systolic and diastolic shock is critical for understanding defibrillation. Diastolic field stimulation has been much less studied than systolic stimulation, particularly regarding transient virtual anodes. Here we investigated high-voltage-induced polarization and activation patterns in response to strong diastolic shocks of various durations and of both polarities, and tested the hypothesis that the activation versus shock duration curve contains a local minimum for moderate shock durations, and it grows for short and long durations. We found that 0.1 - 0.2 ms shocks produced slow and heterogeneous activation. During 0.8 - 1 ms shocks, the activation was very fast and homogeneous. Further shock extension to 8 ms delayed activation from 1.55 ± 0.27 ms and 1.63 ± 0.21ms at 0.8 ms shock to 2.32 ± 0.41 ms and 2.37 ± 0.3 ms (N = 7) for normal and opposite polarities, respectively. The traces from hyperpolarized regions during 3 - 8 ms shocks exhibited four different phases: beginning negative polarization, fast depolarization, slow depolarization, and after shock increase in upstroke velocity. Thus, the shocks of more than 3 ms in duration created strong hyperpolarization associated with significant delay ($P < 0.05$) in activation compared with moderate shocks of 0.8 and 1 ms. This effect appears as a dip in activation versus shock duration curve.

Introduction

Externally applied electric fields are known to cause changes in transmembrane potential (V_m) at locations distant from the stimulating electrodes, a phenomenon termed "far-field" stimulation. These regions of positive and negative polarization are called virtual cathodes and virtual anodes, respectively. Many explanations for far-field stimulation have been suggested. Plonsey and Barr (23) hypothesized that intercellular resistance at gap junctions causes depolarization and

hyperpolarization on opposite ends of each myocyte. However, attempts to experimentally verify the "saw-tooth" effect in intact cardiac tissue have failed (11,36). Theoretical simulations using the bidomain model of cardiac tissue predict that fiber curvature and unequal anisotropy ratios between the intra- and extracellular spaces cause depolarization and hyperpolarization throughout the heart (4,7,31,33), whereas the transmural fiber rotation modulates the polarization gradient through the bulk of tissue (7). Ashihara et al. (1) hypothesize that mechanisms responsible for surface and bulk polarizations can cause "tunnel" propagation of postshock activation, which spreads through the shock-induced intramural excitable area and can underlie isoelectric window and induction of fibrillation.

Other heterogeneities have been hypothesized as contributors to the mechanism of far-field stimulation. Computer models incorporating syncytial heterogeneities of the bulk myocardium revealed islands of hyperpolarization and depolarization during an external electric shock (10). The contribution of local heterogeneities in the mechanism of the upper level of vulnerability was recently investigated in a theoretical study by Mazeh and Roth (22). Using a combination of bidomain and Beeler-Reuter models to represent passive and active properties of cardiac tissue, they found that local microscopic heterogeneities, represented with random fiber geometry, are crucial for determining the fate of the shock-induced wave front at the edge of the virtual anode. Due to the higher threshold for micro-scale heterogeneities in comparison to macro-scale ones, the local microscopic heterogeneities can determine the upper level of vulnerability.

At the scale of macroscopic heterogeneities whose dimensions are on the order of a few cardiac length constants, the heart can be modeled as a relatively insulated collection of fibers that, when exposed to an external electrical field, should produce hyperpolarization and depolarization in a patchy manner (16). In addition, cleavage planes between muscle layers may create "secondary sources" (8,24,29) of activation, causing nonuniform, anisotropic propagation, and provide a substrate for bulk resetting of the myocardium during defibrillation (8,15,35).

The boundary conditions of the heart surfaces also affect how an electric field alters V_m. Latimer and Roth (17) modeled a slab of tissue with an intracavitary electrode in two conditions: the

epicardium bounded by air and the epicardium bounded by a conductive bath. They found that the conductive bath reverses the sign of V_m in some regions and dramatically increases the magnitude of the shock-induced changes in V_m at the epicardial surface. Additionally, V_m falls off rapidly with depth into the tissue, suggesting that the optically measured V_m would be much smaller than the true epicardial V_m. Entcheva et al. (6) modeled an ellipsoid bidomain heart with transmural fiber rotation using different boundary conditions. They found that the induced change in V_m partially results from the tissue boundary conditions, and is not fully determined by tissue anisotropy.

Each of these hypotheses incorporates heterogeneities, from microscale to macroscale, as a mechanism for producing adjacent regions of positive and negative polarization during an external electric shock – cathodal regions that directly stimulate the tissue and accelerate propagation, and anodal regions that can delay propagation and also lead to tissue stimulation upon break (32). These adjacent areas of polarization are potential sources of wave front generation that could cause the far-field stimulation observed during field shocks (19). The extent of virtual electrode polarization depends on the phase of cardiac cycle at the time of stimulus application (3,9,12,37). During fibrillation the various portions of the heart exist in states that range between fully refractory and fully recovered conditions. Therefore investigation of the cardiac response to electric stimulation delivered at different action potential (AP) phases is necessary to understand the mechanisms of defibrillation and for optimizing shape and strength of defibrillation shock.

Although numerous studies have been dedicated to studying effects of field stimulation on systolic tissue, the effects of field stimulation during diastole have been less investigated. Sharifov and Fast applied shocks transmurally across an isolated pig left ventricle (26). They found direct and rapid activation of the ventricular bulk over a wide range of shock strengths and delayed activation and multiphasic V_m responses at very strong shock strengths. However, because they were imaging the cut end of a preparation, the extent to which damage, ischemia, and angles of the cut fibers with the tissue surface contributed to their results is unknown (5).

Recently Maleckar, Woods, et al. (20) used high-speed optical mapping in conjunction with computer simulation to study the effect of polarity and stimulus strength on the activation time (AT) during diastole. They found that both polarity reversal and increasing shock strength lower AT. They also indicated the important role of ventricular geometry in location and size of shock-induced hyperpolarization. The goal of this work was to study the role of stimulus duration on AT and test hypotheses that i) hyperpolarization caused by long shock durations increases total AT and ii) activation versus shock duration curve has a local minimum in response to shocks of mild durations, and it rises in response to shocks of both short and long durations.

Methods

Experimental Preparation

All experiments followed the guidelines of the National Institutes of Health for the ethical use of animals in research and were approved in advance by the Vanderbilt Institutional Animal Care and Use Committee.

Langendorff-perfused hearts (n = 7) from New Zealand White rabbits (2.2-3.5 kg) were used in the current study. A detailed description of the heart preparation has been previously published (27,28). Briefly, the rabbit was preanesthetized with ketamine (50 mg/kg), heparinized (1,000 units) and anesthetized by pentobarbital sodium injection (60 mg/kg). The heart was removed and Langendorff-perfused on a custom-built C-shaped glass arm (20). To minimize motion artifact, the excitation-contraction uncoupler 2,3-butanedione monoxime (BDM, Sigma) in concentration of 15 mM was added to Tyrode's solution. The temperature and pH were continuously maintained at 37^{o}C and at 7.4, respectively. The heart was positioned in a temperature-controlled glass chamber such that the anterior side of the heart faced the optical system.

Optical Imaging and Data Acquisition

The heart was stained with a gradual injection of 200 µl of the stock solution of the voltage-sensitive dye di-4-ANEPPS (0.5 mg/ml dimethyl sulfoxide, Molecular Probes) via injection port above the aorta. The fluorescence was excited by a diode-pumped, solid-state Verdi laser (Verdi, Coherent) at 532 nm. The emitted light was passed through a cutoff filter (607 nm, Tiffen) and collected by means of a high-temporal CCD camera (RedShirt, 26x26 pixels, 5,000 frames/s). The typical field of view was 5 x 5 cm^2.

Stimulation Protocol

The heart was paced at a basic cycle length of 300 ms (S1) with a computer-controlled current source (Bloom Associates) or custom-designed physiological stimulator (14) via an insulated bipolar electrode located near the apex. The spatially uniform electric field, produced by means of a custom high-voltage stimulator (21), was applied through two titanium plates positioned at opposite ends of the rectangular bath to face the right and left ventricle. The S2 field shocks of 50 V/cm in magnitude and of 0.1, 0.2, 0.4, 0.6, 0.8, 1, 1.5, 2, 3, 5 and 8 ms in duration were delivered to diastolic tissue at a S1-S2 coupling interval of 300 ms. Current and voltage wave forms were monitored on a digital phosphor oscilloscope (TDS5034B, Tektronix) via a current probe (TCP305, Tektronix) and a high-voltage differential probe (P5205, Tektronix) connected to two Ag-AgCl electrodes of 2 mm diameter located in the bath. The shocks for which the cathode faced the right ventricle and the anode faced the left ventricle were labeled RV-. Shocks of opposite polarity were referred to as LV- shocks (20).

Data Processing and Analysis

To preserve the shock timing, no temporal filtering was applied. We followed our previous image processing protocol (20). In summary, we digitally removed from the data pixels corresponding to atrial tissue for all subsequent analysis. The data were normalized on a pixel-by-pixel basis according to the change in fluorescence during S1 pacing response. The resulting normalized data (F_{norm}) ranged from 0 (rest) to 1 (peak) for the S1 response. Field shock AT for each ventricular pixel was computed as the elapsed time from shock onset until 50% of the S1 action potential amplitude was reached. To estimate the activation dynamics for the whole heart, the sum of F_{norm} for all ventricular pixels for each movie frame was computed and normalized by dividing by the number of pixels summed to yield averaged fluorescence (F_{avg}).

In total, seven rabbit hearts were utilized to study diastolic tissue response to shocks of different durations. Group data are presented as mean values (SD). Statistical analysis was accomplished using the unpaired *t*-test. Differences were considered significant if $P < 0.05$.

Results

Effects of field shock duration on V_m distribution patterns during and soon after the shock

Fig. 1 illustrates typical V_m distribution resulting from 50 V/cm shocks of 0.2 ms (Panel A), 1 ms (Panel B), and 8 ms (Panel C) in duration. During a short shock, the negative polarization (blue pixels) of the anodal side and depolarization (red pixels) on the cathodal side of the heart is easily discernible at the time of shock termination (0.2 ms) for both RV- and LV-polarities. The hyperpolarization at both right and left ventricle ends immediately after shock cessation. At 4.2 ms, the fraction of activated tissue encompasses 90.5 % and 93.2 % for shocks of normal and reversed polarity, respectively. During 1-ms shock, the hyperpolarization is most prominent at about the middle of the shock for both polarities (Panel B, 0.6-ms frames). In

contrast to the response to the short S2, in this case activation occurs faster and attains 96.1 % at 2.2 ms after S2 onset, when the right ventricle faces the cathode (Panel B, RV-), and 93.1 % at 2.6 ms for the opposite polarity (Panel B, LV-). The response to an 8-ms shock results in strong positive and negative polarization, which is sustained for a longer period compared with the response to a 1-ms shock. When the left ventricle faces the cathode, the fraction of activated tissue reaches 91.4 % at 3.8 ms (Panel C, LV-), and for the reverse polarity a similar fraction of activation of 91.1 % takes place at the 4.2-ms frame. In all hearts the response to an 8-ms shock was much stronger and significantly faster compared with a 0.2-ms shock ($P<0.05$, $N = 7$), and the response to a 1-ms shock was always faster than the response to both 0.2-ms and 8-ms shocks ($P<0.05$, $N = 7$).

Effects of Field Shock Duration on the Activation Dynamics

Fig. 2 demonstrates whole heart activation dynamics in response to different S2 duration in one of the heart preparations. It is seen that for both polarities the shortest shocks (black color, upper row) exhibit slower upstroke velocities than shocks with longer durations (lighter traces). The negative polarization is evident during S2 stimulation as a brief downward deflection at the time of S2. The fluorescence intensity in the time-duration plot (second row) represents the change of activation time with increasing shock duration. The horizontal black line is hyperpolarization, which becomes thicker with S2 extension. The time-duration plot also indicates that faster activation is caused by S2 stimulation of intermediate duration for either shock polarity. To better show upstroke dynamics, the traces during and soon after shock termination were magnified and are presented in the third row. Hyperpolarization after shock onset can be clearly observed in each curve, including the traces resulting from RV- and LV- shocks of 0.1 and 0.2-ms durations, though in these cases hyperpolarization of the left and right ventricles is of small magnitude and therefore has a minimal contribution in the averaged signal. For all other shock durations and polarities, the negative polarization is strong and reveals itself in the whole heart activation dynamics. The slowest activations correspond to shortest shock durations of 0.1

and 0.2 ms. As the duration of the shock grows longer, the stronger hyperpolarization dominates in averaged fluorescence and delays the onset of the response and ventricular activation.

The change in the AT histogram as a result of shock duration is displayed in Fig. 3. The corresponding AT maps are shown as inserts. The S2 with 0.1 ms duration produces very slow and heterogeneous propagation. The increase in shock duration to 0.4 ms causes bimodal AT distribution with maxima at 0.9 ms and 2.5 ms for RV- shock and at 1.3 ms and 2.1 ms for shock of reverse polarity. The first fast peak reflects the activation of the virtual cathode area, whereas the second hump signifies activation of the rest tissue. The 1-ms shock generates fast and homogeneous propagation with maxima of AT distribution at 1.3 ms for both polarities. The successive increase of shock duration to 8 ms causes the histogram to become broader and smaller in amplitude. Such a change is due to hyperpolarization at the virtual anode region, which becomes stronger with S2 extension and impedes rapid activation of the entire heart. The behavior of the AT distribution change is similar for shocks of normal and reverse polarity.

Fig. 4 shows the total mean AT as a function of shock duration and polarity measured in seven separate experiments. Because of high shock strength (50 V/cm), total mean AT decreases rapidly with increasing duration until 0.8 ms. The fastest total mean AT is 1.55 ± 0.27 ms and 1.63 ± 0.21ms (N = 7) and corresponds to shock duration of 0.8 ms for RV- and LV- shocks, respectively. Further extension of the shock duration results in delay in activation in both normal and reverse polarities. The total mean AT measured for 3, 5, and 8-ms shocks is significantly longer than this for 0.8-ms and 1-ms shocks for both polarities. The increasing S2 duration to 8 ms delays total mean AT to 2.32 ± 0.41 ms and 2.37 ± 0.3 ms (N = 7) for RV- and LV- correspondingly. There is no significant difference in total mean AT between two polarities when compared for the same S2 duration.

Analysis of the Right and Left Ventricle Regions of Interest

Because two ventricular chambers activate differently depending on the field direction, we analyzed separately the regions of interest during LV- and RV- shocks. Fig. 5 displays mean

AT in individual regions on the right and left ventricle as a result of shock duration and polarity. The regions of interest in the right and left ventricles are depicted in activation maps with gray and black rectangles, respectively. Two curves exhibit similar dynamics: abrupt descent when shock duration starts to increase, local minimum positioned between 0.4-ms and 0.8-ms S2, and then ascent of the curve with subsequent extending of the shock. The local minimum and ascending phase is more evident in curves generated from hyperpolarized chambers, whereas for chambers facing the cathode there is little change in mean AT for shocks longer than 1 ms. The dip appears earlier in the curves created from depolarized chambers and indicates very fast activation, which corresponds to 0.91 ± 0.16 ms and 0.84 ± 0.17 ms (N = 36) at shock duration of 0.4 ms for normal and reverse polarity, respectively. In the curves generated from hyperpolarized chambers, the dip occurs later and corresponds to AT of 2.02 ± 0.38 ms at 1-ms shock and 2.07 ± 0.39 ms (N = 36) at 0.8-ms shock for RV- and LV- shock, respectively. It is also evident that activation of negative polarized regions is significantly delayed for all shock durations compared with those for positive polarized regions of interest. The activation maps presented in the lower row clearly demonstrate the difference in activation pattern depending on the shock duration and polarity.

To characterize further the differences in right and left ventricle activation in response to different shock duration and polarity, F_{avg} was computed for regions of interest indicated in Fig. 5 and displayed in Fig. 6. The traces were aligned according to time of shock termination and represent activation during and immediately after the shock. Fig. 6 clearly illustrates dramatically different activation dynamics of the regions in the right and left ventricles caused by change in field direction. In the upper row for RV- shock, when the right ventricle faces the cathode, F_{avg} traces for the right ventricle region reveal slow activation for shock durations of 0.1 and 0.2 ms, but for all longer shock durations the activation is rapid and starts at the shock onset. Negative polarization is very prominent in F_{avg} traces computed from the left ventricle facing the anode, especially at long and intermediate shock durations. In general, activation of the left ventricle is much slower in comparison with the right ventricle. The traces from the left ventricle region of

interest in response to shock durations of 3, 5, and 8 ms exhibit complex dynamics, which has four phases: negative polarization with shock onset, fast depolarization, slow depolarization, and sharp increase in upstroke velocity after shock termination. The hyperpolarization in the F_{avg} traces lasts for approximately 1.5 ms for shock durations of 1.5 ms and greater. The increase in shock duration did not lengthen the time of hyperpolarization. In the lower row, the field direction was reversed so that negative polarization is observed in all of the right ventricle traces and four-phase behavior is evident for shocks of long duration. In this case, activation for the left ventricle is stronger and faster than for the right ventricle.

Discussion

The existence of virtual electrodes in the heart as a result of point stimulation was first demonstrated in 1991 (34) and was fully consistent with the predictions of the cardiac bidomain model (25). Subsequently, it became clear that virtual cathodes and anodes supported four different modes of cardiac activation (32). As the significance of virtual electrodes was more widely appreciated, it became clear that they provided the long-sought mechanism for large-scale electrical defibrillation of the heart (4,7,31,33). Most recently, an analysis of global cardiac activation time versus shock strength (20) provided insights into how the effect of distributed virtual electrodes depended upon shock strength, but did not address the source of these distributed virtual electrodes. This result contributed to the development of low-energy electrical control of cardiac rhythm disturbances, where several small shocks were shown to be more effective in halting fibrillation than one large one because of the contributions of virtual electrodes that arise from cardiac heterogeneities produced by the branching structure of the cardiac vasculature (13,19). However, none of these studies resolved the long-running question as to why imaging of activation of the entire heart by field stimulation demonstrated strong virtual cathodes but not the corresponding virtual anodes. We hypothesized that these virtual anodes were transient and were very quickly overrun by activation from anodal break or by wave

fronts propagating into them from adjacent virtual cathodes. As the speed of CCD cameras increased to 5,000 frames per second and we developed a custom defibrillator capable of strong defibrillation shocks (~100 J at 500 volts) with durations as short as 100 μs (21), we began to search for these missing virtual anodes. This paper represents a significant extension of our prior work (20) by exploring global activation of the heart not as a function of shock strength but as a function of shock duration, with an emphasis on very short shocks.

In this study we investigated for the first time the effects of duration of a strong uniform field shock on polarization pattern and activation dynamics in a diastolic whole heart preparation and tested the hypothesis that i) hyperpolarization caused by long shock durations increases AT and ii) activation versus shock duration curve contains a dip. In order to examine this hypothesis, we utilized our custom defibrillator (21) and a high-speed optical mapping system capable of imaging 5,000 frames per second to image the anterior surface of the isolated rabbit heart. In previous work we have shown that hyperpolarization is an important factor, which, if of sufficient size, can halt propagation, causing a paradoxical increase in AT for stronger shocks (20). The existence of hyperpolarization inside the bulk muscle adds complexity to this phenomenon (1). Our experimental evidence confirms the important role of hyperpolarization in cardiac tissue activation. Here we demonstrated complex behavior of the AT shock duration relationship, which has a local minimum for S2 duration of 0.8 and 1 ms. The activation of the heart corresponding to these shocks occurred significantly faster than during shorter or longer durations. We did not observe any statistically significant difference in AT for the same shock duration caused by change in field direction. The separate analysis of right and left ventricles revealed origination of the dip in AT shock duration curve predominantly in hyperpolarized areas of either right or left ventricle, and the activation of the depolarized chamber was significantly faster than the hyperpolarized.

During long shock duration we observed four different phases in F_{avg} from hyperpolarized areas: initial hyperpolarization at shock onset, rapid depolarization, slow depolarization, and fast depolarization after shock cessation. This complex morphology is similar to the morphology of the

optical traces obtained from porcine LV wedge preparations during transmural field stimulation (26). In particular, the second, third, and fourth phases we observed correspond to three phases detected by Sharifov et al. The difference is that they did not analyze hyperpolarization. However, careful examination of one of the curves in their paper (in Fig. 4 C) reveals transient, small magnitude hyperpolarization at shock onset in response to a shock of 38 V/cm of 10 ms in duration. This disagrees with our results, wherein we detect very prominent negative polarization for shocks with these approximate parameters. Such discrepancy could be explained by a difference between our whole heart and their wedge preparations. In response to strong shocks, the whole heart preparation exhibits rather uniform surface polarization of the right and left ventricle, so that hyperpolarization is not much obstructed by intermittent virtual cathodes, as happens during mapping wedge preparations.

Sharifov and Fast (26) hypothesized that the complex upstroke is a result of electrotonic interaction and spatial averaging of virtual electrode polarization at microscopic heterogeneities. The activation is very rapid at the virtual cathode, while at virtual anodes, negative polarization can occur for the duration of the shock. Spatial averaging by the imaging modality of adjacent virtual cathodes and anodes would lead to observations of multi-phasic upstrokes. When a homogeneous electric field affects the whole heart, basically two types of the membrane polarization affect the heart. The surface polarization occupies a thin layer that extends to a few length constants (31) and is affected by tissue structure and fiber orientation with respect to the field lines (7). The bulk polarization occurs throughout the ventricular wall, mostly due to the specific fiber architecture, in particular the fiber curvature and rotation (7). Therefore, though the surface polarization at the tissue-bath interface dominates in the field-induced response, the fourth phase in upstroke of the optical signal more likely relates to bulk activation of deeper layers.

In conclusion, the results of our work are relevant to mechanisms responsible for defibrillation shock failure. It is considered that negative polarization creates excitable gaps and thus produces postshock excitable areas, which can serve as a substrate for existing or new wave

front precipitation (4). In this context the time of propagation through these areas is critical for defibrillation shock outcome. If this time is long enough for adjacent tissue to recover, the reentrant electrical activity can revive (30). Our data evidently demonstrate that strong hyperpolarization causes delay in excitation and thereby can hamper the success of the defibrillation.

Limitations

Along with known limitations of the use of BDM (2,18), in this study we did not image the posterior surface of the heart. This information would allow us to analyze and represent the fractional contribution of negative and positive polarization in activation time of the whole heart. However, we believe that it would not change the main results and conclusion of our work relating to the role of hyperpolarization and shock duration in activation dynamics of cardiac tissue.

Acknowledgment

This work was supported by the National Institutes of Health (R01 HL58241-11) through the American Recovery and Reinvestment Act of 2009 and by the Vanderbilt Institute for Integrative Biosystems Research and Education.

The authors thank Allison Price for assistance with the preparation of this manuscript.

Reference List

1. Ashihara, T., J. Constantino, and N. A. Trayanova. 2008. Tunnel propagation of postshock activations as a hypothesis for fibrillation induction and isoelectric window. Circ. Res. 102: 737-745 PM:18218982.
2. Biermann, M., M. Rubart, A. Moreno, J. Wu, A. Josiah-Durant, and D. P. Zipes. 1998. Differential effects of cytochalasin D and 2,3 butanedione monoxime on isometric twitch force and transmembrane action potential in isolated ventricular muscle: implications for optical measurements of cardiac repolarization. J. Cardiovasc. Electrophysiol. 9: 1348-1357 PM:9869534.
3. Cheng, D. K., L. Tung, and E. A. Sobie. 1999. Nonuniform responses of transmembrane potential during electric field stimulation of single cardiac cells. Am. J. Physiol 277: H351-H362 PM:10409215.
4. Efimov, I. R., F. Aguel, Y. Cheng, B. Wollenzier, and N. Trayanova. 2000. Virtual electrode polarization in the far field: implications for external defibrillation. Am. J. Physiol Heart Circ. Physiol 279: H1055-H1070 PM:10993768.
5. Efimov, I. R., and V. P. Nikolski. 2003. Diastolic shocking experience: do virtual electrodes exist only during systole? J. Cardiovasc. Electrophysiol. 14: 1223-1224 PM:14678139.
6. Entcheva, E., J. Eason, I. R. Efimov, Y. Cheng, R. Malkin, and F. Claydon. 1998. Virtual electrode effects in transvenous defibrillation-modulation by structure and interface: evidence from bidomain simulations and optical mapping. J. Cardiovasc. Electrophysiol. 9: 949-961 PM:9786075.
7. Entcheva, E., N. A. Trayanova, and F. J. Claydon. 1999. Patterns of and mechanisms for shock-induced polarization in the heart: a bidomain analysis. IEEE Trans. Biomed. Eng 46: 260-270 PM:10097461.

8. Fast, V. G., S. Rohr, A. M. Gillis, and A. G. Kleber. 1998. Activation of cardiac tissue by extracellular electrical shocks: formation of 'secondary sources' at intercellular clefts in monolayers of cultured myocytes. Circ. Res. 82: 375-385 PM:9486666.
9. Fast, V. G., S. Rohr, and R. E. Ideker. 2000. Nonlinear changes of transmembrane potential caused by defibrillation shocks in strands of cultured myocytes. Am. J. Physiol Heart Circ. Physiol 278: H688-H697 PM:10710335.
10. Fishler, M. G. 1998. Syncytial heterogeneity as a mechanism underlying cardiac far-field stimulation during defibrillation-level shocks. J. Cardiovasc. Electrophysiol. 9: 384-394 PM:9581954.
11. Gillis, A. M., V. G. Fast, S. Rohr, and A. G. Kleber. 1996. Spatial changes in transmembrane potential during extracellular electrical shocks in cultured monolayers of neonatal rat ventricular myocytes. Circ. Res. 79: 676-690 PM:8831491.
12. Gray, R. A., D. J. Huelsing, F. Aguel, and N. A. Trayanova. 2001. Effect of strength and timing of transmembrane current pulses on isolated ventricular myocytes. J. Cardiovasc. Electrophysiol. 12: 1129-1137 PM:11699521.
13. Gray, R. A., and J. P. Wikswo. 2011. Cardiovascular disease: Several small shocks beat one big one. Nature 475: 181-182 http://dx.doi.org/10.1038/475181a.
14. Holcomb, M. R., J. M. Devine, R. Harder, and V. Y. Sidorov. 2012. Continuous-waveform constant-current isolated physiological stimulator. Rev. Sci. Instrum. 83: 044303 PM:22559554.
15. Hooks, D. A., K. A. Tomlinson, S. G. Marsden, I. J. LeGrice, B. H. Smaill, A. J. Pullan, and P. J. Hunter. 2002. Cardiac microstructure: implications for electrical propagation and defibrillation in the heart. Circ. Res. 91: 331-338 PM:12193466.
16. Krassowska, W., and M. S. Kumar. 1997. The role of spatial interactions in creating the dispersion of transmembrane potential by premature electric shocks. Ann. Biomed. Eng 25: 949-963 PM:9395041.

17. Latimer, D. C., and B. J. Roth. 1999. Effect of a bath on the epicardial transmembrane potential during internal defibrillation shocks. IEEE Trans. Biomed. Eng 46: 612-614 PM:10230141.

18. Liu, Y., C. Cabo, R. Salomonsz, M. Delmar, J. Davidenko, and J. Jalife. 1993. Effects of diacetyl monoxime on the electrical properties of sheep and guinea pig ventricular muscle. Cardiovasc. Res. 27: 1991-1997 PM:8287408.

19. Luther, S., F. H. Fenton, B. G. Kornreich, A. Squires, P. Bittihn, D. Hornung, M. Zabel, J. Flanders, A. Gladuli, L. Campoy, E. M. Cherry, G. Luther, G. Hasenfuss, V. I. Krinsky, A. Pumir, R. F. Gilmour, Jr., and E. Bodenschatz. 2011. Low-energy control of electrical turbulence in the heart. Nature 475: 235-239 PM:21753855.

20. Maleckar, M. M., M. C. Woods, V. Y. Sidorov, M. R. Holcomb, D. N. Mashburn, J. P. Wikswo, and N. A. Trayanova. 2008. Polarity reversal lowers activation time during diastolic field stimulation of the rabbit ventricles: insights into mechanisms. Am. J. Physiol Heart Circ. Physiol 295: H1626-H1633 PM:18708441.

21. Mashburn, D. N., S. J. Hinkson, M. C. Woods, J. M. Gilligan, M. R. Holcomb, and J. P. Wikswo. 2007. A high-voltage cardiac stimulator for field shocks of a whole heart in a bath. Rev. Sci. Instrum. 78: 104302 PM:17979442.

22. Mazeh, N., and B. J. Roth. 2009. A mechanism for the upper limit of vulnerability. Heart Rhythm 6: 361-367 PM:19251212.

23. Plonsey, R., and R. C. Barr. 1986. Effect of microscopic and macroscopic discontinuities on the response of cardiac tissue to defibrillating (stimulating) currents. Med. Biol. Eng Comput. 24: 130-136 PM:3713273.

24. Plonsey, R., and R. C. Barr. 1986. Inclusion of junction elements in a linear cardiac model through secondary sources: application to defibrillation. Med. Biol. Eng Comput. 24: 137-144 PM:3713274.

25. Sepulveda, N. G., B. J. Roth, and J. P. Wikswo, Jr. 1989. Current injection into a two-dimensional anisotropic bidomain. Biophys. J. 55: 987-999.

26. Sharifov, O. F., and V. G. Fast. 2003. Optical mapping of transmural activation induced by electrical shocks in isolated left ventricular wall wedge preparations. J. Cardiovasc. Electrophysiol. 14: 1215-1222 PM:14678138.

27. Sidorov, V. Y., M. C. Woods, P. Baudenbacher, and F. Baudenbacher. 2005. Examination of stimulation mechanism and strength-interval curve in cardiac tissue. Am. J. Physiol Heart Circ. Physiol 289: H2602-H2615 PM:16100241.

28. Sidorov, V. Y., M. C. Woods, and J. P. Wikswo. 2003. Effects of elevated extracellular potassium on the stimulation mechanism of diastolic cardiac tissue. Biophys. J. 84: 3470-3479 PM:12719272.

29. Sobie, E. A., R. C. Susil, and L. Tung. 1997. A generalized activating function for predicting virtual electrodes in cardiac tissue. Biophys. J. 73: 1410-1423 PM:9284308.

30. Trayanova, N., G. Plank, and B. Rodriguez. 2006. What have we learned from mathematical models of defibrillation and postshock arrhythmogenesis? Application of bidomain simulations. Heart Rhythm. 3: 1232-1235 PM:17018358.

31. Trayanova, N. A., B. J. Roth, and L. J. Malden. 1993. The response of a spherical heart to a uniform electric field: a bidomain analysis of cardiac stimulation. IEEE Trans. Biomed. Eng 40: 899-908 PM:8288281.

32. Wikswo, J. P., Jr., S.-F. Lin, and R. A. Abbas. 1995. Virtual electrodes in cardiac tissue: a common mechanism for anodal and cathodal stimulation. Biophys. J. 69: 2195-2210.

33. Wikswo, J. P., and B. J. Roth. 2009. Virtual electrode theory of pacing. In Cardiac bioelectric therapy: Mechanisms and practical implications. I. Efimov, M. Kroll, and P. Tchou, editors. Springer, 283-330.

34. Wikswo, J. P., Jr., T. A. Wisialowski, W. A. Altemeier, J. R. Balser, H. A. Kopelman, and D. M. Roden. 1991. Virtual cathode effects during stimulation of cardiac muscle: Two - dimensional in-vivo measurements. Cardiovasc. Res. 68: 513-530.

35. Zemlin, C. W., S. Mironov, and A. M. Pertsov. 2006. Near-threshold field stimulation: intramural versus surface activation. Cardiovasc. Res. 69: 98-106 PM:16226236.

36. Zhou, X., S. B. Knisley, W. M. Smith, D. Rollins, A. E. Pollard, and R. E. Ideker. 1998. Spatial changes in the transmembrane potential during extracellular electric stimulation. Circ. Res. 83: 1003-1014 PM:9815148.

37. Zhou, X., W. M. Smith, D. L. Rollins, and R. E. Ideker. 1996. Transmembrane potential changes caused by shocks in guinea pig papillary muscle. Am. J. Physiol 271: H2536-H2546 PM:8997315.

Figure Legends

FIGURE 1. The V_m distribution as a function of the time in response to 50 V/cm shocks that were either (*A*) short (0.2 ms), (*B*) intermediate (1.0 ms), or (*C*) long (8.0 ms). For RV-, the electric field is applied from right to left, and for LV-, from left to right. The data were normalized according to change in fluorescence during S1 response.

FIGURE 2. The whole-heart integrated fluorescence, F_{avg}, as a function of the shock duration and polarity. The shock strength is 50 V/cm. Left and right columns: Analysis of activation times (ATs) in response to shocks of RV- and LV- polarities, respectively. Upper row: F_{avg} for each shock duration with the shortest shocks represented by the darkest ink. Second row: Time-duration plot. Third row: Magnified view of the first 5 ms of F_{avg}.

FIGURE 3. Histograms of the AT distribution caused by the shock duration of 0.1 ms, 0.4 ms, 1 ms, and 8 ms. Inserts display the corresponding AT maps.

FIGURE 4. Mean AT, measured from the onset of the shock, as a function of shock duration. The data represent seven separate experiments. Error bars indicate the SD of the mean. For cathode faced to right ventricle: $^{\ddagger}P < 0.05$ compared with mean ATs in response to shock duration of 0.1, 0.2, 0.8, and 1 ms, and $^{\#}P < 0.05$ compared with mean ATs for shock duration of 0.8, 1, 3, 5, and 8 ms. For cathode faced to left ventricle: $^{\dagger}P < 0.05$ compared with mean ATs in response to

shock duration of 0.1, 0.2, 0.8, and 1, and $^{*}P < 0.05$ compared with mean ATs for shock duration of 0.8, 1, 3, 5 and 8 ms.

FIGURE 5. AT of right and left ventricle regions of interest as a function of shock duration and polarity. Lower row shows whole heart AT maps for shock duration of 0.2, 1, and 8 ms. Gray and black rectangles on the maps depict the right and left ventricle regions of interest. *P < 0.01 compared AT in right and left ventricle regions of interest.

FIGURE 6. F_{avg} for right and left ventricle regions of interest as a function of shock duration and polarity. The vertical arrow indicates the termination of the shock, and all waveforms were aligned by their S2 termination to emphasize both the hyperpolarization of the virtual anodes that occurs at the beginning of each shock, and the rapid activation that occurs immediately at the end of the shock, particularly for the shorter shocks. The time scale was chosen to show activation dynamics during and immediately after the shocks. Left column: F_{avg} for the right ventricle region of interest. Right column: F_{avg} for the left region of interest. Upper row: RV-stimulation. Lower row: LV- stimulation.

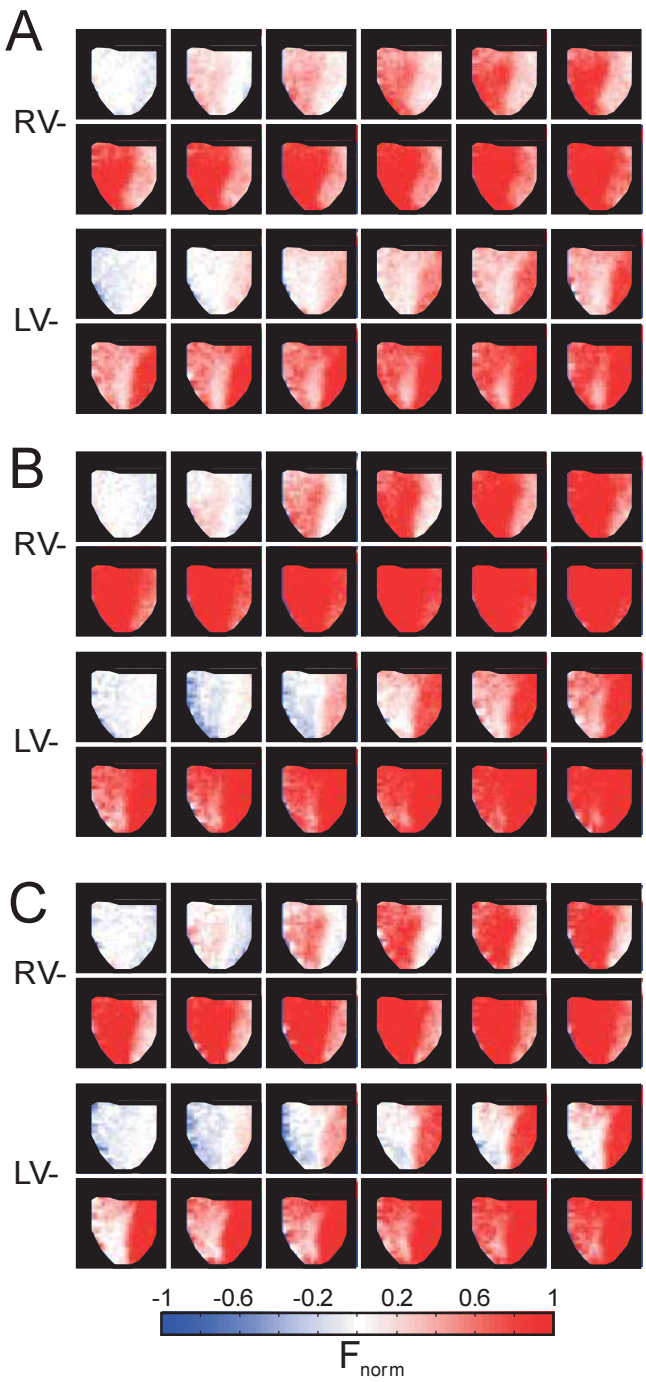

Figure 1.

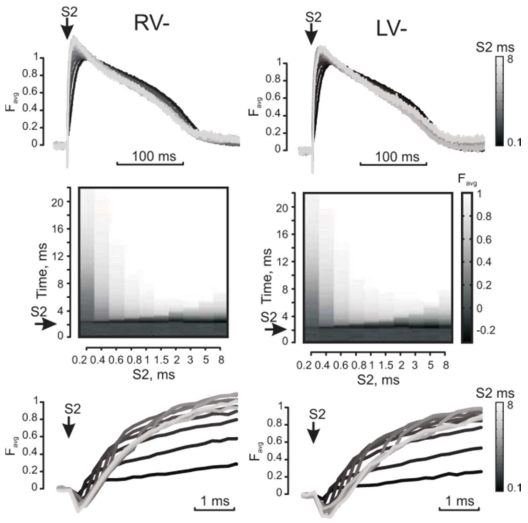

Figure 2.

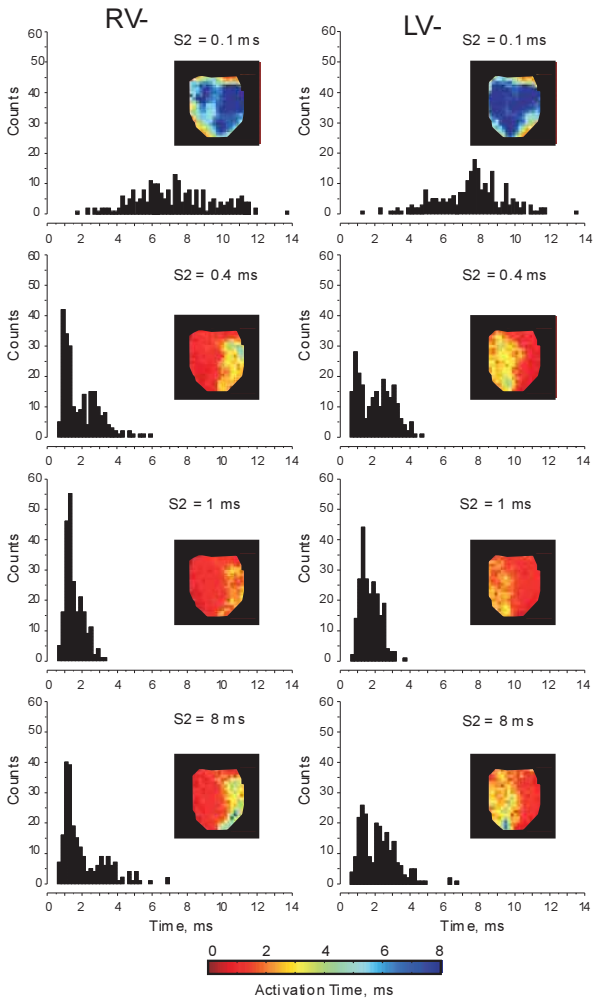

Figure 3.

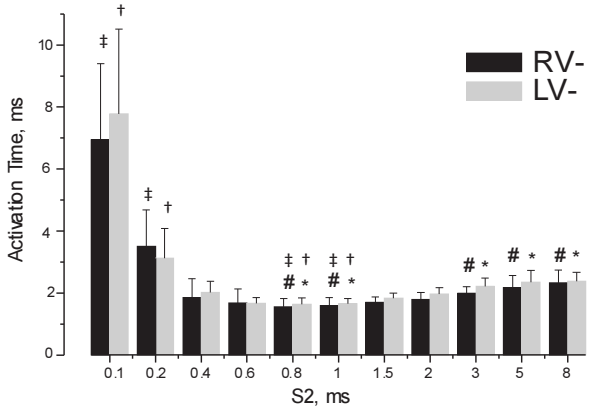

Figure 4.

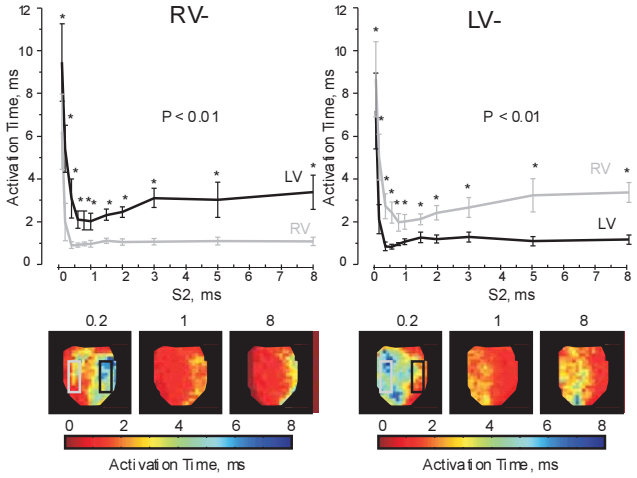

Figure 5.

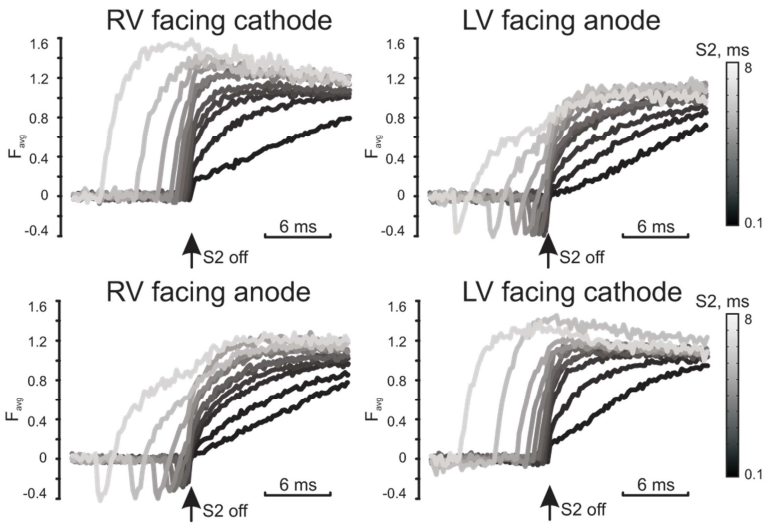

Figure 6.